Cutting forces prediction in orthogonal turn-milling operations

Mondragon Unibertsitatea **Goi Eskola Politeknikoa**

to obtain the title of

Doctor in Applied Engineering

Presented by

Harry Yasir Otálora Ortega

Supervised by

Pedro Jose Arrazola Arriola
Patxi Aristimuño Osoro

In Arrasate 2021

Declaration of originality

Hereby I, Harry Yasir Otálora Ortega declare, that this document is my original authorial work, which I have worked out by my own. All sources, references and literature used or excerpted during elaboration of this work are properly cited and listed in complete reference to the due source.

Yo Harry Yasir Otálora Ortega declaro que esta tesis es original, fruto de mi trabajo personal, y que no ha sido previamente presentado para obtener otro título o calificación profesional. Las ideas, formulaciones, imágenes, ilustraciones tomadas de fuentes ajenas han sido debidamente citadas y referenciadas.

Arrasate, 2021

Abstract

The development of more versatile machine tools is addressing the increased market demand for more complex shapes and workpieces with strict tolerances. This has resulted in more complicated kinematics, designed to align the cutting tool with the intricate workpiece surface for its production. New machining operations supported in the advanced kinematics are emerging such as turn-milling operations, in which rotational movements of the workpiece are coupled with conventional milling operations. Turn-milling presents significant advantages over conventional turning: such as lower cutting forces, temperatures, circularity errors, and surface roughness. In addition, tool life is longer, and the operation generates intermittent chips which eliminates the continuous chip nests typical in turning. Despite these advantages however, turn-milling is difficult to operate in the optimal process window because it requires an increased number of process parameters, making their optional selection challenging. The prediction of process performance can be greatly enhanced by modeling, however traditional milling models do not consider turn-milling parameters evidencing the need for specific models for these operations. To address this gap, this thesis presents analytical and numerical models for orthogonal turn-milling operations to determine the uncut chip geometry and predict cutting forces. These models consider workpiece rotation, tool eccentricity, cutting tool profile, and the process kinematics in the accurate determination of the uncut chip geometry. The models were validated theoretically and experimentally presenting good correlation in each of the validation tests. The models were used to confirm the cutting conditions suggested by the cutting tool manufacturer in a real workpiece manufacturing plan. The engineered cutting conditions showed a reduction of 20% in the overall manufacturing time. Additionally, the cutting edges were used more efficiently decreasing the number of inserts needed to finish the part, which in turn reduced the total manufacturing cost.

Laburpena

Mekanizazio lan mota desberdinak egiteko gai diren makina erremintak garatzeak forma oso konplexuak eta aldi berean tolerantzia estuak dituzten piezen eskaera gero eta handiagoari erantzuten dio. Horrek, erreminta eta landu beharreko piezaren azalera lerrokatu ahal izateko, makinaren zinematika korapilatsuagoa eskatzen du. Zinematika aurreratu hauen bidez mekanizazio eragiketa berriak sortzen ari dira, esate baterako, torneatze-fresatze eragiketetan, ohiko fresaketak dituen mugimenduei piezaren biraketa-mugimendu sinkronizatuak gehitu behar zaizkio. Torneatze-fresatzeak abantaila garrantzitsuak ditu torneaketa konbentzionalaren aurrean: esate baterako, ebaketa-indar, tenperaturak eta biribiltasun akats txikiagoak eta gainazal zimurtasun leunagoa. Gainera, erremintaren bizitza luzeagoa da eta luzera txikiko txirbilak sortzen ditu, torneaketan ohikoak diren txirbil anabasak ekidituz. Hala ere, abantaila horiek gorabehera, torneatze-fresatzean zaila da prozesuaren leiho optimoan funtzionatzea, prozesuak parametro kopuru handiagoa baitu, prozesu honen hautaketa erronka bihurtuz. Prozesu errendimenduaren aurreikuspena asko hobetu daiteke modelizazioarekin, hala ere, fresatze eredu tradizionalek ez dituzte torneatze-fresatze parametro guztiak kontuan hartzen, torneatze-fresatze eredu zehatzen beharra dagoela frogatuz. Hutsune horri aurre egiteko, tesi honek torneatze-fresatze ortogonaleko eragiketen eredu analitikoak eta numerikoak aurkezten ditu, ebakitzen den txirbilaren geometria kalkulatu eta ebaketa-indarrak aurreikusteko. Eredu hauek piezaren biraketa, errementaren eszentrikotasuna, errementaren profila eta prozesuaren zinematika kontuan hartzen dituzte ebakitzen den txirbilaren geometria zehaztasunez kalkulatuz. Ereduak era teorikoan eta esperimentalean balioztatu dira, egiaztapen proba bakoitzean korrelazio ona erakutsiz beraien artean. Modeloak erabiliz hautatutako ebaketa baldintzak eta erreminta fabrikatzaileak proposaturikoak konparatu dira pieza baten mekanizazioan. Modeloaren laguntzaz hautatutako ebaketa baldintzek piezaren fabrikazio denbora totala %20 murriztu dute. Gainera, errementaren ebaketa ertzak modu eraginkorragoan erabili ziren, pieza amaitzeko behar ziren aldaketa kopurua murriztuz, eta horrek fabrikazioaren kostu totala murrizten zuen.

Resumen

El desarrollo de máquinas herramienta más versátiles responde a la creciente demanda del mercado de formas más complejas y piezas con tolerancias estrictas. Esto ha dado lugar a cinemáticas más complicadas, diseñadas para alinear la herramienta de corte con la intrincada superficie de la pieza para su producción. Están surgiendo nuevas operaciones de mecanizado apoyadas en la cinemática avanzada, como las operaciones de torneado-fresado, en las que los movimientos de rotación de la pieza se acoplan a las operaciones de fresado convencionales. El torneado-fresado presenta importantes ventajas sobre el torneado convencional: como menores fuerzas de corte, temperaturas, errores de circularidad y rugosidad superficial. Además, la vida de la herramienta es más larga y la operación genera virutas intermitentes que eliminan los nidos de virutas continuos típicos del torneado. Sin embargo, a pesar de estas ventajas, el torneado es difícil de operar en la ventana óptima del proceso porque requiere un número mayor de parámetros de proceso, lo que hace que su selección opcional sea un reto. La predicción del rendimiento del proceso puede mejorarse en gran medida mediante el modelado, sin embargo los modelos tradicionales de fresado no consideran los parámetros de torneado-fresado evidenciando la necesidad de modelos específicos para estas operaciones. Para abordar esta carencia, esta tesis presenta modelos analíticos y numéricos para las operaciones de torneado-fresado ortogonal con el fin de determinar la geometría de la viruta por cortar y predecir las fuerzas de corte. Estos modelos consideran la rotación de la pieza, la excentricidad de la herramienta, el perfil de la herramienta de corte y la cinemática del proceso en la determinación precisa de la geometría de la viruta por cortar. Los modelos fueron validados teórica y experimentalmente presentando una buena correlación en cada una de las pruebas de validación. Los modelos se utilizaron para confirmar las condiciones de corte sugeridas por el fabricante de herramientas de corte en un plan de fabricación de piezas reales. Las condiciones de corte diseñadas mostraron una reducción del 20% en el tiempo total de fabricación. Además, los filos de corte se utilizaron de forma más eficiente, disminuyendo el número de insertos necesarios para terminar la pieza, lo que a su vez redujo el coste total de fabricación.

"There is nothing impossible to him who will try"

— Alexander the Great —

This work is dedicated to my beloved wife Kerlys, who has been an unbreakable
support and inspiration in this wonderful adventure called life.

ACKNOWLEDGMENTS

Contents

List of Figures

List of Tables

NOMENCLATURE

Symbol	Description	Unit
β	Feed angle	rad
β_i	Friction angle fround from experimental trials	rad
$\beta_{\gamma16\alpha22}$	Friction angle of $\gamma16\alpha22$ geometry	rad
$\beta_{\gamma32\alpha6}$	Friction angle of $\gamma32\alpha6$ geometry	rad
$\beta_{n\gamma16\alpha22}$	Normalized friction angle of $\gamma16\alpha22$ geometry	rad
$\beta_{n\gamma32\alpha6}$	Normalized friction angle of $\gamma32\alpha6$ geometry	rad
$\mathrm{d}F_a(\phi)$	Differential of force in the axial direction	N
$\mathrm{d}F_p$	Penetration force	N
$\mathrm{d}F_r$	Radial force	N
$\mathrm{d}F_r(\phi)$	Differential of force in the radial direction	N
$\mathrm{d}F_t$	Tangential force	N
$\mathrm{d}F_t(\phi)$	Differential of force in the tangential direction	N
$\mathrm{d}r$	Differential of radius	mm
γ	rake angle	^{o}
κ	Tangential angle of the edge	rad
λ	Flute helix angle	rad
λ_e	Rotation angle in the end	rad
λ_f	Rotation angle in the flank	rad
$\overline{x_m}$	Material profile points position in x coordinate	mm
$\overline{x_t}$	Tool profile points position in x coordinate	mm
$\overline{y_m}$	Material profile points position in y coordinate	mm
$\overline{y_t}$	Tool profile points position in y coordinate	mm

$\overline{z_m}$	Material profile points position in z coordinate	mm
$\overline{z_t}$	Tool profile points position in z coordinate	mm
ϕ	Tool rotation angle	rad
ϕ_τ	Shear plane angle	rad
$\phi_{\lambda\{i,j\}}$	Phase angle of each point resulting from the helix angle	rad
ϕ_{eex}	End zone exit angle	rad
ϕ_{eex}	End zone exit angle	rad
ϕ_{est}	End zone start angle	rad
ϕ_{fex}	Flank zone exit angle	rad
ϕ_{fst}	Flank zone start angle	rad
ϕ_i	I line exit angle	rad
ϕ_{Mst}	M line start angle	rad
$\phi_{n\gamma16\alpha22}$	Normalized friction angle $\gamma16\alpha22$ geometry	rad
$\phi_{n\gamma32\alpha06}$	Normalized friction angle $\gamma32\alpha06$ geometry	rad
ϕ_{pist}	Internal profile starting angle	rad
ϕ_{th}	Angles between flutes with respect to the reference flute	rad
τ	Shear stress	N/mm^2
τ_i	Shear stress found from experimental trials	N/mm^2
θ	Workpiece rotation angle per tooth	rad
A	Instantaneous chip area	mm^2
$a_f(\phi)$	End zone thickness plane	mm
a_p	Depth of cut	mm
$a_p(\phi)$	Variable depth of cut of the flank zone	mm
c	Recurrent expression in coefficients detemination functions	–
$d\phi$	Differential of angle	rad
$d\phi_i$	Differential of angle in the ith position	rad
dA	Area of each element	mm^2
E	External vertical line (End zone)	mm
e	Eccentricity	mm
F_a	Total tool axial force	N

f_a	Axial feed	mm/(workpiece rev)
F_c	Cutting force	N
f_i	i^th trial feed or uncut chip thickness	mm
F_r	Total radial force	N
F_t	Total tangential force	N
f_t	Tangential distance	mm/(workpiece rev)
$F_x(\phi)$	Total force signal in X coordinate	N
$F_y(\phi)$	Total force signal in Y coordinate	N
f_z	Feed per tooth	mm/tooth
$F_z(\phi)$	Total force signal in Z coordinate	N
F_{ci}	i^th cutting measured force	N
F_{fi}	i^th feed measured force	N
F_{pc}	Power force	N
F_{qc}	Thrust force	N
$F_{xphn}(\phi)$	Phased force signal in X coordinate of the nth cutting edge	N
$F_{xrf}(\phi)$	Force in X coordinate referenced for a single edge pass	N
$F_{yphn}(\phi)$	Phased force signal in Y coordinate of the nth cutting edge	N
$F_{yrf}(\phi)$	Force in Y coordinate referenced for a single edge pass	N
$F_{zphn}(\phi)$	Phased force signal in Z coordinate of the nth cutting edge	N
$F_{zrf}(\phi)$	Force in Z coordinate referenced for a single edge pass	N
h_i	i^th cut chip thickness	mm
I	Finish end zone line (End zone)	mm
i	Row counter	–
j	Column counter	–
K_a	Axial cutting Coefficient	N/mm^2
K_r	Radial cutting Coefficient	N/mm^2
K_t	Tangential cutting Coefficient	N/mm^2
K_{cc}	Cutting coefficient	N/mm^2
K_{ce}	Friction or edge coefficient in the cutting direction	N/mm
K_{fc}	Feed coefficient	N/mm^2

K_{fe}	Friction or edge coefficient in the feed direction	N/mm
K_{pc}	Penetration cutting coefficient	N/mm^2
K_{pe}	Penetration friction coefficient	N/mm
K_{rc}	Radial cutting coefficient	N/mm^2
K_{re}	Radial friction coefficient	N/mm
K_{tc}	Tangential cutting coefficient	N/mm^2
K_{te}	Tangential friction coefficient	N/mm
L	Oblique feed line (End zone)	mm
l_s	Radial usable length of the egdge	mm
LM	Lag matrix to phase the whole uncut chip geometry	rad
M	Mid vertical line (End zone)	mm
n_t	Tool rotational speed	rpm
n_w	Workpiece rotational speed	rpm
O_t	Tool origin	mm
O_w	Workpiece origin	mm
p_e	External profile (Flank zone)	mm
p_i	Interior profile (Flank zone)	mm
p_{ii}	Inferior interior profile (End zone)	mm
P_{mi}	Material profile in the ith position	mm
P_{ti}	Tool profile in the ith position	mm
r_n	Nose radius or Insert radius	mm
r_t	Tool radius	mm
R_w	Workpiece radius	mm
RC	Compression ratio	–
rc_i	Compression ratio found from experimental trials	–
$t(\phi, r)$	Instantaneous chip thickness	mm
V_a	Axial Speed	mm/min
V_t	Tangential speed	mm/min
X	X coordinate	mm
X_t	Tool x coordinate	mm

X_w	Workpiece x coordinate	mm
Y	Y coordinate	mm
Y_t	Tool y coordinate	mm
Y_t+	Positive direction in the Y tool coordinate	mm
Y_w	Workpiece y coordinate	mm
Z	Z coordinate	mm
z	Number of cutting edges	–
Z_t	Tool z coordinate	mm
Z_w	Workpiece z coordinate	mm

1 | Introduction

There is a growing demand for complex geometries in a diverse range of industries (İç and Yurdakul, 2009), and they are used as functional parts of machinery or design pieces that give added value to a product. One reason to employ complex shapes is to integrate several functions in one piece, a typical example of this is the turbomachinery (Boynton et al., 1992; Zheng et al., 2012). In power generation manufacturing, complex geometries are designed to transform energy for a specific objective, and turn-milling operations among others are commonly employed to achieve these geometries. Examples of workpieces achieved by turn-milling are large-format crankshaft, landing gear, aeronautical combustion cases, aeronautical blades as shown in figure 1.1.
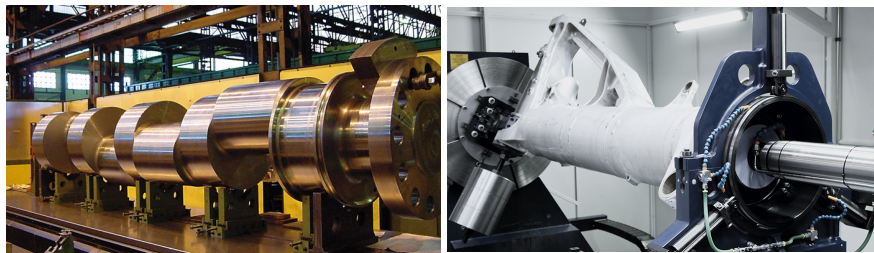
(a) *Large compressor crankshaft (Sideron, 2021).*

(b) *Aeronautical landing gear (Danobat, 2021).*
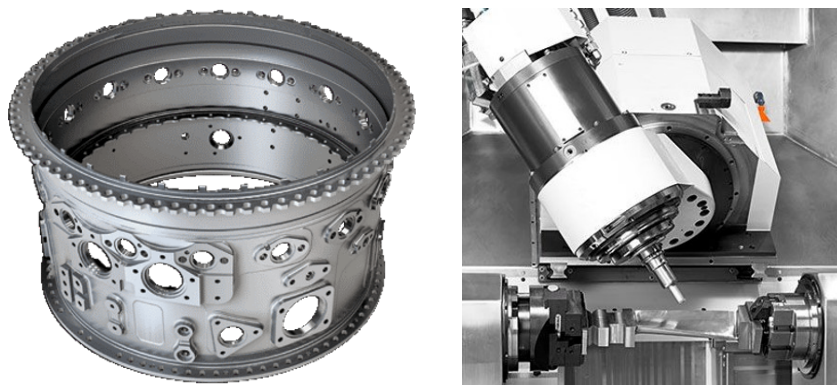
(c) *Aeronautical combustion case (Ingersoll, 2021).*

(d) *Aeronautical blade machining (Ferrotall, 2021).*

Figure 1.1: Examples of parts machined with turn-milling operations.

The machine tool sector impacts directly several markets and Europe is the leader continent of exportation as shown figure 1.2. The machine tool exports n has been affected for the crisis of 2020 considerably, however the market start to
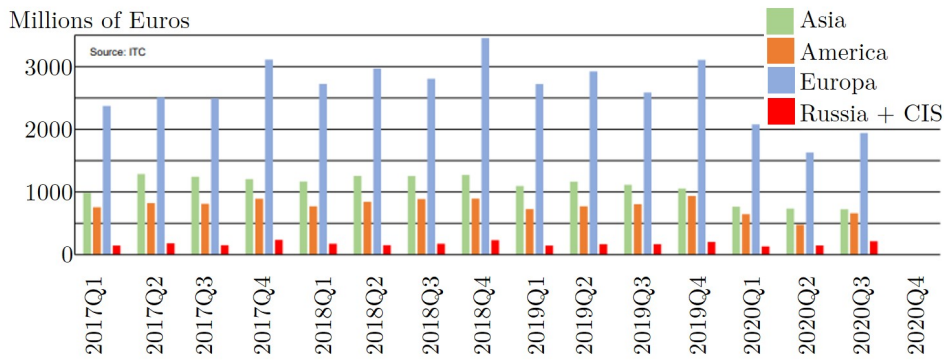
Figure 1.2: *Historical exports of machine tools in diverse markets (CECIMO, 2021).*

show reactivation signs in the third quarter of 2020. Even with the pandemic, the third quarter of 2020 reached almost 2000 million € just for Europe (CECIMO, 2021). As the increasing complexity of the workpiece is addressed by augmented axis machine tools which align the cutting tool with the surface of the component to be machined. These complex movements are achieved by adding controlled motions to the machine tool, resulting in increased linear and rotational degrees of freedom. The objective is to rotate the bulk material to reduce the number of clamp actions as much as possible; as spatial references are lost with each new clamping action. Additionally, small misalignments of the workpiece in the fastening process can induce tolerances errors. Figure 1.3 compares the vertical architecture of milling machines: A conventional 3-axis milling architecture that allow the tool spindle to move to he workpiece in the linear degrees of freedom (X, Y, Z) is depicted in figure 1.3 (a). On the other hand, figure 1.3 (b) illustrates a machining center with augmented axis of freedom, a 5-axis machine that is one of the most common configuration.

(a) *3-Axis milling machine, vertical architecture*

(b) *5-Axis machining center, rotary table configuration*
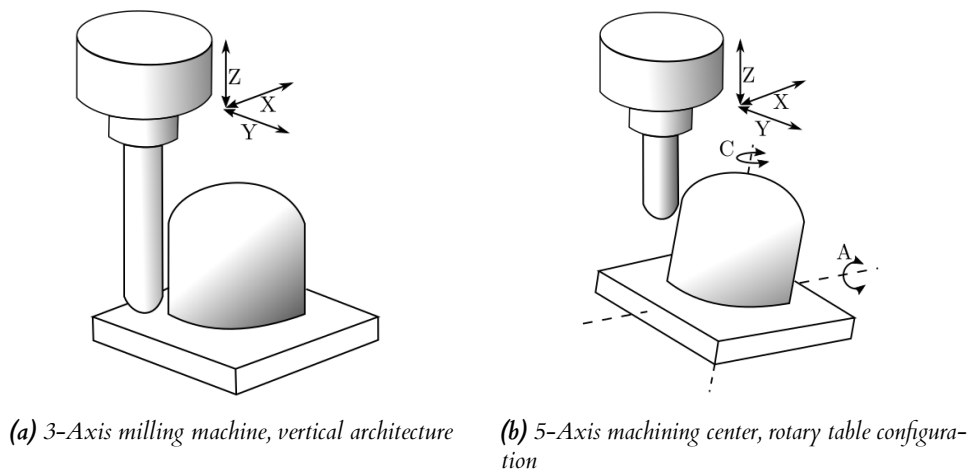
Figure 1.3: *Vertical architecture configuration milling machines.*

The increased versatility of the augmented axis machine tool does not exclude the production of simpler geometries. In fact, the additional axis can be blocked to produce 3-axis geometries. For this reason, there has been a marked increase in the produciton of multitasking machine tools (Anand, 2021), which are able to
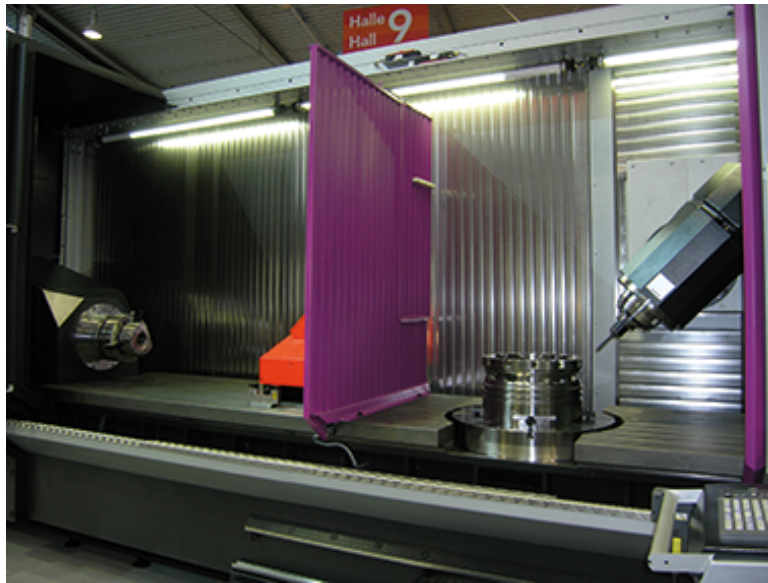
Figure 1.4: *Ibarmia ZVH multiprocess machining center (Ibarmia, 2020).*

perform milling and turning operations in the same machine tool, shortening the production chain and reducing the number of clamping actions. The machining center ZVH from Ibarmia is a clear example of multitasking design in the modern machine tool as shown in figure 1.4.

Table 1.1: *3 & 5-Axis Machine tool characteristics*

3-Axis Milling	Contours in 2D
	Only produces orthogonal features in the workpiece
	Simple contours in 3D
	Strict tolerances
5-Axis Milling	High convoluted surfaces
	More than 4 simultaneous axis movements during machining
	Can also produce non orthogonal features in the part
	Strict tolerances
	Low aspect ratio work pieces
	Shorter tool length

Table 1.1 summarizes the main characteristics of the 3 & 5 axis. Although 5-axis machines are more versatile than the 3-axis; they are also more expensive assets. 5-axis machines also present challenges when machining, due to the complex kinematics involved in moving the five axes simultaneously. One common examples of this is collisions between the tool and the machine tool fixtures.

5-axis machining centers open the window to new operations. One example is turn-milling, in which the surface is milled while the workpiece rotates around its center point. This operation has arisen from the need to achieve cylindroid surfaces impossible to manufacture through conventional turning. Depending on the machine tool architecture, it is possible to perform three turn-milling operations with different alignments of the tool and workpiece axes (Karaguzel et al., 2015b): Orthogonal, Tangential, and Coaxial, see figure 1.5.

(a) Orthogonal turn-milling   *(b) Tangential turn-milling*

(c) Coaxial turn-milling
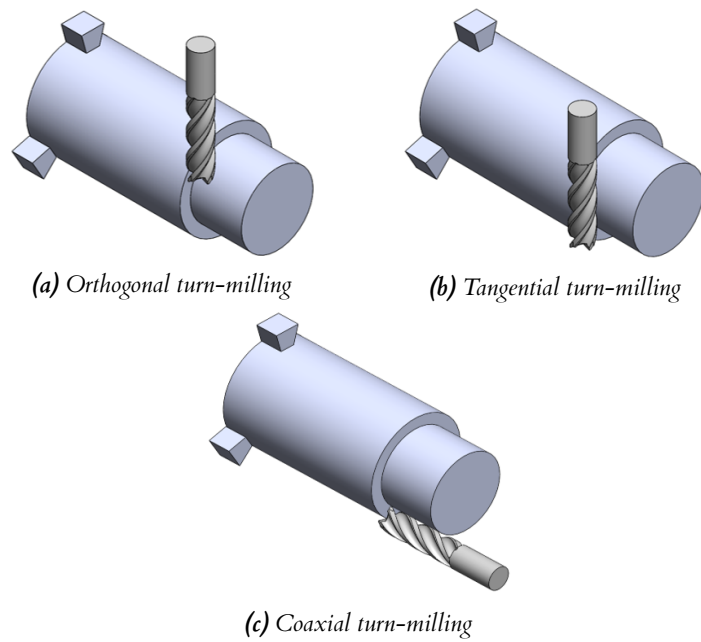
Figure 1.5: *Turn-milling operation classified by the rotational its rotational axes.*

The industrial applications of turn-milling are those cylindrical surfaces which are not achievable via conventional turning, for example, aeronautical combustion cases. These workpieces have a cylindrical or conic base with a set of bosses or holes to perform various tasks in the power generation process, see figure 1.6 (Rk, 2021).

Certain characteristics of turn-milling operations present advantages over the conventional turning. One characteristic is the relatively low workpiece spindle rotational speed. This feature is associated with the process kinematics and is of particular interest when manufacturing big format workpieces (Karaguzel et al., 2015b; Wu et al., 2014). One further advantage is that a relatively low surface roughness is achieved, whit values comparable with those resulting from grinding (Savas and Ozay, 2007). This has the effect of shortening the production chain, as less operation are necessary to achieve the finished part. In addition, tool life increased considerably in comparison with that of conventional milling in comparable cutting conditions (Karaguzel et al., 2015a). This makes turn-milling a feasible alternative to conventional turning when manufacturing hard-to-cut materials. The intermittent cutting typical in milling, presents lower cutting forces and temperatures compared with the continuous cutting in turning (Karaguzel et al., 2012). These decrements in the cutting forces and temperature benefits the thermo-mechanical behavior of the workpiece-tool set, resulting in lower geometrical errors (Karaguzel et al., 2012). Intermittent cutting also produces discontinuous chips, favoring chip management and preventing the chip nest typical in conventional turning (Karaguzel et al., 2012).

Despite these many advantages, turn-milling operations are not regularly operating in the optimal process window. This is due to the increased amount of parameters required to define the kinematics. The rotational movement of the workpiece is not considered by the traditional models developed for conventional
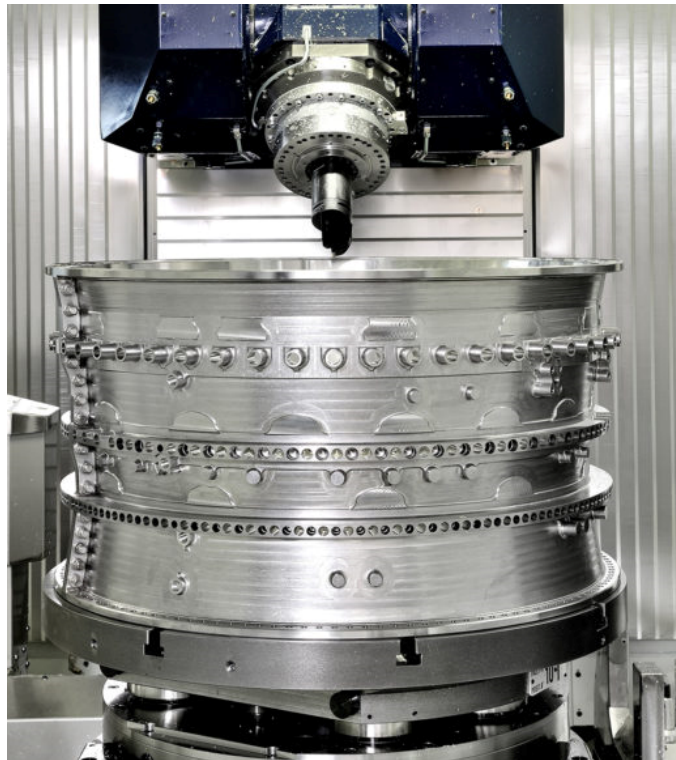
Figure 1.6: Aeronautical combustion case manufacturing Rk (2021).

milling, and it is not entirely clear how the kinematic parameters impact the operational variables such as width per pass or feed per tooth.

To address this gap, the main objective of this thesis is to improve the performance of orthogonal turn–milling operation using the cutting forces as limit of process indicator and the material removal rate as productivity indicator. To achieve this objective the following specific objectives are proposed:

1. To model the orthogonal turn–milling process to determine the cutting forces of the process.

2. To determine the effect of the eccentricity over the uncut chip geometry in orthogonal turn–milling operations.

3. To determine the combined effect of the tool profile and eccentricity considering torus and spherical tools.

4. To ascertain the cutting conditions provided by the manufacturer in turn–milling operations to reach improved material removal rates.

This thesis presents analytical and numerical models for orthogonal turn–milling operations to determine the uncut chip geometry and predict cutting forces. These models consider workpiece rotation, tool eccentricity, cutting tool profile, and the process kinematics in the accurate determination of the uncut chip geometry. These models contribute to the virtualization of the process by representing its behavior and opening the chance to implement them in CAD/CAE/CAM software or to develop specific process cutting conditions calculators. At its core, virtual manufacturing seeks to make available modeling tools to make informed manufacturing decisions that increase the workpiece

quality and reduce production costs.

This document is structured as follows:

The Chapter 2 is the State of the Art here is provided an overview of the literature related with turn–milling operations and cutting force prediction in machining. The Chapter 3 presents an analytical model of the orthogonal centric case with flat end mills in the large and small depth of cut regimens, where the uncut chip geometry is modeled and validated experimentally via cutting force prediction. Chapter 4 consider the eccentricity effect over the uncut chip geometry in flat end mills; where the model is experimentally validated via cutting force prediction. The chapter 5 presents the numerical model that considers eccentricity and tool profile (torus and ball end mills); where the model is validated experimentally via cutting forces and evaluates the effect of eccentricity in orthogonal turn–milling operations. The Chapter 6 presents an industrial application of the models in a workpiece that resembles an aeronautical combustion case; the turn–milling cutting conditions were confirmed through the models in Chapters 3 to 5. Chapter 7 present the conclusions raised from the development of this thesis and the future lines recommended from this academical exercise. Figure 1.7 presents a graphical structure of the thesis.

The research set out in this thesis resulted in two scientific papers published in reputable, first quartile journals. Additionally, a poster was presented at the 22th national congress of machine tools in Spain, and an oral presentation in the first manufacturing seminar between Colombia and Spain. These scientific developments are intended to contribute to the state of the art and provide a deeper understanding of the process and its application in industrial conditions.
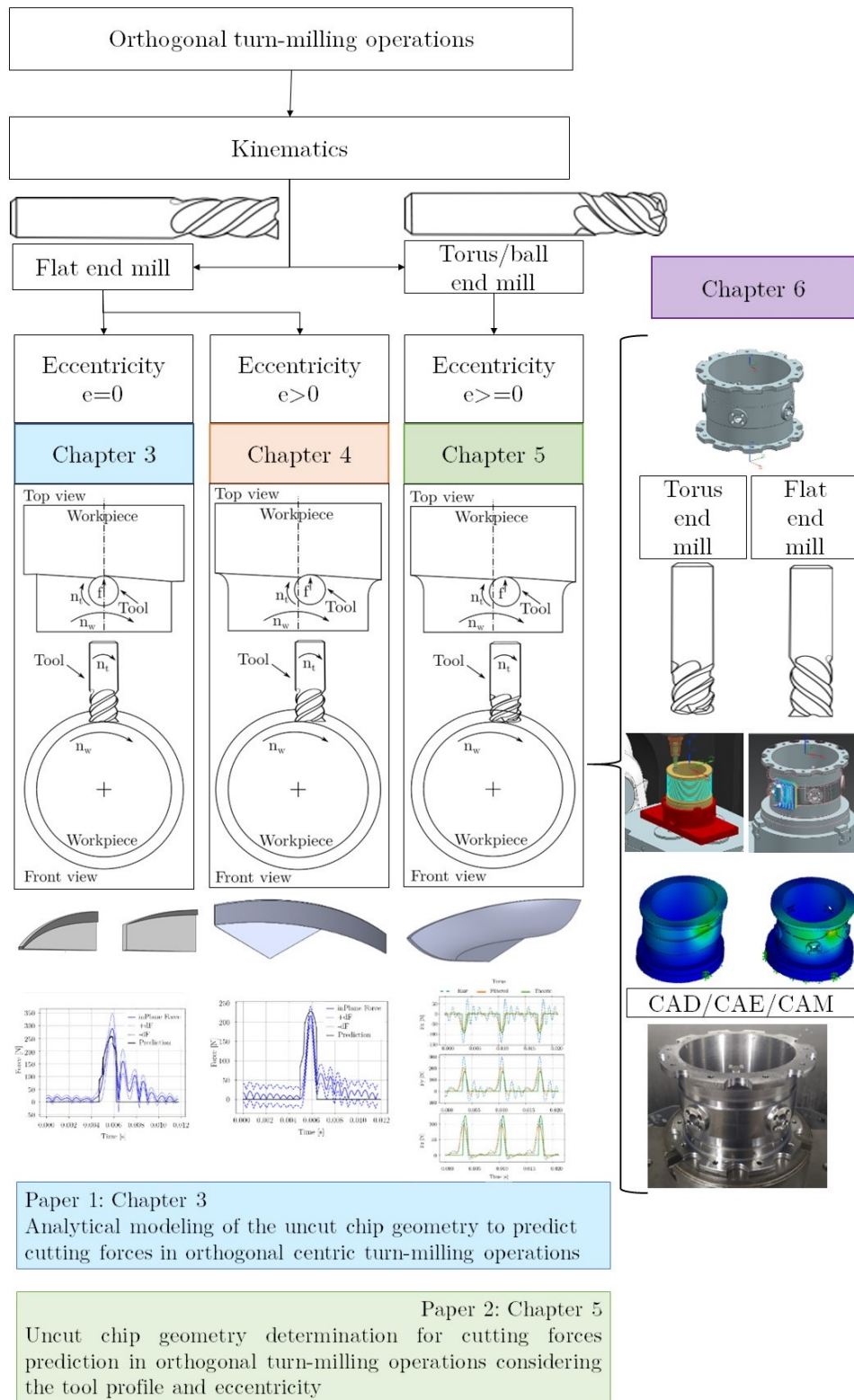
Figure 1.7: *Schematic structure of the thesis.*

2 | STATE OF THE ART

The State of the Art intends to show the evolution of the interest of several researchers that have dealt with turn-milling in their publications. This quest covers the scientific aspects of uncut chip geometry determination, cutting forces, vibrations, and cutting temperature. The industrial aspects covered are the tool wear, surface finishing, and geometrical errors. Publications in virtual machining and artificial intelligence are also considered due to the modeling nature of the thesis contribute to this knowledge area. Subsequently, is presented a critical review of the State of the Art in which the research opportunities are detected. The last section presents the research objectives and the hypothesis that support this thesis.

Turn-milling is not a simple combination of turning and milling; it uses the rotation movements of the cutting tool and workpiece to achieve the synthetic machining on the workpiece (Yuan et al., 2012). This machining process consists of the milling of the workpiece means while it rotates slowly. However, it is possible to align the tool in diverse orientations. In this context, the process has been cataloged by the orientation of the tool axis to the workpiece axis. The machining case selection depends on the application, and machine tool architecture presenting differences between each other, see figure 2.1. These differences depend on the cutting zone of the edge that performs the chip removal modifying the uncut chip geometry (Karaguzel et al., 2015b). Despite the differences that the cases could present, they have seven parameters in common. These parameters define the kinematics of the machining process. Figure 2.1 illustrates the cases and the parameters for each one deeply. These parameters are presented below with the variable name:

- Work piece radius (R_w)
- Work piece rotational speed (n_w)
- Tool radius (r_t)
- Tool rotational speed (n_t)
- Axial feed (f_a)
- Depth of cut (a_p)
- Number of teeth (z)
- Eccentricity (e) only for eccentric turn-milling

The eccentricity is the only parameter exclusive of orthogonal eccentric turn-milling, see figure 2.1 (d and e). It is the separation distance between the workpiece and tool rotational axes. In the case that those axes intersect in the

space, the orthogonal case is called centric. In other words, if the distance e is zero, then the machining operation is called orthogonal centric turn-milling; otherwise, it is called eccentric turn-milling.
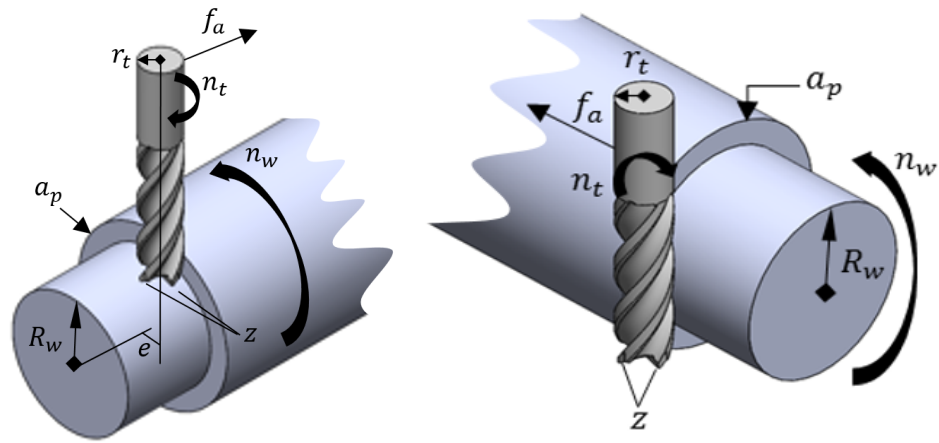
(a) Parameters in orthogonal turn-milling.

(b) Parameters in tangential turn-milling.
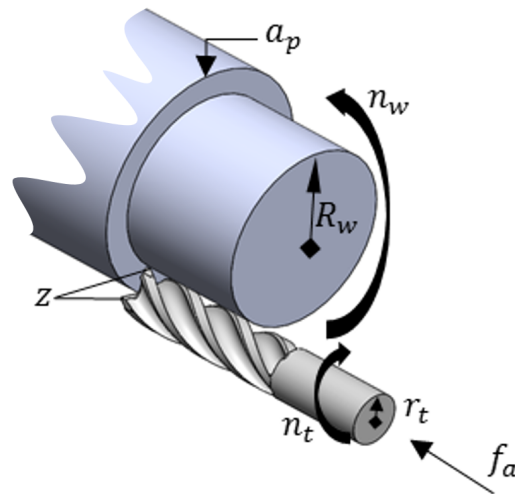
(c) Parameters in coaxial turn-milling.
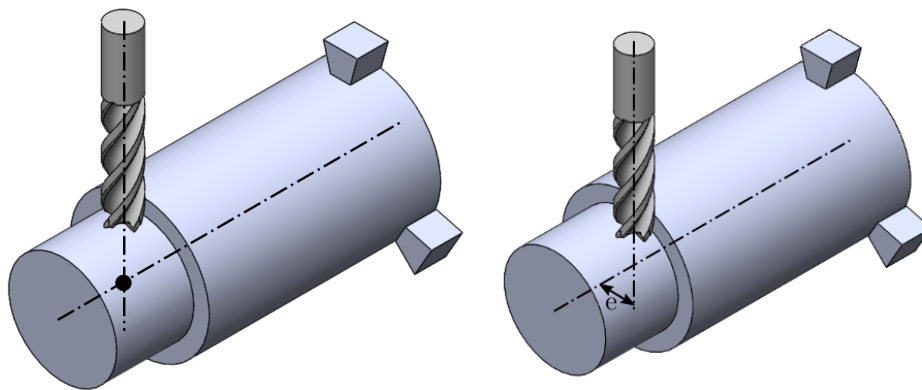
(d) Centric turn-milling

(e) Eccentric turn-milling

Figure 2.1: Defining parameters in the different turn-milling cases.

Turn-milling operations are versatile, and they produce a wide range of rotary surfaces, see figure 2.2. The process selection depends on the feature to be obtained. For instance, if the task is to generate an inner diameter, coaxial turn-milling is the most appropriate operation. In another scenario, if the job is profiling, the orthogonal operation is the right choice to achieve it.
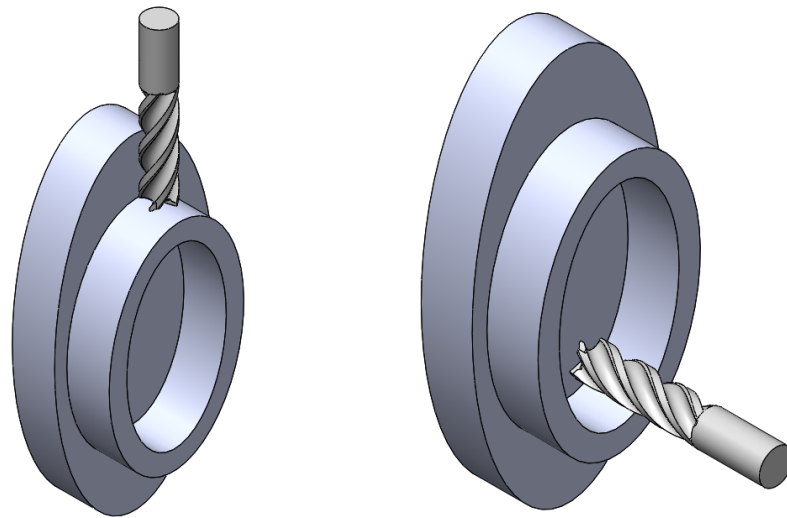
(a) Profiling with orthogonal turn-milling   *(b) Internal holing with coaxial turn-milling*

Figure 2.2: *Cylindroid surfaces produced with turn-milling operations.*

In conventional milling, the cutting tool is intended to remove the material with a specific edge portion. For example in face milling, the flank edge removes the material; while in plunge milling, the cut is performed by the end edge. This fact does not distinguish the geometry for the tool profile, as it is presented in both flat and torus mills, see figure 2.3. The edge classification is necessary because it clarifies which part of the tool performs the cut. In turn-milling, the complexity of the process kinematics demands simultaneous cutting with the flank and end edges. This condition determines the uncut chip geometry and the zone of maximum tool wear. (Choudhury and Mangrulkar, 2000; Uysal et al., 2014; Karaguzel et al., 2015b, 2016; Savas et al., 2016).
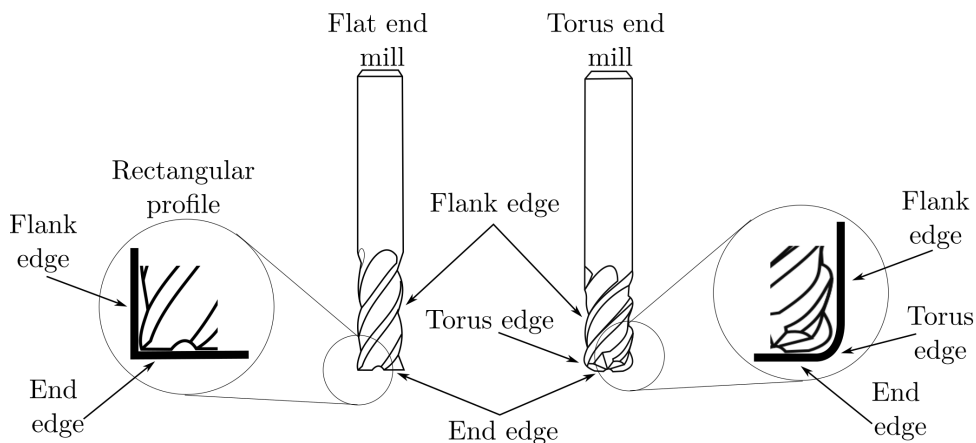
Figure 2.3: *Flat end and torus end mill. Edge classification.*

Although the turn-milling operations are implemented in the early 90's with the development of multi-axis CNC machine tools, there are many aspects to be researched yet. Indeed, there is a lack of consensus in basic aspects. For example, the authors state systematically that turn-milling is a high productivity process (Ekinović et al., 2007; Karaguzel et al., 2015a, 2017; Zelinski, 2021). However, the material removal rate (MRR) reached in academic publications does not corroborate this statement. During the literature review, it was identified some research groups performed experimental trials of orthogonal turn-milling (Choudhury and Mangrulkar, 2000; Choudhury and Bajpai, 2005; Zhu et al., 2013, 2016b; Karaguzel et al., 2012; Uysal et al., 2014; Karaguzel et al., 2015b,a, 2016, 2017; Qiu et al., 2015, 2016; Yan et al., 2016; Utsumi et al., 2020; Comak and Altintas, 2017). Then along with their multiple publications, the cutting conditions were extracted to find the material removal rate if possible. Figure 2.4 displays a comparative summary of the material removal rate reached in their researches. This figure shows clearly that the MRR of turn-milling operation is three times below conventional machining. Another characteristic of this figure is that the researchers are performing turn-milling operations at similar rates. Although this comparison does not consider the bulk material and does not represent the maximum capabilities of the process gives an idea of the productivity reached in laboratory conditions.
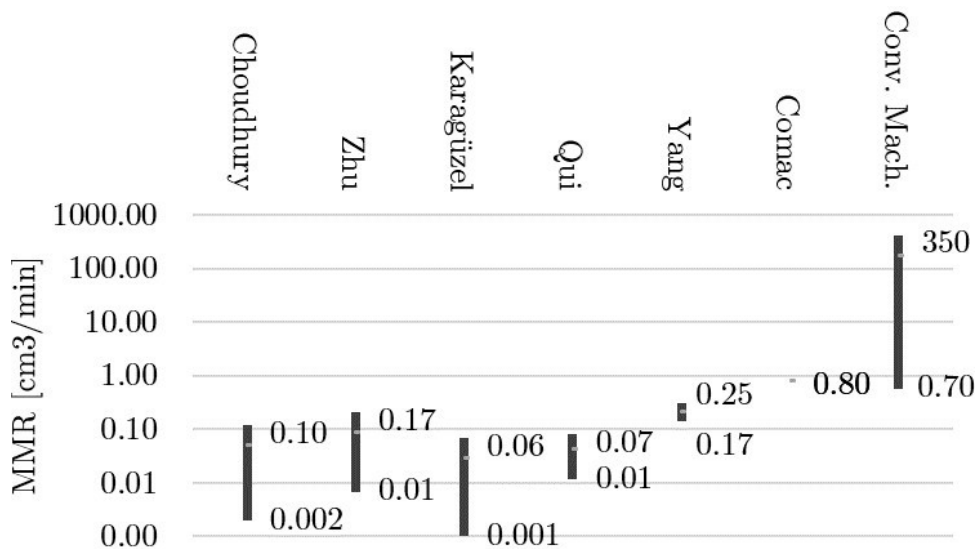
Figure 2.4: Material removal rate in turn-milling compared with conventional machining.

The comparative studies between conventional turning and turn-milling might not be fair because of the differences in the kinematics of the processes. For example, turn-milling perform multi-edge cutting while turning does a single-edge cutting. If the axial feed is equaled, the load in the mill will not be the same as in the turning insert. Otherwise, if the load of the edges is equaled, then the axial feeds do not match. That is why comparative studies have to focus on one specific feature such as the chip load on the edge, or the material removal rate, but they might be the target of strong critics.

The turn-milling research has begun early in the '90s, and the first subject treated by the researchers was the wear and the surface finishing of hard-to-cut

materials. The research focus has been diverging with time to understand the diverse faces of this machining process. The evolution of the subjects has been increasing, and even the wear has recent publications, which means that the interest in the first subject of study still prevails. Figure 2.5 shows the time appearance of the subjects of study. This list is limited to the publications that treat specifically turn-milling, as this is a milling operation, and the list could be easily increased. Turn-milling operations are relatively new considering the machining history (Karaguzel et al., 2012).Schulz and Spur (1990) published a study related to the different edges wear during coaxial turn-milling operations; they also considered the effect of the cutting parameters in the surface roughness and concluded about the geometric accuracy of the process.
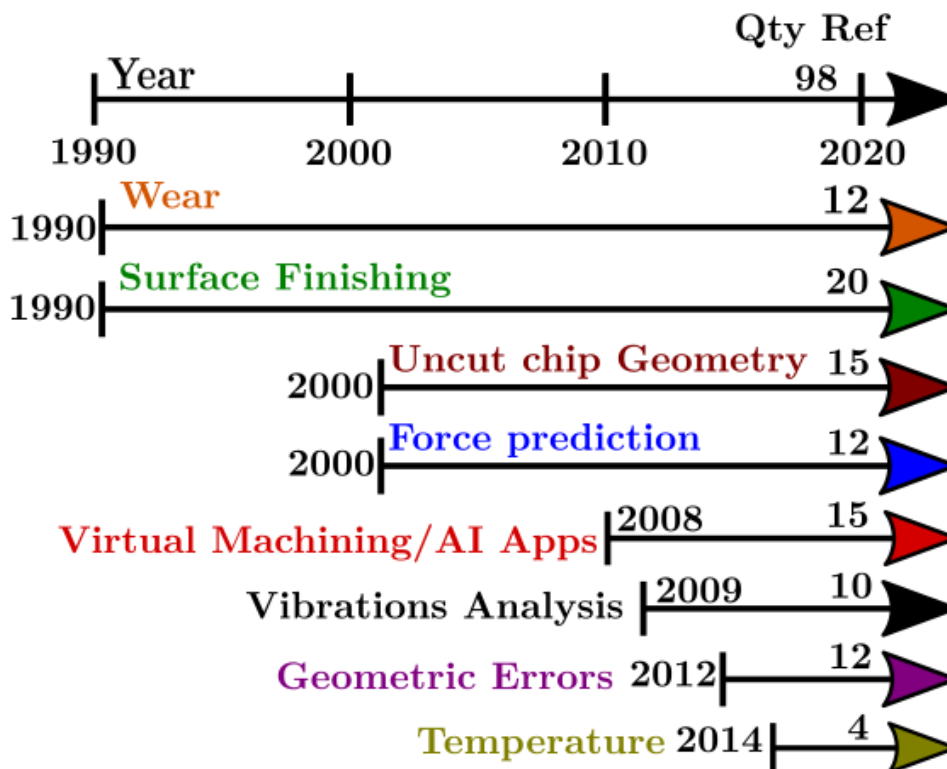
Figure 2.5: *Time line of the publications related with turn-milling operations.*

Following, every research subject is going to be discussed, presenting the remarkable outcomes of the authors. The main subjects presented in figure 2.5 are scientific and industrial parameters. The appearance order of the fundamental parameters is (uncut chip geometry, force prediction, vibration analysis, and temperature), followed by the industrial parameters in the following order (tool wear, surface finish, geometric errors). Subsequently, the virtual machining in turn-milling is discussed that has a special relationship with this research. Finally, it is presented a critical review of the State of the Art finding pertinent questions over the literature reviewed to recognize the research opportunities.

Tables 2.1, 2.2, and 2.3 present a summary of the topics treated in this chapter. The name of the authors has been coded to them three first letters and the year of publication. It is seen the is a strong disregard to tangential and coaxial turn-milling cases. However, even the orthogonal case shows a lack of

paper publications. This scenario presents the opportunity to contribute to the knowledge related to turn-milling operations.

Table 2.1: Summary table of the publications in turn-milling wear, surface finishing, virtual machining, Artificial Intelligence, dynamics, geometrical errors.

Turn-milling case	Wear			Surface Finish			
	Exp. Cut. cond.	Empiric model	Ecc. effect	Exp. Cut. cond.	Ecc. effect	Conv. turn-ing Vs T–M	Analytical model
Orthog.	Shu90, Hua12, Cai12, Kar14, Kar15A, Uys14, Kara15	Su13	Kar15A, Kar14, Uys14, Kara15	Kop97, Cho00, Cho05, Cai12, Uys14, Jin14, Ega15, Cal15	Kop97, Cai12, Uys14	Eki07	Zhu13
Tangent.	Karp17		N/A	Sav07, Sav08, Sav16, Karp17	N/A	Rat16	Fun16
Coaxial	Shu94		N/A	Shu90, Shu94	N/A		

Table 2.2: Summary table of the publications in turn-milling virtual machining, Artificial Intelligence, Dynamics, Geometrical Errors.

Turn-milling case	Virtual Mach. & AI		Dynamics		Geometrical erros	
	Virt. Mach.	AI	Mach. Desgn.	Stability	Exp.	Mod.
Orthogonal	Zhu08A, Zhu08B, Yua09, Zhu10, Zha10, Yu13, Zhu15, Hen17	Sav08, Yus12, Wan12, Chen13, Dwi14, Leo14, Sav16	Zhu07, Zhu09, Zhu11A, Zhu11B, Zhu12, Wan14, Jin13, Liu13	Bud13, Zhu15, Yan16	Shu90, Neg05, Olv12, Uys14, Ega15, Wan15, Kar16, Kar17	Kar12, Kar15, Kar15
Tangential			Karp17			
Coaxial						

Table 2.3: *Summary table of the publications in turn–milling uncut chip geometry, cutting forces, temperature.*

	Uncut Chip Mod	Cutting Forces		Temperature	
Turn-milling case	Predict	Applicat.	Predict	Exp. Cut. Cond.	Analytic
Orthog.	Kop97, Kop00, Fil11, Kar12, Kar14, Kar15B, Kar15C, Kar16, Kar17, Uys14, Qui15, Qui16, Zhu16A, Zhu16B, Com17	Ko00, Wu14, Zhu15, Jin17	Tlu00, Fil11, Alt00, Kar12, Kar14, Pen14, Kar15, Qui15, Qui16, Yan16	Liu14, Put16	Peng14, Kar17
Tangential	Kar12, Kar15, Kar16				
Coaxial	Shu94, Kar15B				

2.1 Uncut chip geometry

The uncut chip geometry prediction is an essential feature in the fundamental analysis of the turn–milling process because it is the primary variable for the cutting forces and thermic predictions. The coupled movement of the workpiece and the tool generates a complex geometry that depends on the cutting parameters and the case of turn–milling (orthogonal, tangential, coaxial). The experimental validation of the proposed models is always through indirect validation. The authors usually measure the cutting forces (Crichigno Filho, 2012; Karaguzel et al., 2014, 2017; Putz et al., 2016; Qiu et al., 2015, 2016; Uysal et al., 2014; Yan et al., 2016; Utsumi et al., 2020). However, Zhu et al. (2016a,b) have validated the chips via weight measuring and geometrical analysis of the cut chips.

2.1.1 Coaxial turn–milling

Schulz and Kneisel (1994) made the first mention of the uncut coaxial geometry, but there was not deeply explained how this geometry is constructed, the process

is schemed in figure 2.6. However, only Karaguzel et al. (2015b) proposed an analytical model to predict the uncut chip geometry. The main approach of the model is based on key points and connecting functions, which variables are the cutting parameters. However, there is no explicit validation of the model proposed by Karagüzel et al. The key points are shown in figure 2.7 as points 1, 2, & 3. Besides, the connecting functions are stated as the line that connects the point 1 & 2 (Ra), 1 & 3(Rt), and 2 & 3 (Re). These points and lines are drawn over a rotated Cartesian plane X–Y shown in Figure 2.7.
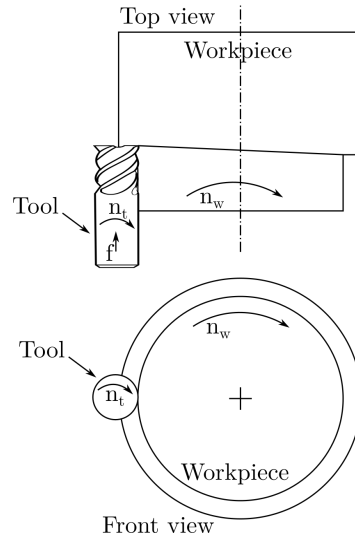
Figure 2.6: Coaxial turn–milling scheme
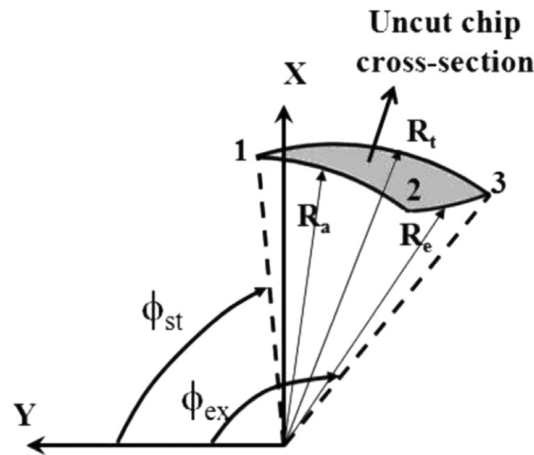
Figure 2.7: Schematic coaxial uncut chip geometry (Karaguzel et al., 2015b).

The research work presented from Karaguzel et al. does not explain how to calculate the key points 1, 2, 3 that are the physical boundaries of the chip. It is not clear neither, the domain of the equations that define the geometry of the chip. It is essential to say that this work is the most complete found for this machining case. Nevertheless, it was impossible to use the mathematical expressions to represent the uncut chip geometry in 3D coordinates.

2.1.2   Orthogonal turn–milling

There are different approaches to predict the uncut chip geometry in the orthogonal case schemed in figure 2.8; Kopač and Pogačnik (1997) mentioned how they believed the uncut chip is; however, there is no validation of this proposed geometry. The same team did a numerical simulation of the engage zone of the tool. The authors state that only eccentricity, axial feed, and the depth of cut are the cutting parameters that define the chip geometry (Pogacnik and Kopac, 2000).
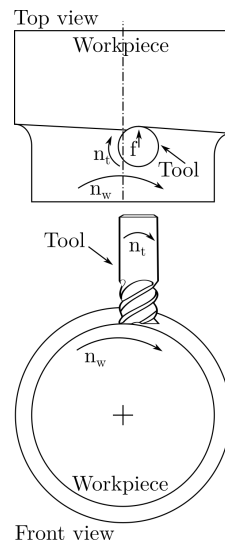
Figure 2.8: Orthogonal turn–milling scheme

The first researcher that introduces the key point approach was Crichigno Filho (2012), in his only work published about this subject. In this work, the author presents the rough down process of a flat end mill while the workpiece rotation. However, the axial feed is not taken inside the model. The main equations are quite similar to the results reached after by Karagüzel et al.

The Karaguzel et al. (2012, 2014, 2015b, 2017); Uysal et al. (2014) teams has worked on the prediction of this geometry a few years ago. They were consistent in their publications in the model proposed for the prediction of the geometry. The general approach of the model is based on key points and connection functions between each other calculated from the cutting conditions as shown in figure 2.9. According to Karaguzel et al. (2014, 2016, 2017); Uysal et al. (2014), there is a modification on the chip geometry when the eccentric is added to the tool. This change is represented in the general connecting equations and is studied in different works. It is essential to say that all these models stated by this team of researchers are validated indirectly by measuring the cutting forces on the machining process.

Qiu et al. (2016) worked on a different approach for predict the chip geometry, using the tool-workpiece engage zone. This approach generates a different geometry than the Karagüzel et al. team stated. Figure 2.10 (a) shows the focus taken by the authors to generate the mathematical model of the geometry. The team focused on the enclosed volume during the equivalent trajectory of the tool
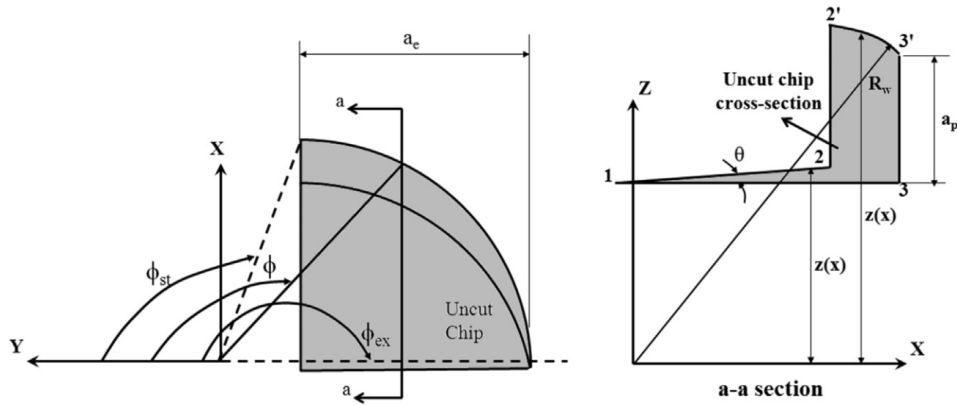
Figure 2.9: Schematic uncut chip geometry orthogonal turn-milling (Karaguzel et al., 2015b).
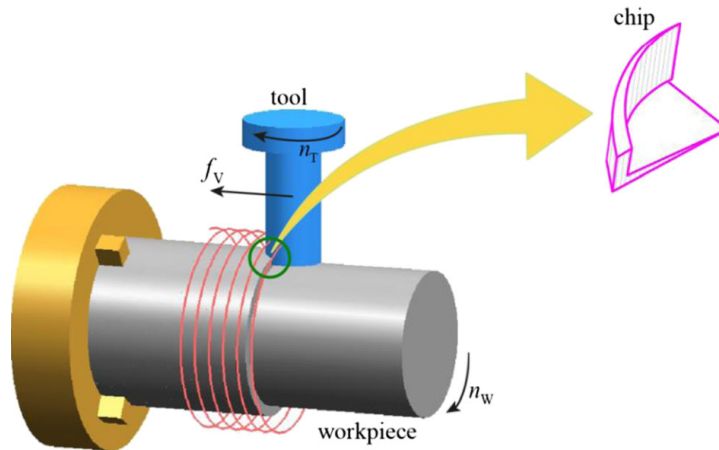
(a) Centric orthogonal turn-milling Qiu approach (Qiu et al., 2016).
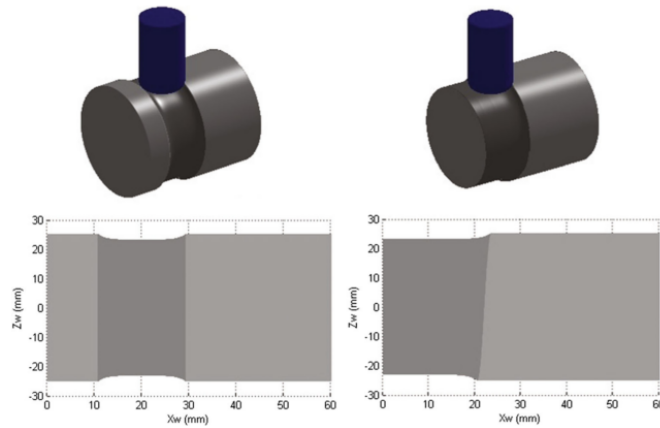
(b) Orthogonal turn-milling round insert approach (Qiu et al., 2015).

Figure 2.10: *Qiu research results (Qiu et al., 2015, 2016).*

if the workpiece would be static. The same group generated another research that changed the tool geometry using round inserts instead of flat end mills (Qiu et al., 2015). The model proposed by the authors can simulate the process of turn-milling starting from the cutting parameters, see figure 2.10 (b). The

authors validated the model proposed indirectly by measuring the cutting forces. Qiu only treated the orthogonal centric case do not have publications in the other cases.

Zhu et al. (2016b,a) have worked in the modeling of the uncut chip geometry based on the engagement zone but with a different approach than the Qiu team. The main difference is that Zhu et al. propose the boundaries equations of the geometry enclosed between two edge passes during the coupled movement of the tool and the workpiece. This research team develops a differentiated model for centric and eccentric cases shown in Figure 2.11. It is crucial to notice that the validation of the models presented is done by analyzing the chips collected after machining and measuring the weight of the material removed.

(a) Schematic uncut chip geometry orthogonal turn-milling.

(b) Schematic uncut chip geometry orthogonal turn-milling.
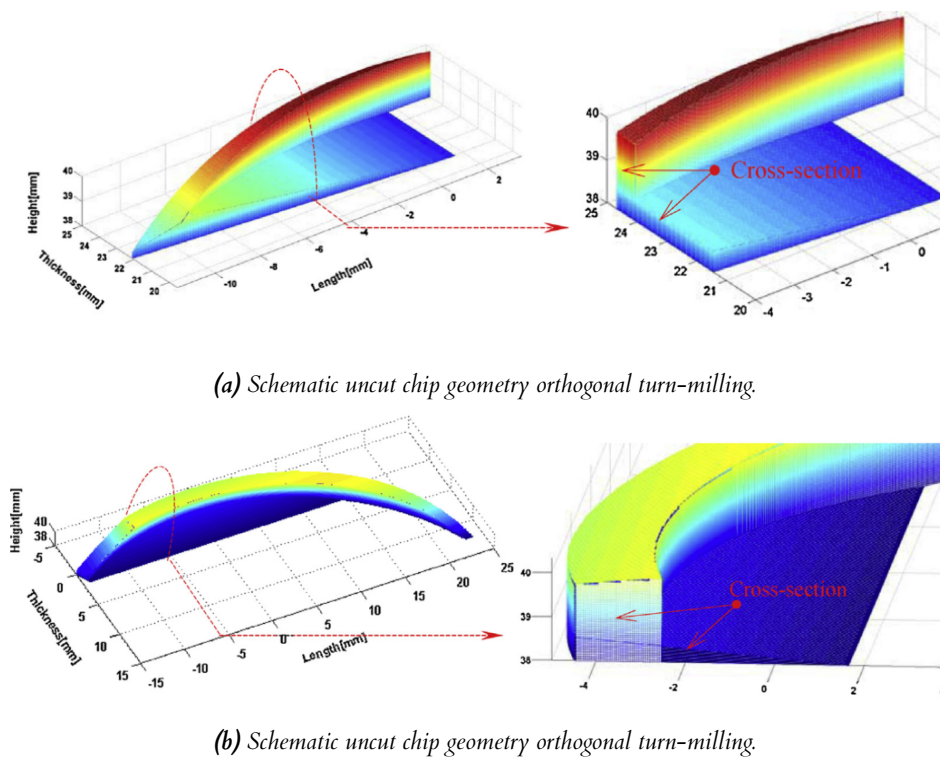
Figure 2.11: *Zhu et al. research results (Zhu et al., 2016b).*

Comak and Altintas (2017) developed a vector approach of the chip geometry on the engagement zone. This model considers a 5-axis movement of the tool around the workpiece, see figure 2.12. The model discretizes the tool geometry to estimate the engage zone in the cutting zone and is validated indirectly by force measuring. The experimental validation process is weak, testing only one cutting condition and comparing it with the predicted cutting forces.

Utsumi et al. (2020) based their development on a point-cloud approach. In this research, the round insert profile and workpiece are modeled as an intersecting point cloud. Then, based on the vector relationships of the points clouds, the engagement zone is determined and used to determine the cutting forces, see figure 2.13. This work tested the model in diverse cutting conditions.
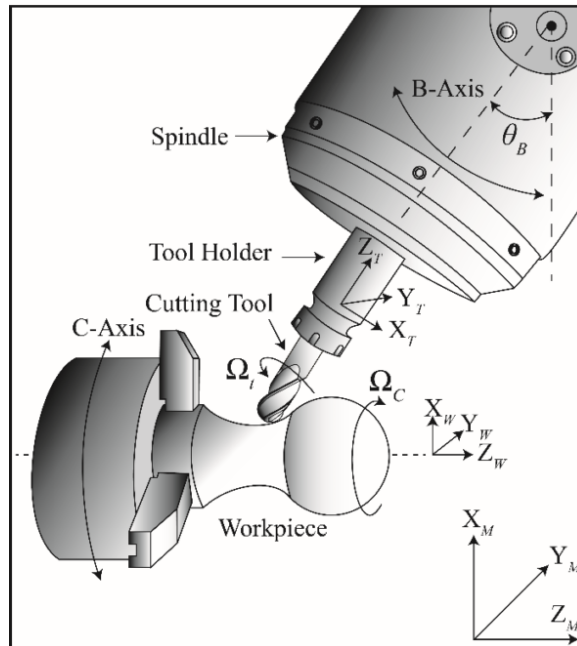
Figure 2.12: Kinematics in 5 axis turn–milling (Comak and Altintas, 2017).
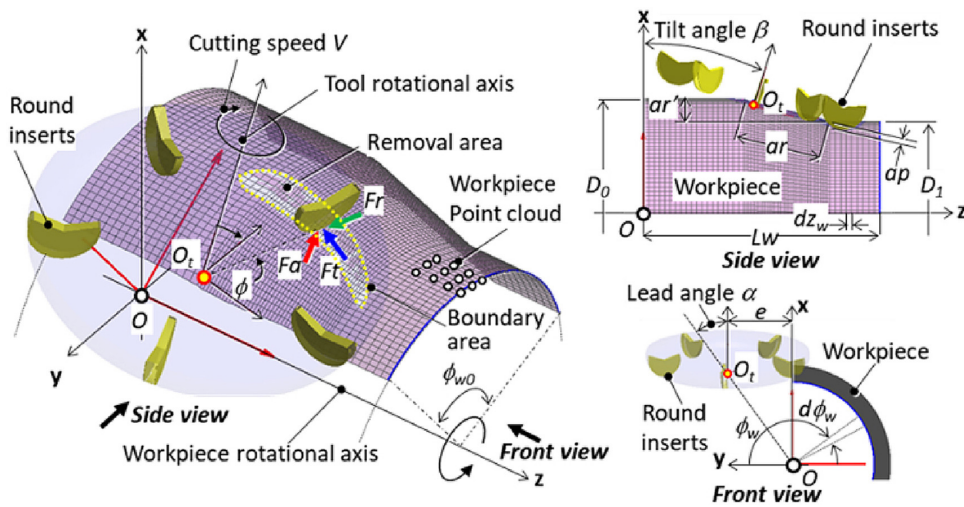
Figure 2.13: Point cloud for uncut chip geometry determination (Utsumi et al., 2020).

2.1.3 Tangential turn–milling

The tangential case is the less studied and is schemed in figure 2.14. Karaguzel et al. (2012, 2015b, 2016) presented a model where some key points connect through functions that depends on the cutting parameters, see figure 2.15. The work presented by the authors is just theoretical because there is not explicit validation of the tangential model in neither of the cited papers. The approach presents some of the problems described in the orthogonal case. Besides, the connecting line between points 1 & 2 has undetermined variables shown in figure 2.15.
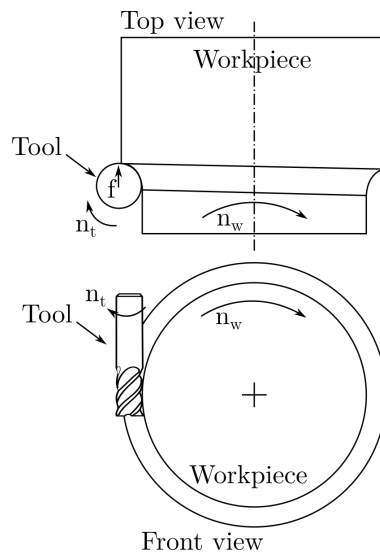
Figure 2.14: *Tangential turn-milling scheme*
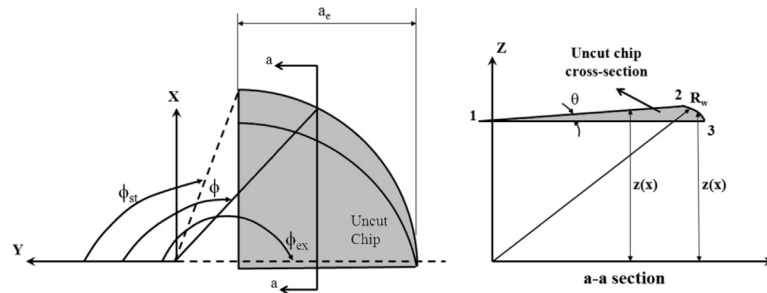
Figure 2.15: *Scheme of uncut chip geometry for tangential turn-milling (Karaguzel et al., 2015a).*

For example, the equation $z(x) = \tan\theta x + \left(R_w - \frac{\left[\sqrt{R_t^2 - y^2} - (R_t - a_p)\right]}{\cos\theta}\right)$ presented in the Karaguzel et al. (2015b) publication includes the variable "y" and it is not described at all. The introduction of this "y" variable do not describe a line but a surface, because the expression has two independent variables "x" & "y". This undetermination is just one example of the mathematical incongruities presented in this approach. Additionally, the orthogonal views do not correspond between each other, it does not appear to be describing the same geometry, see figure 2.14.

2.1.4 Turn-milling modeling approaches comparison

A comparison with the reference work of Karaguzel et al. (2015b, 2016) and Crichigno Filho (2012) is performed below. In this work, uncut chip models of turn-milling operations were modeled. The orthogonal (centric and eccentric), coaxial and tangential cases were described. In this case, only the orthogonal centric model is compared because this is the only case that has been validated experimentally.

CAD representation of the chip

Karaguzel et al. (2015b, 2016) presented a CAD representation of the uncut chip that does not seem to consider the workpiece curvature but the mathematical model does consider it, as shown in figure 2.16 (a). Additionally, it is interesting that the modeling approach of Karaguzel et al. (2015b) is the same than that presented by Crichigno Filho (2012) years previously but the described uncut chip geometry is different, see figure 2.16 (b). It is not clear in the models how the width of pass affect the uncut chip geometry. Despite of the geometrical differences of the approaches they are trying to describe the same process. It seems that Karaguzel et al. (2015b) describe the process in a "large depth of cut regimen" and Crichigno Filho (2012) describes the process in a "small depth of cut regimen".
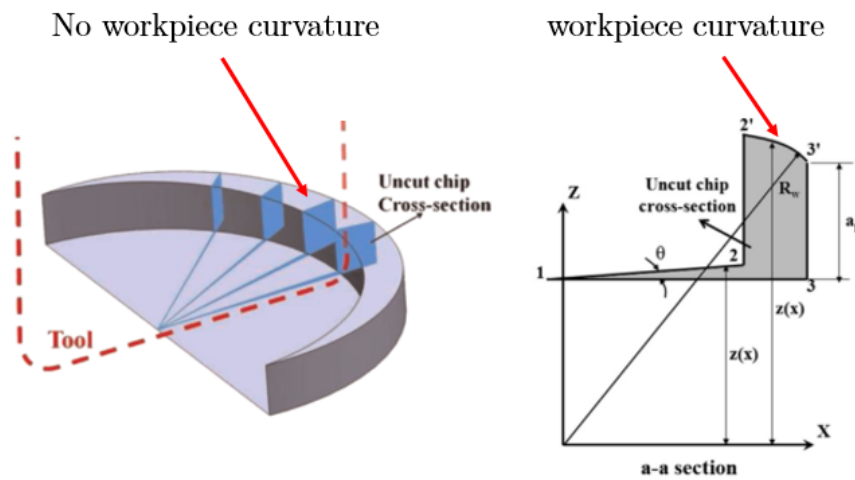
(a) Comparison of the CAD representation of the uncut chip geometry (Karaguzel et al., 2015b).
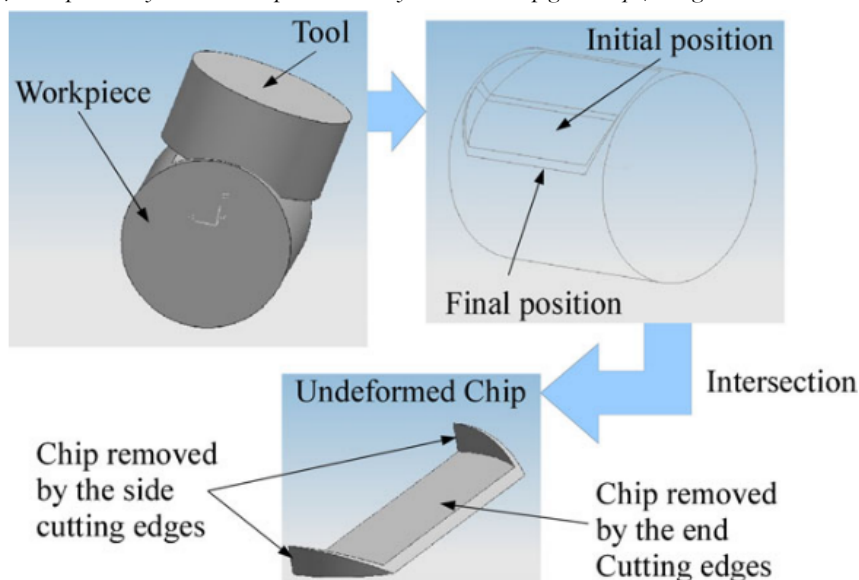
(b) Uncut chip geometry predicted by (Crichigno Filho, 2012).

Figure 2.16: *Comparison of approaches Karaguzel et al. (2015b) and Crichigno Filho (2012).*

Critical analysis of Karaguzel analytical approach

Karaguzel et al. (2015b) modeled the uncut chip geometry from key points projected on the x axis called x_1, x_2, x_3, figure 2.17. These points are linked through lines that represent the height in the Z axis. For instance, the end cutting zone is represented at the bottom by linking points 1-3 and the top by 1-2. The flank zone is built by linking points 2-3 with the 2'-3' function. The equations 2.2, 2.3, and 2.4, determines the geometry that the authors considers as the uncut chip geometry. The only angular parameter is θ which is the rotation of the workpiece per edge pass.
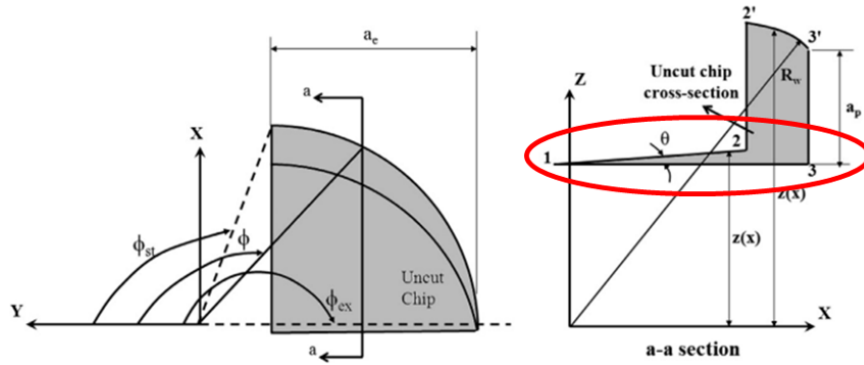
Figure 2.17: *Comparison of the CAD representation of the uncut chip geometry (Karaguzel et al., 2015b).*

$$x_1 = (R_w - a_p) \sin(\frac{\theta}{2})$$
$$x_2 = \left(r_t - \left((R_w - a_p) + \tan\left(\frac{\theta}{2}\right) \tan(\theta)\right) \sin(\theta)\right) \cos(\theta)$$
$$x_3 = r_t$$

$$(2.1)$$

$$z(x_{1-3}) = R_w - a_p \tag{2.2}$$

$$z(x_{1-2}) = \tan(\theta)x + \left(\frac{R_w - a_p}{\cos(\theta)}\right) \tag{2.3}$$

$$z(x_{2'-3'}) = \sqrt{(R_w^2 - x^2)} \tag{2.4}$$

$$\phi_{st} = \frac{\pi}{2} + \arcsin\left(\frac{r_t - a_e}{r_t}\right)$$
$$\phi_{ex} = \pi$$

$$(2.5)$$

From equation 2.1 to equation 2.5 is only possible to plot a 2D geometry, see figure 2.17. There are not mathematical expressions to convert this 2D geometry into a 3D geometry as presented in the CAD representation. The model presents the start and exit angles where the cut is performed as presented in equation 2.5. These angles are stated in the plane $X - Y$. The model relates the independent variable x with the distance in the z coordinate. However, there are not mathematical expressions to set the geometry in the y direction that should determine the geometry in the 3D space.

Table 2.4: Comparison between different authors approach.

Improvement opportunities	Karaguzel et al. (2015b)	Zhu et al. (2016b)	Crichigno Filho (2012)
Identification of the "small and large depth regimen"	X		
Mathematical description of the "large depth regimen"	X	X	
Mathematical description of the "small depth regimen"			X
Identification expression of the operating regimen	X		
Analytical model includes rotation edge angle (ϕ)		X	X
Geometry described mathematically in 3D		X	X
Mathematical description of the variable depth of cut due to the workpiece radius	X	X	X
Experimental validation of the cut geometry measuring the cut chip mass		X	
Experimental analysis of the cut chip geometry		X	
CAD representation of the chip	X	X	X
Validation of the geometrical model comparing with the CAD			
CAD and model describe the same analytical geometry		X	

The features described previously are also presented in the Karaguzel et al. (2016) publication. Table 2.4 is presented as a summary of the main features that different authors have proposed in their approaches. The table shows the huge advance presented by the previous author in the literature; their analytical contributions have strongly developed the field in a relatively short time. However, the approach presented in this thesis proposes a novel methodologies to reproduce

the analytical uncut chip geometry trying to propose a general framework to the orthogonal turn–milling operations.

2.2 General overview of cutting force prediction in machining

The cutting force prediction is a matter of study not only in turn–milling but also in all machining operations because of its impact on tool and machine tool design, geometrical errors for tool-workpiece deformations, surface roughness, process stability, tool wear, etc. The prediction process is reduced to the proposal of mathematical models intending to represent the behavior experimented during the cutting process. In this line, there are three methods to predict cutting forces in machining operations the analytical, empirical, and finite element model (FEM) approaches.

The following is a review of the work of authors with publications related to cutting forces in turn–milling. After that, is presented a review of the current methods for cutting force prediction in machining operations, exposing their main ideas. The diverse methodologies reviewed are compared at the end of this section to consider the advantages and disadvantages of each approach.

2.2.1 Cutting force prediction in turn–milling operations

In turn–milling the force prediction is used for two proposes: the first one is as experimental validation parameter from the uncut chip geometry that present a complex shape in this machining process. the second is less common but some researches uses the cutting forces as performance indicator of the process.

Except Pogacnik and Kopac (2000) that do not show explicitly how to obtain the cutting forces, all of the authors reviewed employ the mechanistic approaches to determine the cutting coefficients and subsequently develop their respective predictions. Crichigno Filho (2012) presented an approach to model the orthogonal turn–milling and used the linear homogeneous model for the cutting force estimation, the most relevant results are presented in figure 2.18 (a). Karaguzel et al. (2012, 2014, 2015a, 2016, 2017), Uysal et al. (2014), Liu et al. (2014), Qiu et al. (2015, 2016), Comak and Altintas (2017), and Utsumi et al. (2020) achieve the cutting force prediction with the linear affine methodology, figure 2.18 (b) and (c) shows the most relevant results of the Karaguzel et al. and Comak et al. publications. All of the authors that use the cutting force as validation parameter report accurate predictions. Karaguzel et al. (2016) studied the effect of the eccentricity in the orthogonal turn–milling stating that there is an "optimum" value of eccentricity that increase the tool life. However, this statement was not demonstrated with theoretical evidence, just a set of experiments that suggested this behavior.

<p align="center">(a) Crichigno Filho (2012).   (b) Karaguzel et al. (2016).</p>

<p align="center">(c) Comak and Altintas (2017).</p>
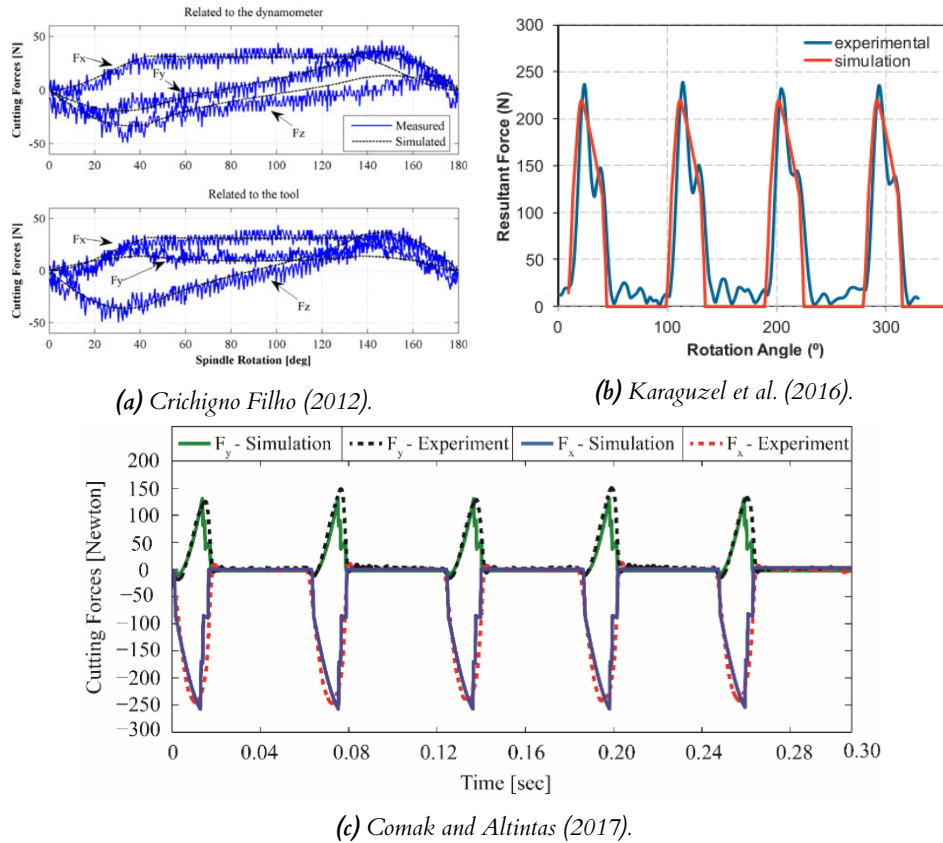
Figure 2.18: *Comparison of instantaneous cutting forces diverse authors.*

2.2.2 Analytical models

The analytical approaches interpret the physics of the cutting process, considering mechanical properties of the material, geometrical properties of the edge, and cutting parameters of the process for predicting the cutting forces resulting from the new surfaces generation.

Merchant approach

Merchant (1945a,b) published in 1945 two papers modeling the orthogonal cutting process. This research consisted of an analytical cutting force predictive model considering the plastic behavior of the bulk material, as shown in equation 2.6. Where F_c is the cutting force, τ_s is the shear stress, γ is the rake angle, β is the friction angle, ϕ_{fr} is the shear angle, and A_0 is the uncut chip area. This variables are related in the cutting process as shows figure 2.19. One of the most challenging parameter to determine by in this approach is the shear angle ϕ_{fr}. An analytical approach to find the shear angle (ϕ_{fr}) was proposed using the Minimum Energy Principle (MEP); see equation 2.7. This approach considers that the cut is performed at an angle where the consumed energy is minimum. However, Astakhov and Xiao (2008) criticized the inaccurate predictions, arguing that the MEP approach oversimplified the phenomena. Additionally, Usui et al.

(1978) stated that this method could not be applied in oblique cutting, which means that the approach can not be extrapolated to industrial cutting operations such as milling, turning, boring, etc.
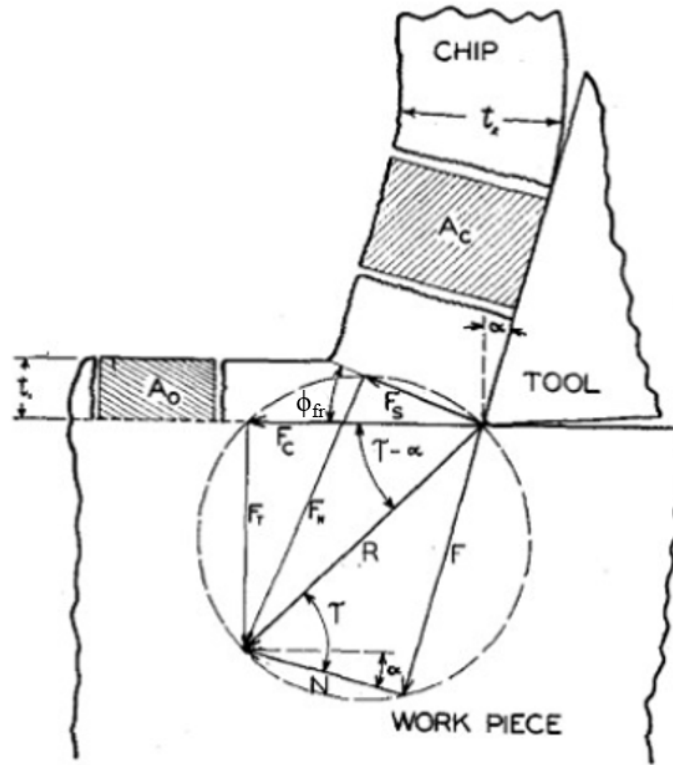
Figure 2.19: Orthogonal cutting mechanics (Merchant, 1945a).

$$F_c = \frac{\tau_s A_0 \cos(\beta - \gamma)}{\sin(\phi_{fr}) \cos(\phi_{fr} + \beta - \gamma)} \tag{2.6}$$

$$\phi_{fr} = \frac{\pi}{4} + \frac{\gamma - \tau}{2} \tag{2.7}$$

The use of MEP of Merchant (1945a,b) defined in equation 2.7, and Shear Stress Principle (MSSP) of Krystof (Krystof, 1939) defined in equation 2.8 was analyzed by Shamoto and Altıntas (1999), but both were proved to be inaccurate. Besides, in some cases, the shear plane angle could be predicted as zero, which is not possible (for example, when friction angle is $\frac{\pi}{4}$ and the rake angle is zero). Furthermore, Kaneko et al. (Kaneko et al., 2018) applied different cutting theories to reduce the number of cutting parameters required for milling force prediction: rake angle, helical angle, shear stress, shear angle, and rotational radius deviation.

$$\phi = \frac{\pi}{4} + \gamma - \beta \tag{2.8}$$

Energy–based models

A different solution for predicting cutting forces was proposed by considering energy-based models. This model looks to estimate cutting forces from the energy spent during the cutting process. A simplification of the 3D cutting process is done using the orthogonal cutting proposed by Usui et al. (1978). Then, in orthogonal cutting, the cutting energy (U) is the sum of the shear (U_s) and friction energies (U_f). Simultaneously, the cutting energy was equal to the product between the cutting force F_c and the cutting speed (V_c), as defined in equation 2.9. Nevertheless, they concluded that the model loses accuracy in high inclination and helix angles and low rake angles. Matsumura and Usui (2010b,a) implemented the same approach for ball end mills in peripheral milling finding that this approach is only valid for single edge tools.

$$U = U_s + U_f = VF_c \qquad (2.9)$$

Astakhov and Xiao (2008) included additional energy parameters to increase the accuracy of the prediction. In this publication, the energy was found by adding five components (energy partition model): plastic deformation, friction at the tool–chip interface, friction at the tool–workpiece interface, the formation of new surfaces, and the effect of the minor cutting edge angle. Kishawy et al. (2012) also used this model to determine the cutting forces in broaching, and also to analyze the surface integrity in the resulting surface. Despite the efforts to increase the accuracy of the models, the improvement of predictions was not enough for that presented in the experimental data.

Zou et al. (2009) developed a different approach consisted of replacing the chip flow angle and the apparent coefficient of friction with two variables: SLIP and RATIO. In that way, the use of the chip flow angle and the apparent friction coefficient were avoided, two variables challenging to measure. SLIP was related to the kinematics and RATIO to the forces in the two main deformation zones. These variables are detailed in equation 2.10. Where, V_{st} is the tangential velocity in the shear plane of the chip, $V_0 \sin(i)$ is the velocity of the material along the cutting edge, F_{fric} is the friction force in the rake face, and F_s is the resultant force in the shear plane; both forces are obtained experimentally and are shown in figure 2.20. For brittle materials, the cut chip thickness is not possible to be measured, and then the shear angle can not be determined by experimental data. Nevertheless, the shear angle also depends on the cut chip thickness (chip compression ratio), and this approach was not taken into account, leading to inaccuracies.

$$
\begin{aligned}
SLIP &= \frac{V_{st}}{V_0 \sin(i)} \\
RATIO &= \frac{F_{fric}}{F_s}
\end{aligned}
\qquad (2.10)
$$

The Merchant approach is analytical, which means that based on external properties and the physics analysis, mathematical expressions intend to describe
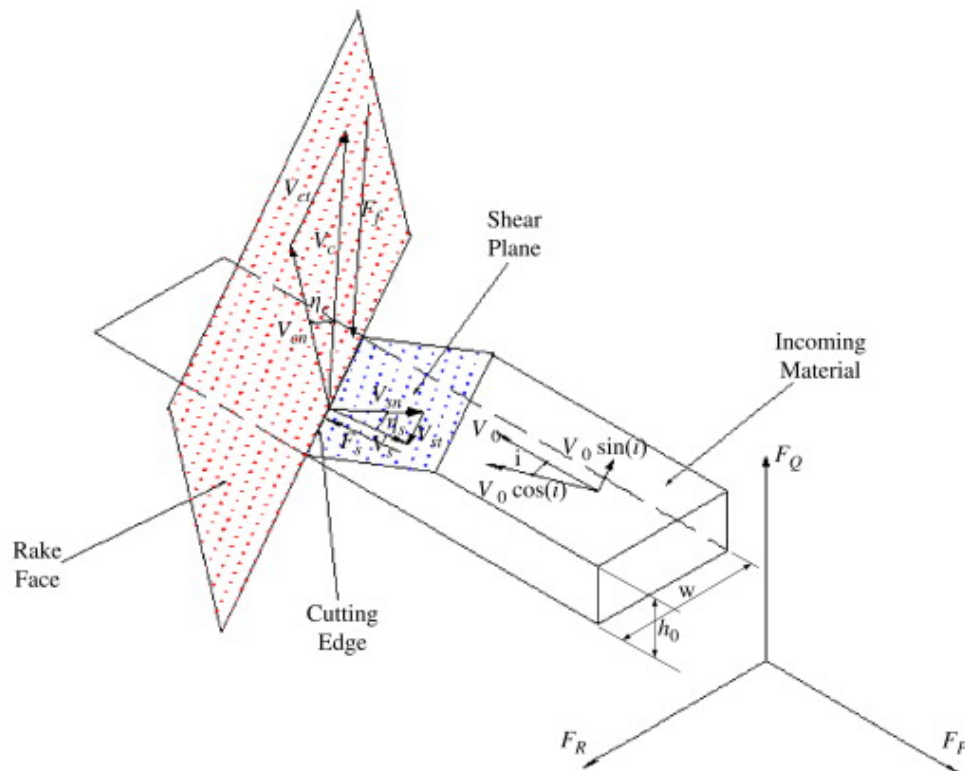
Figure 2.20: Orthogonal cutting mechanics (Zou et al., 2009).

the cutting exerted in the orthogonal cut. The fact of being analytical reduces the cost of experimentation in cutting trials. However, this approach is not accurate, despite the efforts to increase the accuracy for some authors. This feature makes it less attractive to apply this methodology in industrial operations.

A wide range of material properties is needed in energy-based models, demanding material characterization and expensive experimental trials. For example, it is necessary to test like the Split Hopkinson Pressure Bar (SHPB) to obtain the dynamic stress–strain response of the materials. However, these tests suppose high time and economic costs, which have made them not widely used in the industry.

In general terms, the analytic approaches for cutting force prediction do not seem to be the most practical way to achieve accurate predictions. Inaccurate results or expensive and difficult characterization trials become severe obstacles to consider in implementing these methodologies.

2.2.3 Empirical models

Empirical models are those based on experimental cutting trials. The cutting forces are measured during the cutting process and later they are fitted with mathematical expressions that model the behavior of the forces in terms of the cutting parameters of the process. It has been detected three approaches: the specific force or linear homogeneous, linear affine and exponential. This characterization corresponds to the form of the mathematical expression that

models the physical phenomena. However, the publications all have in common the determination of the uncut chip geometry, then the estimation of cutting coefficients and the cutting force prediction in any machining operation.

Linear homogeneous approach

In calculus, the linear functions have the typical form of $y = mx + b$ and always that the parameter $b = 0$ the function is called "homogeneous", and the line passes through the origin of coordinate system (Stewart et al., 2020). Based on this, it is considered that the cutting force F is proportional to the uncut chip area A, and the proportion constant is called specific cutting force K_s, see equation 2.11. This linear approach depends exclusively of the uncut chip area, and considering the specific force K_s constant, the model would take the form shown in figure 2.21. This approach works fine in an interval when the area A is relatively large, because when the model is close to ($A = 0$) the predictions are not very accurate.

$$F = K_s A \hspace{10em} (2.11)$$
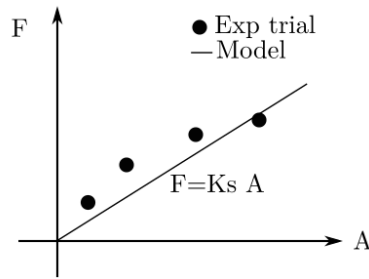
Figure 2.21: Linear homogeneous model behavior scheme.

Fu et al. (1984) developed a model for face milling where cutter geometry, workpiece, and process geometries (relative positions of the cutter to workpiece, spindle tilt, runout) were taken into account, this work used the specific force approach to determine the cutting forces. Jayaram et al. (2001) calculated cutting forces using equations 2.12 for radial forces, see figure 2.22. Face milling tests were performed to obtain the cutting coefficients. Defining K_t and K_r as the specific cutting coefficients for tangential and radial directions, A_c is the cut chip area. These two research considered the evolution of the uncut chip area along the edge rotation in face milling operations. Additionally, the experimental data showed that the cutting coefficients are not constant and depend on the chip thickness. For this reason the tangential and radial coefficients (K_t & K_r) depends on the tool angular position or immersion angle (ϕ).

$$\begin{aligned} F_t(\phi) &= K_t(\phi)A_c(\phi) \\ F_r(\phi) &= K_r(\phi)A_c(\phi) \end{aligned} \hspace{6em} (2.12)$$

The variable nature of the specific force coefficients is strongly influenced by the edge geometry. Wojciechowski (2015) presented an approach for ball
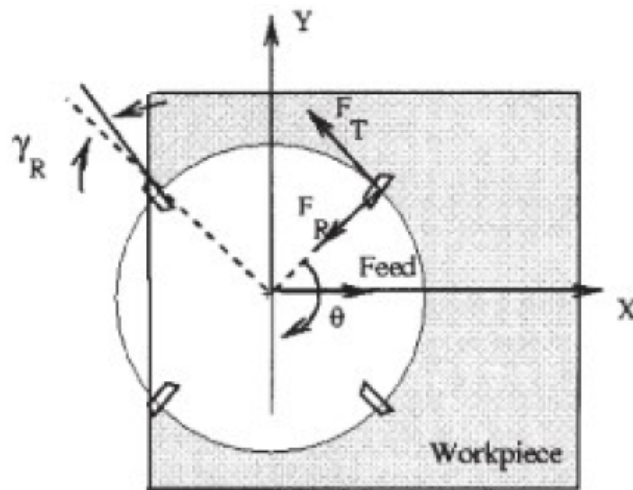
Figure 2.22: *Tangential and radial fores in milling operation (Jayaram et al., 2001).*

end mills where the radial runout was considered to determine the uncut chip geometry. This approach divide the uncut chip geometry in sections based on the tool profile in polar coordinates and determining the specific force coefficients for each portion of the area and integrating the force in the tool axial direction to determine the resultant force see figure 2.23.
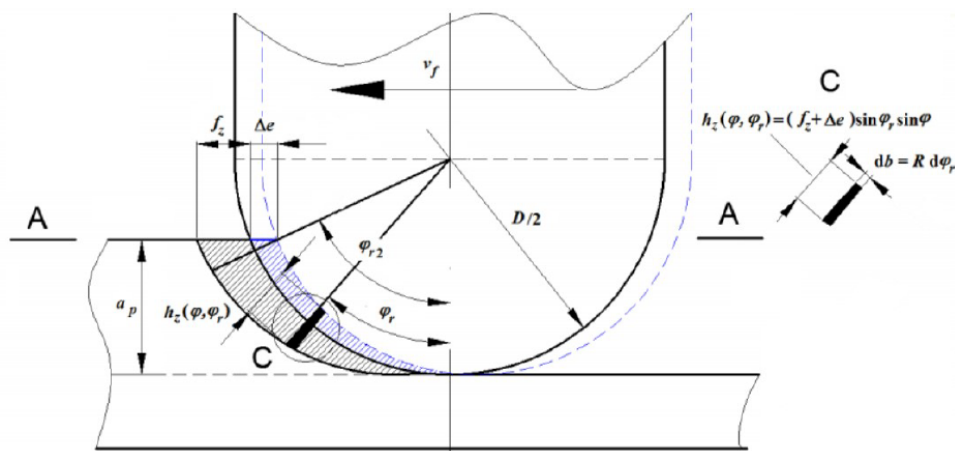
Figure 2.23: *Chip thickness geometry (t_z) on ball-end milling of plane surfaces (Wojciechowski, 2015).*

The problem of the uncut chip geometry is not a problem exclusive of milling. Yang et al. (2002) developed a model for reaming and drilling processes where the relation between cutting forces and machine tool vibrations was taken into account, see figure 2.24. The normal (F_n) and friction (F_f) forces were esteemed as in equation 2.13. K_n and K_f are the specific normal and friction forces, and dA_c is the chip differential of area. This differential of area, is proposed because although the uncut chip area is regular, the vibration modify the uncut chip geometry as shows figure 2.24 (b). The specific normal and friction forces were dependent on workpiece material, cutting velocity, normal rake angle, and chip thickness. Then, normal and friction forces were projected to obtain thrust force,

cutting force, and lateral force. The effect of vibrations was taken into account in the calculation of the chip thickness.

$$dF_n(t) = K_n dA_c$$
$$dF_f(t) = K_f dA_c$$

(2.13)

(a) Top view.

(b) Front view.
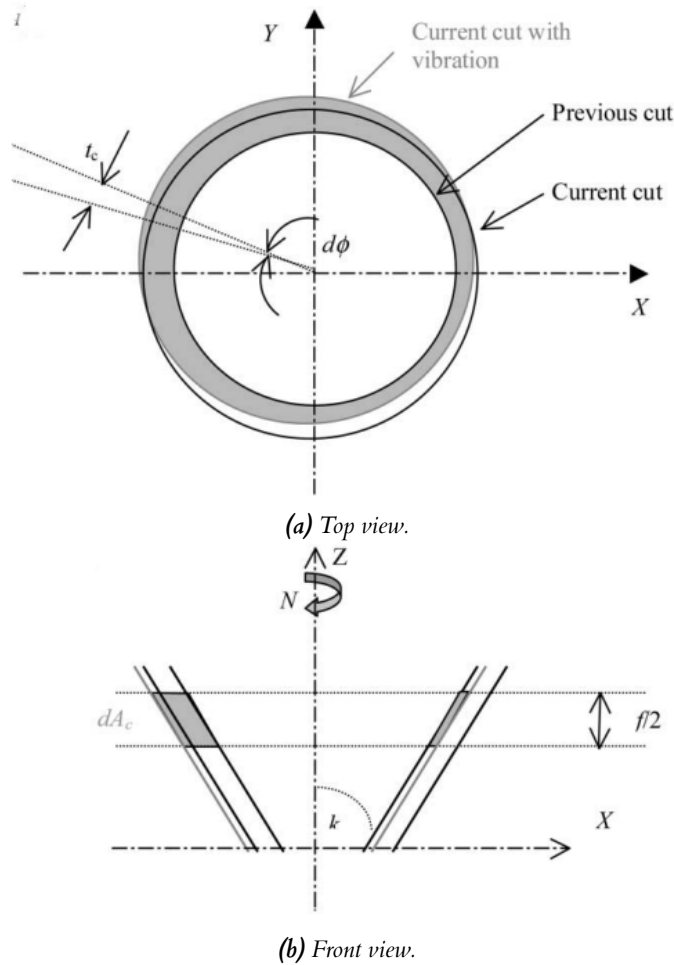
Figure 2.24: *Effect of the vibration in the uncut chip thickness in drilling (Yang et al., 2002).*

Linear affine approach

In calculus, the linear functions $y = mx + b$ that the independent term $b \neq 0$ are called "affine", and they do not pass through the origin of coordinate system (Stewart et al., 2020). With this in mind, the resultant force F is divided in two components. The first component represent the effect of cutting just as the specific force approach, continuing with the assumption that the cutting force is proportional to the uncut chip area A and the proportional parameter is the cutting coefficient K_c. The second component represents the effect of the friction experimented by the edge being dragged against the bulk material. This new component is proportional to the length of the edge (l_c) in contact with the

material, and the proportional parameter is the edge or friction coefficient K_e as shown in equation 2.14. If the cutting and edge coefficients (K_c & K_e) are considered constant the model behavior is shown in figure 2.25. This approach improved the accuracy of the predictions when the area is relative when the model operates in zones close to ($A = 0$) without impact negatively in larger values of area.
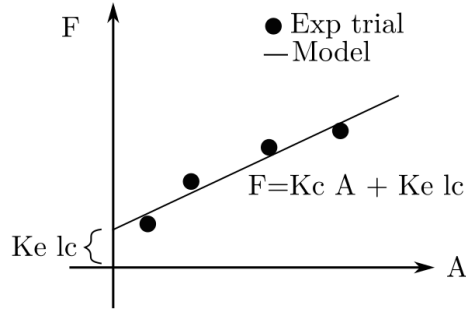
Figure 2.25: Linear affine model behavior scheme.

$$F = K_c A + K_e l_c \tag{2.14}$$

Yucesasn and Altintas considered the ball end mill tool profile as the main parameter to study. This publication predicted the cutting forces but considered that the edge support pressure and friction at the same time during the cutting process. Atabey et al. (2003) analyzed the mechanics of boring, the resultant force was divided in a their 3D components (see figure 2.26) and the cutting forces were estimated using the linear affine approach in the differential form shown in equation 2.15. In this approach the uncut chip geometry was studied deeply, because it presents strong changes with the feed per revolution. Then, the nose radius generates a circular profile defining important the direction of the cutting forces as presented in figure 2.27. As the uncut chip geometry is complex, it is divided in differentials with determine the overall state of force of the tool. The cutting forces are represented by the tangential force (F_t) and the friction force (F_{fr}) that groups the feed and radial forces. The differential of forces are then (dF_t) & (dF_{fr}) respectively. The cutting coefficients (Ktc & $Kfrc$) are these which multiply the differential of area (dA), and the edge coefficients (Kte & $Kfre$) are these which multiply the differential edge contact length (dlc). Yussefian et al. (2008) also worked with boring operations and the determination of the uncut chip geometry based on the cutting parameters.

$$\begin{aligned} dF_t &= dFtc + dFte = KtcdA + KtedLc \\ dF_{fr} &= dFfrc + dFfre = KfrcdA + KfredLc \end{aligned} \tag{2.15}$$

As the specific force approach the linear affine transcends the operations, because is based in uncut chip geometry and cutting coefficients. Gao et al. (2013) developed a mechanistic model for bull–nose milling. The model analyzed
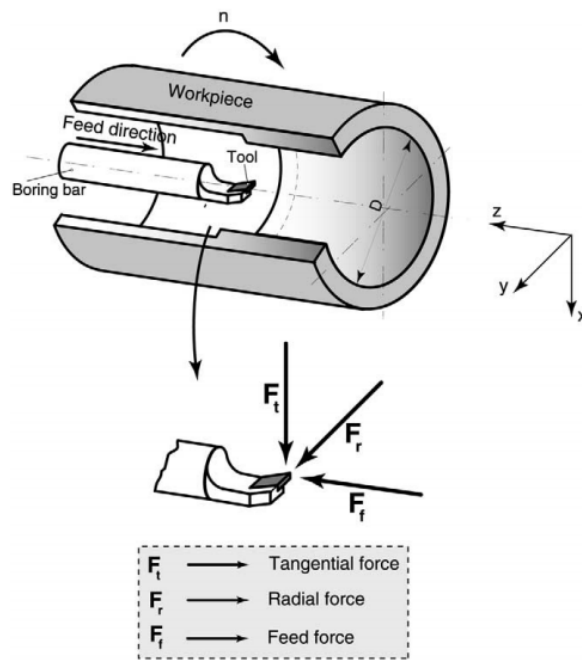
Figure 2.26: Illustration of cutting direction in boring process (Atabey et al., 2003).
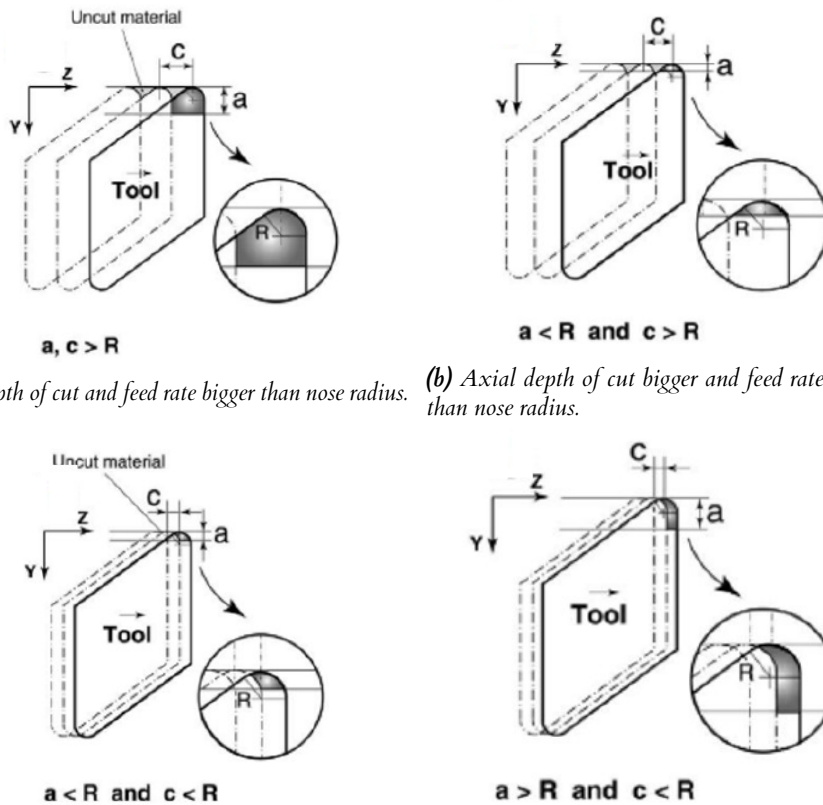
(a) Depth of cut and feed rate bigger than nose radius.

(b) Axial depth of cut bigger and feed rate smaller than nose radius.

(c) Depth of cut and feed rate smaller than nose radius.

(d) Axial depth of cut smaller and feed rate bigger than nose radius.

Figure 2.27: Chip thickness geometry in boring for different cases. (Atabey et al., 2003).

the variations of cutting speed along the tool axis over the cutting coefficients prediction. The approach used to estimate the cutting forces also is the linear affine. However in this research the resultant force division considers the geometry of the tool as tangential (dF_t), radial (dF_r) and axial (dF_a), see equation 2.16. In equation 2.16 Ktc, Krc, Kac are the cutting coefficients contributed by the shearing action during the cutting process in the tangential, radial, and axial directions, respectively. There are also the Kte, Kte, Kte coefficients that correspond to the edge friction coefficients in the mentioned directions .The studied tool profile (bull end nose) is complex and the approach considers the effect of the helix angle then the authors use a coordinate transformation matrix to align the differential of forces to the general coordinate system of the tool, see figure 2.28. Zhu et al. (2001) used this approach to predict cutting forces for multi-axis ball end milling of free-form surfaces.
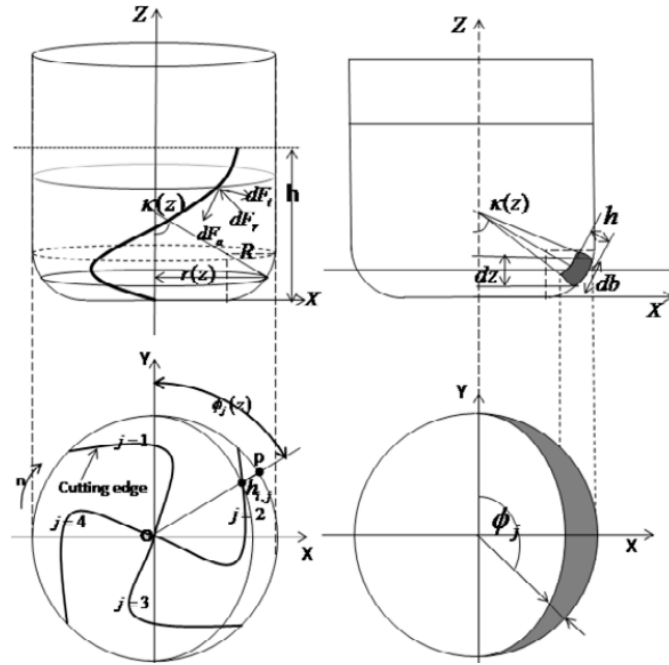
Figure 2.28: *Immersion angle, cutting force components, cutting width and chip load at point P in bull nose end mill (Gao et al., 2013).*

$$\begin{Bmatrix} F_x(\phi, z) \\ F_y(\phi, z) \\ F_z(\phi, z) \end{Bmatrix} = \sum_{i=1}^{n} \begin{bmatrix} dF_{t,i}\sin(\phi) \\ dF_{r,i}\sin(\phi) \\ dF_{a,i} \end{bmatrix} = \sum_{i=1}^{n} \begin{bmatrix} K_{tc}h(\phi) + K_{te} \\ K_{rc}h(\phi) + K_{re} \\ K_{ac}h(\phi) + K_{ae} \end{bmatrix} dz \qquad (2.16)$$

Aristimuño et al. (2018) developed a methodology to refine the behavior of the linear affine approach in small chip thickness conditions. They performed an extensive experimental characterization measuring the forces in thickness even lower than the edge radius, see figure 2.29. Then, it was proposes four different linear models for each edge section (from S1 to S4). Consequently, the model was validated in face milling trials predicting accurately the cutting force behavior in the 3D coordinate system.
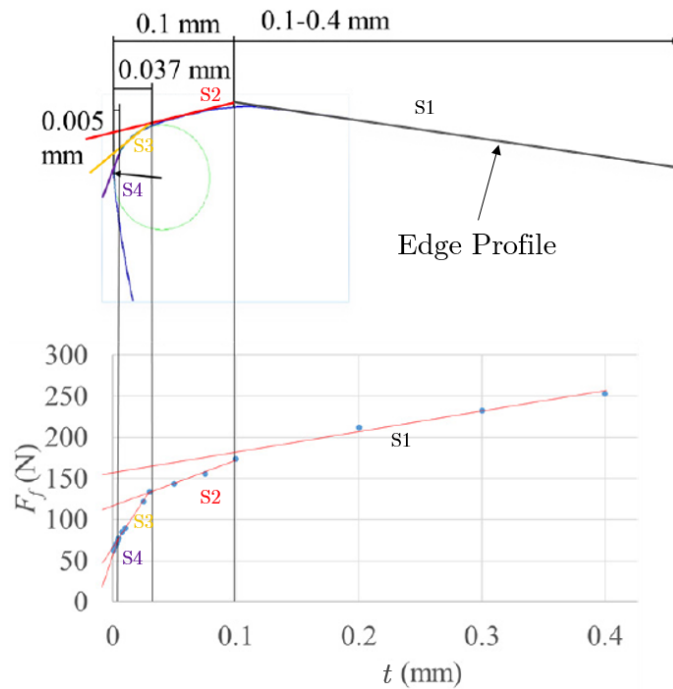
Figure 2.29: *Comparison between the geometry of the walter ODMT060512-D57 insert and the values of the orthogonal experimental feed forces (Aristimuño et al., 2018).*

The presented examples of the application of the linear affine approach for cutting force prediction does not cover the big number of publications related to this approach. This is due to this approach is one of the most popular in literature. There are more studies that cover but are not limitated to the study of effect of the tool profile (flat, torus, ball end mill inserts) cutting conditions, uncut chip geometries, 2 to 5-axis kinematics, etc. (Martellotti, 1941; Lee and Altintaş, 1996; Checchi et al., 2018; Smyczek et al., 2018; Chen et al., 2018; Gradišek et al., 2004; Kaymakci et al., 2012; Crichigno Filho, 2012; Karaguzel et al., 2015b).

Non-linear approaches

The non-linear approaches are the less commons in literature. These approaches are the linear homogeneous and affine approaches but with a term raised to the power of a constant to reduce the errors concerning the experimental data, see figure 2.30. This literature review has detected two publications that use these approach. Kienzle and Victor (1957) proposed in 1957 a model to determine the tangential forces in milling. The authors considered the uncut chip geometry as a constant rectangle formed by the chip thickness (t) and the depth of cut(a_p). If the depth of cut is considered constant, the independent term in the chip area function is the chip thickness, modeling the tangential force as shows equation 2.17. Where (Kst) is the specific tangential coefficient and the exponent $(1 - c_t)$ is constant and determined from the experimental characterization data. Salehi et al. (2018) considered the effect of the friction suffered for the edge in the cutting process introducing the friction tangential coefficient (K_{te}) to the model

presented by Kienzle and Victor (1957) as shows equation 2.18.

$$F_t = K_{st} a_p t^{1-c_t} \tag{2.17}$$

$$F_t = K_{st} a_p t^{1-c_t} + K_{te} a_p \tag{2.18}$$
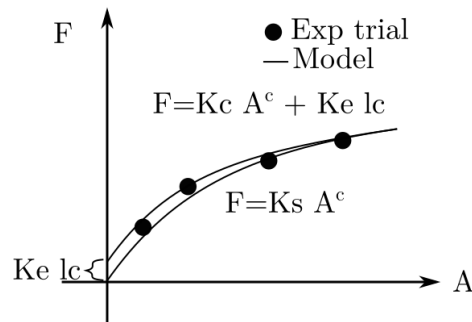
Figure 2.30: *Non-linear models behavior scheme.*

2.2.4 Cutting coefficient determination

As presented previously in machining, the cutting forces depend on the uncut chip geometry and the cutting coefficients. The uncut chip geometry depends on the kinematics of the machining operation and the edge morphology. The cutting coefficients summarize the interrelationship between the edge and the material, considering parameters such as chip thickness, cutting speed, edge geometry, edge coating, and bulk material. In this way, the mechanistic approaches are supported in characterization cutting trials. These trials are complete experimental designs that determine the value of the coefficients relating the measured forces with the considered parameters via parameter variations. This literature review identified two methodologies to determine the cutting coefficients the characterization trials and the orthogonal to oblique transformation.

Characterization trials

Altintas and Ber (2001) explain in their book the process to determine the cuting coefficients with characterization trials. This methodology is the most direct method to determine the cutting coefficients but require a fixed cutting force sensor as shown in figure 2.31 (a). This method consist on the definition of a experimental plan varying the cutting trials usually the feed per tooth and measure the cutting forces to generate fitting expressions that are going to be used lately in the cutting force predictions, see figure 2.31 (b). Qiu et al. (2016) used this methodology to determine the cutting coefficients trough the mean force and the equations exposed by Altintas and Ber (2001), obtaining accurate force predictions lately.
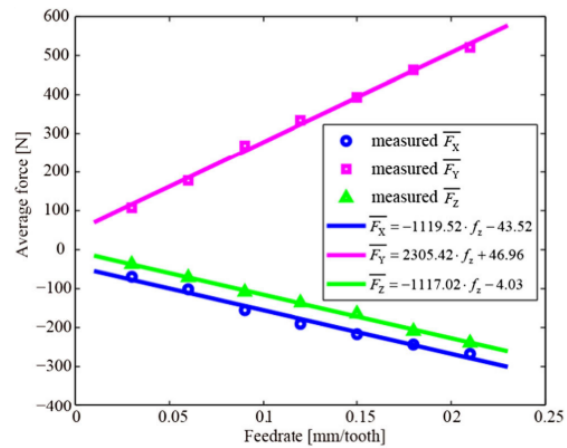
(a) Experimental set up.   *(b) Cutting force results.*

Figure 2.31: *Cutting coefficient determination Qiu et al. (2016) in aluminum 2A12 (2024).*

Grossi (2017) proposed a novel method to determine the effect of the spindle speed to the cutting coefficients in face milling. This research accelerates the spindle speed and capture the cutting forces maintaining the feed and depth of cut constant. The acceleration is discrete but the sampling time is just two spindle rotations, so it can easily cover huge intervals of cutting speeds in one pass, as shows figure 2.32. Gonzalo et al. (2010) developed a method to obtain the cutting coefficients by measuring the cutting forces in face milling trials. Then as the uncut chip geometry is known then they can solve equation 2.16 for the cutting coefficients that are unknown.
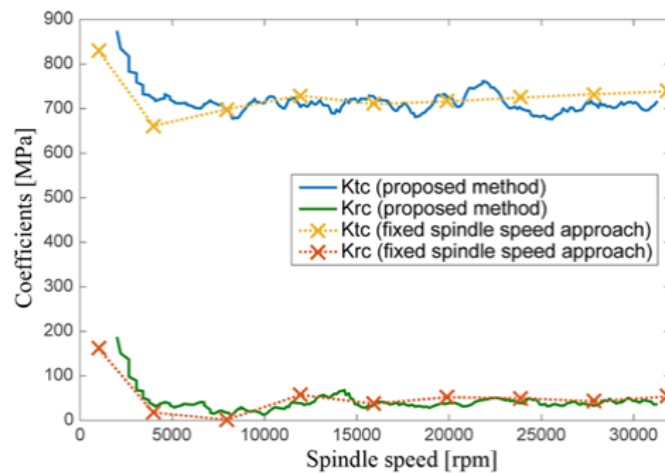
Figure 2.32: *Coefficients validation compared to fixed spindle speed in aluminum 6082-T4*

The characterization trials methodology is relatively simple to implement. However, it is only valid for the machining operation performed and it losses accuracy when the cutting conditions are far from those used in the characterization trials. Considering the variables to introduce in the models the experimental time and cost in tools and material might be considerably high.

Orthogonal to oblique transformation

Orthogonal cutting is a simplification of the machining process, transforming a 3D problem into a 2D one. Astakhov (2010) describes the orthogonal cutting as that type of cutting where the straight cutting edge of the wedge-shaped cutting tool is at right angle to the direction of cutting; hence its name, a scheme of the process is shown in figure 2.33 (a). The distinctive features of orthogonal cutting are:

• The cutting edge is wider than the width of cut.
• No side spread of the layer being removed occurs on its transformation into the chip.
• Plane strain condition is the presented during the chip formation process.

(a) Orthogonal cutting scheme.   *(b) Oblique cutting scheme.*
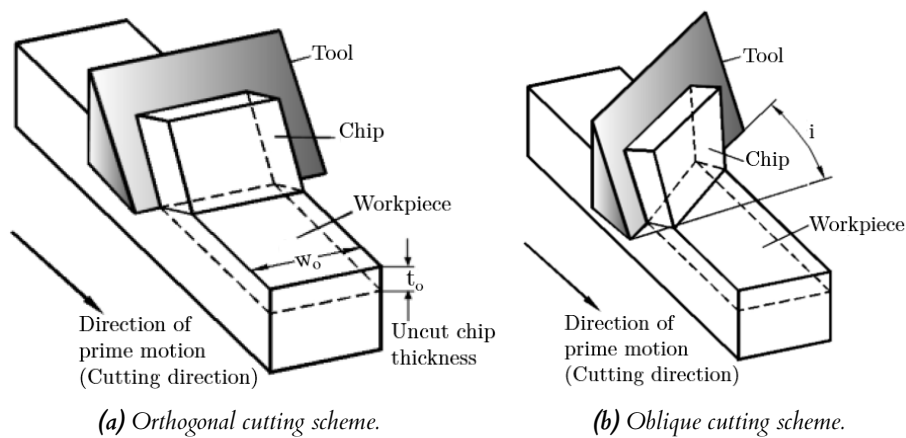
Figure 2.33: Orthogonal and oblique cutting scheme (Astakhov, 2010).

The author continues describing the oblique cutting as that type of cutting where the straight cutting edge of the wedge-shaped cutting tool is not at right angle to the direction of cutting, see figure 2.33 (b). The angle which the straight cutting edge makes with the direction of the cutting speed is known as the cutting edge inclination angle i. The plastic deformation of the layer being removed in oblique cutting is more complicated than that in orthogonal cutting. Therefore, this type of cutting is represented by a 3D model (Astakhov, 2010).

The characterization trials approach is shown to depend on milling force coefficients determined from milling test for each tool geometry. By contrast the unified mechanics of cutting approach relies on an experimentally determined orthogonal cutting data base (i.e., shear angle, friction coefficient and shear stress), incorporating the tool geometrical variables and milling models based on a generic oblique cutting analysis. This methodology finds the milling force coefficients for all force components and tool geometrical designs based on the cutting data base and the generic oblique cutting analysis for use in the mechanistic models. this method eliminates the need for experimental calibration of each milling cutter geometry for the mechanistic approach and can be applied in more complex tool designs (Budak et al., 1996).

Regarding orthogonal to oblique models, Budak et al. (Budak and Altintas) proposed a model for calculating milling force coefficients from orthogonal data.

The model consisted of establishing a material database where the values of shear stress, friction angle, chip compression ratio, and edge force coefficients were defined, as in table 2.5. Where τ is the shear stress, β is the friction angle, r_t is the chip compression ratio, α is the rake angle, t is the uncut chip thickness, and K_{te} and K_{re} are the specific tangential and radial edge coefficients.

Table 2.5: Material database for Ti6Al4V (Budak and Altintas).

τ	613 MPa
β	$19.1 + 0.29\alpha$
r_t	$r_0 t^a$
r_0	$1.755 - 0.028\alpha$
a	$0.331 - 0.0082\alpha$
K_{te}	24 N/mm
K_{re}	43 N/mm

The orthogonal data necessary to develop the material database (cutting forces, feed force, and cut chip thicknesses) were obtained from orthogonal turning tests. To calculate the parameters of the database, equations developed by Merchant (Merchant, 1944) were used as shown in equations 2.19, 2.20, and 2.21. Where r_t is the chip compression ratio, ϕ is the shear angle, F_{pc} & F_{qc} are the power and thrust cutting forces respectively, b is the width of cut and t is the chip thickness, and c is a recurrent combination of variables presented in the cutting coefficients. once the material database was obtained, cutting coefficients were estimated using equations 2.22, 2.23, 2.24, and 2.25.

$$\tan(\phi) = \frac{r_t \cos(\alpha)}{1 - r_t \cos(\alpha)} \tag{2.19}$$

$$\tau = \frac{F_{pc} \cos(\phi) - F_{qc \sin(\phi) \sin(\phi}}{bt} \tag{2.20}$$

$$\tan(\beta) = \frac{F_{cq} + F_{pc} \tan(\alpha)}{F_{cq} - F_{pc} \tan(\alpha)} \tag{2.21}$$

$$K_{tc} = \frac{\tau \cos(\beta_n - \alpha_n) + \tan(\eta_c) \sin(\beta_n) \tan(i)}{\sin(\phi_n)c} \tag{2.22}$$

$$K_{rc} = \frac{\tau \sin(\beta_n - \alpha_n)}{\sin(\phi_n) \cos(i)c} \tag{2.23}$$

$$K_{ac} = \frac{\tau \cos(\beta_n - \alpha_n) \tan(i) - \sin(\beta_n) \tan(\eta_c)}{\sin(\phi_n)c} \tag{2.24}$$

$$c = \sqrt{\cos(\phi_n + \beta_n - \alpha_n)^2 + \tan(\eta_c)^2 \sin(\beta_n)^2} \qquad (2.25)$$

Figure 2.34 shows a comparison between the orthogonal and oblique cutting, illustrating the relationship presented in the previous set of equations. The orthogonal to oblique transformation is a methodology that characterizes the material being machined. This method uses orthogonal cutting data to determine the cutting coefficients. One of the main advantages of this approach is that the database developed applies to diverse machining operations and tool geometries. The cutting coefficients are not constants but mathematical expressions that consider diverse parameters such as the edge geometry, cutting speed, uncut chip thickness, etc. The main disadvantage of this approach is considering all machining parameters, an extensive experimental design must be implemented to include the relationship between various parameters. This situation implies procuring customized edges to cover the wedge–shape interval available in the market. Despite the extensive experimental work, the material database can be used in diverse machining operations with diverse cutting conditions, and in some industries, this is a piece of precious knowledge, for example, the aeronautical propulsion sector.

(a) Orthogonal cutting mechanics.

(b) Oblique cutting mechanics.
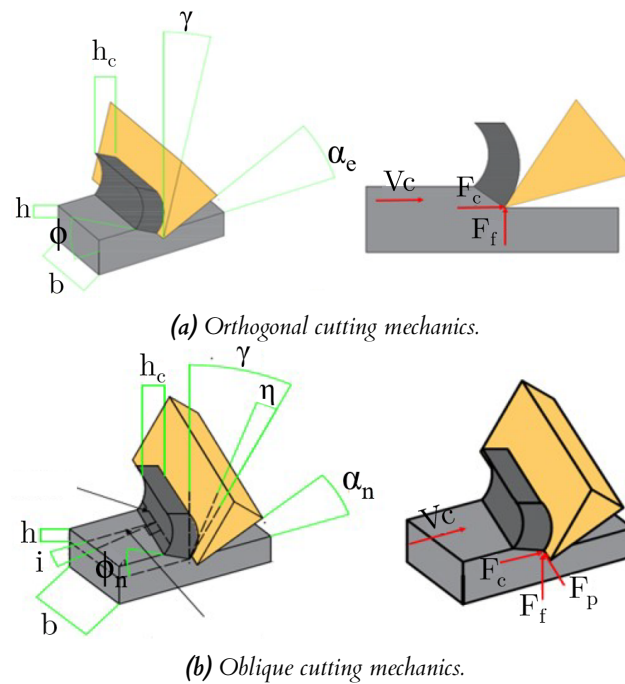
Figure 2.34: *Comparative forces in orthogonal an oblique cutting.*

2.2.5   FEM Approach

The orthogonal cutting is widely simulated due to the kinematic simplicity of the process. Arrazola et al. (2008) proposed a method to identify the friction during machining. This variable and the cutting temperature are very challenging to measure experimentally; then, the FEM models are interesting approaches

to determine them. Gonzalo et al. (2009) presented an approach to determine the cutting coefficients through FEM software substituting the experimental trials for orthogonal simulations in AISI 4340 steel. Considering the extensive experimental work that the orthogonal to oblique transformation demands, the simulation results in a cheap solution to avoid the experimental expenses.

The simulations scopes are becoming bigger with the years. Altintas et al. (2014) presented an overview of digital technologies to simulate diverse manufacturing process such as turning, milling and grinding. The efforts are focused to generate a digital twin where diverse aspects are considered such as geometrical, kinematic, thermomechanical, and sufrace generations. This work considers but is not limited to devleopments in CAD/CAM techniques and the novel implementation of cutting forces, uncut chip geometry determination, stability and geometrical errors, see figure 2.35.

(a) Tool path of a stamping die

(b) Predicted cutting forces

(c) Measured cutting forces
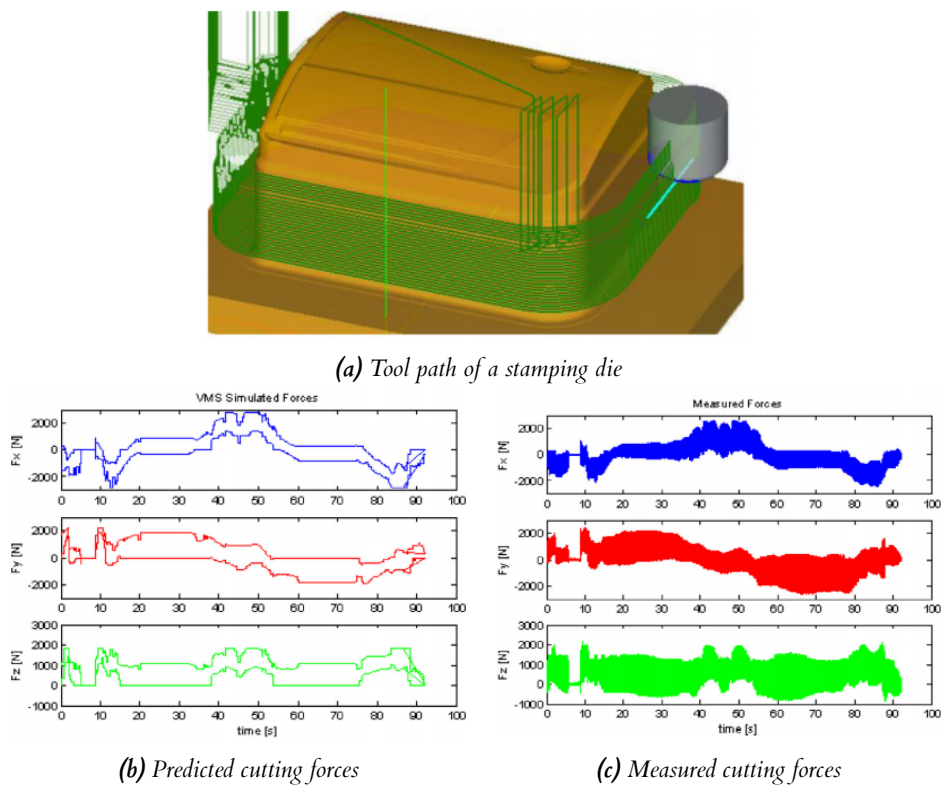
Figure 2.35: *Virtual machining of a stamping die. Comparison between the modeled and measured cutting forces during machining.*

The FEM approaches are an interesting method to determine cutting forces, moreover if the expensive experimental process want to be avoided. However, the costs of experimental setups are transferred the the rental of software licenses that might be considerably high. These software are continuously evolving year to year and sometimes there are incompatibilities between versions. As the theory of some critical variables are still under development sometimes the simulations do not coincide with experimental data; and being this software commercial developments there is limited access to the models. This approaches are usually considered as trending guide more than accurate representation of machining processes.

2.2.6 Comparison of the approaches to predict cutting forces in turn-milling

After the review of methodologies for cutting forces prediction, it was identified some advantages and disadvantages summarized in table 2.6. These features are fundamental to determine the methodology to be used in this thesis. Based on this, and following the trend of the researchers with cutting force in turn-milling operations the mechanistic methodology seems to be the most versatile, accurate and relatively easy to implement.

Table 2.6: Cutting force methodology comparison

Approach	Advantages	Disadvantages
	• Predictions achieved in short time. • No need of expensive software.	• Expensive trials for material characterization. • Non industrial machine to material characterization. • Inaccurate predictions.
Mechanistic	• Highly accurate predictions. • Relatively fast and cheap characterization trials. • Characterization trials achieved with industrial machinery. • No need of expensive software. • Predictions achieved in short time. • in the case of orthogonal to oblique database works for all machining operations.	• Extensive experimental trials for material characterization. • Expensive measuring setup. • Might need of customized tools.
FEM	• Cover huge scenarios with no financial cost • Predictions in challenging to measure variables such as temperature and strain rate • Analysis in several parameters simultaneously • No need of industrial machinery	• Expensive trials for material characterization. • Non industrial machine to material characterization. • Questionable accuracy in the predictions. • Expensive software to perform simulations

2.3 Other topics associated with turn-milling

The study of turn-milling operations does not limit to the topics already discussed. There are also interesting research on other aspects that are not directly aligned with this thesis but shows the potential of this manufacturing process.

2.3.1 Geometrical errors

Modern industry requires high-precision machines and processes, which implies the identification and avoidance of all possible sources of error (Olvera et al., 2012). The turn-milling kinematics, fastening system result in geometrical discrepancies (Egashira et al., 2016). Negau et al. studied the fundamentals of straight shaft manufacturing where some fundamentals aspects such as generation geometry, machining accuracy, cutting kinematics, and tool functional geometry have been proposed (Neagu et al., 2005).

(Schulz and Spur, 1990) mentioned that to avoid wavy and non-circular surfaces during intermittent circular solids is a very important aspect to consider. However, there is a lack in analyzing this characteristic; few research teams have publications in this area. Wang et al. (2012) developed a method for getting the scallops of the same height or cylindricity error and being as small as possible in orthogonal turn-milling reaching heights of scallop close to 50 μm. In this work, the authors developed an algorithm to calculate the optimum path interval for the lowest height geometrical errors.
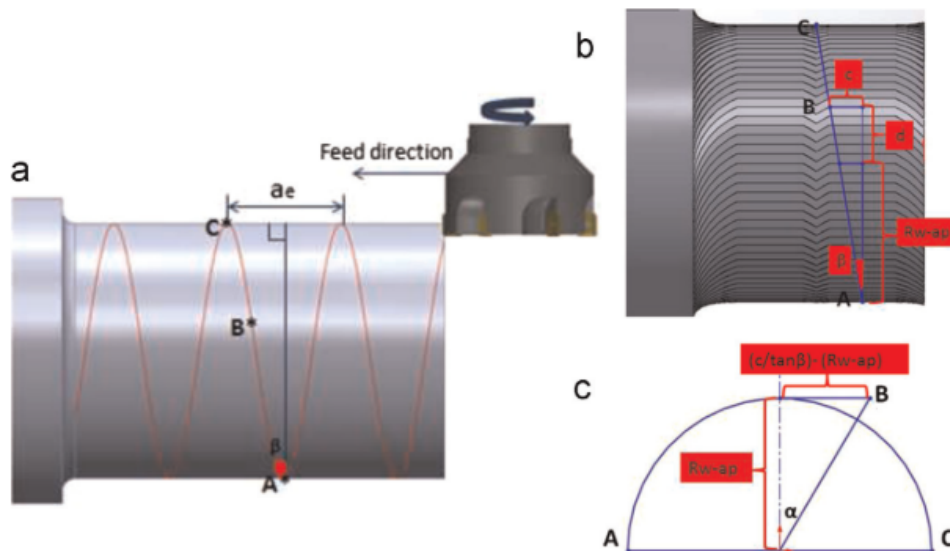
Figure 2.36: *Cusp and circularity errors in orthogonal turn-milling operations Karaguzel et al. (2015b).*

Karaguzel et al. (2012, 2015b) and Kara and Budak (2015) proposed that the circularity errors can be modeled from the kinematics analysis of orthogonal turn-milling by subtracting the produced shape, which depends on the cutting parameters minus the circle of design. The model developed is an asymptotic function that depends strongly on the ratio of rotational speeds from the tool and

the workpiece; this means that there will always be a circularity error (Kara and Budak, 2015; Karaguzel et al., 2015b, 2012). Despite the discussion presented, there is no experimental validation of this theoretical work. Uysal et al. (2014) and Karaguzel et al. (2015b) researched a validated model to predict the cusp height error in orthogonal turn-milling. This model related the cutting conditions with the geometrical errors in cusp and circularity, see figure 2.36.

Karpuschewski et al. (2017) researched the tangential turn-milling obtaining lower roundness errors than those from grinding and hard turning. The results oscillate around 3 μm in the roundness deviation, reducing almost half the geometrical errors compared with hard turning. Figure 2.37 shows the results of Karpuschewski, the sample 1 to 4 are turn-milled surfaces with different cutting conditions and they are compared with the resulting surfaces from hard turning and grinding in similar productivity conditions.
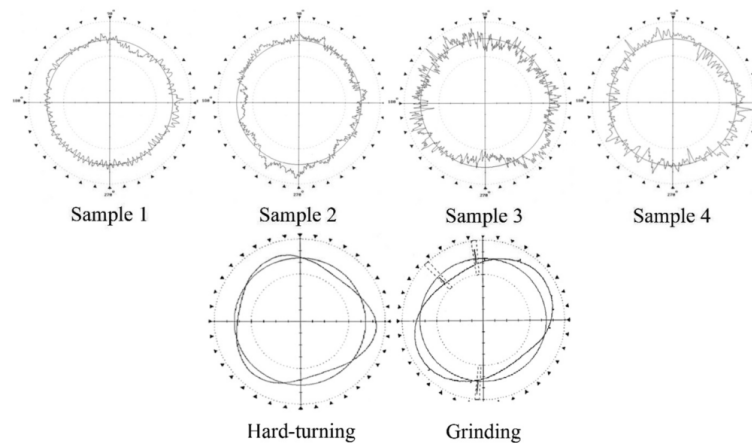
Figure 2.37: Roundness images of the turn-milled and reference samples (Karpuschewski et al., 2017).

The primary approach taken in the study of the turn-milling operations is for roughing for a cylinder. In this approach, circularity and cusp errors are studied analytically and experimentally. The main conclusion of the circularity error is that the workpiece rotational speed should be considerably lower compared with the tool rotational speed to decrease these errors. Additionally, the cusp errors are due to excessive axial feed; thus, if this variable decreases, the cusp error will have minor height. Besides this, the comparative study performed by Karpuschewski suggests that turn-milling operations produce more accurate circles than hard turning and grinding.

2.3.2   Vibrations and dynamics in turn-milling

The stability of turn-milling is an essential factor for machining quality and efficiency. Most researchers and experts have been focusing on general turning or milling but turn-milling have relatively few publications (Zhu et al., 2015a). Budak et al. (2013) worked on the stability and high-performance machining conditions in simultaneous milling where is proposed chatter stability where determined. Yan et al. (2016) researched the stability prediction in the frequency

domain , modeling the uncut chip geometry and considering the variable cutting depth and cutting thickness during the mill rotation. This work concluded that the varying cutting depth effect decreases with the increment of the tool radius (Yan et al., 2016). Nevertheless, the complete work of Yan does not define which of the cutting parameters affects more in the chattering behavior. The geometry model states that the axial feed and the cutting depth are significant to determine the uncut chip geometry that is the primary input for the posterior development.

2.3.3 Temperature in turn–milling

The cutting temperature in turn–milling is a challenging variable to measure because of the coupled movement of workpiece and tool. (Peng et al., 2015) developed experimental research to find the cutting parameters that have a high effect on the workpiece temperature, finding that the depth of cut ant the cutting speed increase considerably the workpiece temperature. Also a heat transfer inside the workpiece has been presented and validated experimentally, see figure 2.38.
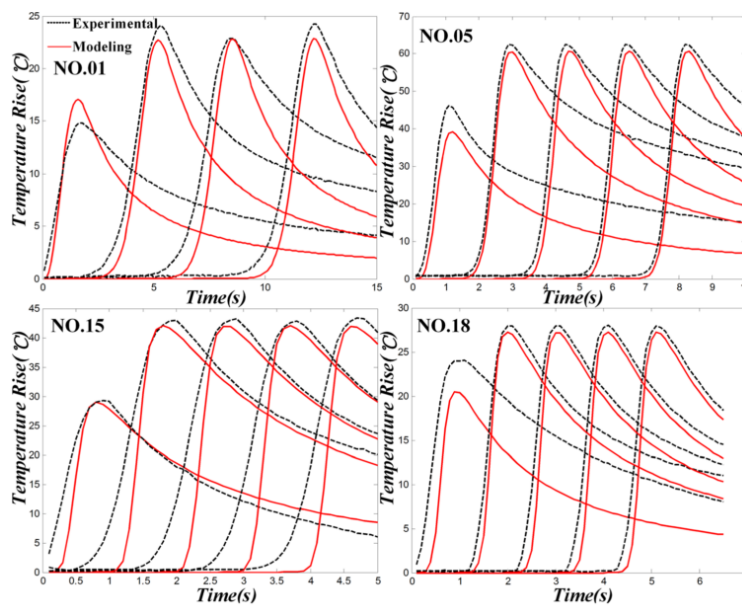
Figure 2.38: *Comparisons of temperature profiles examples (the number of thermocouples are 1-5 from left to right) (Peng et al., 2015).*

Putz et al. (2016) researched the turn–milling improvement by controlling forces and thermally induced center (TPC) displacement and finding that the tool is deformed by the temperature effect and will affect the next pass showing that the second pass applies more force than the first one. Karaguzel et al. (2017) researched the unified analytical model to predict the cutting temperatures based on the cutting forces. This work presented a theoretical study of variating cutting speed, axial feed over the cutting temperature on the time domain. The most potent cutting parameter is the axial feed, doubling the temperature with an increment of feed from 0.3 to 1.2 mm .

In the temperature literature review, most authors concur that the axial feed

has a strong effect on the temperature. The following parameter that has the most influence on the temperature is the cutting depth and cutting speed; the theory and the experiments confirm it. The cutting temperature measurement is a problem to solve yet even in conventional machining.

2.3.4   Tool wear

Schulz and Spur (1990) determined which of the cutting edge (the flank edge and the end edge) suffers more wear in coaxial milling. Finding that the wear on the edge that is perpendicular to the feed suffer higher wear, in this case the end edge. This research implies a complex cutting zone in operation and exposes that the cutting load is not equally distributed. Schulz and Kneisel (1994) researched on the influence of the cutting speed and the feed per tooth over the tool wear in coaxial turn-milling. The experimental trials suggested that the cutting zone is heated intensely, and with increasing the cutting speed, there is a softening of the material with positive effects on the tool path. On the other hand, low feeds per tooth cause increased friction and result in longer cutting paths, but higher feeds lead to higher mechanical stresses on the cutting edge due to the increasing chip section.

Huang and Cai (2013) correlated the wear suffered by the tool with the surface generated; therefore, a model is proposed to predict the tool wear based on the cutting parameters for orthogonal turn-milling. The experimental test showed that changing the cutting parameters in different sections of workpieces is a handy method to balance the cutter wear. Nevertheless, the work is not clear on how this relationship is done and the most sensitive cutting parameters of the process.Cai et al. (2012) presented an experimental approach concluding that the eccentricity, the number of flutes, and the axial feed rate are the most sensitive parameters over the tool wear (Cai et al., 2012). This work states that when the eccentricity is close to the the half of the cutter radius, the cutting edge is using the maximum length distributing the uncut chip geometry increasing the tool life.Su et al. (2013) developed an empiric model based on exhaustive experimentation to relate the effect on the variation of the cutting conditions over the wear experimented by the tool.

(Karaguzel et al., 2015a, 2014) andUysal et al. (2014) also studied the effect of the eccentricity in the orthogonal turn-milling operations. The research began with an experimental approach where the evidence suggests an optimal eccentricity value to maximize the tool life, stating that the optimal eccentricity is when $e_{opt} = r_t - l_s$; however there is any kind of theoretical foundation to state this. Where r_t is the tool radius and L_s is the radial length of the edge of the insert.

Kara and Budak (2015) developed an empirical model where the effect of increasing the cutting speed over the tool wear has been studied, obtaining a decrement in the tool life if the speed increases. (Karaguzel et al., 2015b, 2014) have compared orthogonal turn-milling performance with conventional turning on difficult-to-cut materials reaching longer tool life for the turn-milling operations from 3 to 40 times better than conventional turning depending on the material . Figure 2.39 shows the results which evidence of the effect of implement
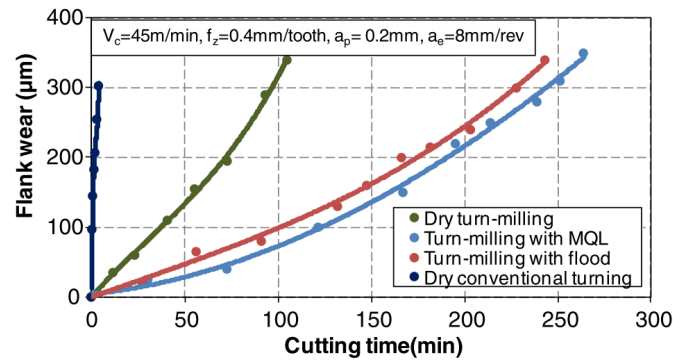
(a) Tool wear results for Ti6Al4V.
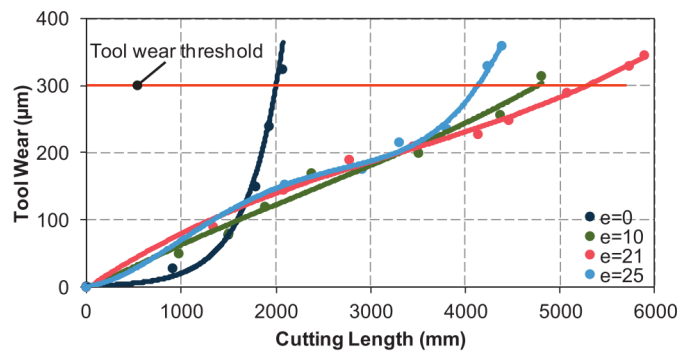
(b) Effect of the tool axis offset on tool wear.

Figure 2.39: *Life trials in turn-milling (Karaguzel et al., 2015a, 2016).*

turn-milling instead of conventional turning and implementing eccentricity for orthogonal turn-milling in AISI 1045 steel.

Karpuschewski et al. (2017) presented a tribological analysis of contact parts. In this work, wear is understood as the amount of mass loss after constant operation of the part for 24 hours. Parts are machined by tangential turn-milling operations, conventional turning, and grinding. As a conclusion of this work, the authors found that tangential turn-milling achieve the surface quality comparable with grinding.

2.3.5 Surface finishing and roughness

The surface finishing obtains through turn-milling operations has been studied over the machining cases (Coaxial, Orthogonal and Tangential) due to the significant differences in the set-up and kinematics. Following is presented the literature review about the surface finish. The main findings are going to be discussed at the end of this section.

Coaxial turn-milling

The turn-milling operations are associated with low roughness manufacturing process. Schulz and Spur (1990) reports surface roughness Ra lower than 0.5 µm with optimized axial feed rates, considering the effect of edge wear over the

surface finishing. This research team has reported values below 10 μm for coaxial turn–milling operations in hard steels.

Orthogonal turn–milling

Kopač and Pogačnik (1997) compared the surface roughness of the orthogonal centric eccentric turn–milling, finding that the eccentricity ($e_{opt} = r_t - l_s$) presents the best surface roughness. Choudhury and Mangrulkar (2000) developed an empirical analysis of the centric orthogonal turn–milling considering the axial feed, the rotational speed of the workpiece and tool to determine the effect over the surface roughness; finding that the increment of the cutting speed and decrement of the axial feed decrease improves the surface roughness. (Choudhury and Bajpai, 2005) presented an empirical study of increasing the workpiece rotational speed, the tool diameter, and the cutting depth in centric turn–milling, finding that the increment of the workpiece rotational speed until 10 rpm and the augment of the cutting tool diameter is beneficial to the surface finish. Cai et al. (2012) found that the the eccentricity level close to the tool radius increases the surface finish.

Ekinović et al. (2007) developed a comparative study between high–speed turn–milling and conventional turning making equal the material removal rate an the axial feed; finding a better surface finish with the turn–milling operation. Zhu et al. (2013) presented models experimentally validated to predict the surface topography considering the cutting parameters within the model.

Tangential turn–milling

(Savas and Ozay, 2007) presented an experimental study of tangential turn–milling where the depth of cut, axial feed, the rotational speed of the workpiece and tool were considered to observe the effect over the surface roughness. This study presented similar results than the orthogonal case addition and outstanding surface roughness around than 1 *μm*. Savas and Ozay (2008); Savas et al. (2016) through a genetic algorithm of the cutting parameters to find the combination with the minor surface roughness. This method is used because turn–milling operations have an increased number of parameters and this makes difficult to set the optimal window by trial and error.

Funke and Schubert (2016) studied the surface topology for different end mill geometry to increase the static friction coefficient over cylindrical parts, developing a mathematical model that predicts the surface topography of the turn–milled part. Obtaining besides the topography of the machined part that the chamfer mill augments the friction coefficient. Ratnam et al. (2016) performed a comparative study between the orthogonal and tangential turn–milling confirming the suggestion of the data of the early work Funke and Schubert (2016); Savas and Ozay (2007, 2008); Savas et al. (2016). With the same cutting conditions, the tangential turn–milling beats with a wide margin the roughness product of the orthogonal process Ratnam et al. (2016). The roughness from the tangential setup is so low that it can be compared with grinding. Indeed, Karpuschewski et al. studied the behavior of a rolling part manufactured by tangential turn–milling,

grinding, and hard turning, see figure 2.40 (Karpuschewski et al., 2017). This study varies the rotational speed of the workpiece and the tool, the axial feed, and the tool inclination to do a tribological analysis of the rolling parts (working piece). The roughness obtained from grinding and hard turning lower than the turn-milling parts. The workpieces are contact parts for a rolling system. The friction coefficient and tribological trials reached by turn-milling parts gave better results than the grinding and hard turning parts. This work concludes that manufacturing these parts by turn-milling operations increases productivity by the reduction of reprocesses. Besides this, the quality of the part is increased, resulting in better tribological behavior (Karpuschewski et al., 2017).
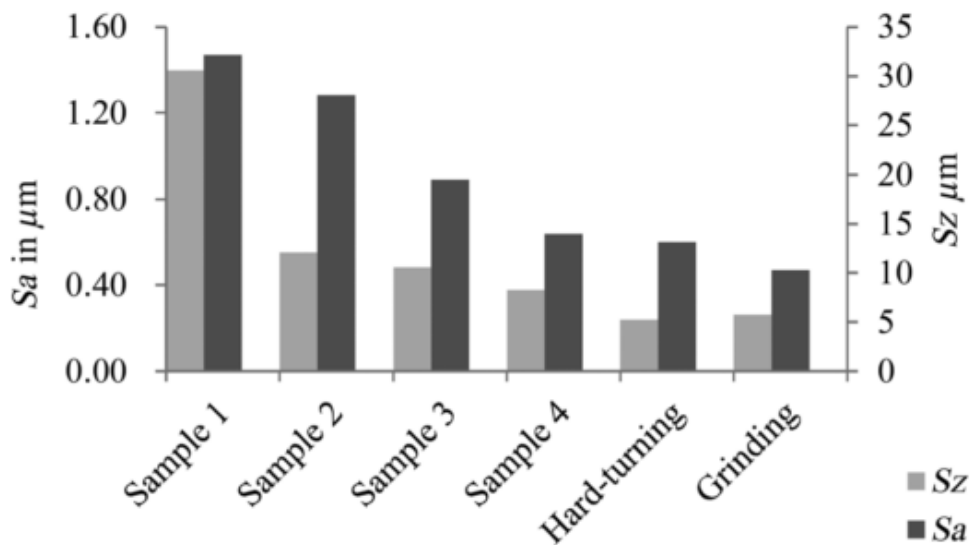
Figure 2.40: *Roughness of the samples compared with the references specimen (Karpuschewski et al., 2017).*

Jiang et al. (2011) developed a mathematical model that predicts the texture of the workpiece machined, considering the turn-milling kinematics that allows performing simulation in different cutting conditions. The texture height increases from 0.25 to 0.8 with the increase of f_z from 0.314 to 0.628 mm. The feed effect in a set of trials of the turn-milling operation was studied, presenting contradictory results. Rahman et al. (2017) studied the effect on the surface finishing and error if the feed is raised from 100 to 400 mm/min. In this case, the low feed resulted in the best finish surface, and it decreases with the increase of the feed. However, it seems that increasing four times the feed the roughness does not increase proportionally.

In general terms the turn-milling operations produce low roughness surfaces. This is the most outstanding feature of turn-milling compared with conventional or hard turning. However, there is no consensus over the parameters that reach these results. The case of turn-milling presents considerable differences between each other; figure 2.41 summarizes the reported roughness in the reviewed publications.
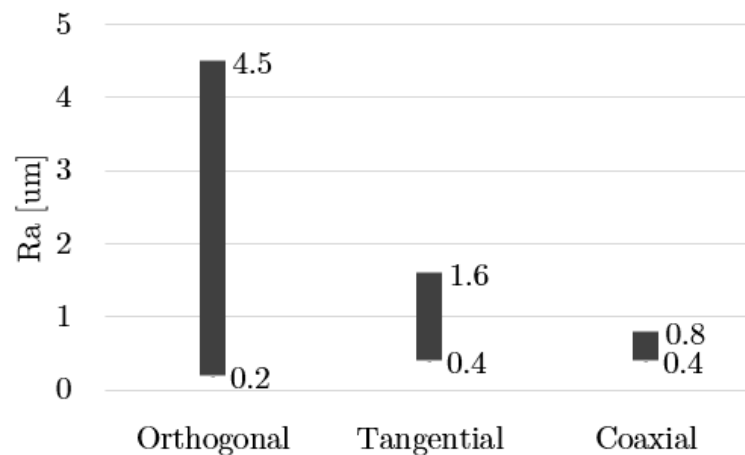
Figure 2.41: Summary of the experimental values found in the literature per case of turn-milling.

2.3.6   Virtual machining and artificial intelligence

Virtual machining is a computational graphic environment that simulates the machining process introducing the machine tool CAD design, kinematics, and mechanics of the machining process; several disciplines within the machining aim to produce the digital twin of the process. In this area, Wang et al. (2008) have worked in the development of a turn-milling simulator with a 5-axis machine tool considering statics, kinematics, dynamics, thermal, and vibration characteristics. Zhu et al. (2008) published a study of the rigidity of the machine tool as a whole by co-simulating the coupling systems in ANSYS® and ADAMS®. The main milestone of this research is the study of the effect of the kinematics on the rigidity of the machine tool that opens the possibility to iterate the design to improve the flaws in the presented design. (Zhu et al., 2011) presented the process of designing high-grade CNC machine tools, using the virtual prototype technology based on the analysis of the kinematics simulation runs and analyzes directly, see figure 2.42. (Yu et al., 2013; Zhu et al., 2015b) presented a different web-based virtual turn-milling system that helps users and process planners obtain more information and production functions globally. It comprises three main functions: machining simulation function, movement demonstration of turn-milling center function, and information communications functions.

Artificial Intelligence (AI) has been applied to turn-milling. In general terms, there are two different approaches: the first one is for optimization proposes, due the turn-milling is a process with an ample amount of initial parameters and is difficult to see at first view how they affect over the finished part (Yusup et al., 2012). (Savas and Ozay, 2008; Savas et al., 2016) applied a genetic algorithm to find the optimum cutting conditions to get a better surface finishing in order to determine the optimum point. (Wang et al., 2012) have worked in the optimization of toolpath to reduce the geometry errors (scallops or cusp errors) as much
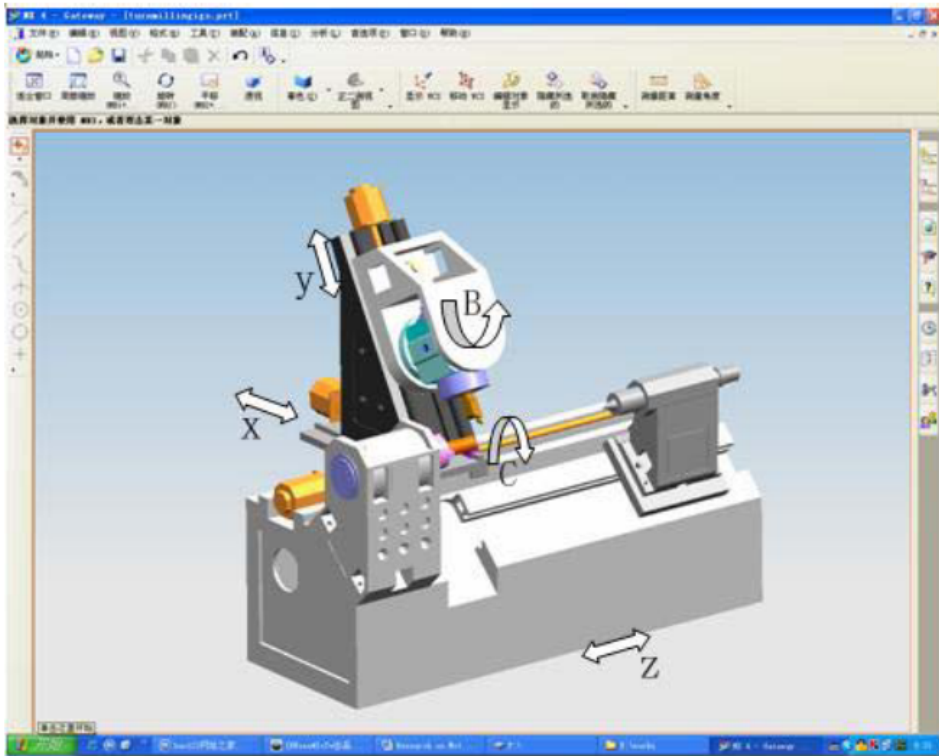
Figure 2.42: *3D model of turn-milling centre in Unigraphic software (Zhu et al., 2011).*

as possible and getting a uniform geometry, see figure 2.43.
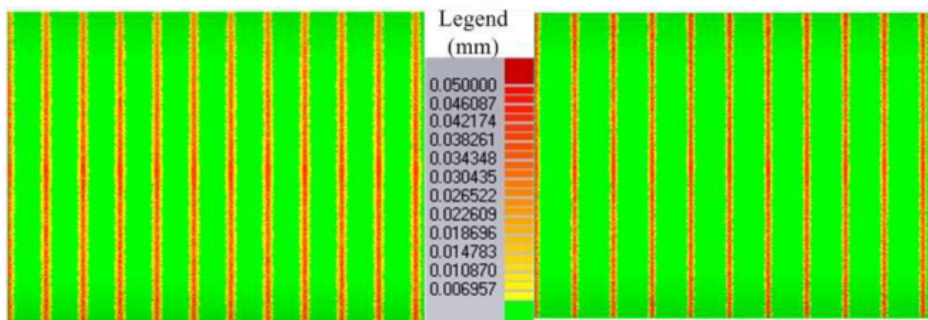
Figure 2.43: *Contrast of scallops height distribution (Wang et al., 2012).*

2.4 State of the Art conclusions

The literature review covered diverse aspects related with turn-milling operations. This machining technology results an interesting alternative conventional turning and also to manufacture large format, slender and protuberance workpieces. This technology

- Despite Karaguzel et al. (2017); Uysal et al. (2014); Zhu et al. (2015a) say that turn-milling is a high productivity process, the MRR values found in literature are not especially high compared with the conventional machining.

This comparison does not consider the machine tool power, and also that the laboratory tests do not seek to maximize the MRR.

• There is no a unified model to predict the uncut chip geometry for the orthogonal case. Furthermore, the current models could not be replicated in this work because of mathematical inconsistencies detected in the equation of the models. These errors were related to show more independent variables than the equation should have.

• A large group of researchers has published works in cutting force prediction in machining operations. However, turn-milling publications tend to use empirical models due to their practicality and high accuracy results.

• The stability modeling of the process is weak and undeveloped; only one publication touches the subject directly. Indeed, the geometric model used to predict cutting forces does not consider the end-cutting zone, only the flank-cutting zone. The dynamic analysis has been focused on finding the natural frequencies of the turn-milling machine tool for design but not for chatter proposes.

• The thermal studies in turn-milling operations only present one publication that measures the increment of temperature over the workpiece, measuring and predicting shallow results. There is no consensus between the authors in the increment of temperature during the cutting. The prediction models state temperatures around 35°C and 800°C that is a significant discrepancy between the research team. They have in common that the models are a function of the uncut chip geometry. The power consumption should increase proportionally to the MRR that is a function of the uncut chip geometry. The cutting speed is the following parameter that influences the temperature during the cutting. The measurement of the temperature on the cutting zone has not been performed jet.

• The tool life is enormously increased by augmenting the eccentricity, number of edges, cutting speed, and reducing the axial feed. Empirical approaches tackled the modeling of wear.

• The surface finish obtained through turn-milling operations reaches values in Ra below 0.4 μm. However, there is no consensus over the primary cutting parameters that influence the surface finish. It seems that the finishing is very sensitive to all the primary cutting parameters. Although experimental work was carried out, data has not been presented to identify which factor affects more than others.

• The geometrical accuracy goes in detriment with the increment MRR. The data suggest that operating in low feed and high cutting speed will reduce the geometrical errors beating turning and grinding.

• Virtual machining focuses on the machining process simulation, looking to develop the digital twin of turn-milling manufacturing centers. A virtual reality simulator has been developed to process planning and operator formation. AI applications have been developed to find optimized cutting parameter combinations due to the extensive set of variables to fix.

• There is a focus on the authors in the orthogonal turn-milling case because this is the most versatile and used case of turn-milling.

After the literature review, it is essential to highlight a weak model development to find the remarkable cutting parameters. The reviewed authors are not agree in the effect of the eccentricity over cutting force, tool life and surface finishing. Some groups conjectured the value of optimal eccentricity without demonstrate with theoretical foundation at all.

The uncut chip geometry has been studied through different approaches. However these models have not been replied with the published information in the consulted papers. This situation raises questions about the validity of the models since these approaches are not falsifiable. Even when some of these approaches are validated experimentally, usually the information of the experimental trials is not complete and it is not possible to repeat them.

The development of falsifiable models that might be reviewed and repeated for diverse researchers will strongly impact in the understanding of the turn-milling operations. Considering the variation of the cutting conditions over industrial parameters such the surface roughness, tool life, geometrical error; and scientific parameters such as cutting forces and temperature, process stability, etc. This efforts contributes to increase the industrial productivity of the process rising the MRR and the quality of the produced parts.

2.4.1 Research opportunities

The lack of comprehensive studies on the industrial application of turn-milling arises several research opportunities covering the following subjects:

• The development or replication of a reliable model for the uncut chip geometry prediction in the orthogonal, coaxial, and tangential.

• The research of the relationship between the cutting conditions, MRR and cutting forces, in order to reach high productivity scenarios.

• The theoretical study of the effect of cutting conditions over the surface integrity, cutting forces, tool life, etc.

Another important aspects that are not considered in this thesis but are highly recommended to develop are:

• Developments on Artificial Intelligence and machine tool adaptative control to operate in the optimal window. Applications of Big Data, analytical modeling, and Data Analytics to improve the productivity of the process.

• The simulation of the process for further understanding the variation of the primary cutting conditions over scientific and industrial variables, such as cutting forces, finishing, and geometrical accuracy.

• The correlation of cutting condition, cutting forces, and effects over the surface finishing and geometrical accuracy.

• The development of digital twin of the process, based on the available CAD/CAM software, implementing accurate analytical models that conduce to the machining strategy analysis.

• The modeling of challenging parameters such as the cutting temperatures, tool wear or surface integrity. This is linked to the previous opportunity increasing the parameters considered within the digital twin.

3 | Cutting force prediction in orthogonal centric turn-milling operations

The orthogonal turn-milling operation in addition to its characteristic rotation of the workpiece has a parameter that relates the orthogonal distance between the workpiece and tool rotational axes. This is the eccentricity already presented in figure 2.1 (d and f). The simplest case of turn-milling is when the eccentricity (e) is zero, intersecting the axes at the center of the workpiece. This condition simplifies the kinematics reducing the amount of parameters to consider and for this reason this is called "orthogonal centric" turn-milling. This chapter studies the kinematics in orthogonal centric turn-milling operations with flat end mills to determine analytically the uncut chip geometry and predict cutting forces.

(a) Flank edge.   *(b) End Edge.*
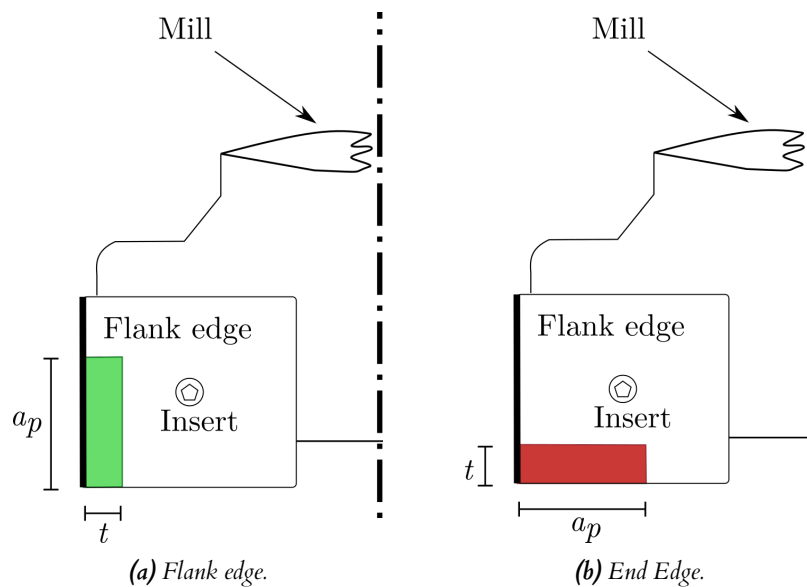
Figure 3.1: *Flat end mill edges.*

A square insert mill can remove the material with different edges as shown in figure 3.1. If the flank edge performs the cut, the depth of cut (a_p) is aligned with the flank edge and the instantaneous chip thickness (t) with the end edge (figure 3.1 A). Nevertheless, if the cut is performed with the end edge of the insert, the situation is the opposite (figure 3.1 B). In turn-milling operations, the cut is performed simultaneously with both edges of the tool due to the coupled tool,

and workpiece rotation Crichigno Filho (2012); Karaguzel et al. (2015b); Zhu et al. (2016b). This simultaneous cutting is taken into account for geometrical modeling and force prediction purposes.

The most common uncut chip geometry representation is shown in figure 3.2 (a), reported by Karaguzel and Zhu Karaguzel et al. (2015b); Zhu et al. (2016b). However, there is a less studied uncut chip geometry as shown in figure 3.2 (b), reported by Crichigno Crichigno Filho (2012). This atypical geometry is associated with the depth of cut a_p and the relationship of tool and workpiece radius. This phenomenon is called "small depth regimen" and is studied in detail in the present chapter. The common representation of the chip is identified as "large depth regimen" and modeled in this chapter.

(a) *Large depth regimen*   **(b)** *Small depth regimen*
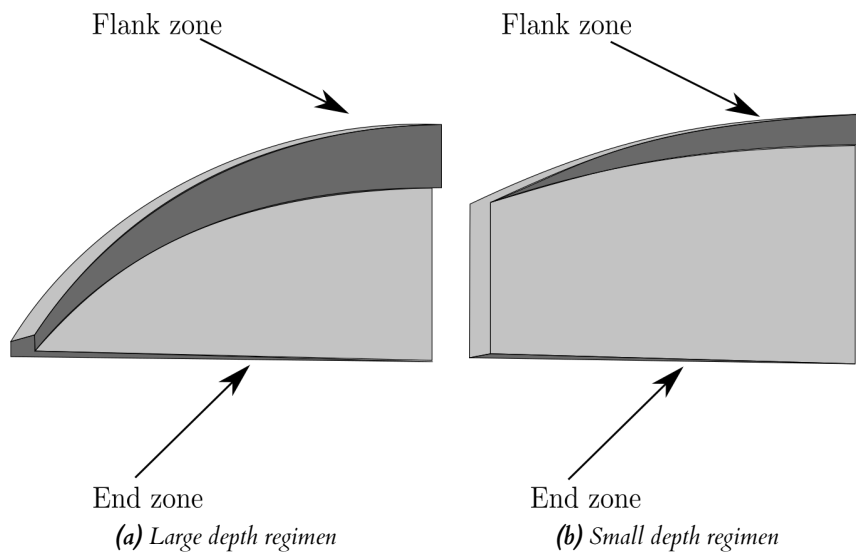
Figure 3.2: *3D representation of the uncut chip geometry.*

This chapter presents a methodology to accurately estimate cutting forces using the uncut chip geometry and the orthogonal to oblique transformation methodology. Geometrical prediction models are developed for the "large and small" depth of cut regimens and validated experimentally in diverse cutting condition scenarios. To this end, the model takes into account chip thickness variations in tool rotation and radial directions. The model detail can be increased if the geometry evolves as the edge rotates during the chip formation process. The geometry can thus be defined by the interaction of the boundary lines of the uncut chip.

The uncut chip is divided into flank and end cutting zones, and the differential cutting force model is applied to each zone to determine the general state of force in the tool. The original contribution of this study is to use the uncut chip boundary lines to describe in detail the instantaneous geometry evolution in the radial, and rotational direction as the edge performs the cut.

The models and results of this research aim to increase the understanding of turn–milling operations and, in particular, the effect of cutting conditions on cutting forces. This knowledge increases the final quality of the piece and the productivity of the machining operation.

A graphical overview of this approach is presented in figure 3.3, which explains how the equations are structured to represent the uncut chip geometry properly. This figure also indicates the procedure to estimate the cutting force starting to form the initial cutting parameters.
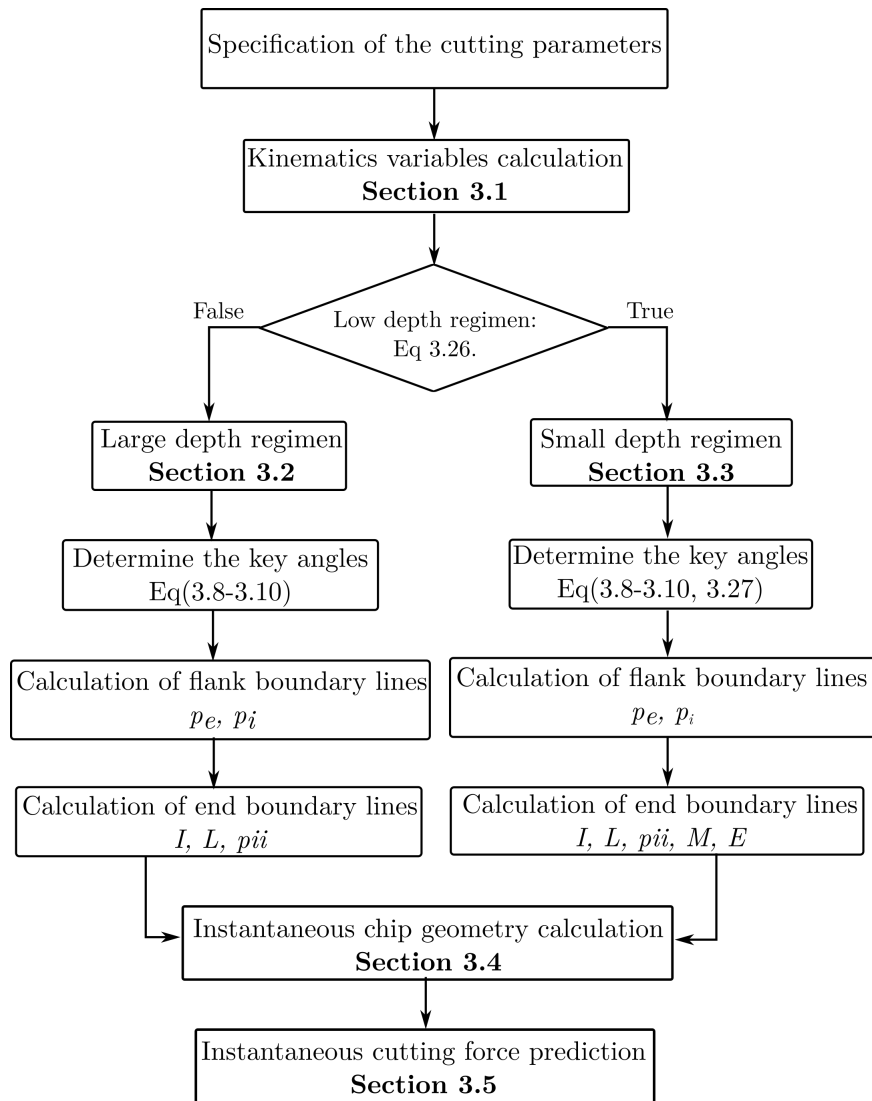
Figure 3.3: *Work flow proposed in this research.*

3.1 Kinematics in turn–milling operations

Kinematics in turn-milling operations is fundamental to determine the uncut chip geometry because it determine the boundaries of the uncut chip geometry. figure 3.4 shows a scheme of the orthogonal centric turn-milling and the movements in this process. As seen in figure 3.4, the tool and workpiece rotational axes are orthogonal to each other. Additionally, they intersect in the center of the workpiece. As a result of these features, the machining operation is called orthogonal centric turn-milling.
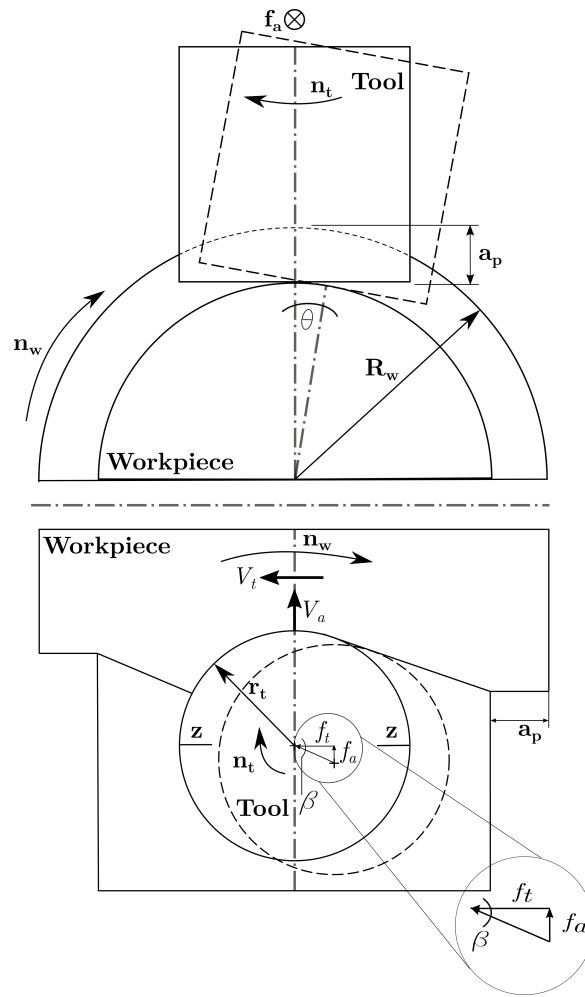
Figure 3.4: *Kinematic in turn–milling operations. (R_w) Workpiece radius, (n_w) Workpiece rotational speed, (r_t) Tool radius, (n_t) Tool rotational speed, (f_a) Axial feed, (a_p) Depth of cut, (z) Number of cutting edges.*

Despite the tool and workpiece are rotating simultaneously, the workpiece rotation is so slow that its effect over the cutting speed is neglectable. Therefore the cutting speed (V_c) is simplified as shown in equation 3.1, depending of the tool radius (r_t) and tool rotational speed (n_t).

$$Vc = \frac{2\pi r_t n_t}{1000} \tag{3.1}$$

The axial feed (f_a) is the distance advanced by the tool in each workpiece rotation in the direction of the workpiece rotation axis. This variable determines the axial speed (V_a) of the tool as shown in equation 3.2. The rotation of the workpiece produces a tangential speed (V_t) in the periphery that is determined by equation 3.3. Besides, the workpiece rotation produces a tangential distance traversed by the tool that is equal to the perimeter of the workpiece, as shown in equation 3.4. The combination of the axial and tangential feeds is equivalent to a

helical trajectory of the tool around the workpiece.

$$V_a = f_a n_w \tag{3.2}$$

$$V_t = 2\pi R_w n_w \tag{3.3}$$

$$f_t = 2\pi R_w \tag{3.4}$$

The axial feed (f_a) and tangential feed (f_t) distances are established per workpiece revolution, but they help to determine the magnitude of the feed per tooth (f_z) based on the displacement triangle shown in figure 3.4. The equation 3.5 explains how to obtain the feed per tooth (f_z). Additionally, the feed angle (β) is determined by equation 3.6. The last kinematic variable is the workpiece rotation angle per edge (θ) that is determined in equation 3.7.

$$f_z = \frac{n_w \sqrt{f_a^2 + f_t^2}}{n_t z} \tag{3.5}$$

$$\beta = \arctan\left(\frac{f_a}{f_t}\right) \tag{3.6}$$

$$\theta = \frac{2\pi n_w}{n_t z} \tag{3.7}$$

The kinematic variables are necessary to define the boundary lines of the chip geometry for both regimens. Therefore, they form the equations of each boundary line that define the chip geometry.

3.2   Analytical model of large depth of cut chip geometry

The approach presented in this research is only valid to a flat end mill with a negligible nose radius. The uncut chip geometry model starts by positioning the coordinate origin in the center of the tool. Thus, the uncut chip is the engagement between the workpiece and the tool based on the previous edge position (Dashed lines) and the present position of the tool (Continuous line), see figure 3.5 (a) and (c). These projections allow identification of the boundary lines that forms the geometry as shown in figure 3.5 (d). The suggested methodology of this chapter aims to identify the functions that describe the position in the 3D cylindrical space of each line. Additionally, it is necessary to define the interval

(a) *Engage zone top view.*

(b) *Key angles*

(c) *Engage zone front view*

(d) *3D Representation of the "large depth" chip geometry.*

Figure 3.5: *Zoom of the engagement zone in "large depth" of cut regimen (orthogonal views). (p_e) External profile (Flank zone), (p_i) Interior profile (Flank zone), (p_{ii}) Inferior interior profile (End zone), (I) Finish end zone line (End zone), (L) Oblique feed line (End zone), ($a_p(\phi)$) Variable depth of cut of the flank zone, ($a_f(\phi)$) End zone thickness plane. Relevant angles in the "large depth" chip geometry. (ϕ_{fst}) Flank zone start angle, (ϕ_{est}) End zone start angle, (ϕ_i) I line exit angle, (ϕ_{eex}) End zone exit angle.*

of angles where the found equations are valid, known as the function domain, see figure 3.5 (b) .

The complex chip geometry is divided into two zones related to the edge that generates them. In the one hand, there is the flank zone that consists of (p_e) and (p_i) lines represented in green in figures 3.5 (a), (b), and (c). On the other hand, the end zone consists of the (I), (L) and (p_{ii}) lines represented in red in figures 3.5 (a), (b), and (c). The polar position of the lines (ϕ,r) can be derived from figure 3.5 (a). The height of the lines is only obtainable from figure 3.5 (c). The flank zone lies on the ($a_p(\phi)$) surface i.e., the workpiece curvature. Furthermore, the end zone is located on the end thickness plane ($a_f(\phi)$) that is generated from the end edge and the workpiece rotation.

The interrelationship between the lines determines the proper valid interval of angles for each line. The lines intersect in some key angles where they start or finish. Thus, the domain (or valid angle interval) of the boundary lines can be obtained from figure 3.5 (b). For instance, the (p_e) line starts at (ϕ_{fex}) and finishes at (ϕ_{fst}) hence the domain of (p_e) is the interval of angles between (ϕ_{fex}) and (ϕ_{fst}), see figure 3.5. It is important to remark that the measure of the angles is opposite to the turning direction of the tool; for this reason, the exit angles are lower than the start angles; this is a consequence of the definition of the terms "start" and "exit". They are associated with the cutting process, not with the

reference framework to determine the boundary line functions.

The calculation of (ϕ_{fex}), (ϕ_{eex}) and (ϕ_{fst}) is done by analytical means as shown in equations 3.8, 3.9 and 3.10 respectively. The rest of the angles (ϕ_i and ϕ_{est}) can be calculated by numerical equalization. In the case of (ϕ_i) the radius of lines (I) and (p_i) are calculated simultaneously increasing (ϕ_i) until both radius are equal. The same numerical method is applied to find (ϕ_{est}) but calculating the radius of lines (L) and (p_i).

$$\phi_{fex} = \arccos\left(\frac{f_z}{2r_t}\right) - \beta \tag{3.8}$$

$$\phi_{eex} = \arctan\left(\frac{r_t - f_a + \left(\sqrt{r_t^2 - (r_t - fa)^2} + \left((R_w - a_p)\sin\left(\frac{\theta}{2}\right)\right)\tan(\beta)\right)}{(R_w - a_p)\sin\left(\frac{\theta}{2}\right)}\right) \tag{3.9}$$

$$\phi_{fst} = \pi - \arcsin\left(\frac{r_t - f_a}{rt}\right) \tag{3.10}$$

The equations of the boundary lines and their domains are presented below. The (p_e) line is defined by equation 3.11 and its domain is shown in equation 3.12. The (z) coordinate height is presented in equation 3.13. It is important to note that the height function is represented on the plane (r, z). Hence, the dependent variable, in this case, is the height of the line (p_e) correspond to the (z) axis (a_{pe}), and the independent variable is the projected length of radius on the (r, z) plane, see figure 3.5 (c).

$$p_e(\phi) = r_t \tag{3.11}$$

$$\phi_{fex} \leq \phi \leq \phi_{fst} \tag{3.12}$$

$$a_{p_e}(p_e) = \sqrt{R_w^2 - (p_e \cos(\phi))^2} - (R_w + a_p) \tag{3.13}$$

Next, the (p_i) line is a piecewise function that is composed by a circular (∗) and a linear segment (∗∗) shown in equation 3.14, see figure 3.5. The respective domain of every piece is represented in equations 3.15 and 3.16 respectively. The height of this line has the same function as the (p_e) line. However, the projection on the plane (r, z) must be the (p_i) line as shown in equation 3.17.

$$p_i(\phi) = \begin{cases} f_z \cos(\phi - \beta) + \sqrt{r_t^2 - (f_z(\sin(\phi - \beta)))^2} & * \\ \dfrac{r_t(\sin(\phi_{fst}) - \cos(\phi_{fst})\tan(\beta))}{\sin(\phi) - \cos(\phi)\tan(\beta)} & ** \end{cases} \tag{3.14}$$

$$\text{circular domain} \quad * \rightarrow \phi_{fex} \leq \phi \leq \phi_{est} \tag{3.15}$$

$$\text{linear domain} \quad ** \rightarrow \phi_{est} \leq \phi \leq \phi_{fst} \tag{3.16}$$

$$a_{p_i}(p_i) = \sqrt{R_w^2 - (p_i \cos(\phi))^2} - (R_w + a_p) \tag{3.17}$$

The end cutting zone description starts with the I line, parallel to the axial feed (f_a), determined by equation 3.18. This line is valid within the domain presented in equation 3.19. Its height is zero and constant along with the domain. This line represents the exit zone of the end edge when the cut is being performed.

$$I(\phi) = \frac{R_w \sin(\frac{\theta}{2})}{\cos(\phi)} \tag{3.18}$$

$$\phi_{eex} \leq \phi \leq \phi_i \tag{3.19}$$

The (L) line is the projection of the linear zone of the (p_i) line. Equation 3.20 presents the expression for this line with a domain shown in equation 3.21. Also, its height is represented on the end zone thickness plane as seen in equation 3.22, see figure 3.5.

$$L(\phi) = \frac{r_t(\sin(\phi_{fst}) - \cos(\phi_{fst})\tan(\beta))}{\sin(\phi) - \cos(\phi)\tan(\beta)} \tag{3.20}$$

$$\phi_{eex} \leq \phi \leq \phi_{est} \tag{3.21}$$

$$a_{f_L}(L) = -\tan(\theta)(L\cos(\phi)) + (L(\phi_{eex})\cos(\phi_{eex})\tan(\theta)) \tag{3.22}$$

The last line to complete the end cutting zone is (p_{ii}), which is a projection of (p_i) on end cutting plane. Therefore, the function of this line has the same form as the circular part of p_i shown in equation 3.23; however, it works in a different domain as presented in equation 3.24. The height of this line is represented on the end thickness plane determined by equation 3.25.

$$p_{ii}(\phi) = f_z \cos(\phi - \beta) + \sqrt{r_t^2 - (f_z(\sin(\phi - \beta)))^2} \tag{3.23}$$

$$\phi_i \leq \phi \leq \phi_{est} \tag{3.24}$$

$$a_{f_{pii}}(p_{ii}) = -\tan(\theta)(p_{ii}\cos(\phi)) + (p_{ii}(\phi_i)\cos(\phi_i)\tan(\theta)) \tag{3.25}$$

3.3 Analytical model of small depth of cut chip geometry

As can be seen in the previous section, the uncut chip geometry is complex. It depends on the cutting and kinematic parameters. The model presented can predict the resultant geometry based on the cutting conditions proposed. Nevertheless, it does not work correctly when the depth of cut is such that the chip is in the "small depth" of cut regimen. This geometric characteristic is related to the cutting parameters shown in equation 3.26. Every time the inequality is fulfilled, the uncut chip is in "small depth" cutting regimen.

$$-\sqrt{R_w^2 - (R_w - a_p)^2} \geq -r_t \cos(\phi_{fst}) \tag{3.26}$$

The modeling methodology for this regimen is the same as the one described for the "large depth" regimen, and its main goal is to describe every single boundary line in detail. Figure 3.6 and shows the lines from the uncut chip geometry in the orthogonal views; the green lines represent the flank zone while the red lines represent the end cutting zone. The orthogonal views present new lines that correspond to the end cutting zone. The flank cutting zone consists of the lines (p_e) and (p_i) presented in the top view of figure 3.6 (a). These lines are located on the surface $(a_p(\phi))$ which defines their height, see figure 3.6 (c). Furthermore, the end cutting zone consist of the $(I),(L),(p_{ii}),(M)$ and (E) lines, see figure 3.6 (b) and (c). Their height are represented in the surface $(a_f(\phi))$, see figure 3.6 (c). Additionally, figure 3.6 (a) presents a 3D view of the uncut chip geometry where the lines in the space can be identified.

Figure 3.6 (d) shows the key angles for the "small depth" regimen. As can be seen, the amount of key angles has increased. The methods for obtaining the angles (ϕ_{fex}), (ϕ_{eex}) and (ϕ_i) are the same as the that presented in the "large depth" approach. Therefore, (ϕ_{fex}) is found through equation 3.8, ϕ_{eex} throughout equation 3.9 and (ϕ_i) by numerical equalization of the radius of (I) and (p_i) lines, see figure 3.6. Nonetheless, the calculation of some angles changes, because this geometry does not present the same points as reference than the "large depth" regimen as in the case of (ϕ_{fst}). The angle (ϕ_{fst}) is found when the height of the line (p_e) is zero. Hence, it can be determined using equation 3.27. The rest of the angles $(\phi_{pist}, \phi_{piex}, \& \phi_{est})$ can be calculated by numerical equalization taking into account the interrelationship of the boundary height of the lines. In the case of (ϕ_{pist}), the height of (p_i) and (p_{ii}) is calculated augmenting (ϕ) until both heights are equal. To find (ϕ_{piex}) the ascendant and descendant domains of (a_{fL}) must be equal. The angle (ϕ_{est}) is found by equaling the radius of (E) and (L) lines.

$$\phi_{fst} = \pi - \arccos\left(\frac{\sqrt{R_w^2 - (R_w - a_p)^2}}{r_t}\right) \tag{3.27}$$

Once the angles are determined, the boundary lines can be defined. The (p_e) line remains as presented in equation 3.11 with the same domain and height

(a) 3D Representation of the "small depth" chip geometry

(b) Engage zone top view

(c) Engage zone front view
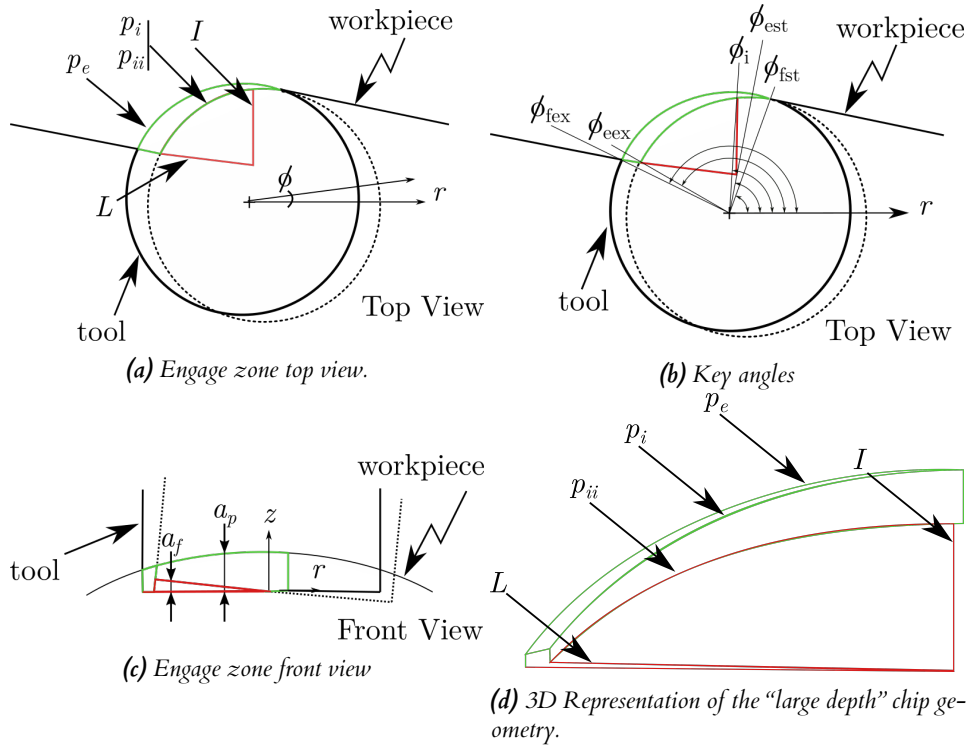

(d) Key Angles
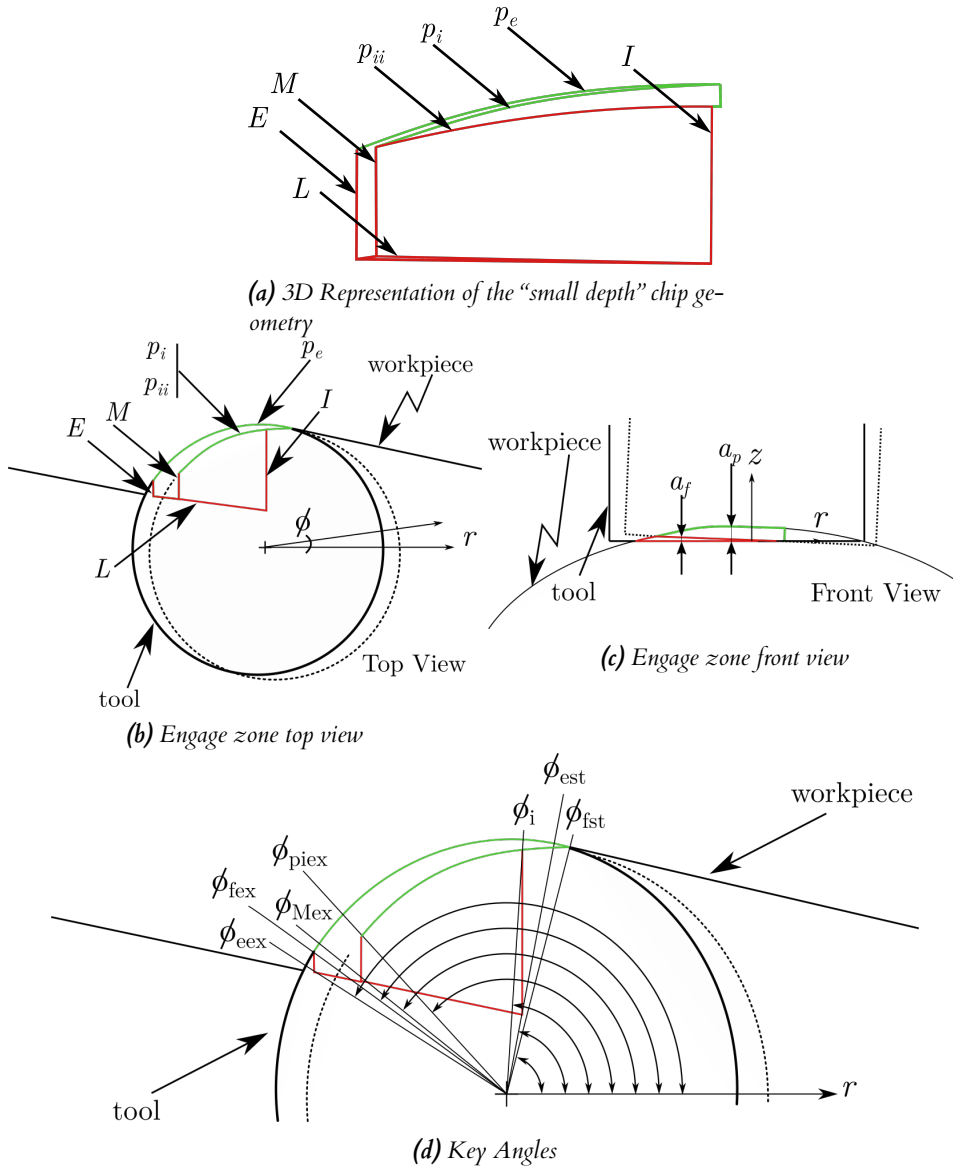
Figure 3.6: *Zoom of the engagement zone in "small depth" of cut regimen (orthogonal views). (p_e) External profile (Flank zone), (p_i) Interior profile (Flank zone), (p_{ii}) Inferior interior profile (End zone), (I) Finish end zone line (End zone), (L) Oblique feed line (End zone), (M) Mid vertical line (End zone), (E) External vertical line (End zone), ($a_p(\phi)$) Variable depth of cut of the flank zone, ($a_f(\phi)$) End zone thickness surface. Relevant angles in the "small depth" chip geometry. (ϕ_{fst}) Flank zone start angle, (ϕ_{est}) End zone start angle, (ϕ_i) I line exit angle, (ϕ_{pist}) Internal profile starting angle, (ϕ_{Mst}) M line start angle, (ϕ_{fex}) Flank zone exit angle, (ϕ_{eex}) End zone exit angle.*

expressions shown in equations 3.12 and 3.13. However, the (p_i) line is no longer a piecewise function and equation 3.28 shows the updated expression. Additionally, the (p_i) domain has changed as presented in equation 3.29. Nevertheless, the height function remains the same as the one presented in equation 3.17.

$$p_i = f_z \cos(\phi - \beta) + \sqrt{r_t^2 - (f_z(\sin(\phi - \beta)))^2} \qquad (3.28)$$

$$\phi_{fex} \leq \phi \leq \phi_{pist} \tag{3.29}$$

The (I) line, located in the end cutting zone, does not present changes with the previous model. Therefore it keeps the same function, domain and height presented in equations 3.18 and 3.19. The (L) line has the same slope in the polar plane (ϕ,r). However, the reference point used to build equation 3.20 does not exist in this geometry and is necessary to set another reference point. This new reference corresponds to the initial radius of the (L) line at the angle (ϕ_{est}) called (r_l) ($r_l = L(\phi_{est})$), see equation 3.30. The expression is extensive so auxiliary variables (v_1) and (v_2) are proposed to facilitate the presentation.

$$r_l = \sqrt{r_t - f_a - \left(\sqrt{r_t^2 - (r_t - f_a)^2} + R_w - a_p \sin\left(\frac{\theta}{2}\right)\tan(\beta)\right)^2 + \left((R_w - a_p)\sin\left(\frac{\theta}{2}\right)\right)^2} \tag{3.30}$$

The (L) line is described in equation 3.31 and its domain is the same presented in equation 3.21. The height of this line is a piecewise function shown in equation 3.32; because the line is located on the end plane before (ϕ_{piex}) and after that angle on the workpiece curvature, see figure3.6 (c). The expressions which describe the composite domain are equations 3.33 and 3.34.

$$L(\phi) = \frac{r_l \sin(\phi_{eex}) - (\cos(\phi_{eex})\tan(\beta)}{\sin(\phi) - (\cos(\phi)\tan(\beta))} \tag{3.31}$$

$$a_{f_L}(\phi) = \begin{cases} -\tan(\theta)(L\cos(\phi)) + (L(\phi_{eex})\cos(\phi_{eex})\tan(\theta)) & * \\ \\ \sqrt{R_w^2 - (L\cos(\phi)^2)} - (R_w + a_p) & ** \end{cases} \tag{3.32}$$

$$\text{ascendant domain} \quad * \rightarrow \phi_{eex} \leq \phi \leq \phi_{piex} \tag{3.33}$$

$$\text{descendant domain} \quad ** \rightarrow \phi_{piex} \leq \phi \leq \phi_{est} \tag{3.34}$$

The (M) line is determined by equation 3.35 and its domain is presented in equation 3.36. The height of this line is constant along with the domain and corresponds to equation 3.37.

$$M(\phi) = \frac{p_i(\phi_{pist})\cos(\phi_{pist})}{\cos(\phi)} \tag{3.35}$$

$$\phi_{pist} \leq \phi \leq \phi_{piex} \tag{3.36}$$

$$a_{fM} = \sqrt{R_w^2 - (p_i(\cos(\phi_{pist})))^2} - (R_w + a_p) \tag{3.37}$$

The (E) line and its function is shown in equation 3.38. Its domain corresponds to equation 3.39 and has a constant height of zero. The last line is (p_{ii}) presented in equation 3.23, its height corresponds to equation 3.25. However, the domain of the line has changed as shown in equation 3.40.

$$E(\phi) = \frac{p_e(\phi_{pist}) \cos(\phi_{fst})}{\cos(\phi)} \tag{3.38}$$

$$\phi_{fst} \leq \phi \leq \phi_{est} \tag{3.39}$$

$$\phi_i \leq \phi \leq \phi_{pist} \tag{3.40}$$

3.4 Geometric validation of the models

The validation process was performed by directly comparing the instantaneous chip cross-sectional area obtained from the models and a CAD representation of the chip. The CAD reproduction was done by projecting the helical path of the tool in SolidWorks 2017, where the geometry is defined by the interference of the tool and the workpiece. Based on the kinematic parameters, the tool displacement in the 3D space was projected within the pass of one cutting edge. Hence, the subtraction of the projected geometry of the tool and the workpiece resulted in the uncut chip geometry. A Python routine was coded to calculate the kinematic variables, the reproduction of the analytical models, and their graphical representation.

3.4.1 "Large depth" model validation

In the first step, a set of cutting conditions must be selected. If this set is in the "large depth" regimen, then the Python routine would plot results like those presented in figure 3.7 A. This representation of the uncut chip geometry was programmed to plot the flank zone in green lines. Consequently, the lines that were plotted in red belong to the end cutting zone. This graphic representation of the analytical approach is distorted due to the scale of the orthogonal axis (X, Y, Z). The default auto-scaling feature of Python helps to focus on the resultant geometry features.

(a) Analytical model results   *(b) CAD results*
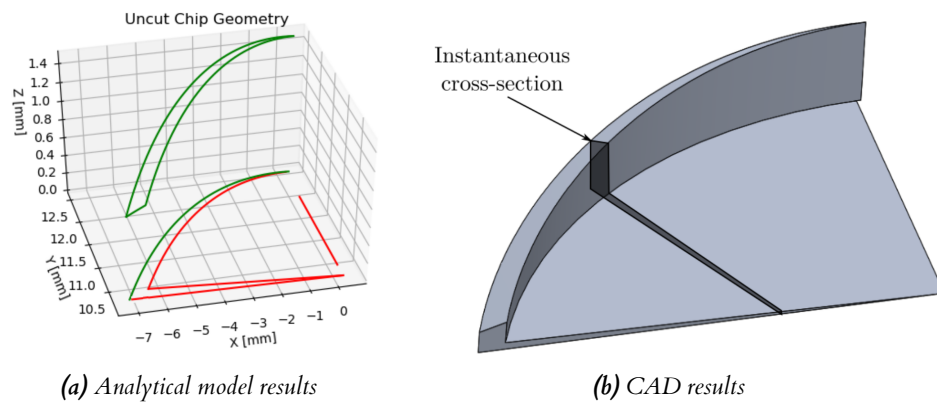
Figure 3.7: *Typical results "large depth" approach R_w= 45mm, n_w= 3rpm, r_t = 12.5mm, n_t = 1250rpm, f_a= 2.25mm/wpr, a_p= 2mm, z= 1.*

The representation of the uncut chip geometry by CAD requires calculating the kinematic and cutting parameters. Figure 3.7 (b) shows the results obtained by this numerical approach. Notably, both figures 3.7 (a and b) represent the uncut chip in the same cutting conditions. However, it is not easy to qualitatively correlate both approaches.
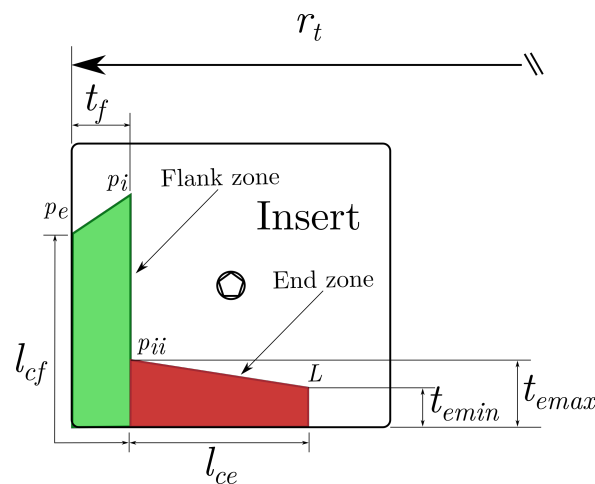
Figure 3.8: *Diagram of the instantaneous chip geometry.*

A quantitative test of the correlation should be definite evidence of the accuracy of the approaches. Both models are detailed enough to obtain the instantaneous cross–section area of the chip. On the one hand, the CAD approach can be sliced, and using the section properties tool of SolidWorks 2017; the area can be found. On the other hand, the analytical model presents the instantaneous points of the chip during the edge rotation. figure 3.8 shows a the typical instantaneous cross–section area. Both the flank and end areas are irregular trapeziums, so by adding their respective areas, it is possible to find the total cross–section area of the analytical approach. Arbitrary cutting conditions were selected in order to evaluate the model behavior versus the CAD representation. Some parameters were varied, but the others were kept fixed because of the large amount of them, as shown in table 3.1.

Table 3.1: Parameters in the "large depth" validation test.

R_w [mm]	r_t [mm]	z [–]	a_p [mm]	n_w [rpm]
45	10	8	2	16.67
	Tag	n_t [rpm]	fa $\left[\frac{\text{mm}}{\text{WpRev}}\right]$	
	T1	1667	2.12	
	T2	3260	4.24	
	T3	1667	4.24	
	T4	3260	8.48	
	T5	2470	4.77	

The validation scenario proposed presents considerable changes to the uncut chip geometry. Five machining scenarios were proposed, and they were tagged as shown in table 3.1. The results of the validation test are presented in figure 3.9. The test showed robust correlation models, with errors of less than 2%. Those errors could be attributed to modeling simplifications. The behavior of both approaches is so close that the numerical points appear to be directly located on top of the continuous lines that represent the analytical prediction.
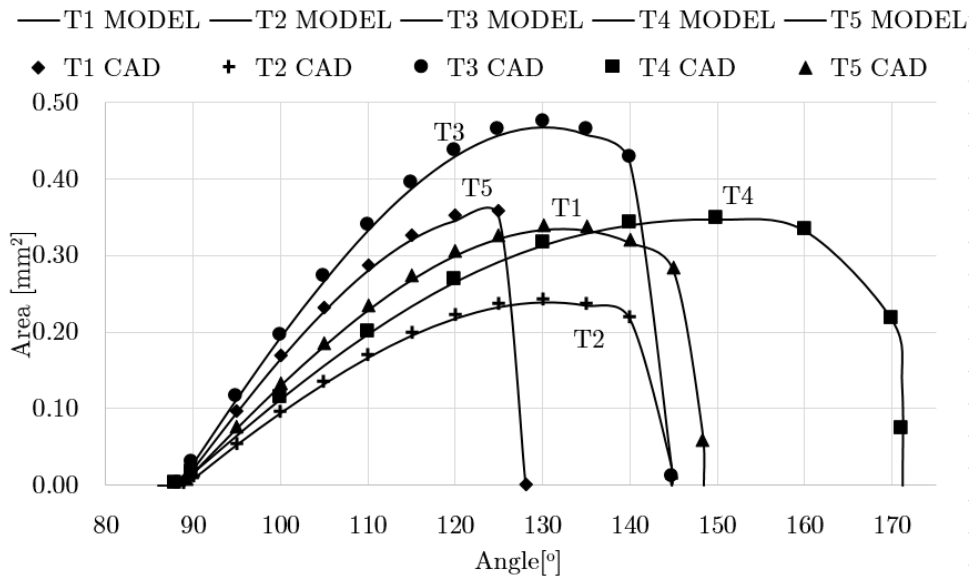
Figure 3.9: Validation of the cutting model in "large depth" regimen.

3.4.2 "Small depth" model validation

Figure 3.10 A shows the results of implementing the model developed for the "small depth" regimen. The green lines of the plot correspond to the flank zone and the red to the end zone, respectively. This plot also has the orthogonal axis (X, Y, Z) with the default scale, so the chip is distorted, but the image is focused on the chip. Moreover, the CAD representation of the chip was then performed. Figure 3.10 B shows the resulting geometry.

(a) Analytical model results   *(b) CAD results*
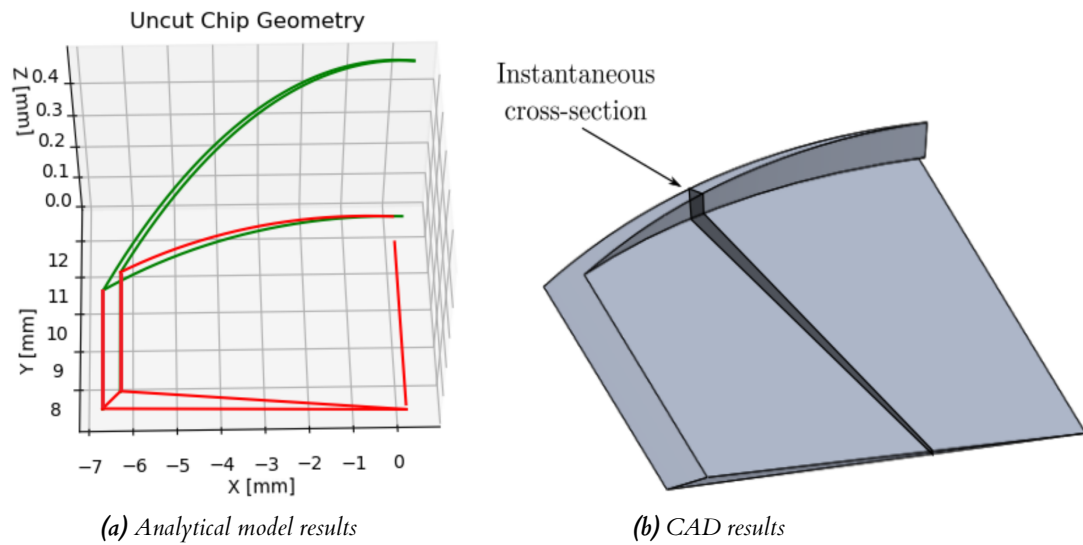
Figure 3.10: *Typical results "small depth" approach R_w=45mm, n_w=120rpm, r_t=12.5mm, n_t=25500rpm, f_a=5mm/wpr, a_p=0.5mm, z=3.*

Figure 3.10 A shows the results of implementing the model developed for the "small depth" regimen. The green lines of the plot correspond to the flank zone and the red to the end zone, respectively. This plot also has the orthogonal axis (X, Y, Z) with the default scale, so the chip is distorted, but the image is focused on the chip. Moreover, the CAD representation of the chip was then performed. Figure 3.10 B shows the resulting geometry. Notably, figures 3.10 A and B are representations of the same cutting conditions, but it was not possible to carry out a qualitative comparison between the resultant geometries.

The analytical model was validated by a quantitative test of the instantaneous cross–section area was performed in the CAD. Calculations of the cross–section area were made as explained in subsection 5.1. It worth highlighting that the flank zone disappears after (ϕ_{fex}), and the remaining geometry belongs to the end zone. Figure 3.11 shows the expected instantaneous geometry after the pass of (ϕ_{fex}). The resultant geometry is not regular, but it can be split into simpler geometries to add their respective areas. Therefore, another cutting scenario was proposed differently from that used in the "large depth" approach. Table 3.2 presents the cutting conditions. Additionally, in this comparison, the workpiece rotational speed (n_w) is also considered a variable.

Figure 3.12 shows the validation test results for the "small depth" regimen. The general behavior of the approaches is quite accurate, presenting errors lower than 1%. The behavior of both approaches is so close that the numerical points appear to be directly located on top of the continuous lines that represent the analytical prediction. Additionally, figure 3.12 suggests that the end zone volume is larger than the flank zone. This condition indicates that the cutting parameters that increase the end zone would result in a strong cutting force and a greater wear increment.
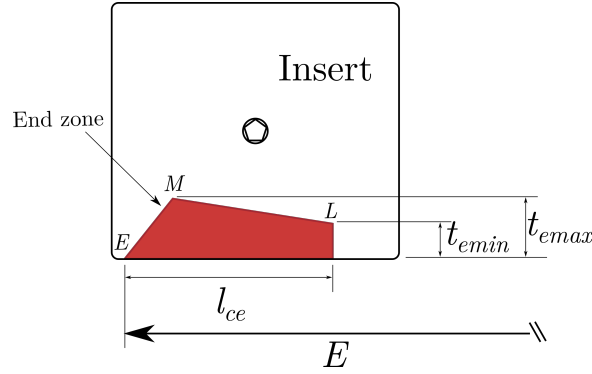
Figure 3.11: *Diagram of the instantaneous chip geometry after* (ϕ_{piex}).

Table 3.2: *Parameters in the "small depth" validation test.*

R_w [mm]	r_t [mm]	z [–]	a_p [mm]	n_w [rpm]
44.5	12.5	3	0.5	16.67

Tag	n_w [rpm]	n_t [rpm]	fa $\left[\frac{\text{mm}}{\text{WpRev}}\right]$
T1	30	12800	2.5
T2	30	12800	5
T3	60	12800	2.5
T4	60	12800	5
T5	30	25500	2.5
T6	30	25500	5

3.5 Cutting force prediction

Turn-milling operations are intermittent cutting processes that present periodical cutting forces. The frequency of the force is a consequence of the rotational tool speed n_t and the number of edges z. The magnitude of the force is a consequence of several aspects but mainly the uncut chip geometry and the workpiece material. In the present chapter, the mechanistic methodology was used to predict this magnitude (Karaguzel et al., 2015b; Altintas, 2012; Budak et al., 1996). This methodology requires the uncut chip geometry as input and calculates the K coefficients. The geometrical variations of the uncut chip in the tool radial direction are considered by a differential approach as suggested in equation 3.41, where:

$$
\begin{aligned}
\mathrm{d}F_r &= (K_{rc}t(\phi, r) + K_{re}) \ \mathrm{d}r \\
\mathrm{d}F_t &= (K_{tc}t(\phi, r) + K_{te}) \ \mathrm{d}r \\
\mathrm{d}F_p &= (K_{pc}t(\phi, r) + K_{pe}) \ \mathrm{d}r
\end{aligned}
\tag{3.41}
$$

The differential approach presented must be performed separately for the flank and end cutting zones. This condition stems from the orthogonal alignment of the cutting edges. As presented in figure 3.1 and discussed throughout the
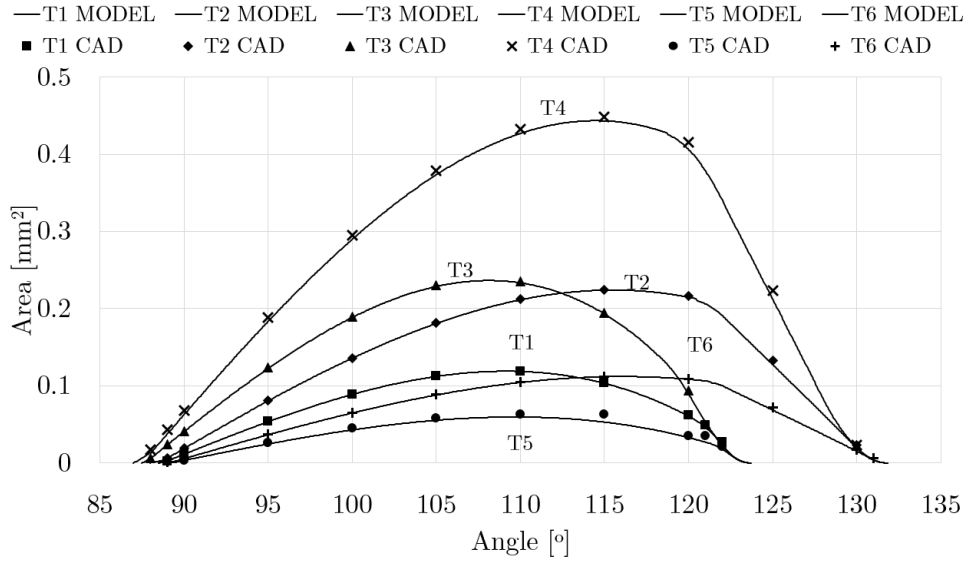
Figure 3.12: Validation of the cutting model in "small depth" regimen.

present approach, the cut is performed with different edges which are orthogonally aligned. Therefore the overall state of forces in the tool is obtained by equation 3.42. Where the general state of force of the tool is composed by three components the radial (F_r), tangential (F_t), and axial (F_a) forces. Each component of force is the combination of the flank (F_{*flank}) and end edge (F_{*end}) in the tangential (F_{t*}), radial (F_{r*}), and penetration (F_{p*}) directions.

$$F_r = \int_{r_{j,1}}^{r_{j,2}} dFr_{flank} \ dr + \int_{r_{j,1}}^{r_{j,2}} dFp_{end} \ dr$$

$$F_t = \int_{r_{j,1}}^{r_{j,2}} dFt_{flank} \ dr + \int_{r_{j,1}}^{r_{j,2}} dFt_{end} \ dr \qquad (3.42)$$

$$F_a = \int_{r_{j,1}}^{r_{j,2}} dFp_{flank} \ dr + \int_{r_{j,1}}^{r_{j,2}} dFr_{end} \ dr$$

3.5.1 Cutting coefficients determination – Orthogonal to oblique transformation

The orthogonal to oblique transformation methodology esteem the cutting forces in an oblique case based on orthogonal trials, and based on this is possible to determine the cutting coefficients. Therefore, figure 3.13 a shows the experimental setup scheme of the orthogonal trials.

It is essential to clarify that the power of the orthogonal to oblique transformation approach resides in the characterization trials. The experimental design should be extensive and include as many parameters as possible to generate representative mathematical expressions of the variables studied. For example, it is necessary to consider the cutting speed (Vc), feed per edge (f_z), rake angle (γ), clearance angle (α), edge radius, helix angle (λ), Etc. The values selected for the experimental setup should sweep the market offer to be representative.

(a) Scheme of orthogonal cutting setup.

(b) ARNO square shoulder cutter FDG190025R0310 (ArnoWerkzeuge, 2015).

(c) ARNO square shoulder insert SDHT100408FNPMAAN1015 (ArnoWerkzeuge, 2015).
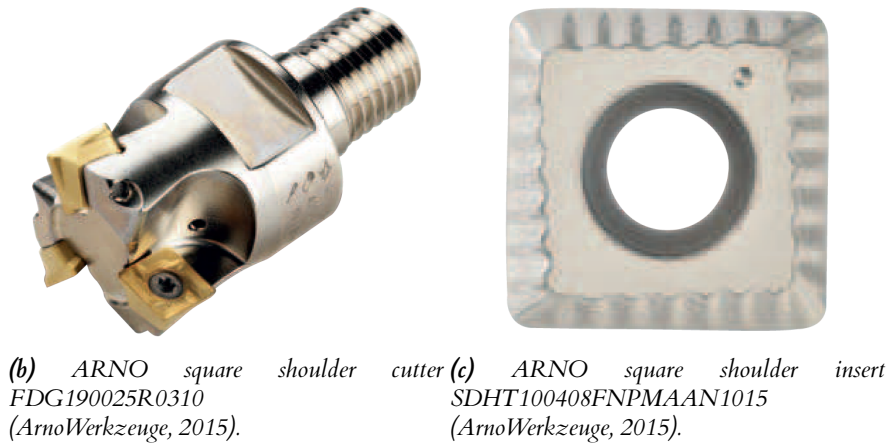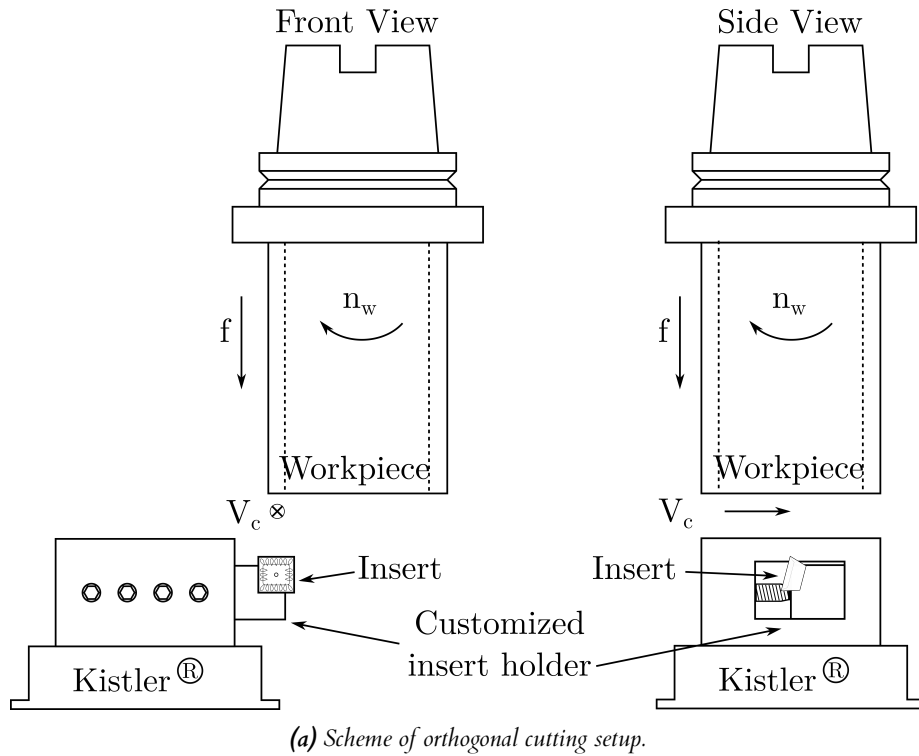
Figure 3.13: *Orthogonal cutting trials scheme and considered for the experiment planning.*

Notwithstanding the mentioned considerations, it was impossible to carry out an extensive experimental plan to generate a representative database of the work material. However, the database is representative enough for the flat end mill chapters presented in the following two chapters.

The set material–edge characterized by this approach is the aluminum 6063 T5 (see table 3.3) with the insert ARNO SDHT100408FNPMAAN1015 in the ARNO indexable mill FDG190025R0310; see figure 3.13 (b) and (c). The selection of the material is based on the low mechanical properties of the selected aluminum. Therefore, using a softer material maintains the cutting forces lower and allows testing a more comprehensive range of cutting conditions.

(a) Insert flank rotation angle 8º.

(b) Insert radial rotation angle −8º.
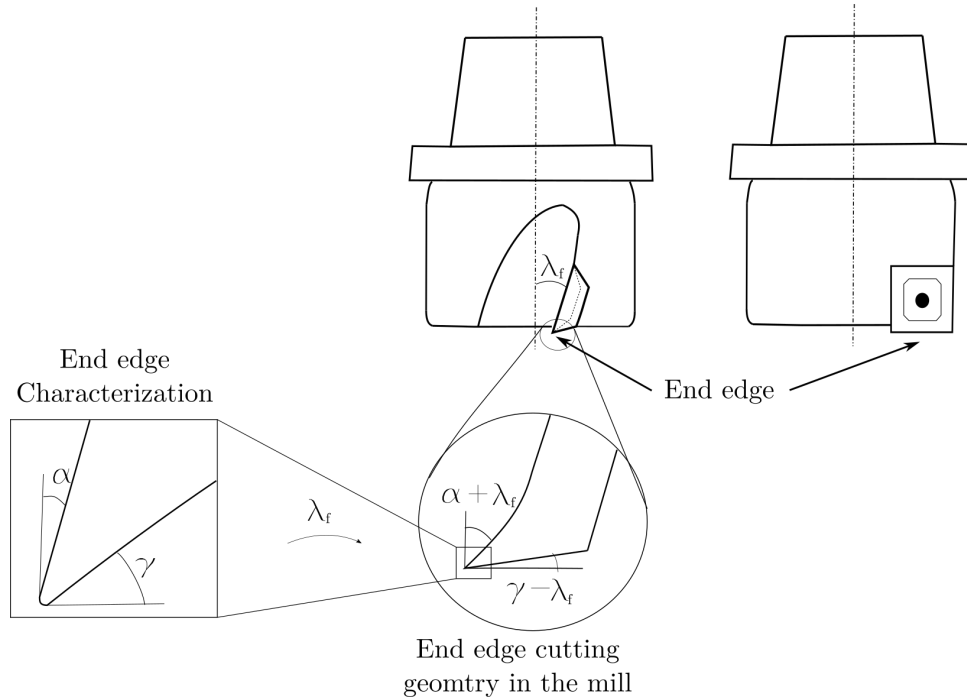
(c) Effect of the flank angle over the end edge geometry.
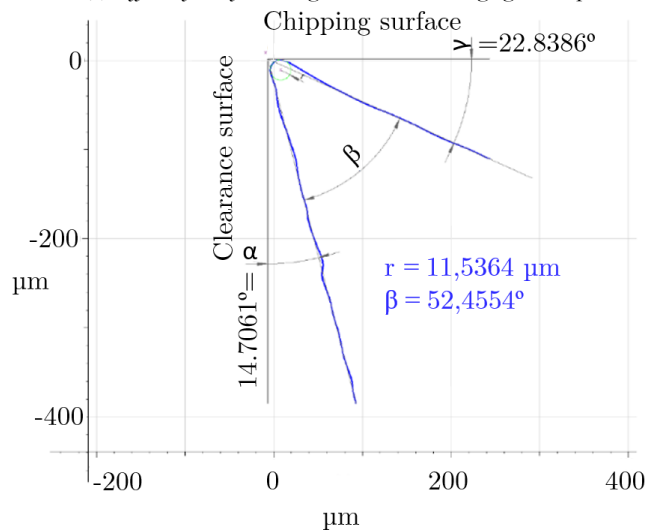
(d) Microscopic edge measurement in Alicona profilometer.

Figure 3.14: *Characterization of the insert mill*

Table 3.3: *Aluminum 6063 T5 alloy elements (Matweb, 2021).*

Al [%]	Cr [%]	Cu [%]	Fe [%]	Mg [%]	Mn [%]	Si [%]	Ti [%]	Zn [%]	Other [%]
<= 97.5	<= 0.10	<= 0.10	<= 0.35	0.45 – 0.90	<= 0.10	0.20 – 0.60	<= 0.10	<= 0.10	<= 0.10

The insert mill is designed to orient it in a specific way, rotating the insert in the flank direction and the radial direction, see figure 3.14 (a) and (b). These angles in a solid mill coincide with the radial and flank rake angle; however, an insert mill does not meet this requirement. This case is due to the cutting edge are designed explicitly with a rake and clearance angles. These characteristic angles are not intended to operate in the cutting process because of the radial and flank rotation angles prepared on the mill. Consider for instance, the end edge in an insert mill; see figure 3.14 (c). The flank rotation angle (λ_f) rotates the end edge changing the rake and clearance radial angles as shows in figure 3.14 (c). The radial rotation angle (λ_e) modifies the flank edge correspondingly. The insert is characterized by a microscopic profilometer as shown in figure 3.14 (d).
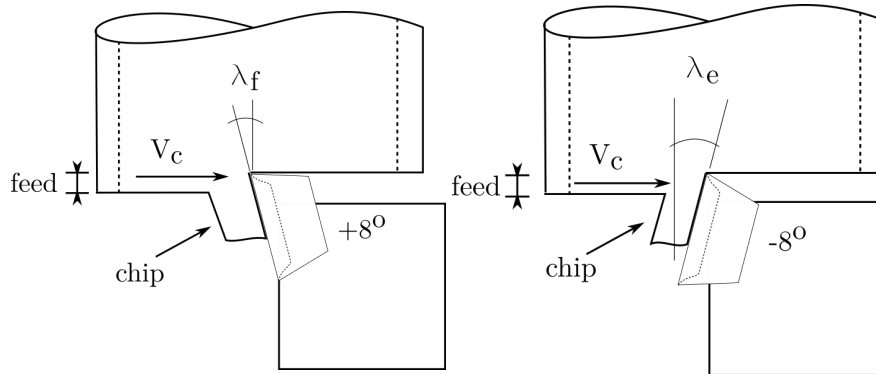
(a) *Scheme of the orthogonal cutting trial 8º.*

(b) *Scheme of the orthogonal cutting trial −8º.*
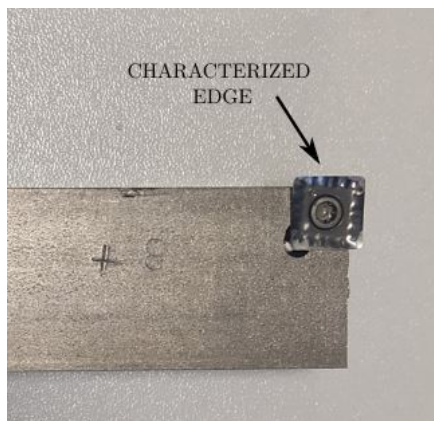
(c) *Customized insert holder (λ_f) 8º.*
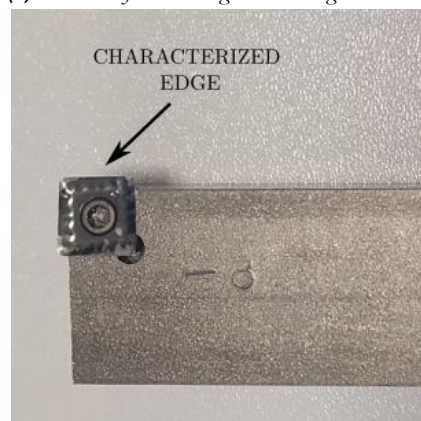
(d) *Customized insert holder (λ_e) −8º.*

Figure 3.15: *Insert fixture for orthogonal cutting trials.*

A customized insert holder was designed to perform the orthogonal cutting trials with the same design angle of the mill presented in figure 3.15. This step

is fundamental because it is impossible to perform the orthogonal trials with the milling insert installed in the mill. Additionally, the flank and end rake and clearance angles strongly impact the magnitude and direction of cutting forces. Figure 3.15 (a) and (b) represent the cutting process scheme in the orthogonal case with the respective rotation angles. The rotation angle measured and presented in figure 3.14 (a) and (b) are included in the customized insert holder. Figure 3.15 (c) and (d) shows photographs of the resulting assembly.

Table 3.4: *Cutting conditions for edge characterization.*

Parameter	Value	Units
Cutting Speed (V_c)	400 – 800	[m/min]
Depth of cut (a_p)	2	[mm]
Feed (f)	0.05 – 0.1 – 0.2 – 0.3	[mm/rev]
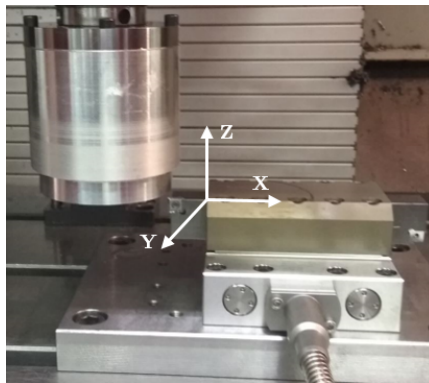
(a) Experimental setup of orthogonal trials.   *(b) Cut chip measurement Vc400fz0.2ap2.*
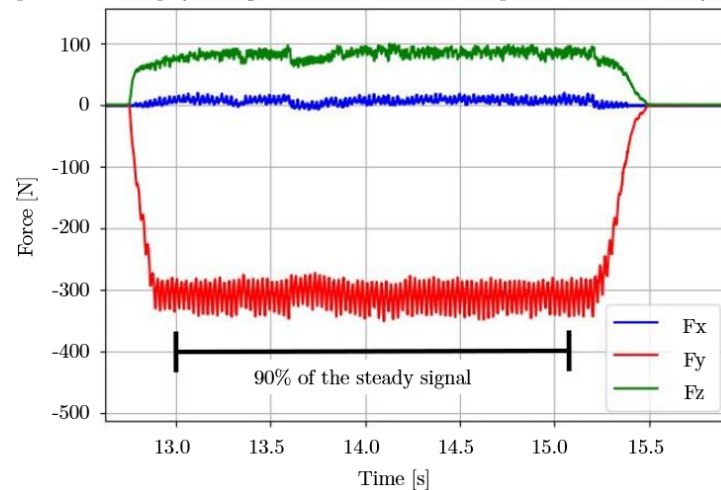
(c) Typical results of the orthogonal cutting trials Vc400fz0.3ap2.

Figure 3.16: *Orthogonal cutting trials setup and typical results.*

Solved the preliminaries of the experimental setup, the trials were performed in the cutting conditions shown in the following experimental plan, see table 3.4. The whole experimental plan was run over the +8° and –8° setup; each cutting condition was repeated three times to ensure statistical representativeness, and the cutting forces were measured during a prolonged period to capture

the signals in stationary conditions, figure 3.16 a shows the final experimental setup. Sub-figure b shows the cut chip thickness measurement; each trial was measured in three different points and averaged with the other repetitions. In the c figure are shown the typical results obtained in the cutting trials. The data considered for the cutting characterization was 90 % of the steady signal. The mean results of the whole experimental trials are presented in table 3.5; these values are the starting point of the cutting coefficient determination. To ensure statistical representativeness every single cutting condition was repeated 3 times and the mean value is presented and used as nominal value.

Table 3.5: Experimental results of the orthogonal cutting trials.

V_c $\left[\frac{m}{min}\right]$	Rake γ [°]	Clear α [°]	a_p [mm]	$f\left[\frac{mm}{rev}\right]$	Mean Fc [N]	Mean Ff [N]	Mean h [mm]
			2	0.05	85	48	0.23
400	32	6	2	0.1	137	60	0.34
			2	0.2	222	70	0.60
			2	0.3	302	77	0.81
			2	0.05	83	46	0.22
800	32	6	2	0.1	127	48	0.33
			2	0.2	208	51	0.54
			2	0.3	282	50	0.78
			2	0.05	108	84	0.32
400	16	22	2	0.1	173	115	0.48
			2	0.2	287	157	0.73
			2	0.3	396	193	0.95
			2	0.05	100	75	0.29
800	16	22	2	0.1	155	90	0.40
			2	0.2	259	118	0.64
			2	0.3	360	144	0.92

The experimental results presented in table 3.5 show the cutting speed of the trials in the first column. The -8° rotational angle aligned the rake and clearance angles of the flank edge into 32° and 6° respectively. Otherwise, the +8° rotation angle aligned the end edge rake and clearance angle to 16° and 22°, see figure 3.14 (c). The next column shows the feed tested followed by the mean cutting force Fc which in figure 3.15 coincides with the *Y* direction. The mean of the feed force Ff is presented; this force coincides in figure 3.15. The last column refers to the mean value of the cut chip thickness measured with a micrometer screw gauge.

The behavior of the cutting forces is illustrated in figure 3.17. The force data is plotted as a function of the feed. The points fit tightly in a linear function, and a linear regression determines the equation. The independent term of each equation is the edge force in both the cut and feed forces; see table 3.6 F_{ce}, F_{fe}, respectively. Dividing those forces into the depth of cut (a_p = 2 mm), the edge coefficient can be determined, see table 3.6 K_{ce} cutting edge and K_{fe} feed edge coefficients. Considering the similarity in the 400 and 800 [m/min] values, it then unified the mean value. Table 3.6 presents the values of the forces with

three decimals to easily relate the table values with the independent terms of the linear regressions presented in figure 3.17.

(a) Cutting force in orthogonal trials rake angle $\gamma = 32^o \alpha = 6^o$.

(b) Feed force in orthogonal trials rake angle $\gamma = 32^o \alpha = 6^o$.

(c) Cutting force in orthogonal trials rake angle $\gamma = 16^o \alpha = 22^o$.

(d) Feed force in orthogonal trials rake angle $\gamma = 16^o \alpha = 22^o$.
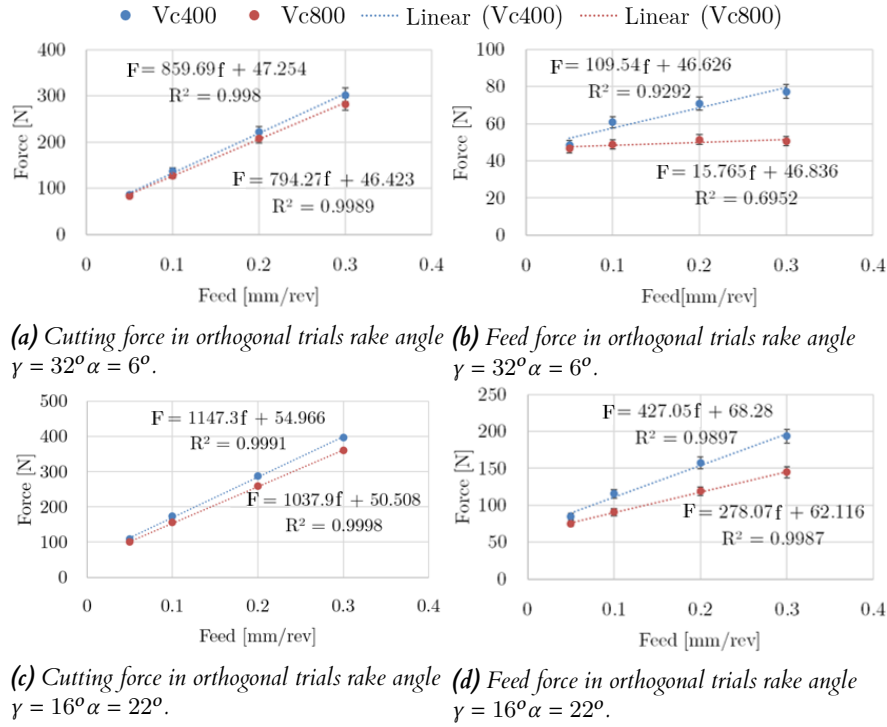
Figure 3.17: *Effect of the feed over the cutting forces.*

Table 3.6: *Friction or edge coefficient determination.*

	V_c $\left[\frac{m}{min}\right]$	F_{ce} [N]	K_{ce} $\left[\frac{N}{mm}\right]$	Mean K_{ce} $\left[\frac{N}{mm}\right]$	F_{fe} [N]	K_{fe} $\left[\frac{N}{mm}\right]$	Mean K_{fe} $\left[\frac{N}{mm}\right]$
$\gamma\ 32^o\ \alpha 6^o$	400	47.254	23.627	23	46.423	23.313	23
	800	46.423	23.211		46.836	23.418	
$\gamma 16^o\ \alpha 22^o$	400	54.966	27.483	26	68.280	34.14	32
	800	50.508	25.254		62.116	31.058	

Determined the edge forces F_{ce} and F_{fe} in table 3.6; the power (F_{pc}) and thrust (F_{qc}) cutting forces were determined by subtracting the measured forces with the edge forces as shown in equation 3.43 and the results are presented in table 3.7.

$$F_{pc} = F_{ci} - F_{ce}$$
$$F_{qc} = F_{fi} - F_{fe}$$

(3.43)

The tangent of the friction angle $(\tan(\beta_i))$ of each trial is determined with the power and thrust forces and the rake angle as shown in equation 3.44. The compression ratio of the chip (RC_i) is the relationship between the uncut chip thickness or the feed (f_i) and the mean cut chip thickness (h_{mi}) presented in the

Table 3.7: *Power and thrust forces calculation.*

V_c $\left[\frac{m}{min}\right]$	Rake γ [°]	Clear α [°]	Feed $\left[\frac{mm}{rev}\right]$	Mean F_c [N]	Mean F_f [N]	F_{pc} [N]	F_{qc} [N]
			0.05	85	48	38	2
800	32	6	0.1	137	60	89	14
			0.2	222	70	175	24
			0.3	302	77	255	31
			0.05	83	46	37	0
800	32	6	0.1	127	48	81	2
			0.2	208	51	162	5
			0.3	282	50	236	4
			0.05	108	84	53	16
400	16	22	0.1	173	115	118	47
			0.2	287	157	232	89
			0.3	396	193	341	125
			0.05	100	75	50	13
800	16	22	0.1	155	90	105	28
			0.2	259	118	208	57
			0.3	360	144	310	82

last column of table 3.5, (see equation 3.45). The tangent of the shear angle ϕ_τ is found from the compression ratio rc and the rake angle (γ) as shown in equation 3.46; and the angle is found by the arctangent of the value shown in equation 3.46. The shear stress (τ_i) in the cutting process is found with the power and thrust forces (F_{pci} and F_{qci}), the shear angle ($\phi_{\tau i}$), the feed of each trial or the uncut chip thickness (f_i) and the depth of cut (a_{pi}), see equation 3.47. The results of these parameter calculation are presented in table 3.8.

$$\tan(\beta_i) = \frac{F_{qci} + F_{pci}\tan(\gamma)}{F_{pci} - F_{qci}\tan(\gamma)} \tag{3.44}$$

$$rc_i = \frac{f_i}{h_{mi}} \tag{3.45}$$

$$\tan(\phi_{\tau i}) = \frac{rc_i\cos(\gamma)}{1 - rc_i\cos(\gamma)} \tag{3.46}$$

$$\tau_i = \frac{(F_{pci}\cos(\phi_{\tau i}) - F_{qci}\sin(\phi_{\tau i}))\sin(\phi_{\tau i})}{f_i a_{pi}} \tag{3.47}$$

The tangent of the friction angle ($\tan\beta$) presented small variations; therefore, those values are consolidated by the average value presented in each studied geometry, see equation 3.48; and the normalized friction angle is the friction

Table 3.8: *Friction Angle, compression rate, Shear angle, Shear stress for the insert geometry and aluminum 6063 T5.*

V_c $\left[\frac{m}{min}\right]$	Geometry	Feed $\left[\frac{mm}{rev}\right]$	$\tan(\beta)$	$rc\left[\frac{mm}{mm}\right]$	$\tan(\phi_\tau)$	ϕ_τ [rad]	Shear stress τ [MPa]
400	$\gamma\,32^o\,\alpha\,6^o$	0.05	1.104	0.217	0.445	0.418	139.835
		0.1	1.377	0.287	0.644	0.572	183.512
		0.2	1.321	0.333	0.800	0.675	190.308
		0.3	1.274	0.368	0.933	0.751	188.133
800	$\gamma\,32^o\,\alpha\,6^o$	0.05	1.015	0.224	0.461	0.432	141.269
		0.1	1.060	0.299	0.681	0.598	185.943
		0.2	1.064	0.368	0.932	0.750	196.530
		0.3	1.036	0.384	0.996	0.783	193.465
400	$\gamma\,16^o\,\alpha\,22^o$	0.05	1.876	0.155	0.642	0.571	194.887
		0.1	2.330	0.207	0.911	0.739	187.628
		0.2	2.243	0.271	1.300	0.915	140.773
		0.3	2.154	0.315	1.607	1.014	105.342
800	$\gamma\,16^o\,\alpha\,22^o$	0.05	1.692	0.169	0.711	0.618	193.849
		0.1	1.740	0.248	1.148	0.854	179.876
		0.2	1.749	0.312	1.581	1.007	134.242
		0.3	1.725	0.326	1.684	1.035	125.337

angle projected in the edge surface ($\tan\beta_n$) as shown in equation 3.49. The compression ratio and the shear angle are affected by the increment of the feed but not by the cutting speed; thus, the corresponding results in each feed condition were averaged as shown in table 3.9. The behavior of those variables are modeled in the function of the uncut chip thickness or the feed; see figure 3.18. Then, the shear stress (τ) and compression rate (RC) $\gamma 32^o \alpha 6^o$ is represented by the equation 3.50 where f is the uncut chip thickness or the feed. The models for the compression ratio and the shear stress of the edge geometry $\gamma 16^o \alpha 22^o$ are presented in equation 3.51. The shear stress (τ) presented an opposite trend between edge geometries increasing with the feed for the geometry ($\gamma 32\alpha 6$) and the opposite trend for the geometry ($\gamma 16\alpha 22$). This mathematically corresponds to the friction angle (ϕ_τ) that is a determining parameter to find the shear stress (τ), however, this trend opposite trends does not have physical meaning.

$$\begin{aligned} \tan(\beta)_{\gamma 32\alpha 6} &= 1.1536 \\ \tan(\beta)_{\gamma 16\alpha 22} &= 1.9384 \end{aligned}$$
(3.48)

$$\begin{aligned} \tan(\beta)_{n\gamma 32\alpha 6} &= 1.1536\cos(\gamma) \\ \tan(\beta)_{n\gamma 16\alpha 22} &= 1.9384\cos(\gamma) \end{aligned}$$
(3.49)

$$\begin{aligned} RC(t) &= 0.5556 f^{0.2977} \\ \tau(t) &= 246.52 f^{0.1663} \end{aligned}$$
(3.50)

Table 3.9: *Compression ratio and shear stress average.*

	Feed $\left[\frac{mm}{rev}\right]$	rc mean $\left[\frac{mm}{mm}\right]$	τ mean [MPa]
	0.05	0.221	140.552
$\gamma\ 32^o\ \alpha\ 6^o$	0.1	0.293	184.728
	0.2	0.351	193.419
	0.3	0.376	190.799
	0.05	0.162	194.368
$\gamma\ 16^o\ \alpha\ 22^o$	0.1	0.227	183.752
	0.2	0.292	137.508
	0.3	0.321	115.340
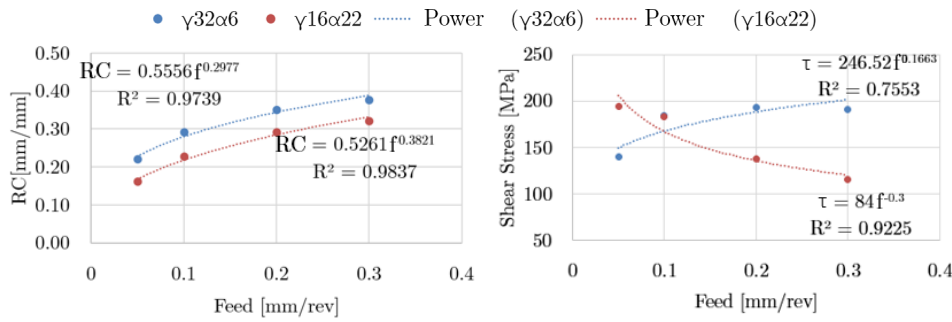
(a) *Compression ratio vs uncut chip geometry.*

(b) *Shear stress vs uncut chip geometry.*

Figure 3.18: *Fitting of the compression ratio and the shear stress.*

$$RC(t) = 0.5261f^{0.3821}$$
$$\tau(t) = 84f^{-0.3} \tag{3.51}$$

The normalized shear angle is found using the helix angle as presented in equation 3.52. There is a recurrent combination of variables in the cutting coefficient estimation grouped in the parameter c shown in equation 3.53.

$$\phi_{n\gamma32\alpha06} = \frac{RC_{\gamma32\alpha06}(f)\cos(\gamma)}{1 - (RC_{\gamma32\alpha06}(f)\sin(\gamma))}$$
$$\phi_{n\gamma16\alpha22} = \frac{RC_{\gamma16\alpha22}(t)\cos(\gamma)}{1 - (RC_{\gamma16\alpha22}(t)\sin(\gamma))} \tag{3.52}$$

$$c = \sqrt{\cos(\phi_n + \beta_n - \gamma)^2 + (\tan(\lambda_f)^2)\sin(\beta_n)^2} \tag{3.53}$$

The coefficients associated to the cut process (K_{*c}) are then estimated with the variables determined previously. There are three coefficients to be determined associated with the cutting process; see equation 3.54. These coefficients are composed of many parameters described below that depend only on the

chip thickness or the orthogonal trials feed (f). Table 3.6 showed the friction coefficients that represent the edge being dragged against the material, and the equation 3.54 shows the cutting coefficient, which represents the behavior of the edge cutting the material.

$$
\begin{aligned}
K_{cc}(f) &= \frac{\tau(f)\cos(\beta_n - \gamma) + \tan(\gamma)\sin(\beta_n)\tan(\gamma)}{\sin(\phi_n(f))c} \\
K_{fc}(f) &= \frac{\tau(f)\sin(\beta_n - \gamma)}{\sin(\phi_n(f))\cos(\gamma)c} \\
K_{pc}(f) &= \frac{\tau(f)\cos(\beta_n - \gamma)\tan(\lambda_f) - \sin(\beta_n)\tan(\gamma) - \sin(\beta_n)\tan(\gamma)}{\sin(\phi_n(f))c}
\end{aligned}
\tag{3.54}
$$

The cutting force state in the mill during the cutting force is then estimated with the linear approach presented in the equation 3.55. This state of force represents an orthogonal three-dimensional state of force with origin in the cutting edge.

$$
\begin{aligned}
F_c(t) &= K_{cc}(t)tlc + K_{ce}(t)lc \\
F_f(t) &= K_{fc}(t)tlc + K_{fe}(t)lc \\
F_p(t) &= K_{pc}(t)tlc
\end{aligned}
\tag{3.55}
$$

(a) Geometrical parameter of flank milling.

(b) Force distribution of flank milling.

(c) Geometrical parameter of end milling.

(d) Force distribution of end milling.
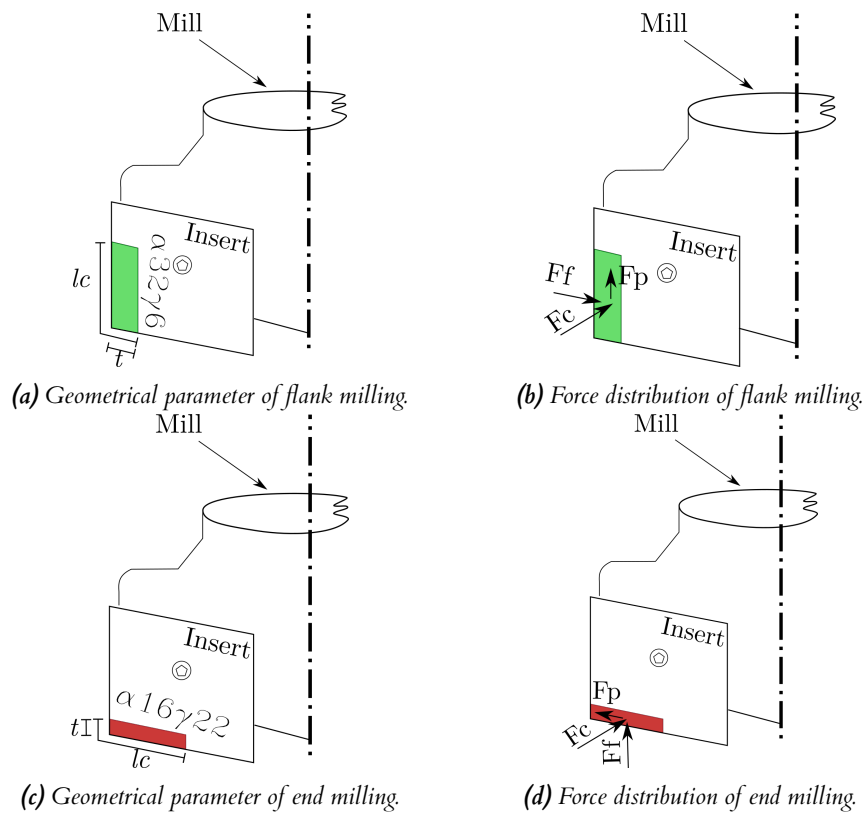
Figure 3.19: *Cutting force distribution by edge.*

The cutting force F_c normal to the rake angle is composed by the cutting coefficient K_{cc}, the uncut chip area represented by the uncut chip thickness (t) and the contact length (lc), plus the effect of the friction in the cutting direction represented by the friction or edge coefficient (K_{ce}) multiplied by the edge contact length (lc). The feed (f) in orthogonal cutting coincides with the uncut chip thickness (t); however, in milling and turn–milling does not. For this reason, the cutting coefficients in equation 3.55 does not depends on the feed (f) but in the uncut chip thickness (t). In the plane of the rake angle exist the feed and penetration forces that are co-planar and orthogonal. The feed force is analog to the cutting force but in the feed direction, see equation 3.55; and the penetration force does not present friction component but only the cutting one. Consider a side milling operation with a straight-tooth milling cutter; see figure 3.19. This distribution of forces depends of the uncut chip geometry alignment, with the coordinate system of the tool. For example the flank milling is illustrated in figure 3.19 (a) and (b) and the end milling in the figure 3.19 (c) and (d). As the orthogonal centric turn–milling operations presents simultaneous cutting with both edges the general state of force of the mill correspond to that described in equation 3.42.

3.6   Experimental validation of the cutting forces

Experimental tests were carried out in order to validate the theoretical models presented in the previous sections. The goal was to perform orthogonal centric turn–milling operations in diverse cutting scenarios to change the uncut chip geometry and then compare the measured forces with the cutting force prediction.

Figure 3.20: Orthogonal centric turn–milling experimental setup.

3.6.1 Experimental methodology

The experimental trials were developed in a Lagun vertical CNC milling machine with a rotary table attached which holds the workpiece. The tool was held in place by a rotational dynamometer Kistler 9123. The material characterized with the cutting tool presented previously were used to the experimental trials, see figure 3.20. Three repetitions of every trial were done to ensure statistical validity sampled at sampled at 25kHz.

Table 3.10: Experimental parameters for model validation.

Rw [mm]	rt [mm]	$z[-]$		
44	12.5	1		
ap *Large Depth*			ap *Small Depth*	
2 mm			0.5 mm	
V_c [m/min]	f_a [mm/wpr]	n_w [rpm]	n_t [rpm]	f_z [mm]
400	2.5	8	5093	0.43
750	2.5	15	9549	0.43
400	2.5	5	5093	0.27
750	2.5	9.35	9549	0.27
400	5	8	5093	0.43
750	5	15	9549	0.43
400	5	5	5093	0.27
750	5	9.35	9549	0.27
400	7.5	8	5093	0.43
750	7.5	15	9549	0.43
400	7.5	5	5093	0.27
750	7.5	9.35	9549	0.27

As in the virtual validation case, some input parameters varied while the rest remained fixed, as shown in table 3.10. These cutting conditions were selected not to exceed the maximum chip thickness or the cutting speed (V_c) recommended by the tool manufacturer. The analytical models were implemented to verify whether the selected cutting conditions fulfilled the manufacturer restrictions. The cut chips were collected and weighted in order to establish the volume removed by the edge pass. Weights were measured using a high precision scale with a minimum measure of 0.1 *mg*. Sets of five, ten, and twelve chips were weight and averaged to determine the mean chip mass in each cutting condition. The chip volume was calculated by taking the average weight and dividing it between the density of workpiece material. Three measurement repetitions were performed for statistical validation for both volume and cutting forces. Despite of the material characterization was performed at ($V_c = 800$ m/min) the Kistler rotational dynamometer cannot rotate at more than 10000 rpm; considering this and the slight effect of the cutting speed over the cutting forces the turn–milling trials were tested at ($V_c = 750$ m/min).

Raw force of each edge pass
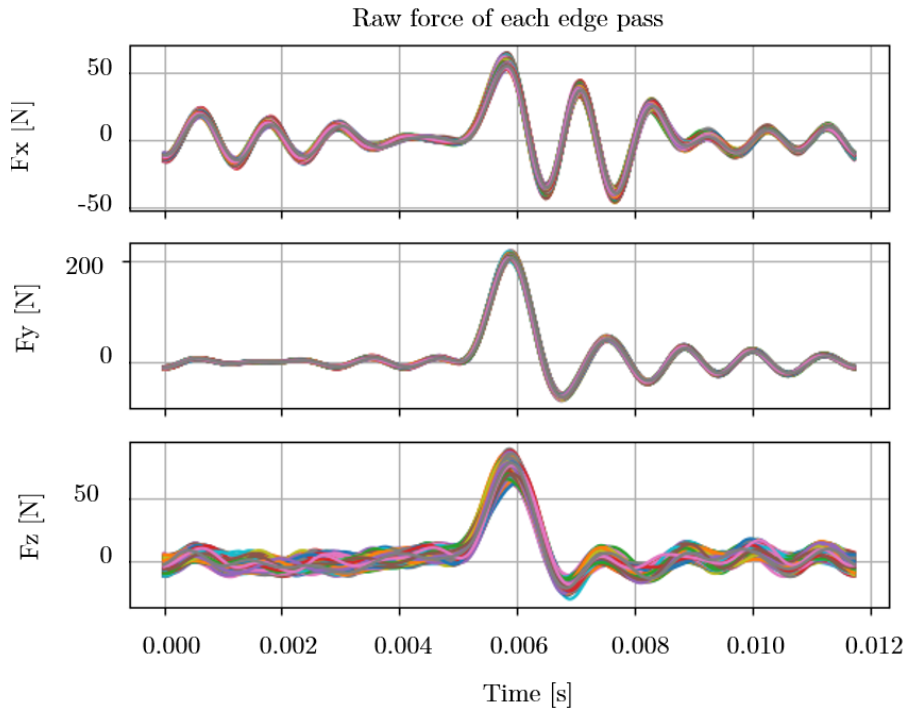
(a) Example of force signal superposition (Vc 400 fz0.27 fa 2.5 ap 2).
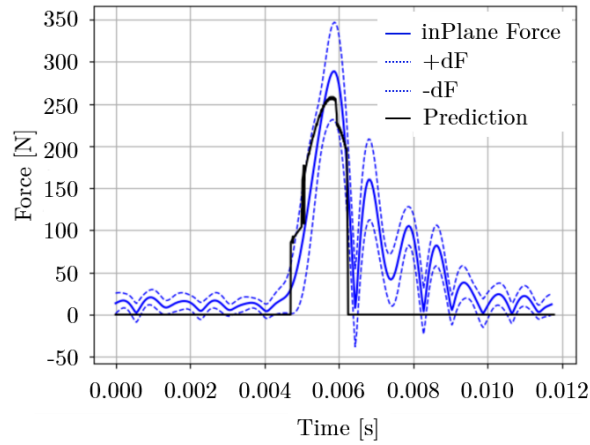
(b) Inplane instantaneous cutting force.
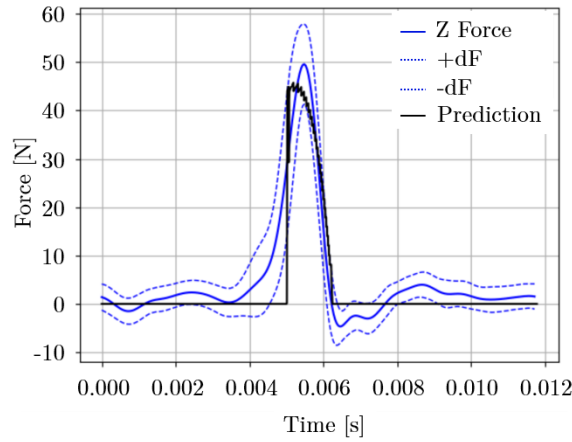
(c) Axial instantaneous cutting force.

Figure 3.21: *Prediction and experimental cutting forces direct comparison (Vc 400 fz 0.27 fa 2.5 ap 2).*

The force in-plane was found by the vectorial sum of (x) and (y) components of the measured forces see figure 3.21 (a). These components of force are the responsible of the bending moment, that considering the tool as a cantilever beam deflect the tool. These signal treatments were performed for the comparison as presented in figure 3.21 (b and c) where the theoretical and the experimental signals are compared. The in-plane and axial forces were validated by taking only the maximum value of the signal. The (+/- dF) signals are the standard deviation of the experimental signals presented in figure 3.21 (a) to determine the interval of the cutting forces with 95% of confidence.

3.6.2   Experimental results and discussion

The regimen of depth presents the experimental results; see table 3.10. Figure 3.22 presents the mass data where LD corresponds to the "large depth" and SD "small depth". The cutting speed does not seem to represent a change in the removed volume of the chip. This behavior stems from the proportional increment of the workpiece rotational speed (nw), which keeps the feed per tooth (f_z) constant. In this experimental design, the axial feed (f_a) determined the increment of volume of the chip. A positive correlation was found between experimental and theoretical chip volume prediction as expected.
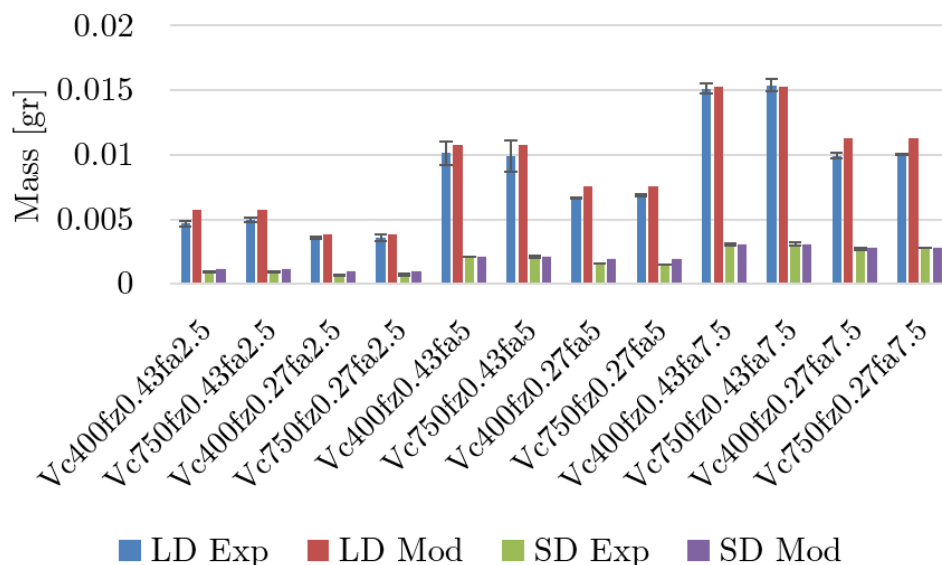
Figure 3.22: *Chip volume comparison experimental vs predicted. LD: Large depth approach. SD: Small depth approach.*

Figure 3.23 (a) shows the theoretical top view of the uncut chip for the whole whole V_c : 400 m/min and f_z : 0.43 mm conditions, and figure 3.23 (b) shows photos of the cut deformed chips. The effect of the cut can be noticed because of the differences between the theoretical and experimental chips. However, some features remain on the collected chips that work as evidence to validate the analytical approach qualitatively. The effect of increasing the axial feed f_a can be observed in both experimental and analytical results and behave in good agreement. The end zone presents a considerable increment because the axial
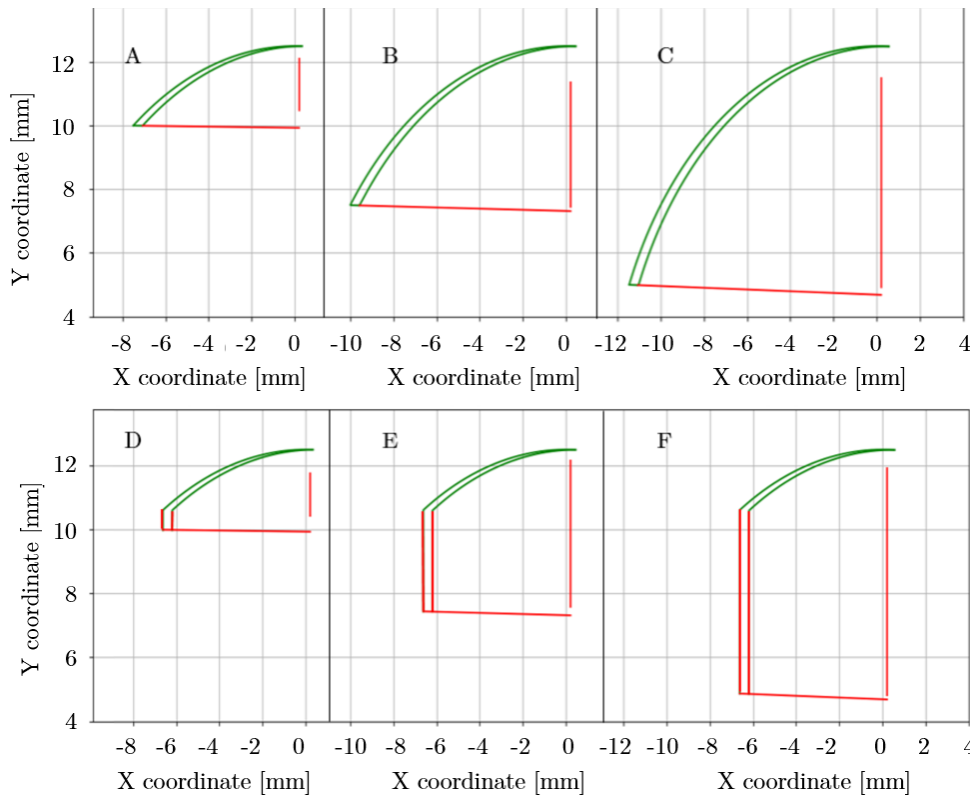
(a) Theoretical estimation of the uncut chip.
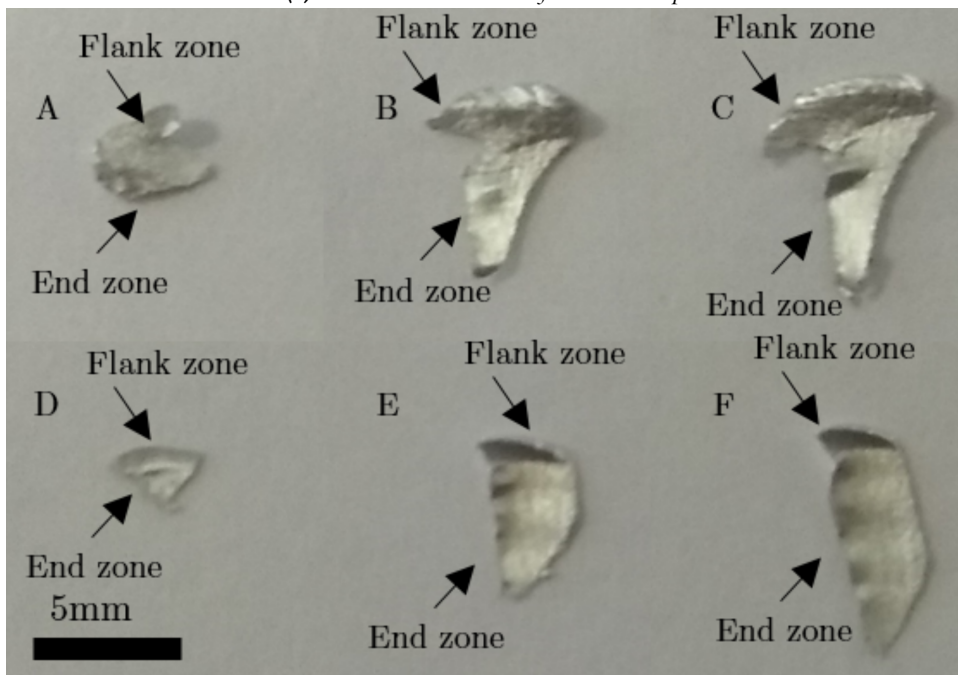
(b) Collected chips of turn-milling trials.

Figure 3.23: *Uncut chips Top view in Vc400 fz0.43. A:fa2.5ap2. B:fa5ap2. C:fa7.5ap2. D:fa2.5ap0.5. E:fa5ap0.5. F:fa7.5ap0.5.*

feed f_a increases for both "large and small depth" regimens. The flank zone

increase with the axial feed f_a as predicted by the analytical model in the "large depth" regimen. This behavior was not expected in the "small depth" regimen as indeed did not occur as shown in figure 3.23 (b) D, E, and F. The early flank zone disappearance is compensated by an augmented end zone when the axial feed f_a is increased in the "small depth" regimen. The collected chips of the "large depth" trials are consistent with the results reported by Zhu et al. (2016b), but they did not study the small depth regimen.

(a) Large depth regimen trials.

(b) B: Small depth regimen trials.
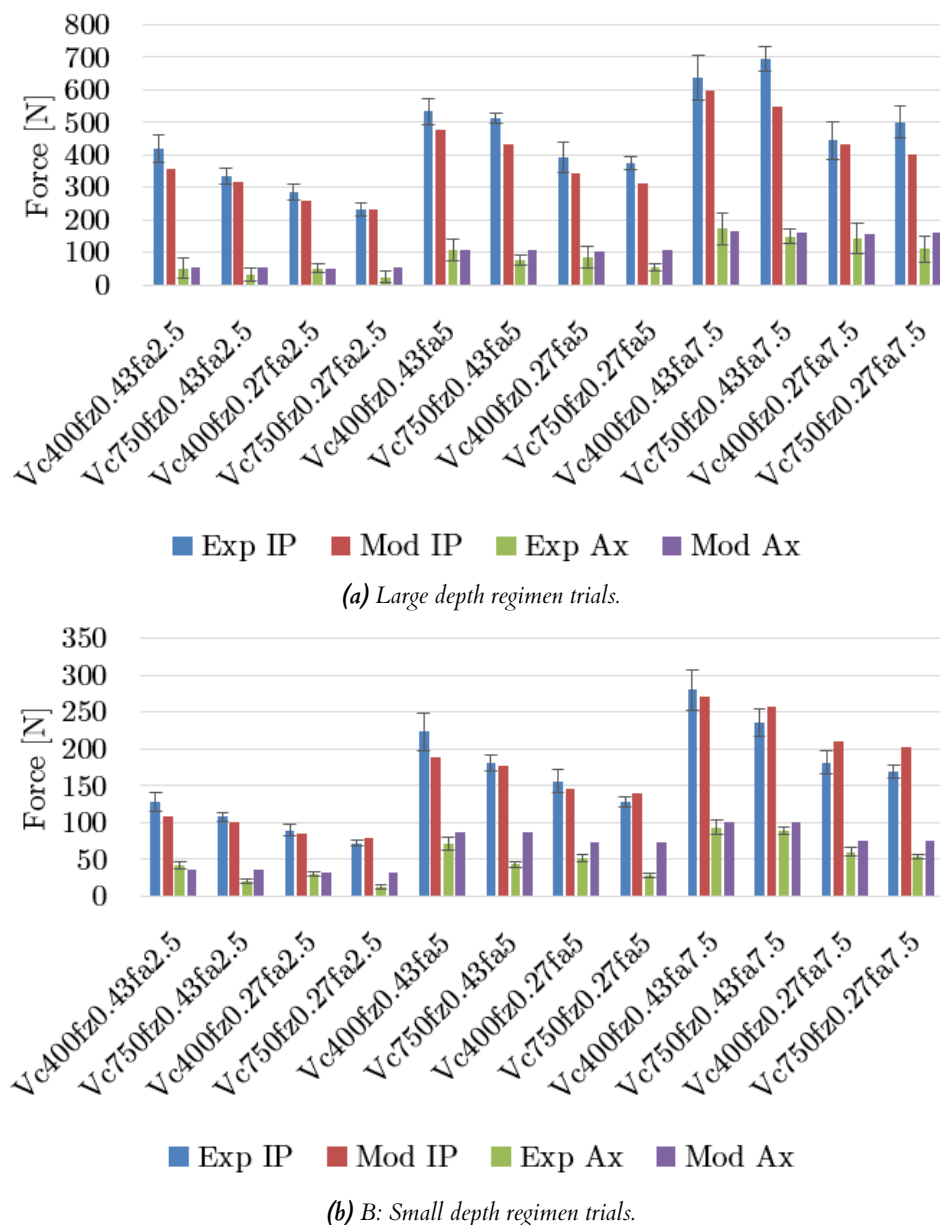
Figure 3.24: *Theoretical vs experimental cutting forces results. (IP: In plane resultant forces. Ax: Axial force).*

The force comparison of the "large depth" is shown in figure 3.24 (a). The predicted cutting forces tend to follow the observed behavior presenting errors of around 15%. This fact is agree with the results observed with the analytical models presented in this research being a reliable and representation of the

cutting process. The maximum error obtained was 25% ($V_c 750 f_z 0.43 f_a 7.5$). One reason for this might be dynamic instabilities during the cutting process. Surprisingly, an increment of force was presented in the (f_a : 7.5 [mm]) trials when the cutting speed (V_c) was augmented, this occurred even though the cutting conditions selected were within the tool manufacturer recommendations, and the orthogonal trials showed the opposite behavior. This might be explained through the dynamic response of the system, due to the Kistler dynamometer is not as rigid as a conventional tool holder. Additionally, the low-speed condition predictions (V_c : 400) are within the error bar for both cases of feed per tooth (f_z : 0.43 − 0.27 mm/tht). The experimental and modeled forces under (f_a : 7.5 mm/workpiece_rev) behave in the same line with the orthogonal cut trials and presented a good fitting between the experimental and modeled data.

The force comparison of the "small depth" is shown in figure 3.24 (b). The force prediction seems to follow the experimental trend presenting errors below 19%. The maximum error was presented in the (V_c : 400, f_z : 0.43, f_a : 5) condition, although the prediction is not too far from the experimental interval error. The "small depth" predictions present a tighter fit with the experimental data than the "large depth" case. Indeed, it seems that several predictions fitted within the experimental error interval. Interestingly, all the experimental data presented a decrement in the cutting forces in this regimen when the cutting speed was increased. This would seem to reinforce the conjecture of dynamic instabilities in the "large depth" trials. An excessively increased force state on the tool could lead to operating under unstable conditions.

In both regimens, the increase in the axial feed (f_a) results in a fundamental increment in the end zone but not in the flank zone. Additionally, the end zone thickness is thin compared to the flank zone. An increased end zone probably contributes enormously to the tool state of force. The reason for this might be related to the calculation of the (K) cutting coefficients. They depend highly on the chip thickness and, to a lesser extent, on the cutting speed (V_c). When the chip thickness decreases, the cutting coefficients tend to increase. Additionally, the increased end zone results in considerable contact length. All these characteristics would seem to explain the effect of increasing the axial feed (f_a) on the cutting forces. Therefore, the end zone could be considered the most critical load component of the general state of force. In agreement with the findings reported by Schulz Schulz and Spur (1990).

In summary, the workpiece (n_w) and rotational tool speeds (n_t) determine the maximum chip thickness in both cutting zones. A balance between these variables would locate the cutting conditions within the optimum operating window. The axial feed (f_a) determines the radial engagement of the tool. Its increment results in a higher material removal rate scenario, but there is the risk of reaching unstable cutting conditions. This might be explained as an overload of the flank and end edges, because the increment on the axial feed (f_a) results in more thickness in the flank and more friction length in the end edge as shown in figure 3.23 (a). Additionally, the excessive axial feed (f_a) wears two edges simultaneously, reducing the life of square inserts by half and increasing the production costs. Moreover, operating under extremely demanding conditions might produce poor surface finishing and geometrical error.

3.7 Conclusions

In this study, analytical models are presented to predict cutting forces of the centric orthogonal turn–milling process. Mathematical expressions for the boundary lines of the uncut chip geometry in 3D are determined. Depending on the cutting parameters, the process can be on "large or small" depth regimens presenting different chip geometries associated with the regimen. From the boundary lines, the instantaneous thickness and contact length of the flank and end zone can be found respectively. The following conclusions can be drawn:

1. A novel approach to calculate the instantaneous uncut chip geometry for orthogonal centric turn–milling operations was proposed. The wide range of cutting conditions used for the virtual and experimental trials showed that the analytical models were robust and reliable. The cutting parameters are different from those in conventional milling and turning and the models help to understand the effect of the parameters on the machining process.

2. The "large and small" cutting regimens were identified and modeled. The condition which determined the operating regimen was also proposed. These contributions might help to explain the reason for the dissimilar geometries found by Crichigno Filho (2012), Karaguzel et al. (2015b) and Zhu et al. (2016b) for the same machining process.

3. The analytical approaches accurately represented the uncut chip geometry. Errors below 2% were obtained compared with a CAD reproduction. Additionally, the volume of the collected cut chips corresponded with the prediction, and the qualitative comparison between the modeled uncut and cut chips collected was in good agreement.

4. The suggested approach is a quick way to understand the effect of the cutting parameters on the uncut chip geometry and more importantly on the cutting forces in diverse operating scenarios. The overall force error was around 15% and the predictions were in good agreement with the experimental data. The most important load component is applied on the end edge which is in line with the findings of Schulz Schulz and Spur (1990).

4 | Cutting force prediction in eccentric orthogonal turn-milling operations

The orthogonal turn-milling operations have a specific parameter called eccentricity. This parameter modifies the uncut chip geometry, and it should be considered in the process planning. This fact obsoletes the models presented in the previous chapter. Therefore the analytical equations must be redefined considering this parameter. Figure 4.1 shows a comparison scheme of the uncut chip geometry in centric and eccentric conditions. The uncut chip geometry has schemed in dotted lines in the top and front views for each case. This parameter is important because has presented outstanding results on surface finishing and tool life Karaguzel et al. (2015b,a). Additionally, inducing eccentricity in the operation leads to higher MRR scenarios resulting in cylindrical surfaces as showed Zhu et al. (2015a).

(a) Uncut chip centric orthogonal turn-milling.   *(b) Uncut chip eccentric orthogonal turn-milling.*
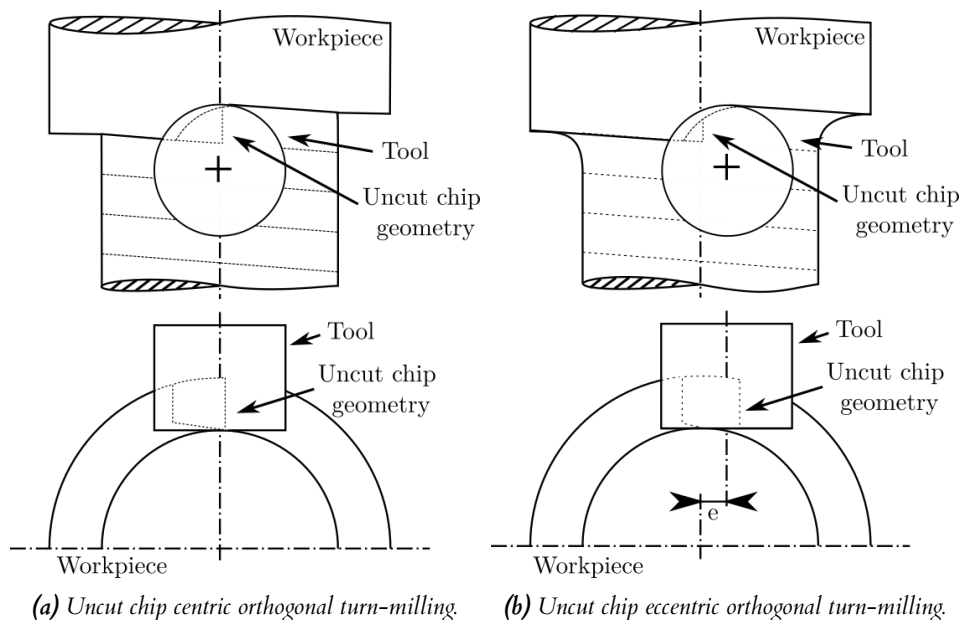
Figure 4.1: *Centric and eccentric uncut chip scheme comparison.*

The most noticeable difference in the uncut chip geometry is the reduced cutting end zone resulting from the eccentricity. Another change is in the flank zone; the variable depth of cut can be modified with the eccentricity by taking

advantage of the curvature of the workpiece. These characteristics are studied in deep in this chapter thanks to the modeling, simulating, and experimental work presented.

4.1 Analytical model of eccentric turn-milling operations

The eccentricity in orthogonal turn-milling operations is a new cutting parameter to consider. However, it does not modify the kinematics considerably; therefore, the kinematics section presented in the previous chapter is still valid (see equations 3.1 to 3.7). Nevertheless, figure 4.2 presents the projections of the movements considering the eccentricity. This schematic representation is deformed to exaggerate the kinematic variables because they are small compared to the geometrical parameters.
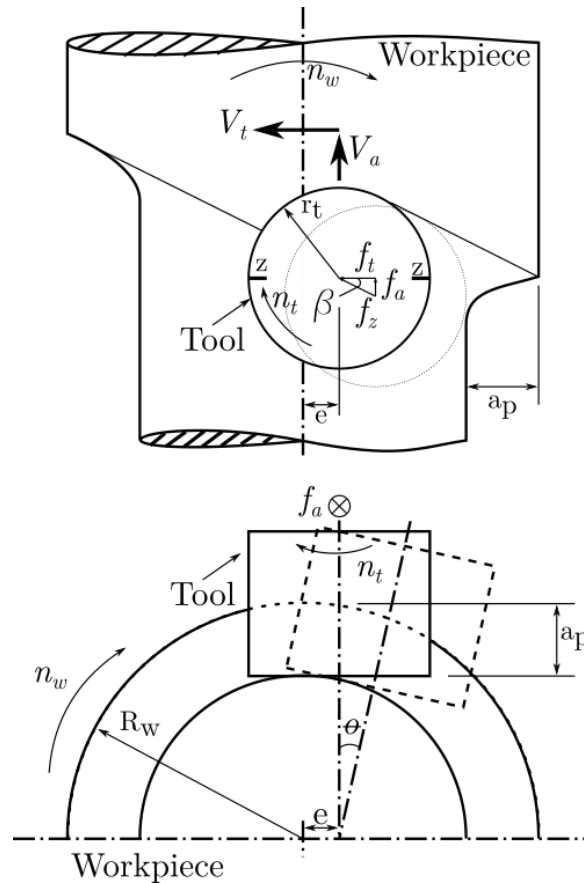
Figure 4.2: *Orthogonal eccentric turn-milling kinematics. (R_w) Workpiece radius, (n_w) Workpiece rotational speed, (r_t) Tool radius, (n_t) Tool rotational speed, (f_a) Axial feed, (a_p) Depth of cut, (z) Number of cutting edges, (e) Eccentricity.*

The eccentricity does not present any new line than the centric case; however, some of the functions present modifications. The external and internal profiles (p_e, p_i) join the flank zone, and the inferior internal profile, the I, and L lines (p_{ii}, I, L) determines the end zone, see figure 4.3 (a and b). All the modeling equations are presented below for the reader convenience, even if they do not present any change compared with the centric model, making it easier to read this chapter.

(a) Top View

(b) Front View

(c) 3D uncut chip representation.

(d) Relevant angles in eccentric turn–milling uncut chip geometry.
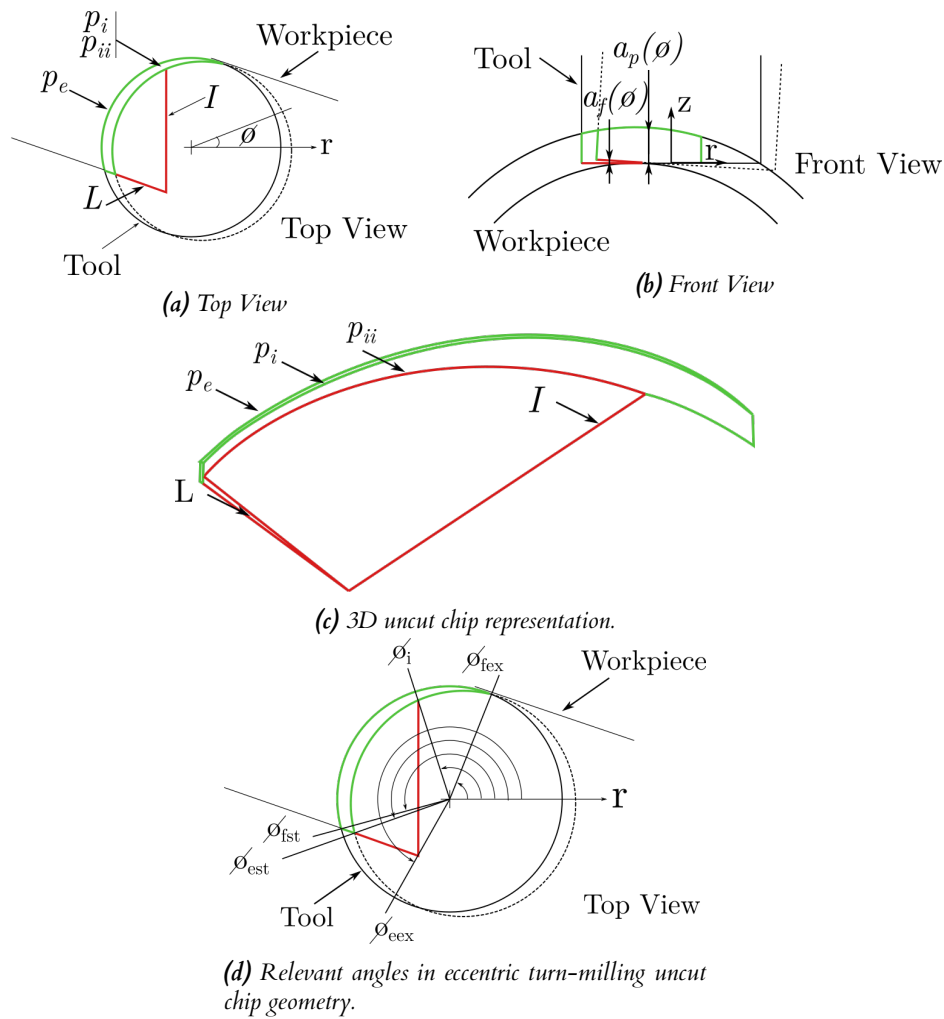
Figure 4.3: *Zoom of the engagement zone (orthogonal views). 3D uncut chip representation and angle distribution. (ϕ_{fst}) Flank zone start angle, (ϕ_{est}) End zone start angle, (ϕ_i) I line exit angle, (ϕ_{eex}) End zone exit angle.*

The eccentricity does not present any new line than the centric case; however, some of the functions present modifications. The external and internal profiles (p_e, p_i) compound the flank zone, and the end zone is determined by the inferior internal profile, the I, and L lines (p_{ii}, I, L). All the modeling equations are presented below for the convenience of the reader, even if they do not present any change compared with the centric model, making it easier to read this chapter. Figure 4.3 (c and d), shows an arbitrary uncut chip geometry; the internal and external profiles meet at the (ϕ_{fex}) angle. The determination of ϕ_{fex}, ϕ_{fst}, and ϕ_{eex} angles is done by analytical means as shown in equations 4.1, 4.2, and 4.3. The resulting value ϕ_{eex} found by equation 4.3 might be positive or negative, depending on the cutting parameters. This due to the domain of the arctan function covers the interval $(-\frac{\pi}{2}, \frac{\pi}{2})$. However, based on the cylindrical coordinate approach take by this methodology, once the angle overcomes the second quadrant, the angle should increase, not become negative; to solve this problem, every time ϕ_{eex} becomes negative, it was added 2π radians to become the angle positive. The remaining angles (ϕ_i, and ϕ_{est}) follow the same numeric

iterative methodology used in the previous chapter.

$$\phi_{fex} = \arccos\left(\frac{f_z}{2r_t}\right) + \beta \tag{4.1}$$

$$\phi_{fst} = \pi - \arcsin\left(\frac{r_t - f_a}{r_t}\right) \tag{4.2}$$

$$\phi_{eex} = \arctan\left(\frac{r_t \sin(\phi_{fst}) - \left[\left(r_t \cos(\phi_{fst}) - \left(\left((R_w - a_p)\sin\left(\frac{\theta}{2}\right)\right) - e\right)\right)\tan(\beta)\right]}{(R_w - a_p)\sin\left(\frac{\theta}{2}\right) - e}\right)$$
$$\tag{4.3}$$

In eccentric turn-milling, it is possible to operate with large axial feed values and obtain a cylindrical surface. This characteristic impacts the relationship between (ϕ_{fst}) and (ϕ_{est}). In the case of the angle ($\phi_{eex} < \pi/2$) it results on ($\phi_{fst} \leq \phi_{est}$); however, in the case of ($\phi_{eex} > \pi/2$) the relationship changes to ($\phi_{fst} \geq \phi_{est}$), see figure 4.4. This detail is essential because it modifies the modeling approach of the internal and external profiles (p_e and p_i). The flank zone comprises three lines: circular profiles and a segment of a straight line. In the previous chapter, the straight line segment was attached to the interior profile (p_i); because in the centric case, the (I) line is always in the first quadrant. The eccentricity application moves the line to the second or even the third quadrants, as shown in figure 4.4. Therefore, external profile (p_e) is defined by equation 4.4 and its domain is presented in equation 4.5, and in any case the height of the line is expressed in equation 4.6.
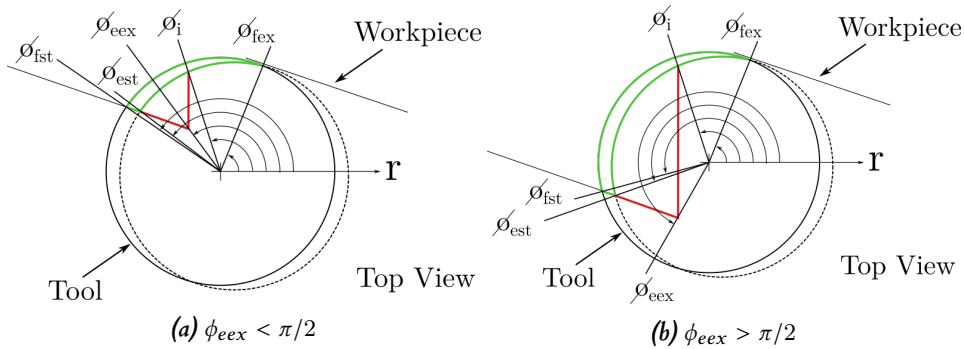
Figure 4.4: *Comparison of the feed domains regimens in eccentric turn-milling operations.*

if ($\phi_{eex} < \pi$) then,
$$p_e(\phi) = r_t \qquad *$$
else ($\phi_{eex} > \pi$) then,
$$\tag{4.4}$$
$$p_e(\phi) = \begin{cases} r_t & * \\ \dfrac{r_t(\sin(\phi_{fst}) - \cos(\phi_{fst})\tan(\beta))}{\sin(\phi) - \cos(\phi)\tan(\beta)} & ** \end{cases}$$

Circular domain   → *

$$\phi_{fex} \leq \phi \leq \phi_{fst}$$

Linear domain   → **

if ($\phi_{eex} < \pi$) then,

$$\phi_{est} \leq \phi \leq \phi_{fst}$$

else ($\phi_{eex} > \pi$) then,

$$\phi_{fst} \leq \phi \leq \phi_{est}$$

(4.5)

$$a_{p_e}(p_e) = \sqrt{(R_w^2) - (p_e \cos(\phi) + e)^2} + (ap - Rw) \tag{4.6}$$

The internal profile is modeled considering the the magnitude of (ϕ_{eex}) as shown in equation 4.7. The domain of the internal profile is presented in equation 4.8. The height of the profile is presented in equation 4.9 and is valid for the whole boundary line.

if ($\phi_{eex} < \pi/2$) then,

$$p_i(\phi) = \begin{cases} f_z \cos(\phi - \beta) + (\sqrt{(r_t)^2 - (f_z \sin(\phi - \beta))^2}) & * \\ \dfrac{r_t(\sin(\phi_{fst}) - \cos(\phi_{fst}) \tan(\beta))}{\sin(\phi) - \cos(\phi) \tan(\beta)} & ** \end{cases}$$

else ($\phi_{eex} > \pi/2$) then,

$$p_i(\phi) = f_z \cos(\phi - \beta) + \sqrt{(r_t)^2 - (f_z \sin(\phi - \beta))^2} \quad *$$

(4.7)

Circular domain   → *

$$\phi_{fex} \leq \phi \leq \phi_{est}$$

Linear domain   → **

if ($\phi_{eex} < \pi/2$) then,

$$\phi_{est} \leq \phi \leq \phi_{fst}$$

else ($\phi_{eex} > \pi/2$) then,

$$\phi_{fst} \leq \phi \leq \phi_{est}$$

(4.8)

$$a_{p_i}(p_i) = \sqrt{(R_w^2) - (p_i \cos(\phi) + e)^2} + (ap - Rw) \tag{4.9}$$

The flank zone is thoroughly described by determining the external and internal profiles (p_e and p_i) in the 3D coordinates. The I line is presented in

equation 4.10. Its domain does not present changes with the axial feed and is shown in equation 4.11. The height of this line is zero for the whole line.

$$I = \frac{\left((R_w - a_p)\sin(\frac{\theta}{2})\right) - e}{\cos(\phi)} \tag{4.10}$$

$$\phi_i \leq \phi \leq \phi_{eex} \tag{4.11}$$

From the I line start the inferior internal profile p_{ii}. This line has the same circular form of the internal profile (p_i) but is projected in the end cutting zone. The polar form of the line is presented in equation 4.12. The domain of the line is presented in equation 4.13. The projected height of the line in the end cutting zone is presented by equation 4.14.

$$p_i(\phi) = f_z \cos(\phi - \beta) + \sqrt{(rt2) - (f_z \sin(\phi - \beta))^2} \tag{4.12}$$

$$\phi_i \leq \phi \leq \phi_{est} \tag{4.13}$$

$$a_{f_{pii}}(p_{ii}) = -\tan(\theta)(p_{ii}\cos(\phi)) + (p_{ii}(\phi_i)\cos(\phi_i)\tan(\theta)) \tag{4.14}$$

The last line to complete the geometry is the L line. This line is ruled by a linear function presented in equation 4.15, the line domain is shown in equation 4.16. The height of the line is presented in the equation 4.17.

$$L(\phi) = \frac{r_t(\sin(\phi_{fst}) - \cos(\phi_{fst})\tan(\beta))}{\sin(\phi) - \cos(\phi)\tan(\beta)} \tag{4.15}$$

$$\phi_{eex} \leq \phi \leq \phi_{est} \tag{4.16}$$

$$a_{f_L}(L) = -\tan(\theta)(L\cos(\phi)) + (L(\phi_{eex})\cos(\phi_{eex})\tan(\theta)) \tag{4.17}$$

4.2   Geometric validation

The model is validated through the instantaneous area comparison between the analytical model and a CAD representation of the uncut chip geometry; to reach this objective, a set of simulations are presented in diverse cutting conditions challenging the analytical modeling to represent the uncut chip geometry in different scenarios. Table 4.1 shows the cutting conditions selected to perform the simulations and compare their results. The area comparison is necessary due to the direct comparison is difficult due to the different visualization of each software, see figure 4.5.

Table 4.1: Cutting conditions for geometrical validation.

R_w [mm]	r_t [mm]	a_p [mm]	z [-]	n_w [rpm]
44.5	12.5	2	2	3
Tag	V_c [m/min]	n_t [rpm]	$f_a \left[\frac{\text{mm}}{\text{wprev}}\right]$	e [mm]
T1	100	1273	6	2
T2	200	2546	6	5
T3	200	2546	20	2
T4	200	2546	20	11

(a) T2 modeling results. *(b) T2 CAD representation.*
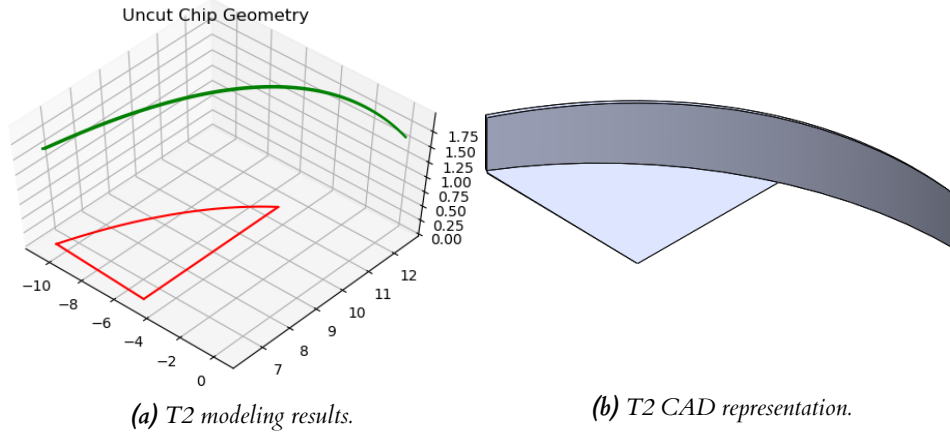
Figure 4.5: Visual comparison between the model and CAD.

The results of the comparison are shown in figure 4.6. There is a tight correlation between the analytical model and the CAD representation in Solidworks 2017. There is a slight error that the approach simplifications might explain. The maximum error ascertained was lower than 1.6%. The eccentricity behavior in the end zone was covered by the analytical model, performing accurate predictions in large and small feed conditions.
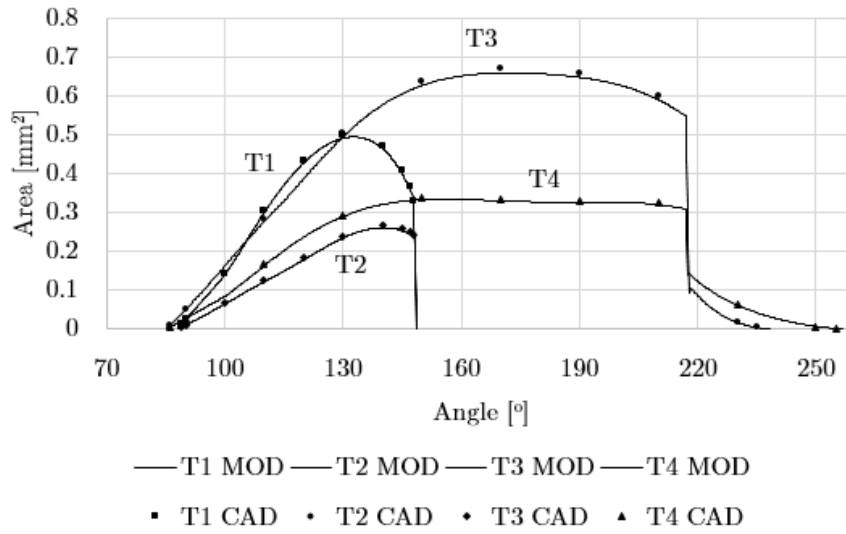
Figure 4.6: *Comparison of the CAD and model instantaneous area evolution.*

4.3 Effect of the eccentricity in the uncut chip geometry

The development of an accurate model representing the uncut chip geometry allows presenting an extensive simulation plan to determine the effect of the eccentricity in orthogonal turn–milling operations. At first view, the increment of the eccentricity decreases the end zone as shown in figure 4.7. In this set of simulations, the only variable is the eccentricity, and it is evident how the flank zone in green remains constant while the end zone in red considerably decreases.

Figure 4.7 might suggest an apparent change in the uncut chip volume due to the end zone reduction in red, that does not seem to be compensated with increments in green flank zone thickness. A comparative set of simulations is proposed to evidence the effect of the eccentricity in the chip volume. Additionally, the chip volume is determined from the material removal rate equation proposed by Karaguzel et al. (2015b), see equation 4.18.

$$MRR = z n_t f_z a_p a_e \qquad\qquad\qquad (4.18)$$

The first important characteristic is that the equation suggested by Karaguzel et al. underestimates the actual material removal rate due to this equation is the same for face milling, see figure 4.8. Indeed, this research showed that the uncut chip geometry in turn-milling is considerably different from that obtained in face milling. The specific behavior of the chip showed a slight increase with the eccentricity until the value (e = 6 mm) when the chip volume decreases more pronouncedly, approximating the value predicted by Karaguzel et al. with an advanced value of eccentricity (e = 14 mm). The end zone has almost disappeared, and the uncut chip geometry is practically the same as the face a face milling operation. Therefore, the slight volume increment results from the increment in the depth of cut in the maximum thickness in the flank zone when the eccentricity

is augmented. Once this point is reached, the end cutting zone reduction affects the chip volume, reducing in almost 11% the chip volume.

(a) e = 2 mm.

(b) e = 5 mm.

(c) e = 11 mm.
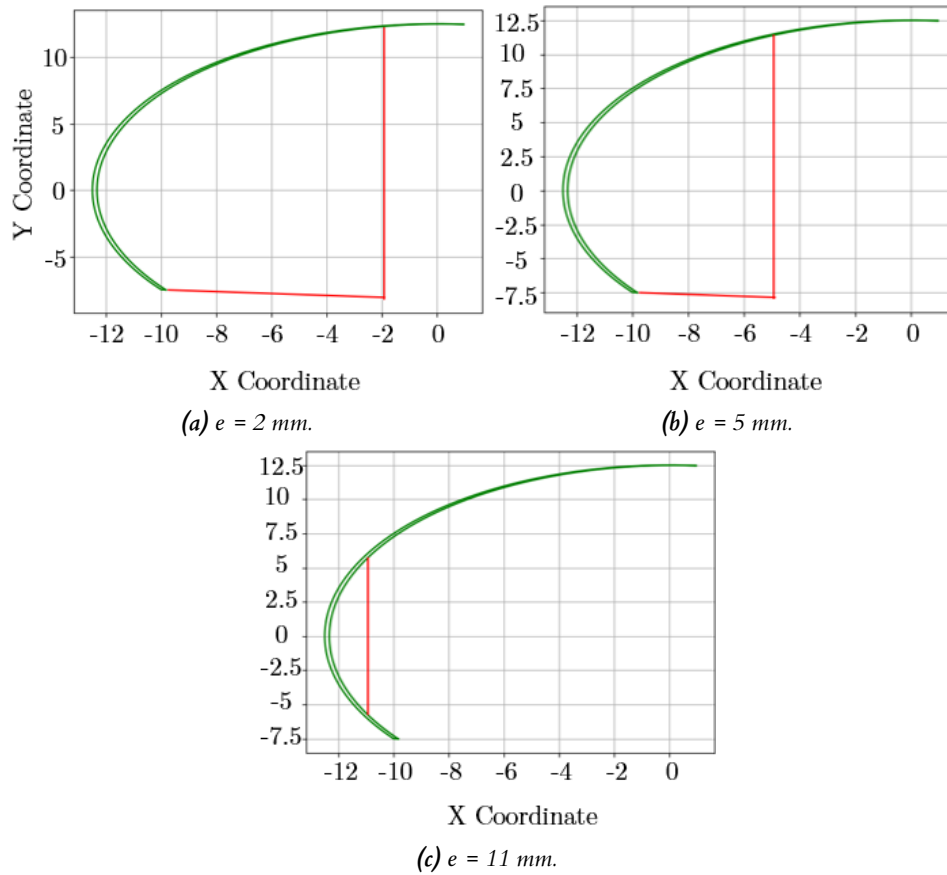
Figure 4.7: *Top view of uncut chip geometry. V_c = 200 m/min, r_t = 12.5 mm, R_w = 44.5 mm, n_w = 3 rpm, f_a = 20 mm/wprev, a_p = 2 mm, z = 2, e = 2, 5, 11 mm.*
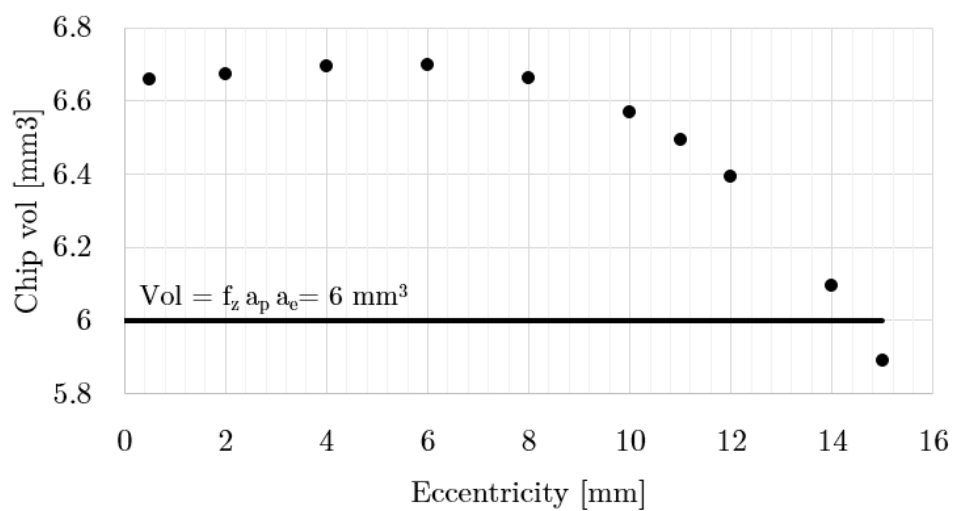
Figure 4.8: *Chip volume change in function of the eccentricity. V_c = 400 m/min, r_t = 16 mm, R_w = 44 mm, n_w = 3 rpm, f_a = 15 mm/wokrpiece_rev, a_p = 2 mm, z = 1, e = 0.5, 2, 4, 6, 8, 10, 12, 14, 15 mm.*

4.4 Experimental validation

The model has been validated theoretically in the geometric validation. However, it is necessary to validate the model experimentally through turn–milling trials. Therefore, an experimental plan focusing on the eccentricity, feed per tooth, and axial feed. Table 4.2 shows the cutting parameters used in the trials. Each parameter was repeated three times in order to ensure statistical representativeness.

Table 4.2: Turn–milling cutting parameters for experimental validation of the model.

R_w [mm]	r_t [mm]	a_p [mm]	z [-]	n_w [rpm]	
44.5	12.5	2	1	3	
Tag	V_c [m/min]	n_t [rpm]	f_z [mm]	f_a $\left[\frac{\text{mm}}{\text{wprev}}\right]$	e [mm]
Vc400fa3.5fz0.16e2	400	5092	0.16	3.5	2
Vc400fa3.5fz0.16e4	400	5092	0.16	3.5	4
Vc400fa3.5fz0.16e6	400	5092	0.16	3.5	6
Vc400fa3.5fz0.32e2	400	5092	0.32	3.5	2
Vc400fa3.5fz0.32e4	400	5092	0.32	3.5	4
Vc400fa3.5fz0.32e6	400	5092	0.32	3.5	6
Vc400fa10fz0.32e4	400	5092	0.32	3.5	4
Vc400fa7fz0.32e6	400	5092	0.32	3.5	6
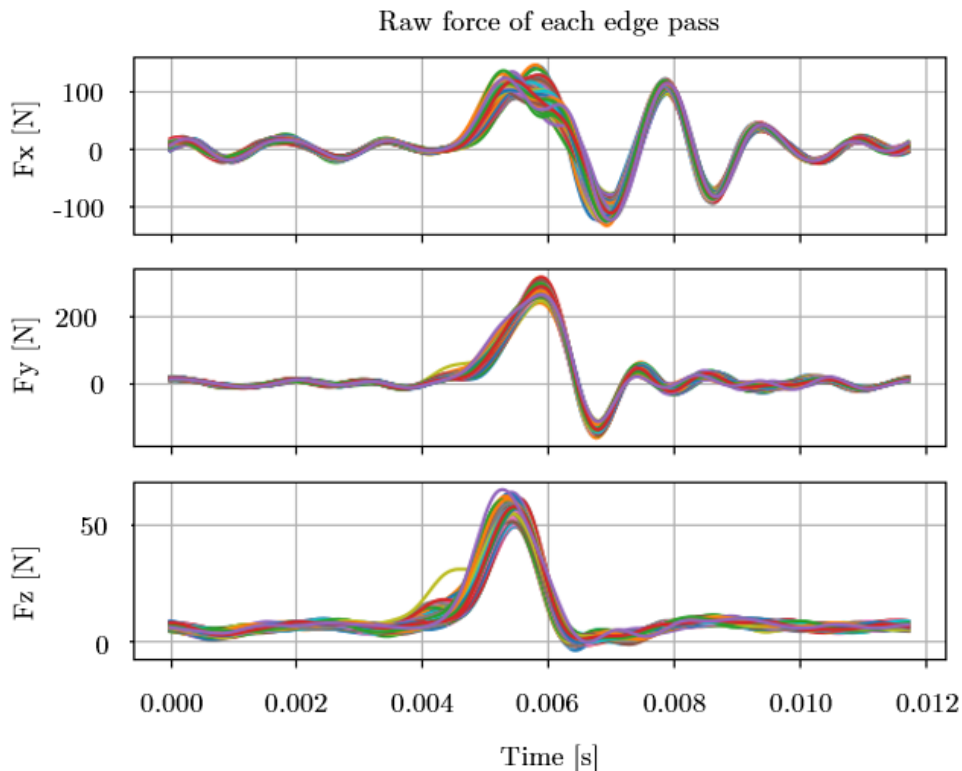
Figure 4.9: Example of force signal superposition ($Vc400f_a3.5f_z0.16e2$).

In these trials, the cutting forces were measured with a dynamometer Kistler 9123 in the diverse cutting trials and compared with those obtained through

simulations esteemed by the presented model. This model is only valid to flat end mills; the same tool–material set was used in the previous chapter. The mill is the ARNO FDG190025R0310 and the same SDHT100408FN-PMAAN1005 insert as presented in figure 3.20.

The cutting force comparison methodology is the same as used in the previous chapter. The signals in the trials are divided in each edge pass to determine the representative signal, as shown in figure 4.9. This treatment determines the mean signal and the standard deviation of each trial. The mean signal is then averaged with the mean signal found in the other two repetitions. For example, figure 4.10 shows the mean signal in solid blue with the representative standard deviations in dashed blue lines for the $Vc400f_a3.5f_z0.16e2$ cutting conditions. These results are then compared with the cutting forces obtained from the presented model.
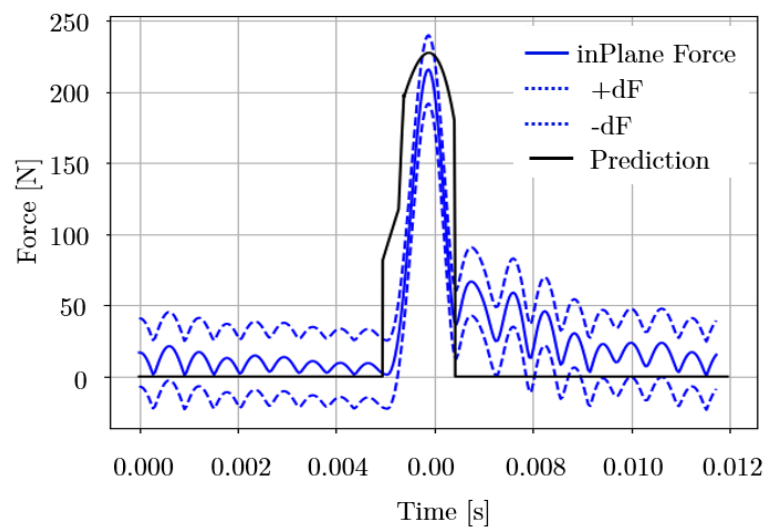
(a) In-plane instantaneous cutting force.
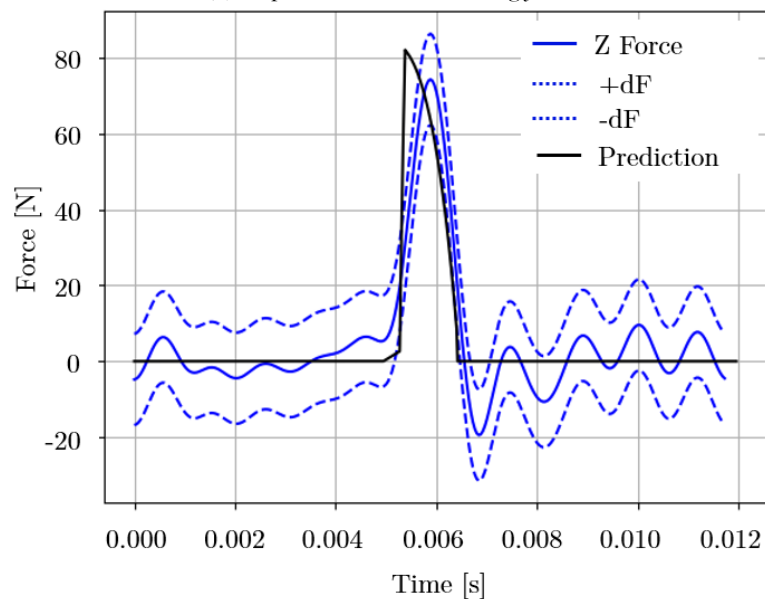
(b) Axial instantaneous cutting force.

Figure 4.10: *Prediction and experimental cutting forces direct comparison ($Vc400f_a3.5f_z0.16e2$).*

The resulting mass predicted from the presented model was in good agree-
ment with the experimental data; the maximum error found from the prediction
is under 2%, see figure 4.11. The chip mass is proportional to the axial feed (f_a)
and the feed per edge (f_z). This comparison clearly shows that the geometrical
model accurately represents the uncut chip geometry and is sensitive to the
cutting condition variations.
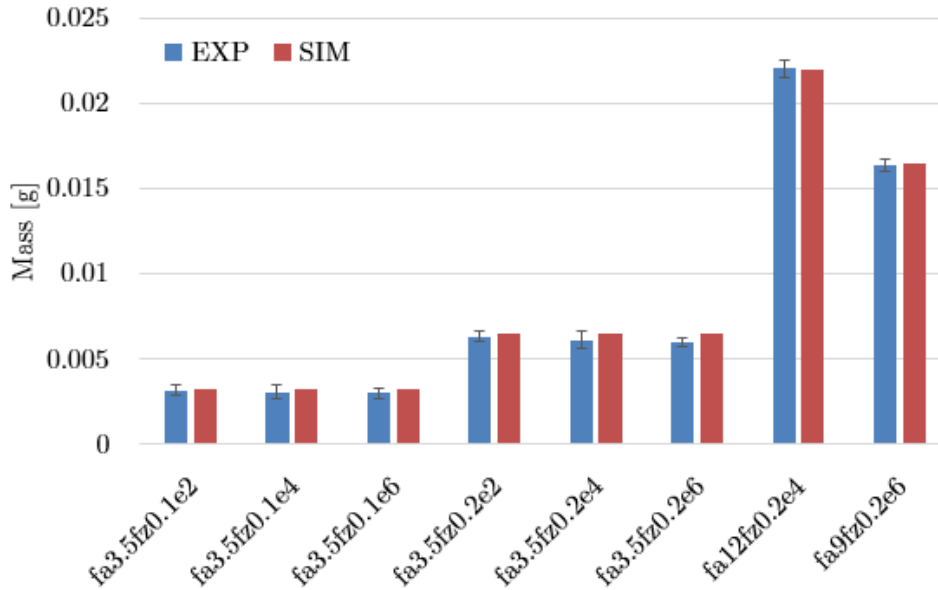
Figure 4.11: *Chip volume comparison experimental vs predicted*

The complete comparison of the experimental plan presented in table 4.2 is
shown in figure 4.12. The peak force is the comparison variable due to, from
the model is possible to establish the dynamic parameters of the signal, and this
variable is the most sensitive to the cutting force parameters. In general terms, the
model is a good representation of the cutting process, presenting good agreement
with the experimental data. The error presented in the comparison is below 15%.
The model seems sensitive to the axial feed f_a and the feed per tooth f_z. The
effect of the eccentricity in the force is not quite sensitive for the force in-plane.
However, the reduction in the axial force was observed as expected for the end
cutting zone reduction.

In summary, the eccentricity effect modifies the instantaneous depth of cut of
the flank zone, and consequently, the end zone trends decrease as the eccentricity
augments. This impacts the axial force exerted on the cutting tool, reducing it
when the eccentricity is increased. However, the in-plane does not seems to
present a relevant change with the eccentricity even when the flank height is
instantaneously higher. The reduction in the end zone is compensated with the
increment on the depth of cut in the flank zone, maintaining the in-plane force
relatively stable.
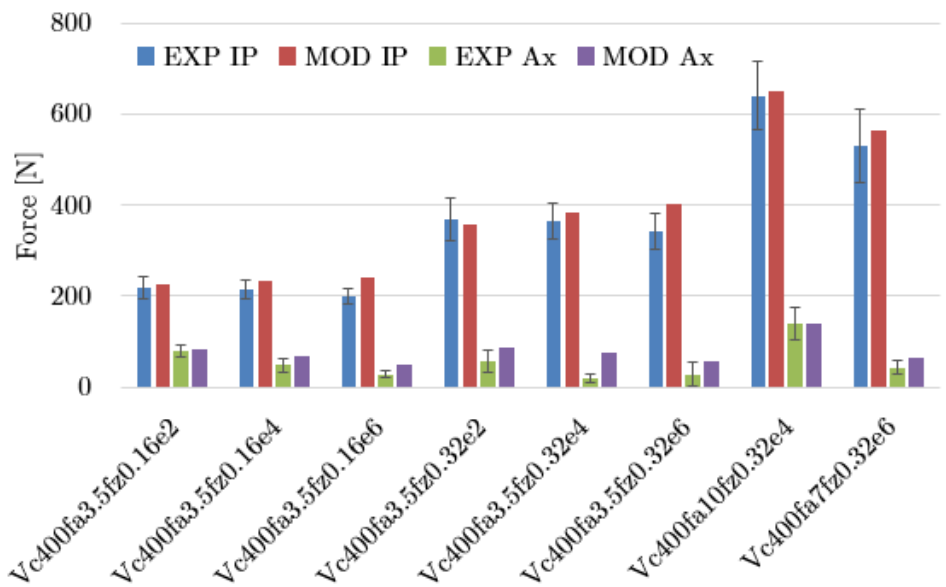
Figure 4.12: *Theoretical vs experimental cutting forces results. (IP In-plane resultant forces. Ax: Axial force).*

4.5   Conclusions

In this study, analytical models are presented to predict cutting forces of the machining process. Mathematical expressions for the boundary lines of the uncut chip geometry in 3D are determined. Depending on the cutting parameters. From the boundary lines, the instantaneous thickness and contact length of the flank and end zone can be found respectively. The following conclusions can be drawn:

1. A novel approach to calculate the instantaneous uncut chip geometry for orthogonal eccentric turn-milling operations was proposed. The wide range of cutting conditions used for the virtual and experimental trials showed that the analytical models were robust and reliable. The cutting parameters are different from those in conventional milling and turning and the model helps to understand the effect of the parameters on the machining process.

2. The eccentricity modifies the uncut chip geometry and the chip volume considerably, reducing the end cutting zone and affecting the variable depth of cut of the flank zone. The eccentricity modifies the chip volume presenting a maximum value that does not fulfill the relationship $e_{opt} = r_t - l_s$. The simulated edge length (l_s) was always equal to the tool radius (r_t), resulting in the centric case as the optimum scenario, but the simulated data showed this conjecture is false.

3. The analytical approaches accurately represented the uncut chip geometry. Errors below 2% were obtained compared with a CAD reproduction. Additionally, the volume of the collected cut chips corresponded with the prediction.

4. The suggested approach is a quick way to understand the effect of the eccentricity on the uncut chip geometry and more importantly on the cutting forces in diverse operating scenarios. The overall force error was around 15%

and the predictions were in good agreement with the experimental data. The cutting forces did not suggested an optimal behavior with the increment of the eccentricity. The forces in plane followed an slight trend to decrease with eccentricity and the axial force presented a marked decreasing trend caused by the reduced end cutting zone.

5 | Tool profile and eccentricity effect in orthogonal turn-milling operations

The market offers a wide variety of tool profiles such as flat, torus, spherical, or barrel end mills. Additionally, there is a wide offer of indexable insert mills with diverse tool profiles. This feature determines the shape of the uncut chip geometry, mostly the inner and outer chip boundaries. For example, the uncut chip generated from a flat end mill is not the same as that got from a spherical nose mill, even with the same cutting conditions. Based on this, the tool profile shape, together with the instantaneous chip section is fundamental to predict the cutting forces accurately in any machining operation, and turn-milling is not the exception. With this in mind, it is essential to model the geometry of the tool in turn-milling.

5.1 Tool profile modeling

The modeling process starts simplifying the mill geometry just to the profile the mill presents when it is rotating in the machine tool, momentarily neglecting the specific parameters of the tool such as the number of teeth, helix angle, etc. The bi-dimensional profile of the tool is revolved, and it results in the 3D mill geometry. If the $X - Z$ plane is selected to define the bi-dimensional profile, mathematical expressions can be stated to follow the profile geometry. These expressions could be even piecewise functions because all of the expressions have the same independent variable X. In this specific scenario, the volume of the mill is defined with the rotated profiles around the Z axis in a full turn. It is proposed that the main domain of the profile is saved in the $\overline{x_t}$ variating between zero to tool radius (r_t) and is going to be divided in differentials of radius set by the programmer as shown in equation 5.1. Depending on the profile functions, the z coordinate can be calculated point by point and saved in the $\overline{z_t}$ vector, as represented in equation 5.1. Based on the selection of the plane $X - Z$, the Y coordinate is zero, so these values are saved in the vector $\overline{y_t}$, see figure 5.1 A and B. With this information is possible to plot the points in a 3D coordinate system space, where the coordinates of each point (X, Y, Z) are the correspondent in the saved vectors $\overline{x_t}, \overline{y_t}, \overline{z_t}$. For example, the first point should have the following coordinates $(0, 0, f(0))$ and the last point $(r_t, 0, f(r_t))$ based on equation 5.1.

(a) Arbitrary bi-dimensional tool profile   *(b) Rotated profile around the z axis*
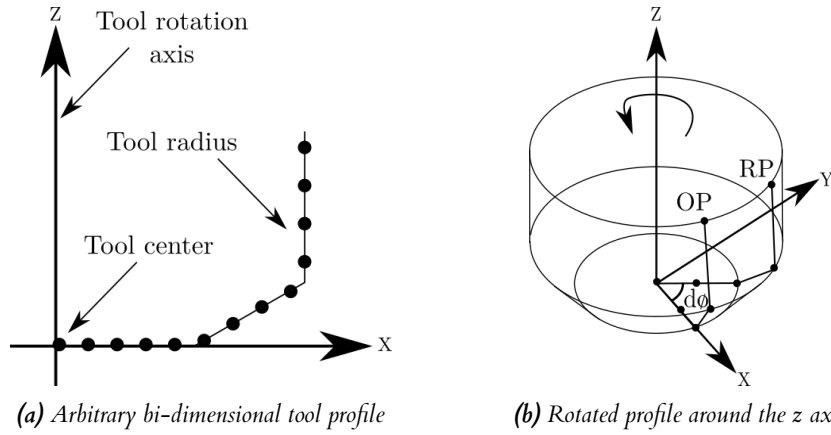
Figure 5.1: *3D Tool profile modeling (OP: Original profile. RP: Rotated profile).*

$$
\begin{aligned}
\overline{x_t} &= [0, x_1, x_2, x_3, ..., r_t] \\
\overline{y_t} &= [0, \quad 0, \quad 0, \quad 0, ..., 0] \\
\overline{z_t} &= [f(0), f(x_1), f(x_2), f(x_3), ..., f(r_t)]
\end{aligned}
\tag{5.1}
$$

If these three vectors are concatenated in a matrix, it is possible to systematically rotate a differential of angle ($d\phi$) around the *z* axis as shown in equation 5.2. Notice the subindex *i* of the angle differential ($d\phi_i$) in the equation; this is because the revolution is expressed like a vector that starts in zero, augmenting in fixed steps until it reaches 2π; the number of steps will define the angular resolution of the mill. Each rotated profile must be saved to built-in the whole mill geometry as presented in figure 5.1 B. This geometry is compound by a set of points in the 3D Cartesian coordinate system.

$$
P_{ti} =
\begin{bmatrix}
\cos(d\phi_i) & -\sin(d\phi_i) & 0 \\
\sin(d\phi_i) & \cos(d\phi_i) & 0 \\
0 & 0 & 1
\end{bmatrix}
[\overline{x_t}, \overline{y_t}, \overline{z_t}]
\tag{5.2}
$$

The tool profile might be complex, and it might not correspond exactly with the shape left in the material; this is due to the whole edge is not supposed to remove material. Indeed, it is expected that only the outer segment of the edge performs the cut, as shown in figure 5.2. Therefore, it is necessary to define the material profile as explained previously, where the point positions are saved in the vectors shown in equation 5.3.

$$
P_{mi} =
\begin{bmatrix}
\cos(d\phi_i) & -\sin(d\phi_i) & 0 \\
\sin(d\phi_i) & \cos(d\phi_i) & 0 \\
0 & 0 & 1
\end{bmatrix}
[\overline{x_m}, \overline{y_m}, \overline{z_m}]
\tag{5.3}
$$

The neglected features of the mill, such as the amount of cutting edges and the helix angle, affect the uncut chip geometry strongly. However, these features are subsequently taken into account.
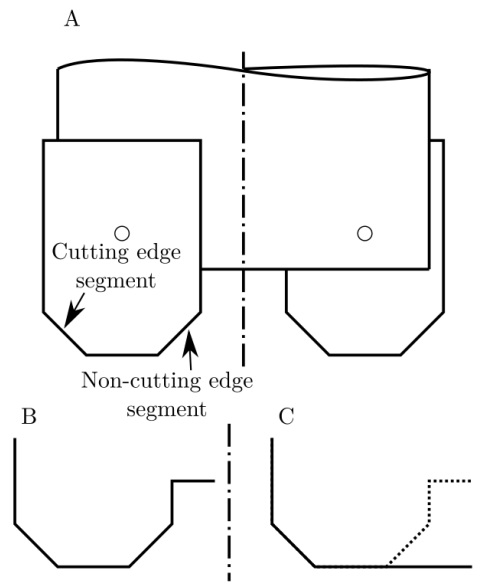
Figure 5.2: *A:Indexable insert tool with arbitrary geometry. B: Tool profile to be rotated. C: Material profile obtained after the pass of the tool.*

5.2   Kinematics in turn–milling operations

The relative movements between the tool and workpiece are also determining in the chip formation process. The rotational movement of the workpiece changes the traditional kinematic variables in milling. The workpiece is considered static while the tool performs the movements. Figure 5.3 shows the kinematic variables that take place in the orthogonal turn–milling process. The thicker arrows represent movements driven by the machine: workpiece rotational speed (n_w), tool rotational speed (n_t), and axial feed (f_a). Then, are the geometrical variables: workpiece radius (R_w), tool radius (r_t), number of cutting flutes (z), and helix angle of the tool (λ). The following are the operative parameters: depth of cut (a_p) and eccentricity (e). Hereinafter, the origins and directions of each one of them: workpiece origin (O_w) with its $X, Y, \& Z$ directions (X_w, Y_w, Z_w) and tool origin (O_t) with its correspondent linear directions (X_t, Y_t, Z_t) as presented in figure 5.3.

   The tool and material profiles explained in the previous section were described from the tool origin. However, the turn–milling movements are studied from the workpiece coordinate framework due to the workpiece is also rotating. Therefore, it is necessary to relate both origins of coordinates between each other, as shown in equation 5.4 and represented in figure 5.3. Therefore, it is possible to translate the material and tool profiles to the cutting position viewed from the workpiece coordinate system.

$$
\begin{aligned}
X_t &= X_w + e \\
Y_t &= Y_w \\
Z_t &= Z_w + (R_w - a_p)
\end{aligned}
\tag{5.4}
$$
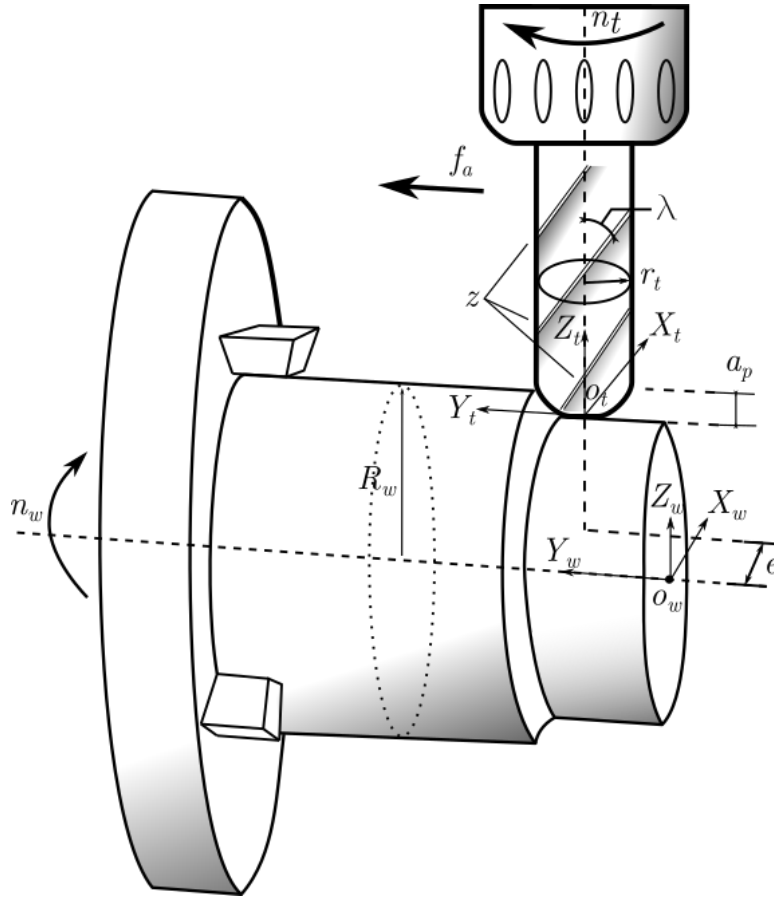
Figure 5.3: *Orthogonal turn-milling kinematics. R_w Workpiece radius, n_w Workpiece rotational speed , r_t Tool radius, n_t Tool rotational speed, f_a Axial feed,a_p Depth of cut, z Number of cutting edges, e Eccentricity, λ Helix angle, O_t Tool origin, X_t Tool x direction, Y_t Tool y direction, Z_t Tool z direction, O_w Workpiece origin, X_w Workpiece x direction, Y_w Workpiece y direction, Z_w Workpiece z direction.*

The approach followed in this research is to define the uncut chip geometry, projecting the material profile points considering the turn-milling movements in one tooth pass and comparing them with the tool profile. Therefore, the kinematic variables of the process are fundamental to set where were translated and rotated the material profile points to the previous tooth pass position. The numerical approach requires the kinematic variable determination, just as presented in the previous two chapters. The only new variable that has not been explained is the axial feed per tooth (f_{at}) shown in equation 5.5.

$$f_{at} = \frac{f_a n_w}{n_t z} \qquad\qquad\qquad (5.5)$$

The relative movements occurring during the turn-milling operation can be associated with the material and toolsets of points. This approach assumes that the linear transformations done to these sets are commutative in the workpiece origin. Additionally, it is supposed that the uncut chip geometry is the volume between the material profile and tool profile; hence the sets of points can represent these

instants by linear transformations of the matrix of points coordinates. Note that the tool geometry on the workpiece origin is considered an instant after the edge has performed the cut. Consequently, the linear transformations performed to the material profile matrix will find the set of points representing the material to be removed.

The workpiece rotation effect is represented as a rotation of the material set of points at a (θ) angle in the cutting position. Hence, the coordinate matrix in the workpiece origin is the scalar product of the material set of points viewed from the workpiece origin with the rotation matrix around the Y_w axis as shown in equation 5.6. The compound effect of the axial feed per tooth (f_{at}) translation and the workpiece per tooth angle (θ) rotation is equivalent to the feed per tooth (f_z), see figure 5.4.

$$[X_m i, Y_m i, Z_m i] = \begin{bmatrix} \cos(\theta) & 0 & \sin(\theta) \\ 0 & 1 & 0 \\ -\sin(\theta) & 0 & \cos(\theta) \end{bmatrix} [X_{mw}, (Y_{mw} - f_{at}), Z_{mw}] \quad (5.6)$$
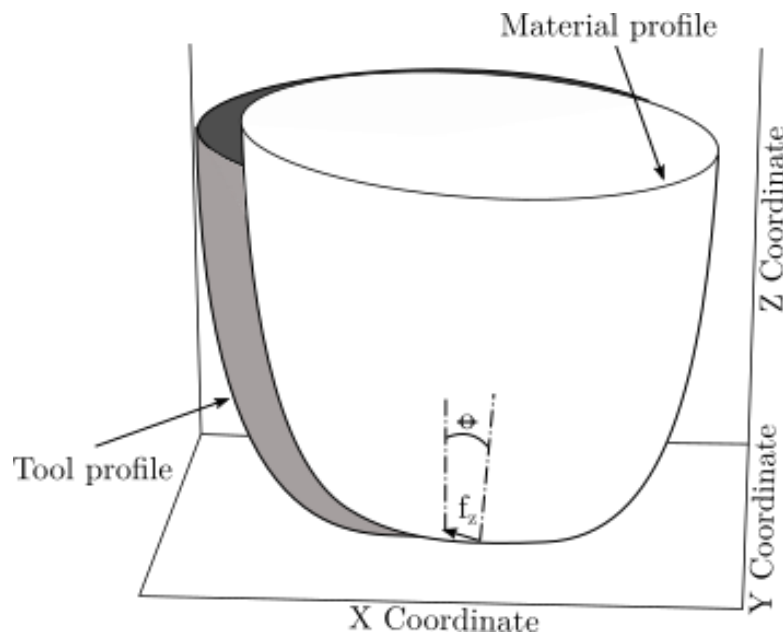
Figure 5.4: *Rotation and translation of the material profile.*

5.3 Determination of instantaneous chip geometry

Both sets of points are in the previous and after cut positions, but they do not represent the uncut chip geometry. Therefore, it is necessary to perform the point interpolation, the invalid point removal processes, and include the tool helix angle effect.

5.3.1   Comparable point interpolation

The challenge is that the profiles are not comparable to find the chip thickness, although all of the points are in the right position. Figure 5.5 presents a tool profile scheme. In black, the tool profile in the $X - Z$ plane, notice the coordinate Y is zero. Additionally, it is represented as a rotation of this profile at a ($d\phi$) angle, shown as the next black line. In solid gray, the material profiles are represented once the workpiece rotation and axial feed movements have been performed.
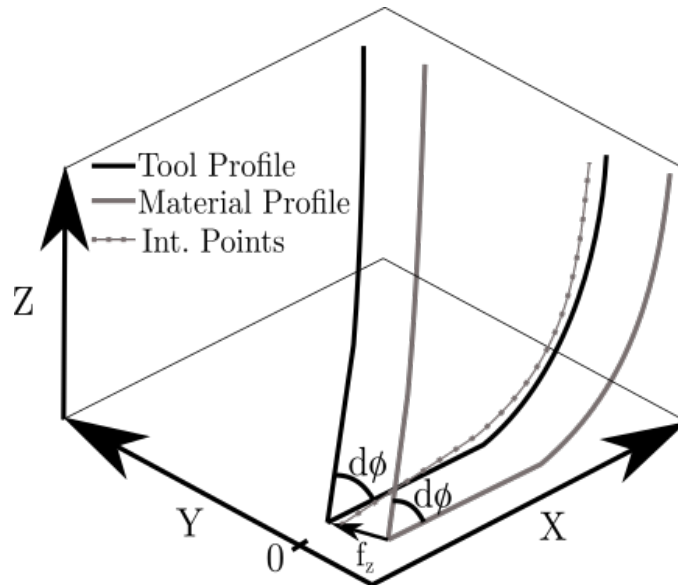
Figure 5.5: *Diagram of some portion of the sets of points of the tool profile, material profile, and material interpolated profile.*

The rotated and translated material profile is not comparable with the tool profile, because the points are not co-planar. However, the material profile contains the complete information to calculate the uncut chip geometry. For this reason, it is necessary to interpolate the points in the same plane of the correspondent profile in the "tool profile" position.

The sets of points were described in a cylindrical coordinate system since the geometry is described in terms of the radius (X coordinate), angle ($d\phi$), and height (Z coordinate). Therefore, if the polar system of the "tool profile" (radius and angle) is used to interpolate the points based on the "material profile" set, it is possible to approximate the height of the points valid to establish the uncut chip geometry. These points are represented in figure 5.5 as the dotted gray line in the coordinate tool system.

The interpolated points share the radial domain of the "material profile interpolated" set. For this reason, the expectable results per each ($d\phi$) are presented in figure 5.6. The interpolation reconstructs the whole geometry of the tool based on the radial and angular coordinates taken from the "tool profile" position. Hence, the interpolated points lie exactly in the same radial coordinate of the after cut position but in a different height of Z.

5.3.2   Selection of feasible points

The feasible point selection is performed by taking into account the material removal zone, the workpiece curvature, and the axial feed effect, which is necessary because the point interpolation process recreated the whole tool geometry. However, the cutting process is performed only with a fraction of this geometry.

Selection of points that represent material

It is crucial to notice that the "Material profile" position defines the boundary where the tool will find material to remove. Therefore, the space below the material interpolated profile represents non removed material, while the space over the tool profile has already been removed. Therefore, all of those points where the "tool profile" is greater than the "material profile" in the Z direction are neglected. This selective process is performed in both "material interpolated and tool" profiles, see figure 5.6.
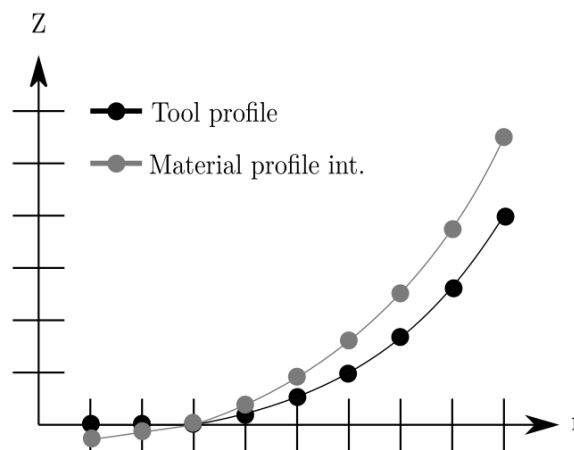
Figure 5.6: Tool profile in position and the material interpolated profile in the same plane.

Effect of the workpiece curvature

Additionally, it is necessary to consider the effect of workpiece curvature. For this reason, all the points above of this curvature are discarded. The points are discriminated based on the following inequality presented in equation 5.7. The expression to the right represents the curvature seen from the tool origin of coordinates. The eccentricity (e) is the distance of separation of the workpiece and tool rotating axes, see figure 5.7.

$$Z_{i,j} > \sqrt{R_w^2 - (X_{i,j} + e)^2} - (Rw - ap) \tag{5.7}$$
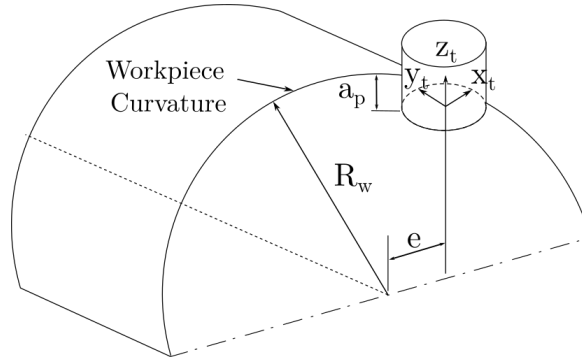
Figure 5.7: Variables in the workpiece curvature effect calculation.

Effect of the axial feed

The axial feed is a significant parameter to describe the uncut chip geometry, as have shown by Zhu et al. (2016b). The axial feed is the parameter that indicates how much distance is covered by the tool in the axial direction by each workpiece rotation. Then, as the tool describes a helical trajectory around the workpiece, the helix pitch corresponds to the axial feed parameter (f_a), as shown in figure 5.8. Here are presented the variables that define the point selection due to the axial feed (f_a) and the axial feed angle (β).
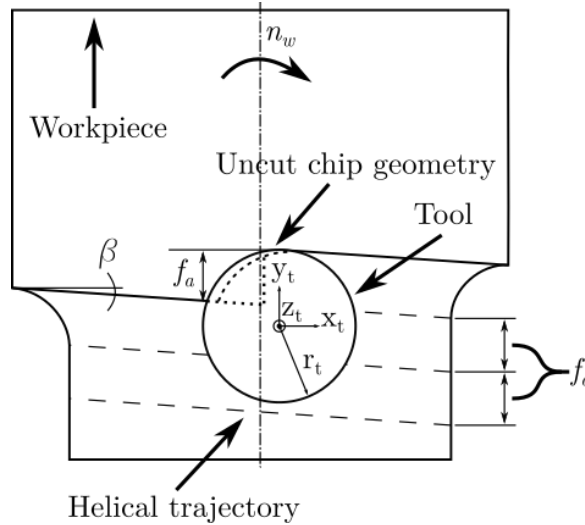
Figure 5.8: Effect of axial feed on the helical trajectory of the tool around the workpiece.

The axial feed is also related to the radial engagement of the tool, determining as well which portion of the mill performs the cut. Therefore, there is a physical boundary line where axis feed angle (β) is indicated in figure 5.8. In this way, the material to be removed is in the (Y_t+) direction starting from this line. Therefore the uncut chip geometry is defined by this boundary. Then, all the points that fulfill the inequality presented in equation 5.8 should be removed.

$$Y_{i,j} \leq \tan(\beta)X_{i,j} + \left(\tan(\beta)\sqrt{rt^2 - (rt - fa)^2} + (rt - fa)\right) \tag{5.8}$$

Closing the uncut chip geometry

Neglecting points of the material and tool profile result in an open geometry with different shapes. It is necessary to add points to the material interpolated profile to close the uncut chip geometry. Figure 5.9 shows an arbitrary plane of the uncut chip geometry where the realistic points are represented as circles. The neglected points are represented with "x" markers, and the added points are represented with triangle markers. The added points are at the same height as the maximum valid point in the material interpolated profile.
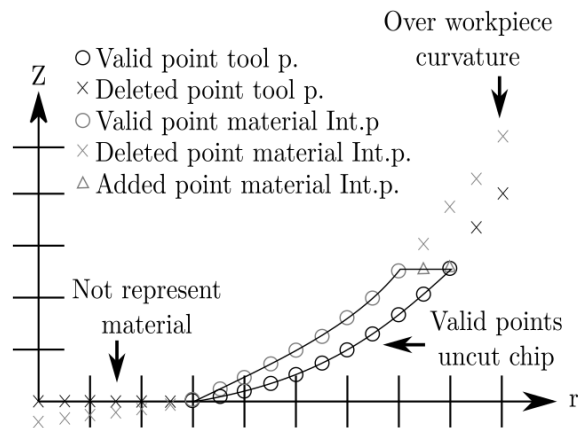
Figure 5.9: Point selection and addition to close the uncut chip geometry.

5.3.3   Effect of the tool helix angle

The tool helix angle (λ) has a strong effect on the cutting forces and the chip forming process. Figure 5.10 shows the helix angle in a flat end mill. This characteristic is also presented in exchangeable insert mills.
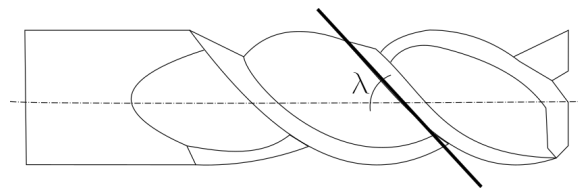
Figure 5.10: Tool helix angle in a flat end mill.

At first sight, the workpiece-tool intersection does not present any change due to the helix angle due to the tool kinematic is not related to this feature. However, it does present an effect on the chip formation process. The cutting edge is rotating around the tool axis; then, the edge tip performs approximately a circular movement during the cutting process, as shown in figure 5.11 (a). Consequently, the material lies on the rake face following the tool helix angle λ. As a result, it is necessary to increase the tool rotation to compensate for the helix angle effect. It is easier to see if the process is unrolled, considering the edge moves linearly but not rotationally. A diagram of this scenario is presented in figure 5.11 (b). So, the edge tip covers an arc segment ($r_t\phi$), and the uncut chip geometry is deformed following the helix angle.

(a) *Chip formation in rotational perspective*

(b) *Chip formation in linear perspective*
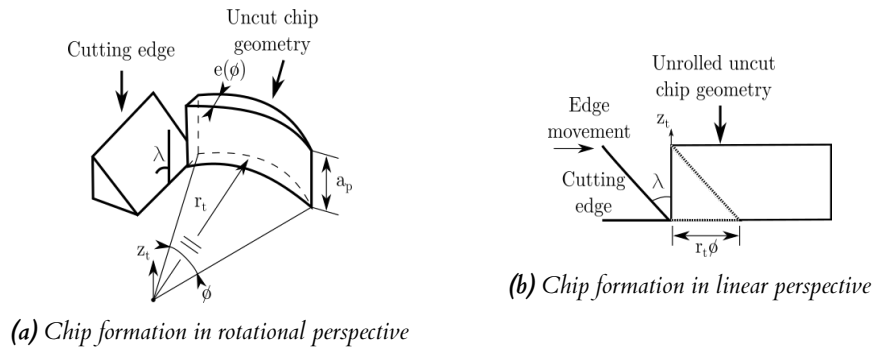
Figure 5.11: *Chip formation process considering the helix angle.*

The geometry can be deformed, adding a phase angle to the points. This phase angle is found by a simple trigonometric expression, assuming the helix angle constant; equation 5.9 shows how to find the phase angle of each profile. Moreover, this phase angle depends on the (Z_t) direction because the rest of the terms are simply constants, which means more height in the profile more phase angle. As the approach is numeric, it is necessary to discretize and introduce it to the points.

$$\phi_{\lambda\{i,j\}} = \frac{Z_{i,j}}{\tan(\lambda)r_t} \tag{5.9}$$

The discretization is done based on the differential of rotation angle ($d\phi$) selected to perform the 2D profile rotation to recreate the tool geometry in the "after cut" position presented in the kinematics section. Equation 5.10 shows how to determine the lag matrix (L) that stores the phase angle information associated to the helix angle. Notice that the values of the matrix belong to the natural numbers. Consequently, they must be integer quotient of the fraction expressed in equation 5.10. This integer matrix shows the number of positions each point has to be phased in the (ϕ) direction.

$$LM_{i,j} = \frac{\phi_{\lambda\{i,j\}} \ d\phi}{2\pi} : \{L_{i,j} \in \mathbb{Z}\} \tag{5.10}$$
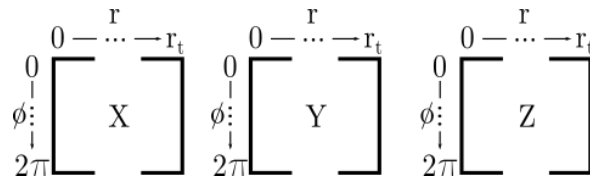
Figure 5.12: *Data structure in the 3D coordinate system.*

The data have a cylindrical coordinate structure separated in the Cartesian coordinates (X, Y, Z) as shown in figure 5.12. In other words, each matrix has the coordinates of the points in its corresponding Cartesian direction. However, the rows of each matrix are associated with the position in the tool radius and

the columns to the angular (ϕ) position around the Z_t axis; which is convenient because the lag matrix L has the exact dimension of the coordinates matrix (X, Y, Z). Consequently, it is possible to relate the number of cells that have to be displaced in the angular direction to deform the geometry. In graphical terms, the displacements of the cells in the angular direction (vertical) within the matrix (X, Y, Z) displace the points generating the effect sketched in figure 5.13.
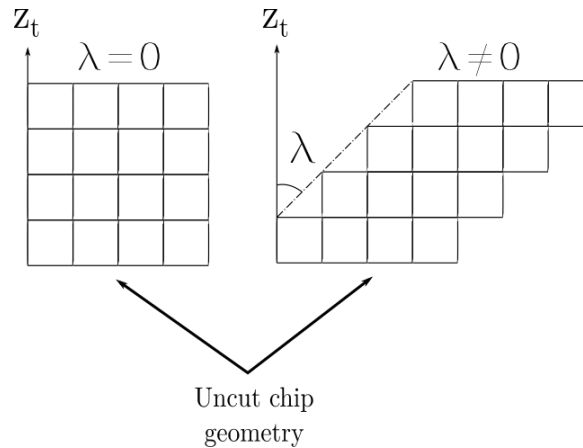
Figure 5.13: *Effect of the helix angle λ over the modeled uncut chip geometry.*

5.3.4   Model implementation in an arbitrary case

As a matter of example, the procedure explained previously is reproduced with the conditions presented in table 5.1. These cutting conditions are not necessarily realistic. They were selected to amplify the workpiece rotations and axial feed to exaggerate the uncut chip geometry and have noticeable graphical results. The idea is to perform simulations through this model with workshop cutting conditions as presented afterward. The radial discretization counts with 100 divisions and the angular with 72 divisions. These values are selected for visualization purposes in order to obtain clear images of the points sets.

Table 5.1: *Arbitrary cutting conditions to recreate the uncut chip geometry.*

Parameter	Symbol	Value	Units
Cutting speed	V_c	297	m/min
Tool radius	r_t	12.5	mm
Tool rotational speed	n_t	3782	rpm
Nose Radius	r_n	6	mm
Workpiece radius	R_w	95	mm
Workpiece rotational speed	n_w	30	rpm
Axial feed	f_a	15	$\frac{mm}{w_{orkpiece}rev}$
Depth of cut	a_p	2	mm
Eccentricity	e	4	mm
Cutting edges	z	2	–
Helix Angle	λ	85	^{o}

The geometry to be analyzed is the torus mill with a nose radius of $r_n = 6mm$ as presented in table 5.1 and figure 5.14 (a). Then, the bi-dimensional tool and materials profiles in the $(X - Z)$ plane are described by the piecewise functions presented in equation 5.11.

$$Z_t(x) = \begin{cases} rn & : 0 \leq x \leq (r_t - r_n) \\ - \quad \sqrt{r_n^2 - (x - (r_t - r_n))^2} + r_n \\ & : (r_t - 2r_n) < x \leq r_t \end{cases}$$

$$Z_m(x) = \begin{cases} 0 & : 0 \leq x \leq (r_t - r_n) \\ - \quad \sqrt{r_n^2 - (x - (r_t - r_n))^2} + r_n \\ & : (r_t - r_n) < x \leq r_t \end{cases}$$

(5.11)

Figure 5.14 (b) shows the resulting profiles in the $(X - Z)$ space, where the Y coordinate is zero for all the points. The profile covers heights from zero to 6 mm. Then, These profiles are rotated around the Z axis, as shown in figure 5.14 (c). After this operation, the tool and material profiles are fully described; however, it is necessary to translate them to the cutting position viewed from the workpiece origin. Notice the effect of the eccentricity in the center of the geometry changes from $(0, 0, 0)$ to $(4, 0, 93)$ in figure 5.14 (d). Additionally, the workpiece radius effect occurs, modifying the Z axis variating from 94 to 98.

With the geometry in this position, it is possible to include the workpiece rotation and the axial feed translation. Figure 5.14 (e) shows a front view of both tool (orange) and material (blue) profiles. Although these surfaces intersect each other, forming the uncut chip geometry, it is impossible to compare them directly. Figure 5.14 (f) illustrates the situation. As the geometry has been displaced and rotated, the resulting material profile (continuous green line) can not be compared with the tool profile (continuous blue line). Therefore, the interpolation of the material geometry is performed, generating an approximation of the profile suitable to carry out the profile comparison (dotted green line). This interpolation is executed to the whole tool geometry, generating the comparable scenario shown in figure 5.14 (g).

It is carried out the selection of feasible points to create the uncut chip geometry due to now there are two comparable geometries. As explained in the previous subsection each profile is compared to the material interpolated with tool profiles, and all of these points where the material interpolated profile has less height than the tool profile are neglected as shows figure 5.14 (h). In this figure, the arrow indicates the limit where the geometry starts to be realistic. After this point, all of the points to the left of this arrow were discarded. As a result of this operation, the geometry is reduced to that presented in figure 5.14 (i). It is then necessary to remove all of the points over the workpiece curvature as presented in figure 5.14 (j). Notice that the maximum Z axis value in figure 5.14 (i) pass from 6 to 1.75 mm in figure 5.14 (j) effect of the workpiece curvature and the eccentricity. The last point selection is performed to introduce the axial feed effect. Figure 5.14 (k) shows the point selection result. Notice the remaining geometry is a portion of that presented in figure 5.14 (i).
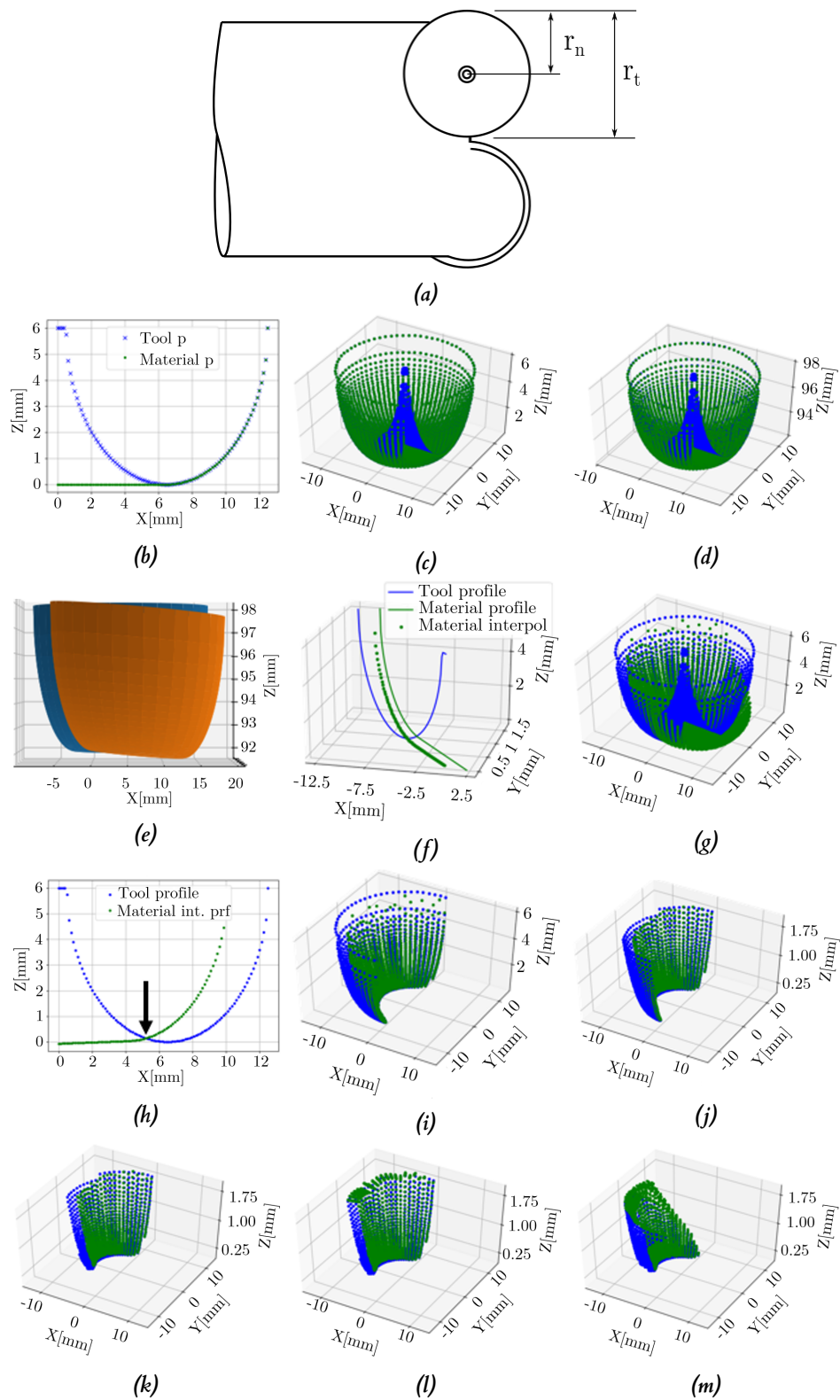
Figure 5.14: (a):tool scheme. (b): 2D tool profile in $X - Z$. (c): Tool geometry generated by the 2D rotation around the Z axis. (d): Tool geometry in the workpiece coordinate system O_w. (e): Previous cut surface (Orange). After cut surface (blue). (f): Random tool profile. After cut (Blue). Previous cut (Green). Interpolated profile (Dotted green). (g): After cut tool geometry (blue). Previous cut interpolated geometry (green). (h): Random tool profile to remove the unrealistic points. (i): Points considered material to remove. (j): Effect of the workpiece curvature. (k): Effect of the axial feed. (l): Uncut chip geometry with augmented angular resolution. (m): effect of the helix angle over the uncut chip geometry.

It is now necessary to close the profiles by adding the points representing the workpiece cylindrical surface. Therefore, figure 5.14 (l) shows green points at the top of the uncut chip geometry closing the profiles. The last manipulation to the geometry performed is the lag associated with the helix angle; considering the significant value of the helix angle, the uncut chip geometry is deformed as presented in figure 5.14 (m). As described previously, the phase or lag increases proportionally with the height of the point in the Z direction.

5.4 Theoretical validation of the uncut chip geometry

The numerical model presented until now needs to be checked to verify if it accurately predicts the uncut chip geometry. Then, the predicted geometry obtained from a Python routine is compared with the geometry obtained by CAD means reproducing the tool geometry and movements in the 3D space with SolidWorks 2017. As the comparison object is another representation of the uncut chip geometry, it is considered as a theoretical validation; in other words, to compare the uncut chip geometry obtained by two different methods. The evolution of the uncut chip area obtained by numerical means and CAD means are compared varying the cutting conditions.Hence, four simulation scenarios were proposed (T1, T2, T3, T4) with arbitrary cutting conditions, as shown in table 5.2. The main reasons to perform this test are that it is necessary to ensure that the movements performed by the tool correspond to the linear transformations performed to the set of points proposed by this approach. Additionally, the direct visual comparison between CAD and Python approaches is a non–conclusive qualitative method considering the visualization differences of the approaches as shown in figure 5.15. From now on, the radial and angular discretization count with 1000 and 720 points, respectively. These mesh values correspond to half-degree values in the angular domain and about 10 microns in the radial direction.

Table 5.2: *Cutting conditions of four validation scenarios (T1-T4). V_c: Cutting speed.r_t: Tool radius. n_t: Tool rotational speed. R_w: Workpiece radius. n_w: Workpiece rot. speed. f_a: Axial feed. f_z: Feed per tooth. a_p: Depth of cut. e: Eccentricity. z: Qty. of cutting edges. r_n: Nose radius.*

Parameter	Unit	T1	T2	T3	T4
V_c	m/min	400	200	300	100
r_t	mm	10	15	8	12
n_t	rpm	6366	2122	5968	1326
R_w	rpm	45	45	45	45
n_w	mm	12	8	8	15
f_a	mm/wrv	12	9	3	15
f_z	mm/tht	0.26	1.06	0.37	1.06
a_p	mm	2	1	1.5	2
e	mm	3	1	5	2
z	–	2	1	1	1
r_n	mm	4	8	2	12

(a) T1

(b) T2

(c) T3

(d) T4
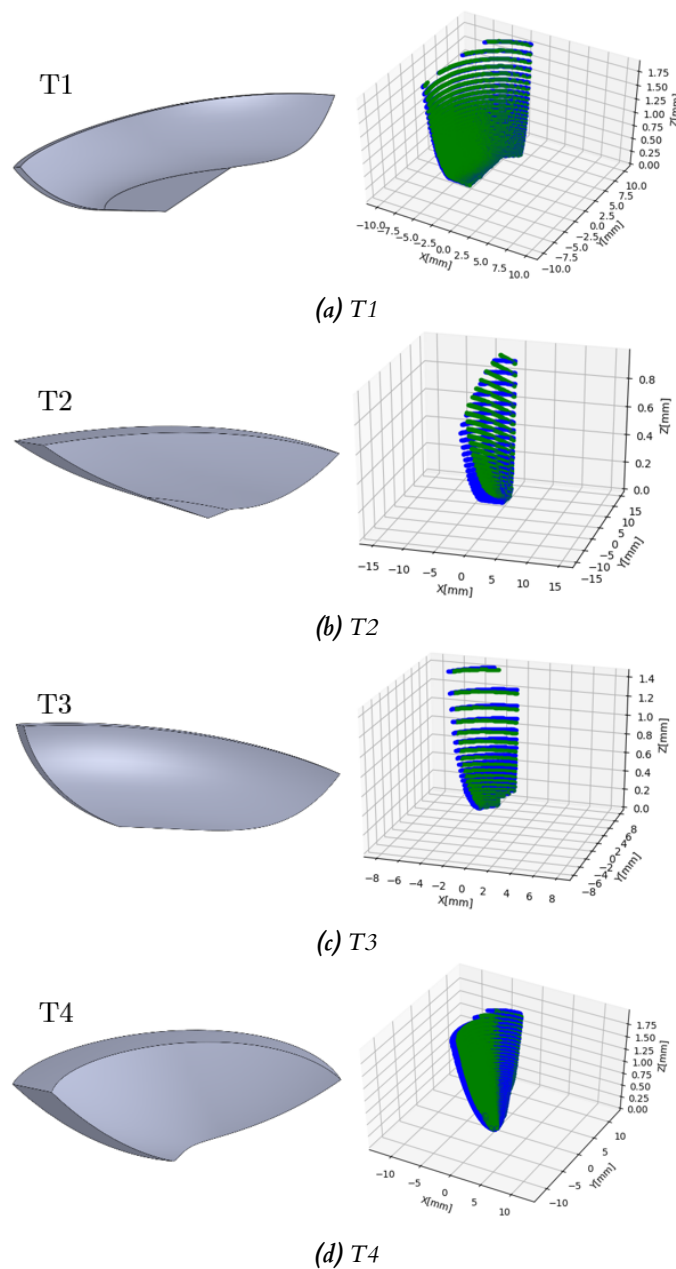
Figure 5.15: *Graphical comparison of the CAD representation versus the results obtained from the numerical approach with the same cutting conditions presented in table 5.2.*

The instantaneous area calculation is based on the profiles that form the uncut chip geometry, see figure 5.16. This geometry is formed by the set of valid profiles, as explained in the determination of the instantaneous chip geometry section. Therefore, each valid pair of profiles (tool & material Int.) generate the instantaneous area. As the tool and material profiles have the same amount of points, it is possible to build quadrilateral elements. The area of each element is found through the Gauss area formula, due each angular profile presents the ordered pair from the points in the radius and height direction (R, Z), see equation 5.12. It is essential to order the element points clockwise to obtain positive magnitudes. Additionally, the first point should be repeated to close

(a) Numerical instantaneous area determination.

(b) CAD instantaneous area determination.
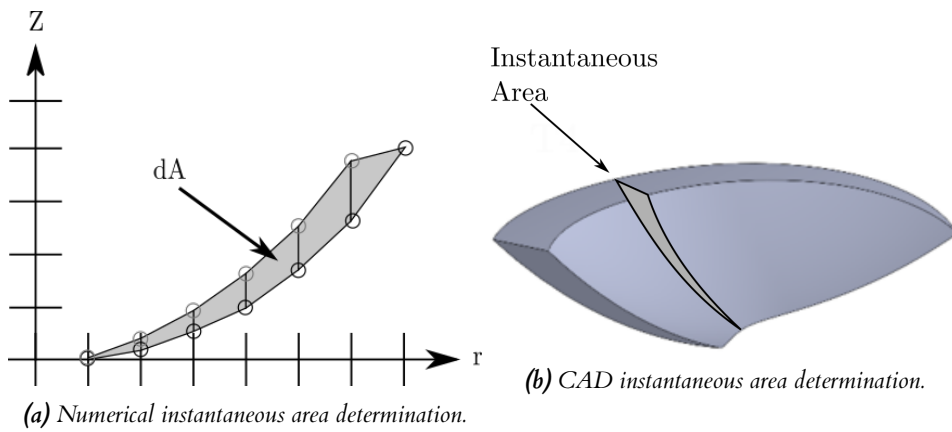
Figure 5.16: Instantaneous area determination in numerical and CAD approaches.

the polygon. The addition of all area differentials in the same cutting plane corresponds to the instantaneous area at some determined angle of rotation of the tool.

$$dA = \frac{1}{2}|\sum_{i=1}^{n-1} R_i Z_{i+1} + R_n Z_1 - \sum_{i=1}^{n-1} R_{i+1} Z_i + R_1 Z_n| \qquad (5.12)$$
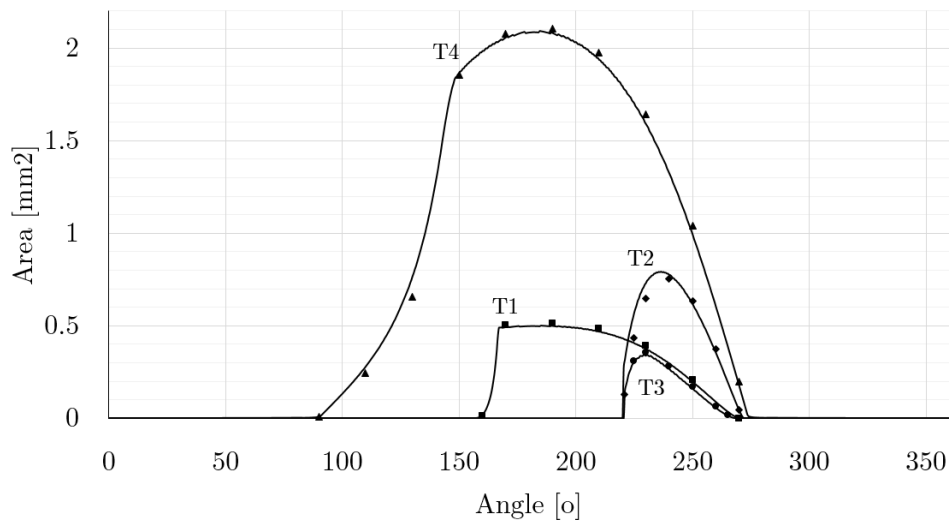
Figure 5.17: Comparison of instantaneous chip area evolution from the numerical approach vs the CAD.

Figure 5.17 shows the behavior of the instantaneous area. For example, the CAD representation of T4 is presented in figure 5.15. From left to right, it is easy to see how rapidly the chip area increases until it reaches the maximum and eventually drops. Besides, a significant portion of the domain is zero, which

means that the edge is not cutting material in this rotation portion. This behavior is presented in all the tests and shows the evolution of the instantaneous area. It is important to remark that the chip thickness is not constant in the Z direction, and the uncut chip geometry follows the workpiece curvature. Therefore, the instantaneous area evolution is the parameter for comparing approaches. The results are in good agreement presenting errors below 3%. These minor discrepancies might be associated with the simplifications assumed in the model.

5.5 Cutting forces prediction

The determination of the uncut chip geometry determines the magnitude and direction of the cutting forces. As the geometrical model discretizes the geometry in finite elements, it is possible to determine the force differential of each element. Those differentials were estimated using the characterization trials methodology. This approach considers that the cutting forces are proportional to the instantaneous area removed by the edge during the rotation. It is important to remark that the differentials of force found by this approach are in the cutting, feed, and penetration directions. These directions are three-dimensional and orthogonal, but they do not necessarily coincide with the cutting forces coordinate system.

5.5.1 Analysis of cutting forces based on uncut chip geometry in milling operations

The characterization trials methodology considers that the cutting forces are proportional to the instantaneous area removed by the edge during the rotation. It is important to remark that the differentials of force found by this approach are in the cutting, feed, and penetration directions. These directions are three-dimensional and orthogonal, but they do not necessarily coincide with the dynamometer coordinate sensor. Indeed, the cutting, feed, and penetration directions are deeply related to the edge geometry, see figure 5.18. In this figure, the (X, Y, Z) coordinate system of the cutting force sensor does not coincide with the tangential, radial and axial direction ($\mathrm{d}Ft$, $\mathrm{d}Fr$, $\mathrm{d}Fa$).

Consider a round insert tool in an arbitrary position removing material, as shown in figure 5.18. It is possible to see the front and side views of the tool performing the cut. Detail A shows how this instantaneous chip geometry is discretized in finite elements and aligned the differential of force with the edge shape. Additionally, detail A shows the uncut chip normal to the rake plane of the mill. However, this plane is not necessarily aligned with the dynamometer coordinate system. In this scheme is rotated the helix angle (λ). Zooming in one finite element, detail B shows the rake plane, the force differentials, and the tangential angle of the edge (κ) concerning the plane $(X - Y)$ from the uncut chip geometry and the force differentials. The cutting direction is normal to the rake plane, inclined the helix angle (λ). Then, there are the feed and penetration directions that are co-planar and orthogonal, completing the orthogonal base described in equation 5.13. The feed direction is perpendicular to the edge instead of the penetration, parallel to the edge. Then, by determining the tangential angle of the edge (κ), the state of force in-plane can be determined.
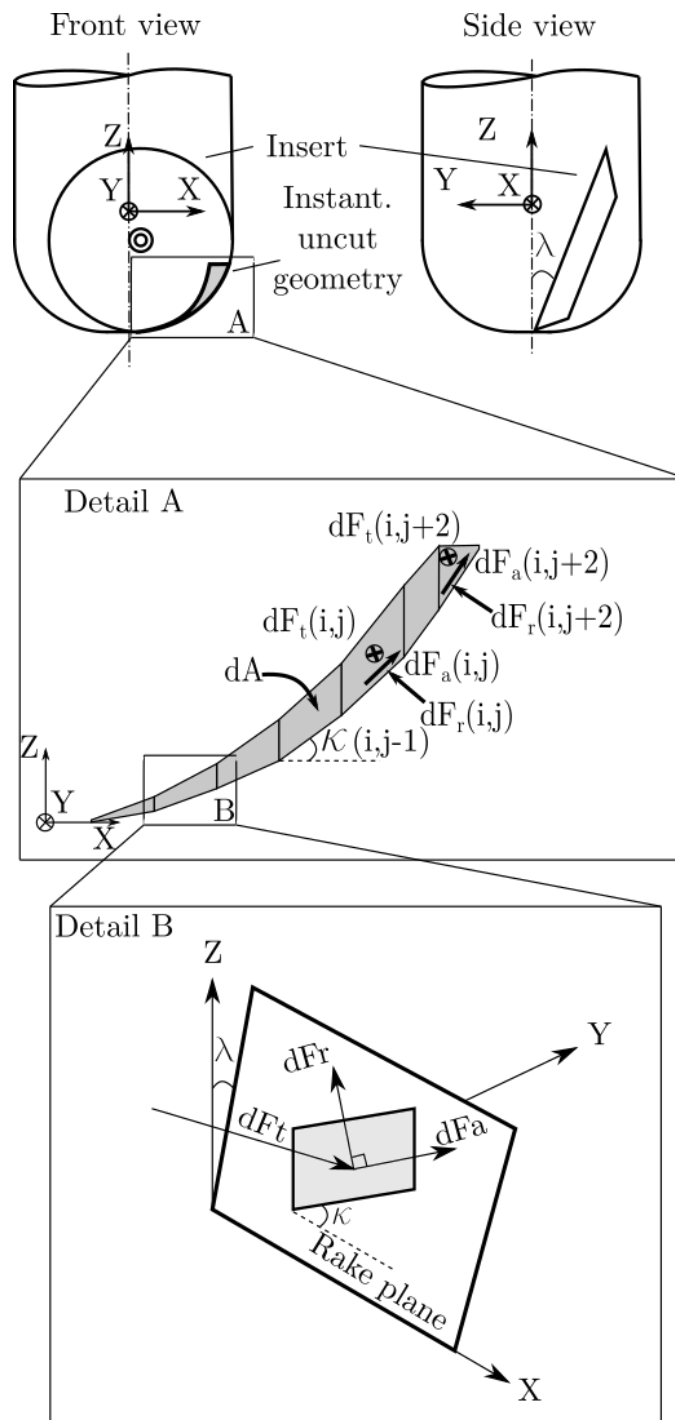
Figure 5.18: *Differential of force per element and geometrical parameters for cutting force prediction.*

Equation 5.13 determines the general state of the forces of each element; however, it is not practical because the element directions are changing with the edge shape and helix angle (λ) as presented in figure 5.18. Therefore, it is necessary to change the coordinates system from the elements(F_r, F_t, F_a) which varies with the edge profile to the dynamometer reference (X, Y, Z) that is sta–

tionary; this is done by projecting the general state of the forces of each element in the dynamometer reference system and summing the components of force, as shown in equation 5.14. Note that the differential of force has a subindex ⋆rf, which means reference edge, see figure 5.19.

$$
\begin{aligned}
\mathrm{d}F_t(\phi) &= K_t \ \mathrm{d}A(\phi, r) \\
\mathrm{d}F_r(\phi) &= K_r \ \mathrm{d}A(\phi, r) \\
\mathrm{d}F_a(\phi) &= K_a \ \mathrm{d}A(\phi, r)
\end{aligned}
\tag{5.13}
$$

$$
\begin{bmatrix}
\mathrm{d}F_{xrf}(\phi) \\
\mathrm{d}F_{yrf}(\phi) \\
\mathrm{d}F_{zrf}(\phi)
\end{bmatrix}
=
\begin{bmatrix}
0 & -\sin(\kappa(i,j)) & \cos(\kappa(i,j)) \\
\cos(\lambda) & \cos(\kappa(i,j))\sin(\lambda) & \sin(\kappa(i,j))\sin(\lambda) \\
-\sin(\lambda) & \cos(\kappa(i,j))\cos(\lambda) & \sin(\kappa(i,j))\cos(\lambda)
\end{bmatrix}
\begin{bmatrix}
\mathrm{d}F_t(\phi) \\
\mathrm{d}F_r(\phi) \\
\mathrm{d}F_a(\phi)
\end{bmatrix}
\tag{5.14}
$$

The reference edge is the one aligned with the X coordinate of the dynamometer in the radial direction and the Y coordinate in the tangential direction of the mill. This important clarification defines the whole state of the forces of the mill. Equation 5.14 allows to predict the magnitude of force of each element in the X ($\mathrm{d}F_x$), Y ($\mathrm{d}F_y$) and Z direction ($\mathrm{d}F_z$). It is required to integrate the forces in the radial direction as shown in equation 5.15. This integration is the force exerted by the material on the reference edge as long as one revolution.

$$
\begin{aligned}
F_{xrf}(\phi) &= \int_0^r \ \mathrm{d}F_x(\phi) \ \mathrm{d}r \\
F_{yrf}(\phi) &= \int_0^r \ \mathrm{d}F_y(\phi) \ \mathrm{d}r \\
F_{zrf}(\phi) &= \int_0^r \ \mathrm{d}F_z(\phi) \ \mathrm{d}r
\end{aligned}
\tag{5.15}
$$

These results also regard the scenario where the cutting edge is aligned with the rotational dynamometer X–axis, also called the reference edge. Then, to determine the cutting force of the rest of the edges is necessary to phase the reference forces $\left(F_{xrf}(\phi), F_{yrf}(\phi), F_{zrf}(\phi)\right)$. For this reason, the phase process considers the angle between the reference edge and the rest of the edges (ϕ_{th}). This phasing consists of rotating the uncut chip geometry around the Z_t axis the angle ϕ_{th} and project the cutting forces over the tool coordinate system as shown in equation 5.16. This process is performed as many as cutting edges have the tool obtaining the phased forces $\left(F_{xph1}, F_{yph1}, F_{zph1}, ..., F_{xphn}, F_{yphn}, F_{zphn}\right)$.

$$
\begin{aligned}
\begin{bmatrix}
F_{phn}(\phi) \\
F_{phn}(\phi) \\
F_{phn}(\phi)
\end{bmatrix}
&=
\begin{bmatrix}
\cos(\phi_{thn}) & \cos(\phi_{thn}) & 0 \\
\sin(\phi_{thn}) & \sin(\phi_{thn}) & 0 \\
0 & 0 & 1
\end{bmatrix}
\begin{bmatrix}
F_{xrf}(\phi) \\
F_{yrf}(\phi) \\
F_{zrf}(\phi)
\end{bmatrix} \\[2mm]
\begin{bmatrix}
F_x(\phi) \\
F_y(\phi) \\
F_z(\phi)
\end{bmatrix}
&=
\begin{bmatrix}
F_{xrf}(\phi) \\
F_{yrf}(\phi) \\
F_{zrf}(\phi)
\end{bmatrix}
+
\begin{bmatrix}
F_{xph1}(\phi) \\
F_{yph1}(\phi) \\
F_{zph1}(\phi)
\end{bmatrix}
+
\begin{bmatrix}
\cdots \\
\cdots \\
\cdots
\end{bmatrix}
+
\begin{bmatrix}
F_{xphn}(\phi) \\
F_{yphn}(\phi) \\
F_{zphn}(\phi)
\end{bmatrix}
\end{aligned}
\tag{5.16}
$$

As a matter of example, consider an end mill with three flutes; see figure 5.19 (a). One of the flute radial edges must be aligned with the X coordinate of the rotational dynamometer. Equations 5.13 to 5.15 estimate the behavior of the force in the 3D direction during the whole tool revolution but only for the reference edge. These force estimations are the reference signals ($F_{xfr}, F_{yfr}, F_{zfr}$) and depend on the tool rotation. Then, these same signals but phased the angle ϕ_{thn} by equation 5.16 results in the general tool state of force as shown in figure 5.19 (b).
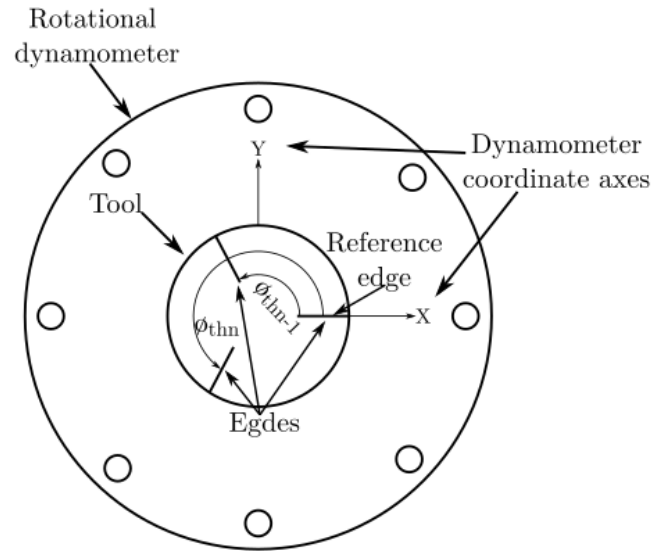
(a) Suggested set up Tool–dynamometer.
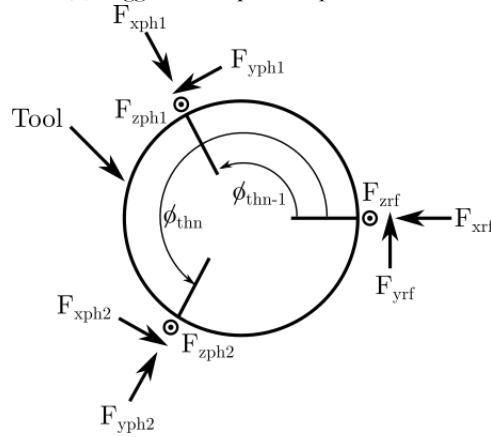
(b) Cutting forces in the reference and the remaining edges.

Figure 5.19: *General state of forces in the rotational dynamometer.*

5.5.2 Specific force coefficients determination methodology

The previous paragraphs have described detailed how to find the general force state of the tool within a revolution. Therefore, the only detail remaining to complete the force prediction is determining the specific force coefficients, based on the mechanistic methodology Orra and Choudhury (2018). In general terms, it is considered that the force is proportional to the instantaneous area Orra and

Choudhury (2018); Zheng et al. (1996). The specific force is the ratio between the force and the instant area. Based on this, face milling characterization trials determine the behavior of the tool-material set. In these trials, the feed per tooth (f_z) is the independent variable, and the forces in the dynamometer coordinate system are the dependent variable.

In groove milling the maximum area instant corresponds to that shown in figure 5.20 (b), indistinct of the tool profile. Additionally, consider to rewrite equation 5.14 as presented in equation 5.17. Figure 5.20 (a) shows the maximum area where it can be stated an expression for the the area differential (dA) as presented in equation 5.18. Replacing dA from equation 5.18 in equation 5.17 results in equation 5.19. Reorganizing the terms is built equation 5.20. Based on the assumption that the equation 5.18 is valid in the maximum chip thickness of the mill rotation in a groove operation, integrating the force differentials is equal to the maximum cutting forces measured from experimental trials. The integration range is related to the κ angle. The grooving case starts in zero and finishes in κ_m, which is the maximum value of inclination presented by the uncut chip geometry as presented in equation 5.21 (see figure 5.20). The result of the integration evaluated in the defined range is presented in equation 5.22; this set of equations determines a linear system in which the only unknown variables are the specific force coefficients. As a result of solving this linear system, finding the cutting coefficients for a specific trial is possible.
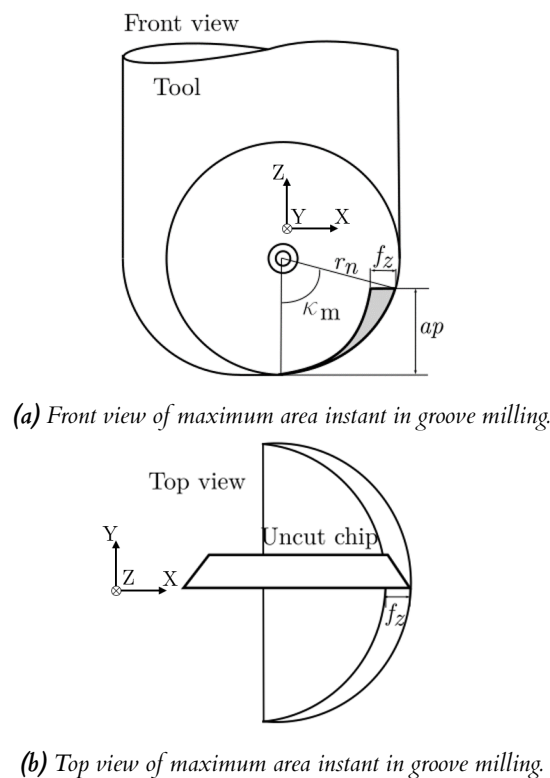

(a) *Front view of maximum area instant in groove milling.*

(b) *Top view of maximum area instant in groove milling.*

Figure 5.20: *Maximum force instant in grooving for specific force coefficients determination.*

$$\mathrm{d}F_x = K_t 0 - K_r \sin(\kappa) \ \mathrm{d}A + K_a \cos(\kappa) \ \mathrm{d}A$$
$$\mathrm{d}F_y = K_t \cos(\lambda) \ \mathrm{d}A + K_r \sin(\lambda) \cos(\kappa) \ \mathrm{d}A + K_a \sin(\lambda) \sin(\kappa) \ \mathrm{d}A \qquad (5.17)$$
$$\mathrm{d}F_z = -K_t \sin(\lambda) \ \mathrm{d}A + K_r \cos(\lambda) \cos(\kappa) \ \mathrm{d}A + K_a \cos(\lambda) \sin(\kappa) \ \mathrm{d}A$$

$$\mathrm{d}A = f_z r_n \sin(\kappa) \ \mathrm{d}\kappa \qquad (5.18)$$

$$dF_x = -K_r \sin(\kappa)(f_z r_n \sin(\kappa)d\kappa) + K_a \cos(\kappa)(f_z r_n \sin(\kappa)d\kappa)$$
$$dF_y = K_t \cos(\lambda)(f_z r_n \sin(\kappa)d\kappa) + K_r \sin(\lambda)\cos(\kappa)(f_z r_n \sin(\kappa)d\kappa) + \cdots$$
$$\cdots + K_a \sin(\lambda)\sin(\kappa)(f_z r_n \sin(\kappa)d\kappa) \qquad (5.19)$$
$$dF_z = -K_t \sin(\lambda)(f_z r_n \sin(\kappa)d\kappa) + K_r \cos(\lambda)\cos(\kappa)(f_z r_n \sin(\kappa)d\kappa) + \cdots$$
$$\cdots + K_a \cos(\lambda)\sin(\kappa)(f_z r_n \sin(\kappa)d\kappa)$$

$$dF_x = -K_r f_z r_n (\sin^2(\kappa)d\kappa) + K_a f_z r_n (\cos(\kappa)\sin(\kappa)d\kappa)$$
$$dF_y = K_t f_z r_n \cos(\lambda)(\sin(\kappa)d\kappa) + K_r f_z r_n (\sin(\lambda)\sin(\kappa)\cos(\kappa)d\kappa) + \cdots$$
$$\cdots + K_a f_z r_n (\sin(\lambda)\sin^2(\kappa)d\kappa) \qquad (5.20)$$
$$dF_z = -K_t f_z r_n \sin(\lambda)(\sin(\kappa)d\kappa) + K_r f_z r_n (\cos(\lambda)\cos(\kappa)\sin(\kappa)d\kappa) + \cdots$$
$$\cdots + K_a f_z r_n (\cos(\lambda)\sin^2(\kappa)d\kappa)$$

$$Fx = \int dF_x = -\int_0^{\kappa_m} K_r f_z r_n (\sin^2(\kappa)d\kappa) + \int_0^{\kappa_m} K_a f_z r_n (\cos(\kappa)\sin(\kappa)d\kappa)$$
$$Fy = \int dF_y = \int_0^{\kappa_m} K_t f_z r_n \cos(\lambda)(\sin(\kappa)d\kappa) + \int_0^{\kappa_m} K_r f_z r_n (\sin(\lambda)\sin(\kappa)\cos(\kappa)d\kappa) + \cdots$$
$$\cdots + \int_0^{\kappa_m} K_a f_z r_n (\sin(\lambda)\sin^2(\kappa)d\kappa)$$
$$Fz = \int dF_z = \int_0^{\kappa_m} -K_t f_z r_n \sin(\lambda)(\sin(\kappa)d\kappa) + \int_0^{\kappa_m} K_r f_z r_n (\cos(\lambda)\cos(\kappa)\sin(\kappa)d\kappa) + \cdots$$
$$\cdots + \int_0^{\kappa_m} K_a f_z r_n (\cos(\lambda)\sin^2(\kappa)d\kappa)$$
$$(5.21)$$

$$F_x = -K_r f_z r_n \left(\frac{k_m}{2} - \frac{\sin(2\kappa_m)}{4}\right) + K_a f_z r_n \left(\frac{\sin^2(k_m)}{2}\right)$$
$$F_y = K_t f_z r_n \cos(\lambda)(1 - \cos(\kappa_m)) + K_r f_z r_n \sin(\lambda)\left(\frac{\sin^2(k_m)}{2}\right) + \cdots$$
$$\cdots + K_a f_z r_n \sin(\lambda)\left(\frac{k_m}{2} - \frac{\sin(2\kappa_m)}{4}\right) \qquad (5.22)$$
$$F_z = -K_t f_z r_n \sin(\lambda)(1 - \cos(\kappa_m)) + K_r f_z r_n \cos(\lambda)\left(\frac{\sin^2(k_m)}{2}\right) + \cdots$$
$$\cdots + K_a f_z r_n \cos(\lambda)\left(\frac{k_m}{2} - \frac{\sin(2\kappa_m)}{4}\right)$$

5.5.3 Specific force coefficients estimation

With a set of trials incrementing the feed per tooth, it is possible to determine the cutting coefficients in terms of the mean chip thickness to generalize the cutting force prediction model presented in equation 5.16. The characterization trials were conducted in a vertical mill. The cutting tools selected to machine the aluminum 6063T5 samples consisted of a Sandvik exchangeable insert mill R300-15T08-07L with the helix angle ($\lambda = 0^o$) and round inserts R300-0724E-PM 1130 with nose radius ($r_n = 3.5$) mm for the torus profile. In the case of the spherical profile, an R216-16T08 indexable insert mill with the helix angle ($\lambda = -10^o$) and R216-16 03 E-M 1025 inserts with nose radius ($r_n = 8$) mm, see figure 5.21. The forces were captured by a Kistler rotational dynamometer 9123. Face milling trials were performed at the cutting conditions presented in table 5.3. The peak of the force was taken after filter the signal with a low pass, cutoff 500 Hz, and order 2 to attenuate the sensor dynamic response. The typical results of the filtering are shown in figure 5.22; as a result the whole results of the characterization trials in table 5.4. Three repetitions of each trial were carried out to ensure statistical representativeness.
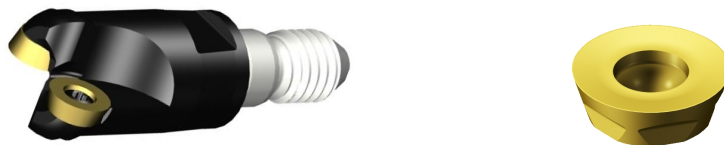
(a) Indexable mill R300-15T08-07L (Sandvik, 2021).

(b) Insert R300-0724E-PM 1125 (Sandvik, 2021).

(c) Indexable mill R216-16T08 (Sandvik, 2021).

(d) Insert R216-16 03 E-M 1025 (Sandvik, 2021).

Figure 5.21: Experimental setup and tools used to validate the model.

Table 5.3: Cutting parameters for specific force coefficient determination.

Parameter	Symbol	Value	Units
Cutting speed	V_c	400	m/min
Depth of cut	a_p	2	mm
Width of pass	a_e	full width	–
Feed per tooth	f_z	0.025 – 0.05 – 0.1 – 0.175 – 0.2	mm/tooth
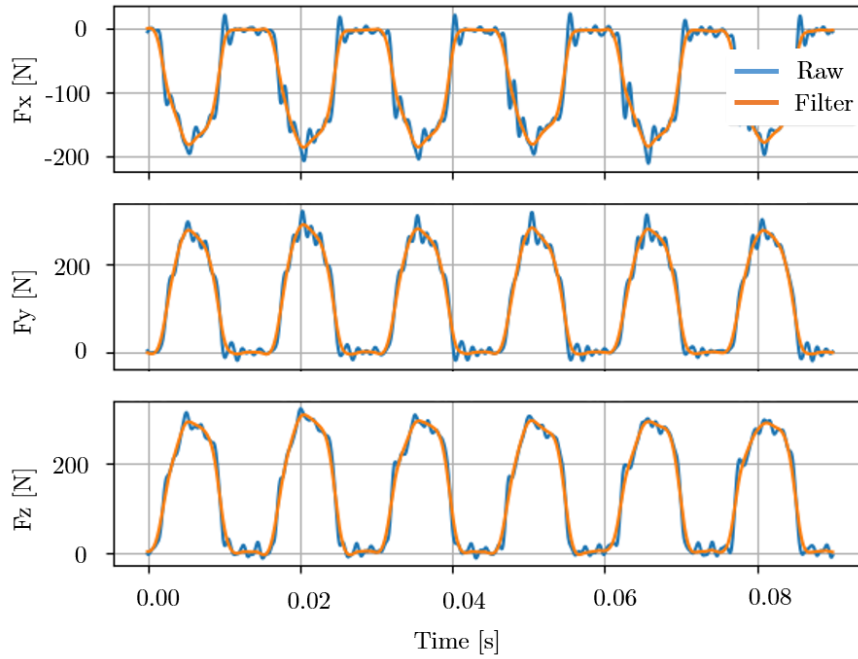
Figure 5.22: *Cutting forces of face milling trial f_z : 0.025 mm/tooth with R216-16T08 spherical insert mill.*

Table 5.4: *Cutting forces characterization trials*

f_z [mm]	F_{xmax} [N]	F_{ymax} [N]	F_{zmax} [N]
Torus Mill			
0.025	–58.44	87.73	73.67
0.05	–85.64	134.03	103.53
0.1	–121.44	207.63	147.04
0.15	–144.65	244.40	171.69
0.2	–160.55	296.92	189.78
Spherical Mill			
0.025	–169.92	267.33	271.91
0.05	–235.39	394.52	371.38
0.1	–346.66	600.73	547.41
0.15	–432.61	778.53	694.15
0.2	–469.59	887.14	771.92

With the insert profile, it is possible to reproduce the uncut chip geometry during the grooving at the point of maximum force. Solving the equation system presented in equation 5.22 for each trial is possible to find the value of the ordinate showed in figure 5.23 and the abscissa values are the mean chip thickness of each trial. The most important feature is that this dataset is adjusted to power functions that have only the chip thickness as the independent variable; which means that using these expressions and inserting the chip thickness of each element is possible to find the magnitude of the specific force coefficient as shows equation 5.23. The modeling expressions complete the cutting force model presented in equations 5.13 to 5.15.
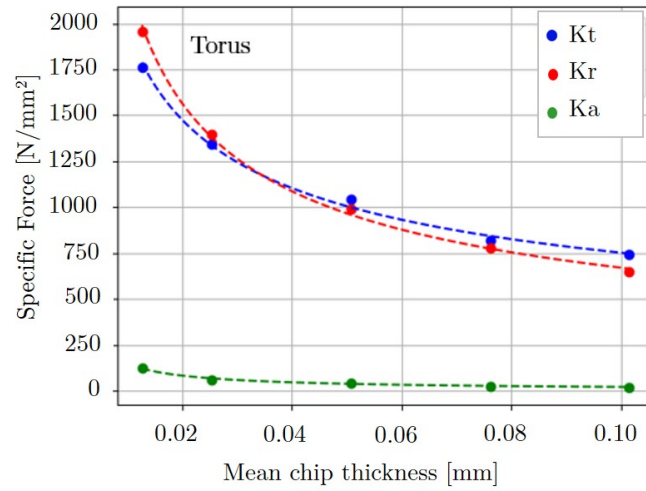
(a) *Torus R300-15T08-07L mill cutting coefficients.*
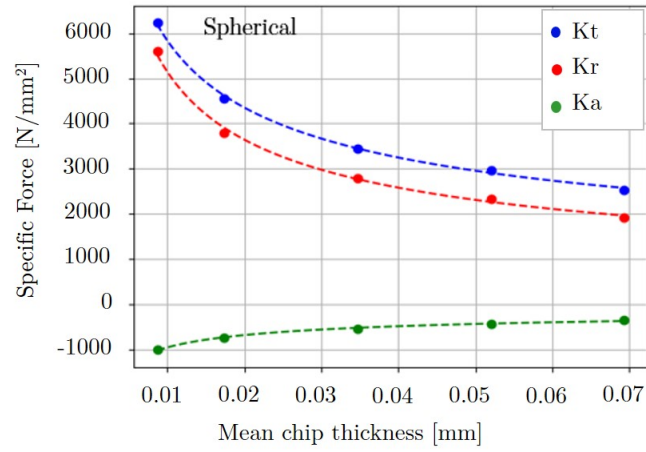
(b) *Spherical R216-16T08 mill cutting coefficients.*

Figure 5.23: *Specific Force coefficient in the cutting, feed and penetration directions.*

Torus mill

$$K_a = 3.36(t(r,\phi))^{-0.822}) \left[\frac{N}{mm^2}\right]$$

$$K_t = 199.69(t(r,\phi)^{-0.526}) \left[\frac{N}{mm^2}\right]$$

$$K_r = 286.94(t(r,\phi)^{-0.418}) \left[\frac{N}{mm^2}\right]$$

Spherical mill

$$K_a = -104.20(t(r,\phi))^{-0.482}) \left[\frac{N}{mm^2}\right]$$

$$K_t = 830.71(t(r,\phi)^{-0.423}) \left[\frac{N}{mm^2}\right]$$

$$K_r = 518.19(t(r,\phi)^{-0.498}) \left[\frac{N}{mm^2}\right]$$

(5.23)

5.6 Experimental validation of the model

The model to estimate the cutting forces has been completely defined in the previous sections. Therefore, it requires experimental validation, consisting of running a set of cutting trials. Varying some cutting conditions and then comparing the resulting chip weight and cutting forces with the predictions obtained by this research model.

5.6.1 Methodology

The cutting trials were carried out in a Lagun vertical milling center. The cutting tools, inserts, and material used were detailed in the characterization trials section previously exposed. The experimental setup counted with a rotary table to hold the workpiece as shown in figure 5.21. Consequently, the cutting conditions presented in table 5.5 are proposed to validate the model developed. These conditions were selected to evidence the change in the uncut chip geometry with the cutting conditions. Additionally, the effect of the eccentricity in orthogonal turn–milling is also considered. It was intended not to exceed the suggestions of chip load given by the tool manufacturer using the developed models. The experiment uses the torus and spherical mill characterized in the previous section, see figure 5.21. The cutting conditions selected explore the effect of varying the chip geometry with two feed per tooth levels (f_z) and three levels of axial feed (f_a). Additionally, the eccentricity values selected were lower, in the "optimum eccentricity" value ($e = r_t - l_s$), and greater of this value for as reported by Karaguzel et al. (2014). The cutting forces of the trials were measured by a Kistler 9123 rotational dynamometer with 25 kHz of sampling frequency. The chips weights were determined using a high precision scale with a minimum measure of 0.1 *mg*. Sets of five, ten, and twelve chips were weight and averaged to determine the mean chip mass. Each cutting condition was repeated three times to ensure statistical representativeness.
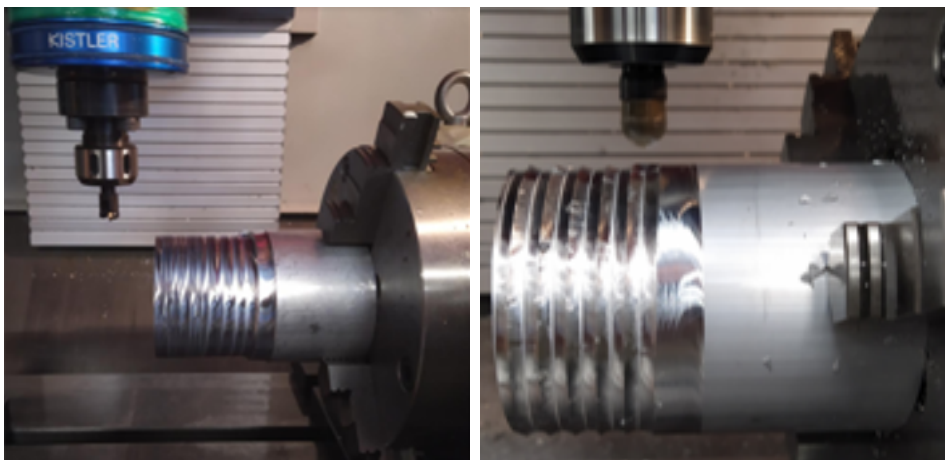
(a) Experimental setup for torus mill.   *(b) Experimental setup for spherical mill.*

Figure 5.24: *Experimental setup and tools used to validate the model.*

Table 5.5: Experimental parameters for model validation.

Rw [mm]	rt [mm]	z [-]	a_p [mm]	V_c [$\frac{m}{min}$]
44	7.5	1	2	400

Torus Mill				
Tag	f_z [$\frac{mm}{th}$]	e [mm]	f_a [$\frac{mm}{W_p rev}$]	n_w [rpm]	MRR [$\frac{cm^3}{min}$]
---	---	---	---	---	---
fa3.5fz0.1e20.1	2	3.5	3	5.94
fa3.5fz0.1e40.1	4	3.5	3	5.94
fa3.5fz0.1e60.1	6	3.5	3	5.94
fa3.5fz0.2e20.2	2	3.5	6	11.88
fa3.5fz0.2e40.2	4	3.5	6	11.88
fa3.5fz0.2e60.2	6	3.5	6	11.88
fa12fz0.2e4	0.2	4	12	6	40.74
fa9fz0.2e6	0.2	6	9	6	30.56

Spherical Mill				
fa8fz0.1e2	0.1	2	8	3	13.5
fa8fz0.1e4	0.1	4	8	3	13.5
fa8fz0.1e6	0.1	6	8	3	13.5
fa8fz0.2e2	0.2	2	8	6	27
fa8fz0.2e4	0.2	4	8	6	27
fa8fz0.2e6	0.2	6	8	6	27

5.6.2 Results and discussion

The chip mass results are shown in figure 5.25 for both tool geometries. The mass presents a thigh fitting between the theoretical value obtained through the model. The mean error is close to 3.5%; the minor discrepancies may be related to the mass loss of the collected chips for their impact on the surroundings during the cutting process. The effect of increasing eccentricity is a slight decrease in the overall chip mass, suggesting that the eccentricity does affect the material removal rate. The presented mass changes support the idea that the eccentricity modifies the uncut chip geometry. Although the differences are slight, the effect of eccentricity should not be discarded because, in larger diameter mills, the mass change might be more pronounced.

Additionally, the feed per tooth (f_z) response agreed with the expectation. An augment of the double of the mass could be appreciated in both simulation and experimental data. Interestingly, the decrement of mass resulting from the eccentricity is presented in both feed per tooth levels ($f_z = 0.1$ and $0.2\ mm/tooth$). The axial feed effect for the torus mill (f_a) behaved as expected by the model, increasing considerably with the increment of this parameter, strongly affecting the material removal rate (MRR).

From the cutting conditions proposed in the experimental plan shown in table 5.5, the typical force signals obtained are similar to those shown in figure 5.26. The cutting force presents a dynamic and repetitive behavior as expected; this is due to the intermittent cutting proper from milling operations. The maximum peak frequency coincides with the rotational tool speed. The raw

signal's dynamic response is strongly influenced by the dynamic parameters of the rotational dynamometer in the $(X - Y)$ plane. The forces in this plane are added as vectors generating the InPlane (IP) force. The reimaing force lies on the Z direction and coincides with the tool axis, then is called axial (AX) force. The dynamical behavior might difficult the study of the forces; then, it is recommended to pass a butter low pass filter with 500 Hz of cutoff frequency and order 2 to mitigate the dynamic response of the sensor.

(a) Torus mill.

(b) Spherical mill.
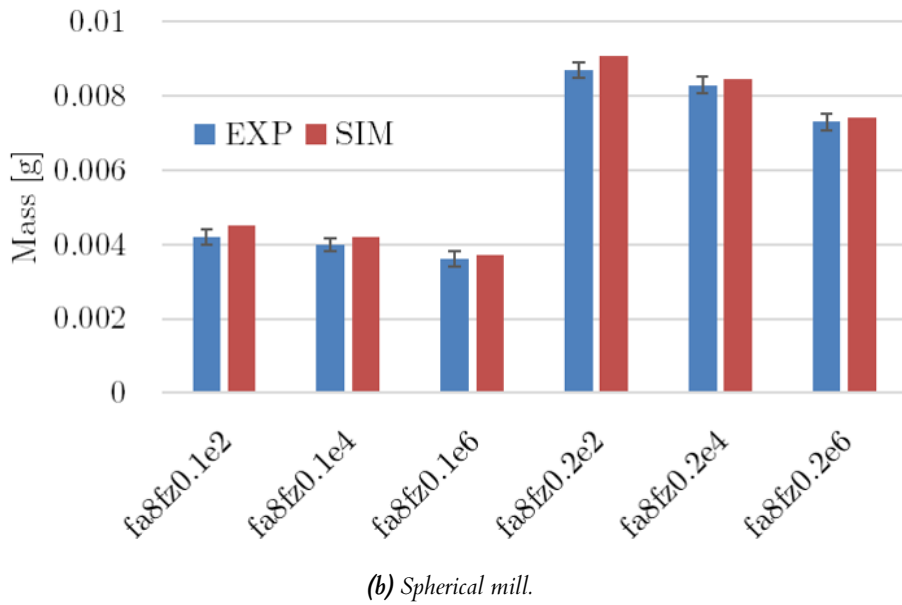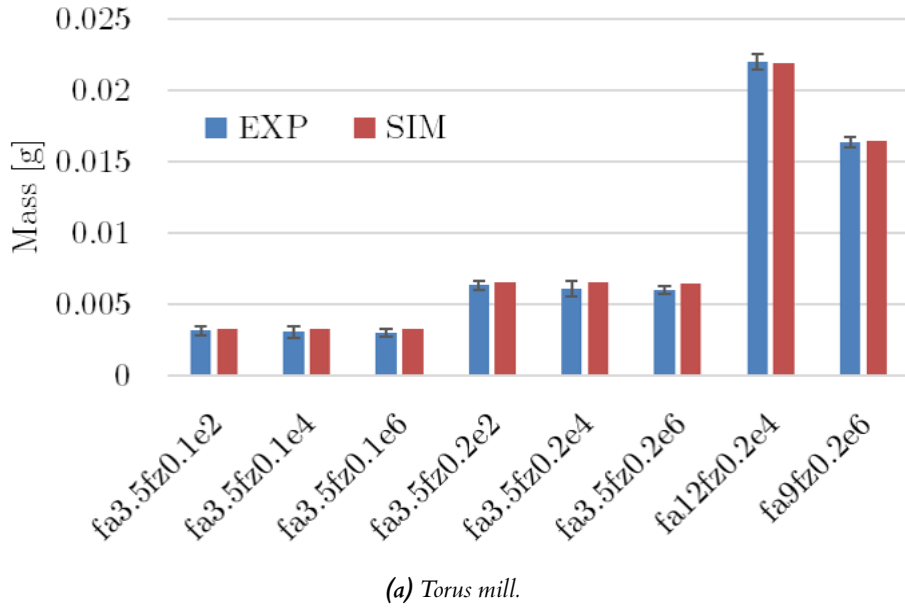
Figure 5.25: *Cut chip mass compared with uncut chip mass.*

(a) Torus mill f_a : 3.5, f_z : 0.2, e : 2.

(b) Spherical mill f_a : 8, f_z : 0.1, e : 2.

Figure 5.26: *Cutting forces in the time domain.*

The intermittent cutting presents an oscillating behavior where the force signal is proportional to the area during the cut and is zero when the edge has exceeded the exit angle completing the rotation. The cutting forces influence the workpiece deformation, the surface integrity, and the tool wear; thus, it is important to compare the maximum peak of the signal to validate the model

and compare the cutting strategies. Therefore, figure 5.27 shows the complete experimental plan comparison. The cutting forces show a slight decrease when the eccentricity is augmented. This behavior correlates with the mass results, explaining the force reduction. The feed per tooth (f_z) has presented increments in the force as expected. Additionally, the model accurately determines the behavior of the forces when the axial feed is augmented. In general terms, the simulations fit tightly with the experimental data presenting errors around 12% for the InPlane (IP) and axial (AX) directions. The mass variation concerning the eccentricity evidence that this parameter slightly modifies the material removal rate (*MRR*).
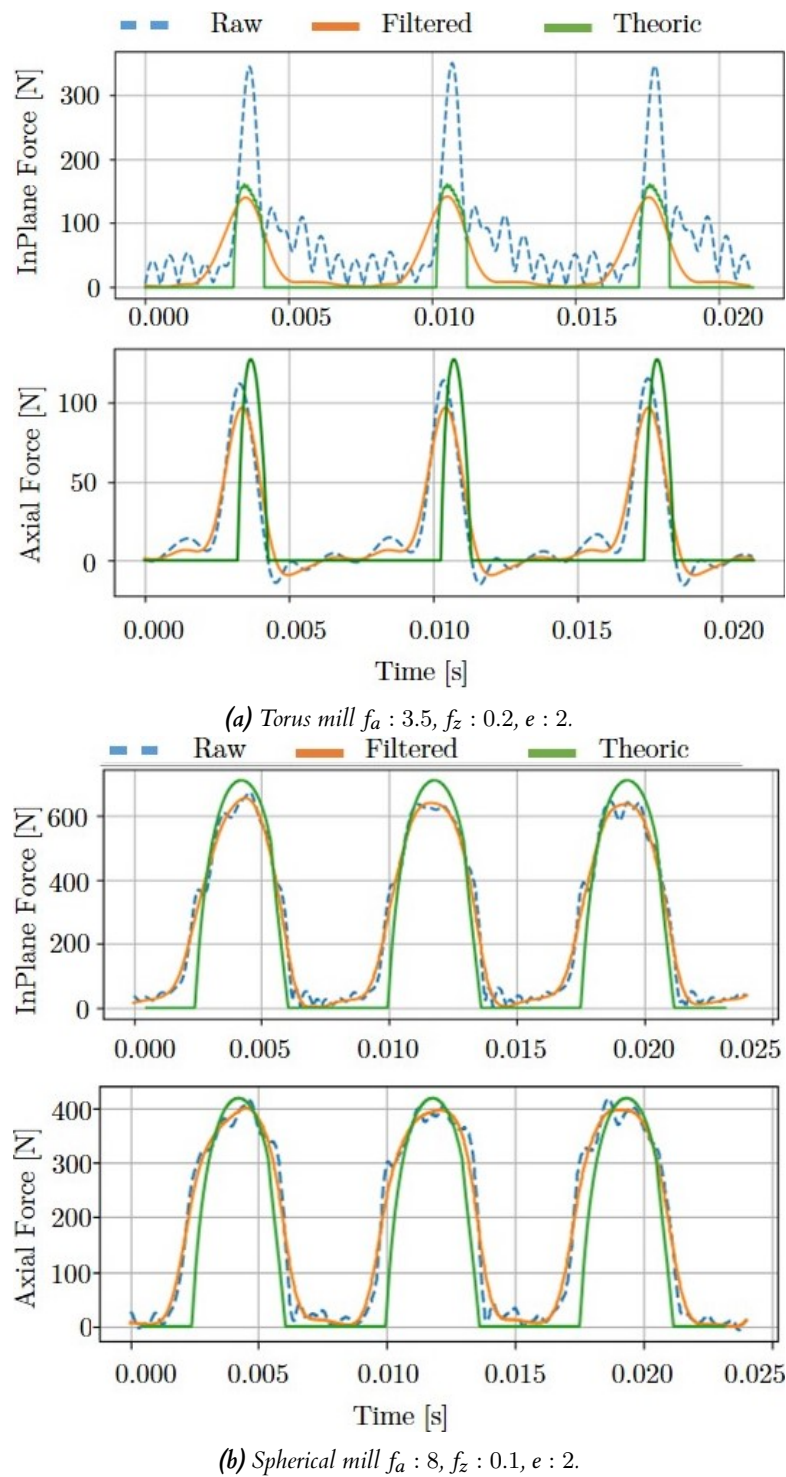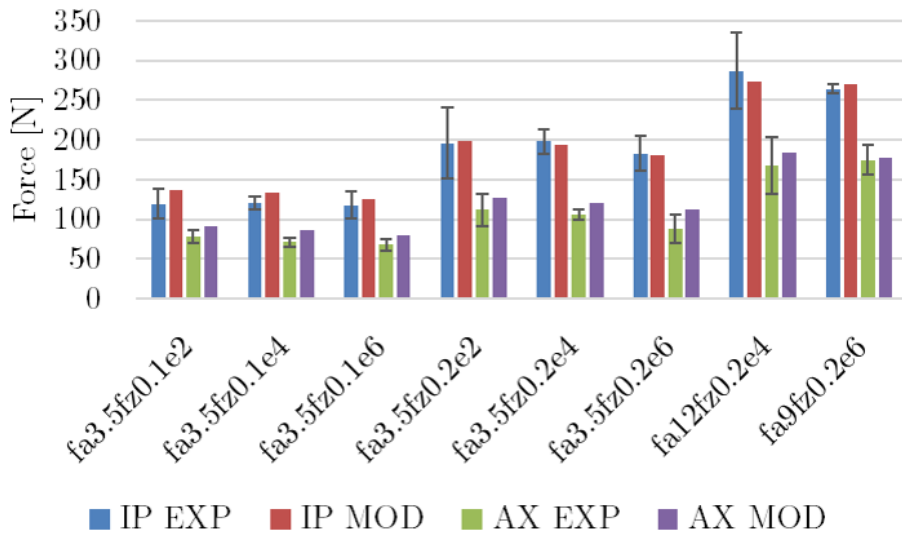

(a) Torus mill.
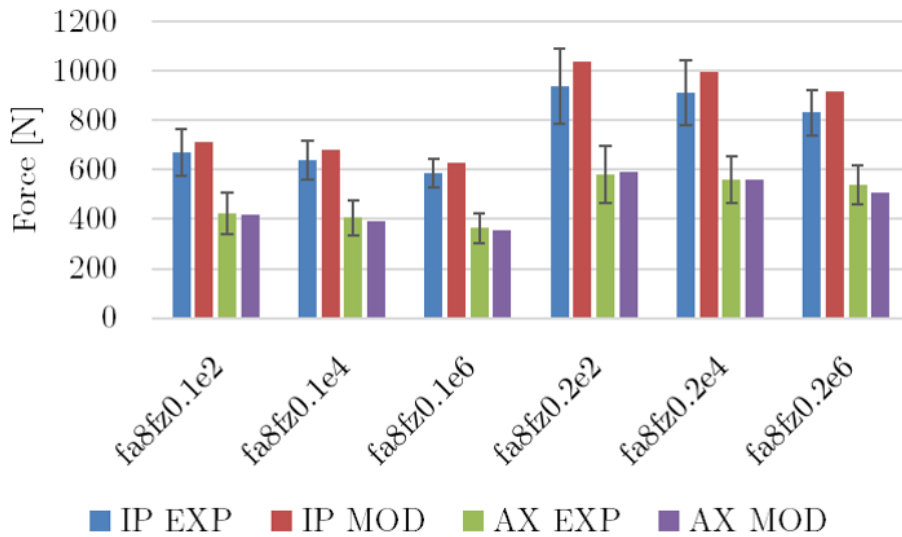
(b) Spherical mill.

Figure 5.27: *Maximum cutting force comparison in the whole experimental plan.*

5.7   Effect of the tool profile geometry and eccentricity

This section aims to simulate a wider scenario to predict the behavior of cutting forces, the uncut chip area evolution, chip volume, and material removal rate (*MRR*) in orthogonal turn-milling operations. As the model has been experimentally validated in the previous section, its results are considered representative enough from reality. Until this point, it is evident that the turn-milling operations present an augmented amount of parameters compared with conventional milling. Thus, the simulations are focused on varying the tool nose radius and eccentricity due to these features having been few studied. Table 5.6 presents the cutting conditions selected to run the simulations.

Table 5.6: *Simulation cutting conditions*

Rw [mm]	rt [mm]]	z [-	a_p [mm]	V_c [$\frac{m}{min}$]	MRR [$\frac{cm^3}{min}$]
44	16	1	2	400	23.87
Tag	f_z [$\frac{mm}{th}$]	e [mm]	f_a [$\frac{mm}{W_p rev}$]	n_w [rpm]	r_n [mm]
rn4e6	0.2	6	15	3	4
rn4e12	0.2	12	15	3	4
rn4e15	0.2	15	15	3	4
rn5e6	0.2	6	15	3	5
rn5e11	0.2	11	15	3	5
rn5e15	0.2	15	15	3	5
rn6e6	0.2	6	15	3	6
rn6e10	0.2	10	15	3	6
rn6e15	0.2	15	15	3	6
rn8e6	0.2	6	15	3	8
rn8e8	0.2	8	15	3	8
rn8e15	0.2	15	15	3	8

The rest of the cutting conditions remained constant to focus the attention on the effect of the tool profile and the eccentricity. As a result of this condition and based on equation 5.24 reported by Karaguzel et al. (2015b), the calculated material removal rate (*MRR*) is the same for all the simulations. The tool radius selection was based on the search for an actual tool that accepts different geometry inserts. Sandvik R300 mills are indexable round insert mills representing the same tool radius (r_t) for different insert radius (l_s) and has been used previously in this chapter. Hence, the selected tool radius is $r_t = 16$ *mm* and it have tools which accepts inserts of nose radius $r_n = [4, 5, 6, 8]$ *mm*. Another factor in choosing those tools is that the presented numeric model is versatile, representing diverse tool geometries. However, the specific cutting coefficients are very sensitive to the edge geometry, rake angle, and clearance angle, as shown in figure 5.23 and equation 5.23. It is then assumed that the specific force functions do not change if the same mill-inserts family is selected considering that the material is the same aluminum 6063 T5. That is to say that the torus experimental validations are simulated (Sandvik R300), assuming that the edge geometry (circular) rake and

clearance angles do not change.

$$MRR = z n_t f_z a_p a_e \qquad (5.24)$$

Several authors such as Crichigno Filho (2012); Karaguzel et al. (2015b, 2017, 2014); Zhu et al. (2016b); Kopač and Pogačnik (1997); Uysal et al. (2014); Kara and Budak (2015) mention there is an "optimum" value of eccentricity ($e_{opt} = r_t - l_s$) determined by the tool radius (r_t) and the usable radial length of the tool (l_s), see figure 5.28. Nevertheless, they just only state the value but does not present any demonstration. Additionally, the selected eccentricity in the process conditions the maximum axial feed (f_a) reached within the orthogonal turn–milling. Zhu et al. (2015a) relates the maximum axial feed considering the tool radius (r_t) and the radial usable length (l_s) as shown in equation 5.25. The described scenarios in equation 5.25 are intended to produce cylindrical surfaces not threaded.
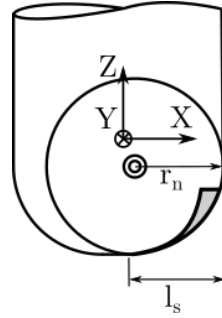

**Figure 5.28:** *Nose radius and radial usable distance in round inserts mills.*

$$r_t - l_s > e > 0 \longrightarrow f_{a_{max}} = \sqrt{r_t^2 - e^2} - \sqrt{(r_t - l_s)^2 - e^2}$$
$$r_t - l_s = e \longrightarrow f_{a_{max}} = 2\sqrt{2 r_t l_s - l_s^2} \qquad (5.25)$$
$$r_t > e > r_t - l_s \longrightarrow f_{a_{max}} = 2\sqrt{r_t^2 - e^2}$$

The optimal eccentricity value depends on the radial edge usable length (l_s) and as figure 5.28 shows, this parameter depends on the tool profile for the selected mills (Sandvik 300). Therefore, the eccentricity values are going to be lower, in the "optimum" value and greater of this values. In order to provide a comparable scenario, the lower and greater eccentricity values will be the same ($e = 6$ and $e = 15$ mm) and the optimal eccentricity changes with the nose radius (r_n). However, Karaguzel et al. Uysal et al. (2014); Karaguzel et al. (2016) report increments in the tool life as the eccentricity is augmented; additionally, the maximum life was reported at the condition $e = r_t - l_s$, considered the as its "optimum" value. Although the experimental evidence suggests that this value of eccentricity improves the behavior, it is not rigorous to state "optimum" without the respective theoretical demonstration of the mentioned optimization. Varying the eccentricity in the simulations is intended to show its effect over the uncut chip geometry.

The results of the cutting forces are presented in figure 5.29. Although in the whole thesis the $(X - Y)$ forces have been vectorial summed in the InPlane force, the simulations shows the 3D components to analyze in detail the effect of the studied parameters. As shown in figure 5.28 the (X) coordinate coincides whit the tool radius direction, the (Y) with the tangential direction and the (Z) with the axial direction. The effect of the nose radius is presented in figure 5.29 when the graph is analyzed horizontally.
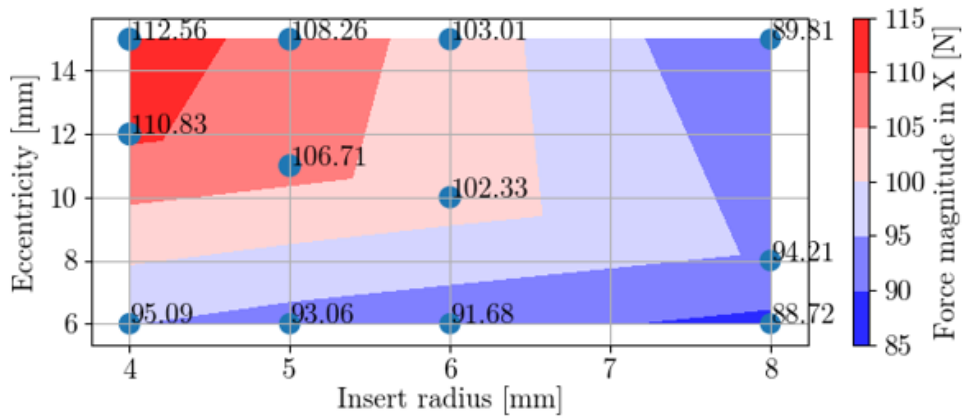
(a) Cutting forces in X.
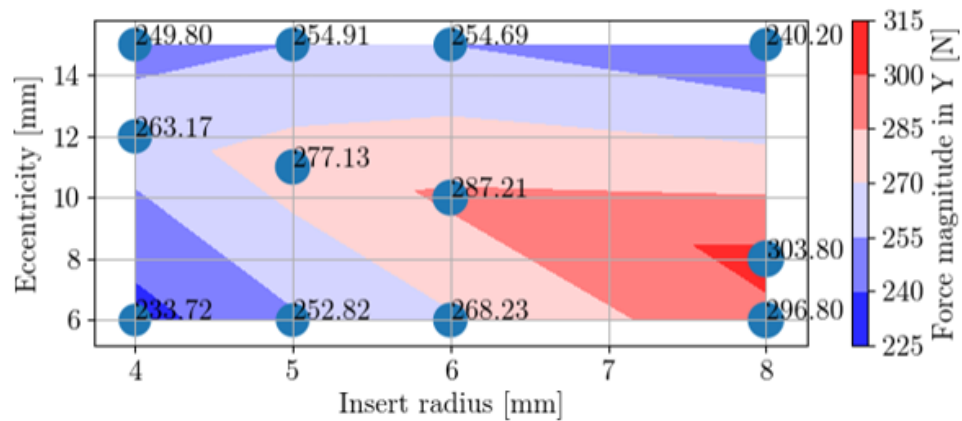
(b) Cutting forces in Y.
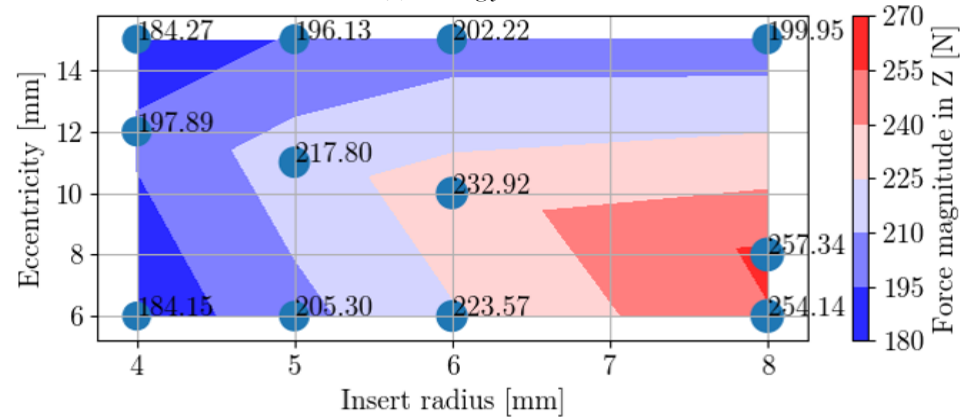
(c) Cutting forces in Z.

Figure 5.29: *Simulated cutting forces results.*

The maximum magnitude of the forces in the X direction is presented in the figure 5.29 (a). These results show a general trend to decrease when the nose radius increases. This slight decrement obeys to a higher nose radius (r_n) results in a more horizontal tool profile, which aligns the feed and penetration forces with the Z axis. This effect necessarily increments the Z direction forces as presented when the figure 5.29 (c) is analyzed horizontally. However, the force respective increment in X and decrement in the Z direction respectively is also a consequence of the decrement of chip thickness when the nose radius increased (see figure 5.29 (a and c)). Figure 5.30 presents the insert radius in scale, and it is possible to see how the chip thickness presents a noticeable reduction even when the depth of cut (a_p) and feed per tooth (f_z) are the same. This thickness reduction corresponds to a higher specific force, as presented in figure 5.23. This also explains the increments in the Y and Z direction caused by the nose radius (r_n), see figure 5.29 (b and c).
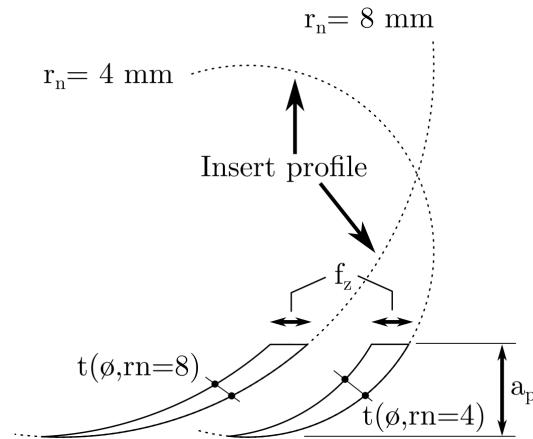

Figure 5.30: *Effect of increasing the nose radius over the chip thickness with the same depth of cut a_p and feed per tooth f_z.*

The eccentricity (e) effect is presented when the figure 5.29 is analyzed vertically. The eccentricity (e) slightly increments the force with the increment of the nose radius (r_n) in the (X) direction, see figure 5.29 (a). However, the nose radius ($r_n = 8$) does not follow this trend, due to the maximum force is presented in eccentricity ($e = r_t - l_s$). In the directions (Y and Z) it have been identified maximums of force in the condition ($e = r_t - l_s$) as well, see figure 5.29 (b and c). The eccentricity (e) modifies the uncut chip geometry that, combined with the workpiece curvature, changes the edge exit angle and the instantaneous depth of cut, presenting the maximum initial instantaneous area scenarios as shown in figure 5.31. This effect suggests that the chip volume is affected by the eccentricity (e). The area below the curves shown in figure 5.31 is an indicator of the chip volume changes with the increment of the nose radius (r_n) and eccentricity (e).

Therefore through the model, it is possible to estimate the chip volume presented in figure 5.32 a. The chip volume presents a considerable change with both variables, the eccentricity (e) and the nose radius (r_n). Even when the cutting conditions for conventional milling are the same for the whole simulations. This condition necessarily means that the material removal rate change, as shown in
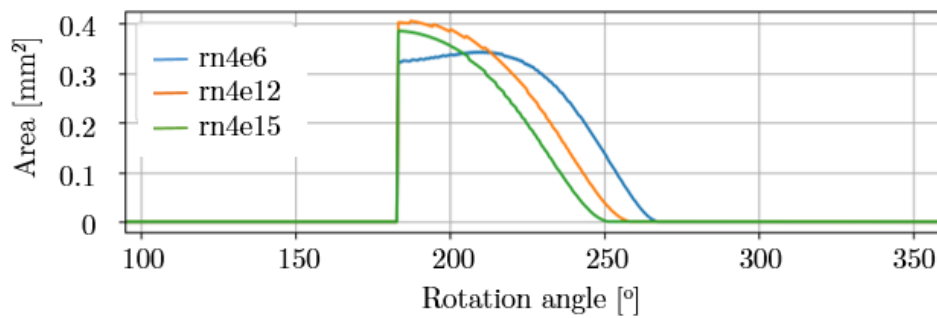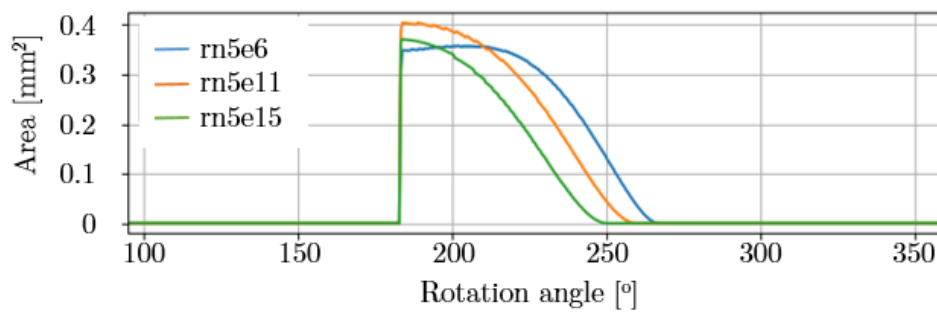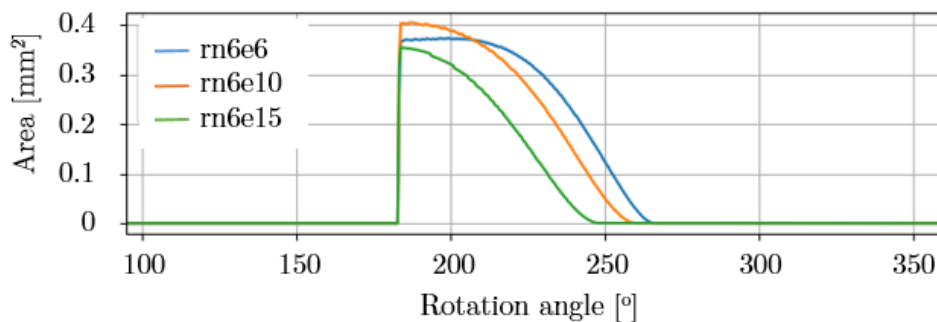
(a) Nose radius r_n = 4 mm.

(b) Nose radius r_n = 5 mm.

(c) Nose radius r_n = 6 mm.
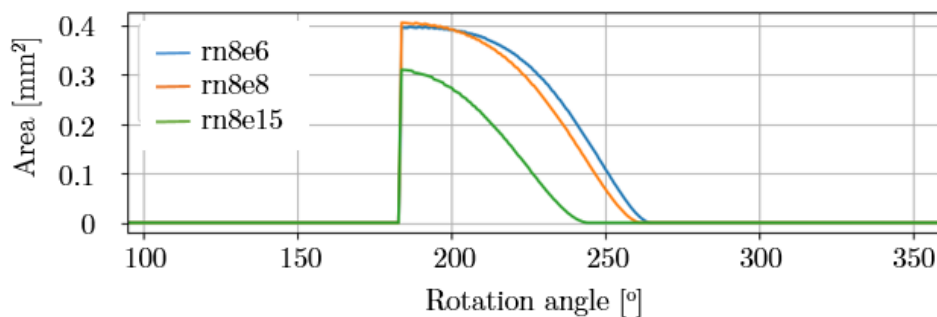
(d) Nose radius r_n = 8 mm.

Figure 5.31: *Simulated instantaneous area evolution.*

figure 5.32 b. These results are found by multiplying the chip volume by the rotational tool speed (n_t).

None of the estimated MRR presented in the figure 5.32 coincides with the

(a) Volume vs Eccentricity

(b) MRR vs Eccentricity
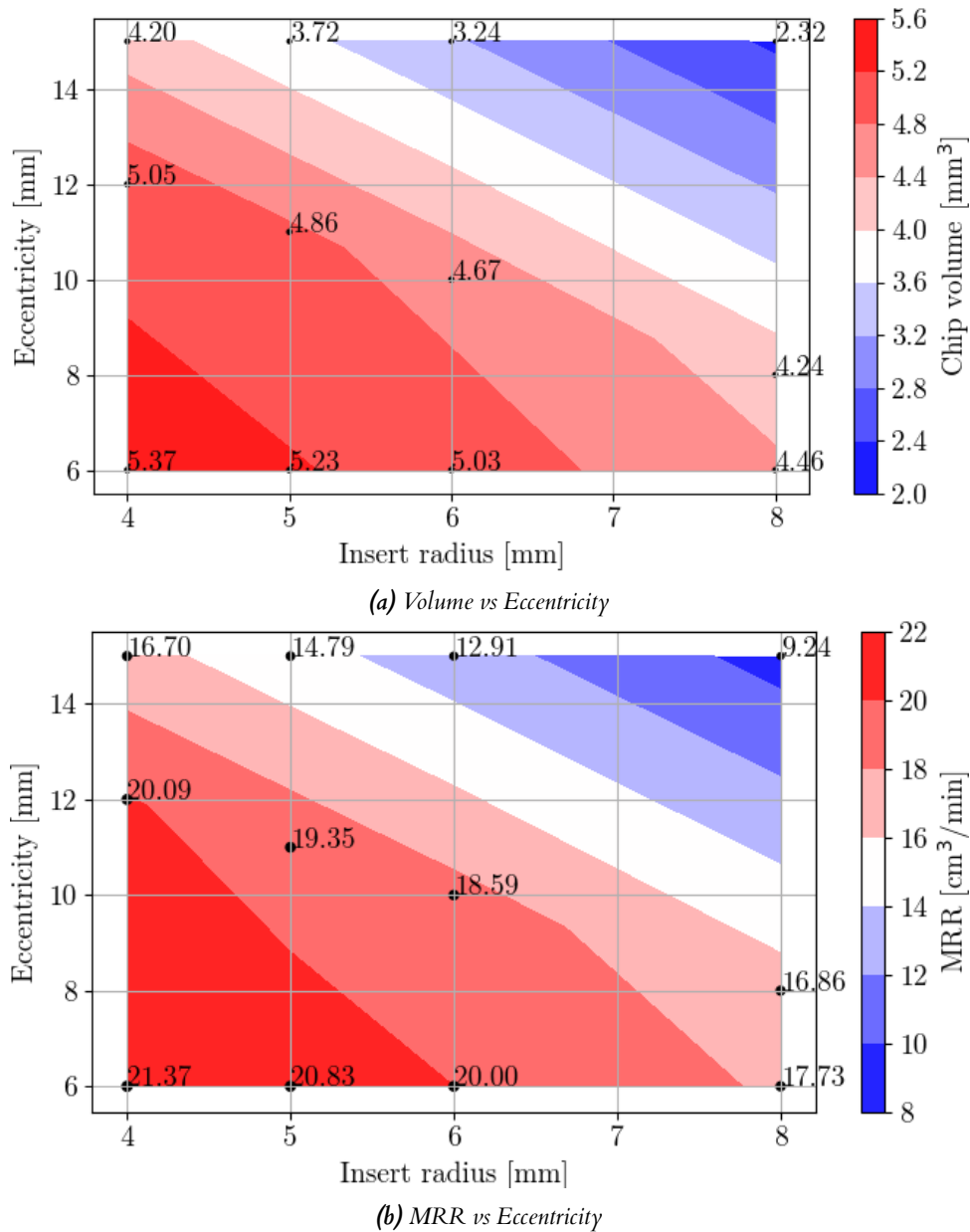
Figure 5.32: *Simulated chip volume and material removal rate results.*

calculated with the equation 5.24 reported by Karaguzel et al. (2015b), thus it is not recommended to use it for turn-milling planning. The volume graph presents a trend to reduce the chip volume if the nose radius (r_n) and the eccentricity (e) is augmented. The decrements in the material removal rate are matched with increments in cutting force due to the modification of the uncut chip geometry. The volume removed by the edge seems to present a maximum local value where the eccentricity (e) is close to 6 *mm*. Additionally, a smaller insert radius (r_n) shows increments in the removed volume in agreeing with conventional milling, and it coincides with the lowest cutting force prediction. This scenario would be more appropriate than having a low material removal rate and high cutting forces, as shown in the present simulations. The behavior of the cutting forces

depends on the uncut chip geometry, and the usable radial length of the edge is an arbitrary parameter. It is possible to find different tools with the same tool radius (r_t) but the different radial usable length of the edge (l_s). Meaning that the "optimum eccentricity" may present diverse values, but the presented simulations and the experimental results suggest the opposite.

Importantly, the reduction in the material removal rate means that the eccentricity and the tool profile are not removing material that was expected to be. Equation 5.24 showed a scenario of MRR close to 23 cm^3/min but figure 5.32 present the minimum value of 9.24 cm^3/min which is a reduction of 61.2%. Consequently, under these conditions, $rn = 8 \& e = 15$, the workpiece might present strong cusp errors due to 61.2% of the mass has not being removed by the tool. Meaning in reprocesses and loosing of productivity by poor operation planning.

The behavior of the chip volume observed can be detailed through a more extensive set of simulations. Figure 5.33 shows the selected mill set (Sandvik 300) and a theoretical flat end mill (rn0) with the same cutting conditions used in table 5.6. The behavior of the flat end mill (rn0) is the same presented in the previous chapter presenting an slight increment of the chip volume and then a pronounced decrease. This behavior is more exaggerated in the presence of nose radius because all of the rest mills (rn4, rn5, rn6, rn8) presents a more pronounced increment and decrement slopes. These simulations does not comply the model presented by Karaguzel et al. (2015b); even the error between the mentioned equation and the simulated chip volume is higher if the nose radius (r_n) is incremented. The maximum chip volume does not fulfill the "optimum" eccentricity statement ($e_{opt} = r_t - l_s$) thus refuting this conjecture. The maximum chip values does not follow a linear trend related with the studied variables (eccentricity (e) and nose radius (r_n)), seen table 5.7.
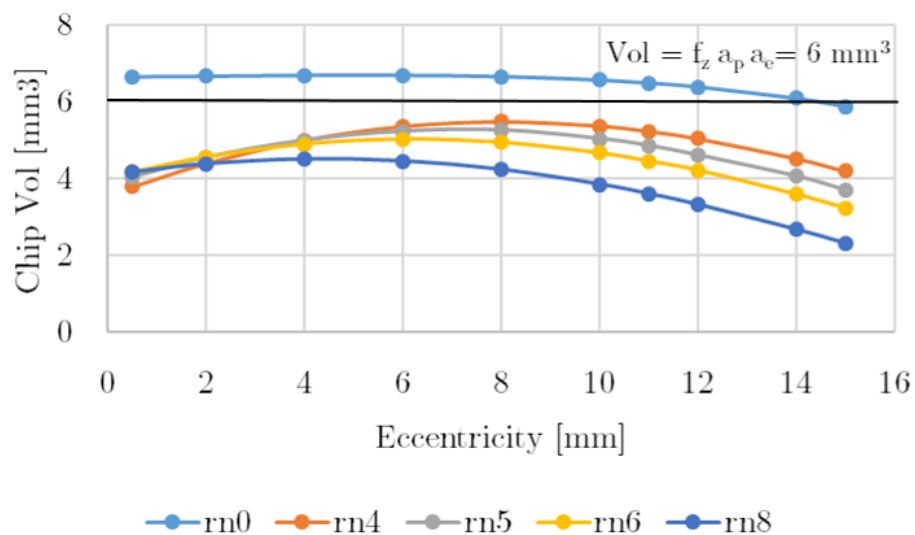

Figure 5.33: *Effect of the eccentricity over in the chip volume.*

This numerical tool helps evaluate diverse machining conditions in a relatively short period. For example, the average time of all of the simulations presented

Table 5.7: *Maximum chip volume.*

Tool profile	Max. Volume [mm^3]	Eccentricity [mm]
rn0	6.70	6
rn4	5.49	8
rn5	5.27	8
rn6	5.03	6
rn8	4.51	4

in this research is around 1.5 minutes. It is considering that the discretization process results in 720.000 points, 720 for the angular and 1000 for the radial direction. The variables that affect most the simulating time are the axial feed (f_a) and depth of cut (a_p) because they limit the number of points analyzed in the uncut chip geometry. These short periods contrast with the commercial software such as AdvantEdge or Abacus that takes several hours to run the calculations facilitating the decision-making on the workshop. The simulating time may vary depending on the number of points of the mesh and the available computational power.

5.8 Conclusions

This chapter presented a numerical methodology for studying the effect of the tool profile and the eccentricity in orthogonal turn-milling operations. This machining operation requires several geometrical and kinematic parameters to define the process without including the tool profile geometry selection. Therefore, estimating the operating windows in industrial environments is considerably difficult. Consequently, this chapter increased the knowledge related to this machining operation. Thereby the following conclusions raise:

1. The development presented in this research is a powerful tool to simulate vast cutting condition scenarios in a relatively short time. Additionally, it helps to understand that the eccentricity does modify the material removal rate giving a chance to identify geometrical errors by presenting a threaded excess of material in the workpiece result of the insert geometry.

2. The geometric model presented was validated in various stages, such as theoretical and experimental, with two different tool profiles, torus and spherical. The cutting forces errors were bellow of 12% and the cut chip mass was in good agreement with the predicted by this approach.

3. Thanks to the versatile approach, the tool profile can be a matter of study; due to, mills profile are in constant innovation, and it is relatively easy to modify it within the model.

4. The simulations performed in the last section evidenced the importance of the tool profile in the turn-milling operations performance. This feature could raise scenarios where the tool DOES NOT remove the material leading to a threaded surface, producing geometrical errors. These scenarios are feasible if the wrong eccentricity is selected. Even when the eccentricity is under the

considerations presented by Zhu et al. (2015a), these recommendations are only valid for flat end mills.

5. This research did not find theoretical evidence that supports the condition of eccentricity ($e = r_t - l_s$) is "optimum". Indeed, the simulated results showed maximum forces at this condition of eccentricity. This scenario is detrimental to the slender parts, inducing higher dimensional errors, and tool wear.

6 | Industrial Application: Fake combustion case manufacturing

The developments presented in the previous chapters are intended to be used in the workshop. For that reason, it is proposed in this thesis to manufacture a fake part similar to an aeronautical combustion case; see figure 6.1 (a). This part is not intended to be part of any mechanical set; however, it presents real manufacturing challenges of this kind of component. The technical drawings of the bulk material and the final workpiece are shown in the appendix of this manuscript.

The objective of this exercise was to evaluate the cutting conditions suggested by the cutting tool manufacturer for the turn–milling operations. Then, propose new conditions based on the models and compare the results obtained with and without using the models developed in this thesis. However, the exercise does not limit to operate the turn–milling operation but manufacturing the whole workpiece.

In this frame, a simplified geometry has been designed scaled to the machine tool available in Mondragon Unibertsitatea a GF+ Mikron Mill p800 UD. The fake combustion case is presented in figure 6.1 (b, c, and d). Considering that the workpiece has academic purposes, its dimensions and material obey the closer bulk and cutting tools available in the market. So, as the workpiece has an internal hole, the bulk material could be a perforated bar, and the material available was AISI 1024.

6.1 Manufacturing plan

The manufacturing plan to finish the workpiece is shown in this section. The operations and cutting tools are exposed with schemes to expose the manufacturing process. The machine-tool used is a 5 axis milling GF+ Mikron Mill p800 UD, that achieve the workpiece in two steps presented in figure 6.2 (a). This machine tool presents a rotary table architecture and the translational movements are attached to the cutting tool. The IV axis is a infinite rotational axis able to rotate the workpiece 360°. The V axis is a limited rotational axis of 202°. The provider cut the perforated bar and cleaned the serrated faces as shown in figure 6.2 (b). The machine is equipped with a three-jaw plate clamp to fix the bulk material. The cutting tools are mainly from Sandvik (2021) except of the boring head that is manufactured from Laip (2021). As the cutting edge (inserts and solid
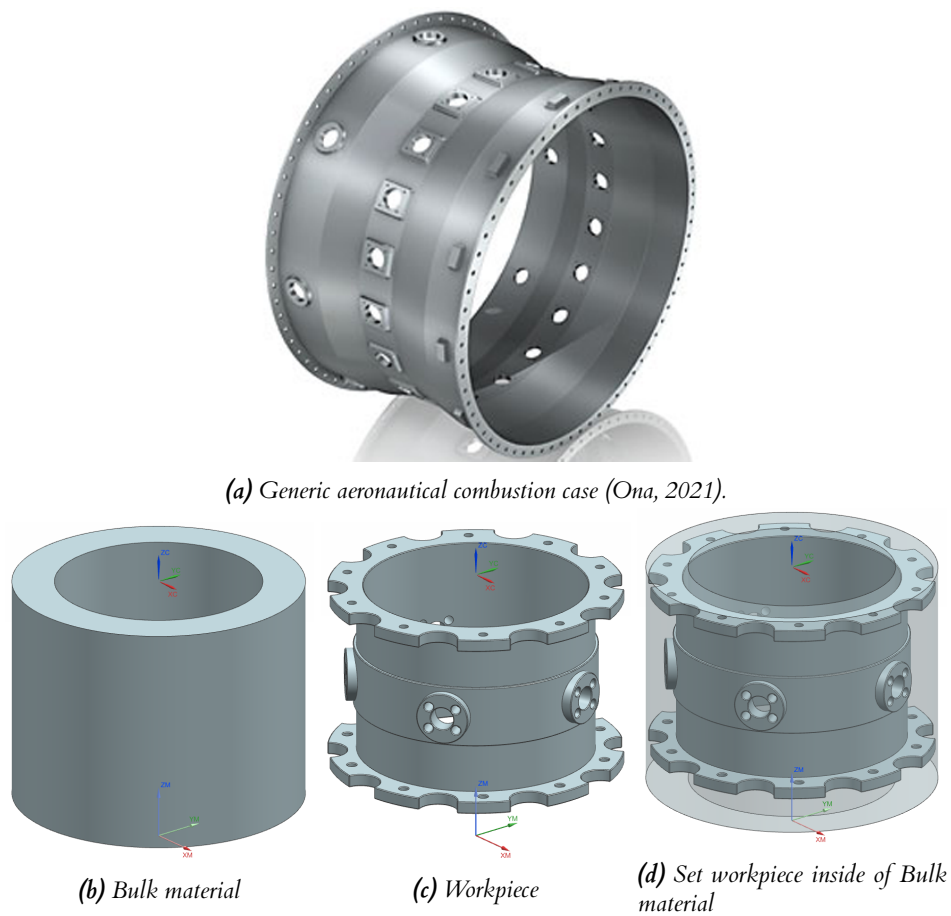
(a) Generic aeronautical combustion case (Ona, 2021).

(b) Bulk material   *(c) Workpiece*   *(d) Set workpiece inside of Bulk material*

Figure 6.1: *Complex shape workpiece achievable through the use of turn–milling operations. Technical drawing in the appendix.*

tools) are all from Sandvik the cutting conditions were obtained by the CoroPlus tool guide, a free service available on the web page of Sandvik Coromant (Sandvik, 2021). The manufacturing process is summarized in the following figures presenting all of the operations needed to achieve the workpiece.
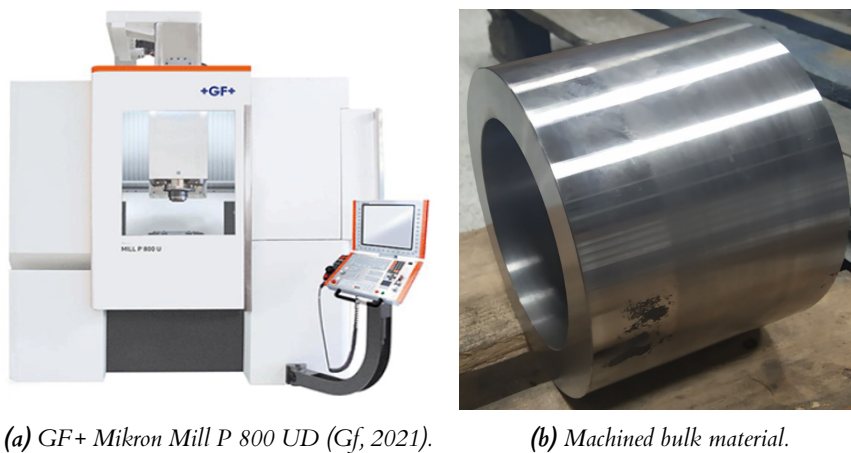

(a) GF+ Mikron Mill P 800 UD (Gf, 2021).   *(b) Machined bulk material.*

Figure 6.2: *5-axis machining center and the bulk material for the workpiece manufacturing.*

Operation	Tool (Holder and insert)	Cutting conditions		
1101-1102 Top face milling Roughing (1101) Finishing (1102)	Exchangeable insert flat plate TM490-744483 — Square insert 490R-08T304E-ML 2040	Vc [m/min]	n [rpm]	fz [mm/tht]
		252	1197	0.14
		f [mm/min]	ap [mm]	ae [mm]
		1340	(1101) 2.5 (1102) 0.5	15
	Operation scheme and final result			
	1101 1102			

Operation	Tool (Holder and insert)	Cutting conditions		
1103 Internal diameter hole milling	Exchangeable insert flat plate TM490-744483 — Square insert 490R-08T304E-ML 2040	Vc [m/min]	n [rpm]	fz [mm/tht]
		247	1173	0.15
		f [mm/min]	ap [mm]	ae [mm]
		1407	1.5	3
	Operation scheme and final result			
	Machined Surface			

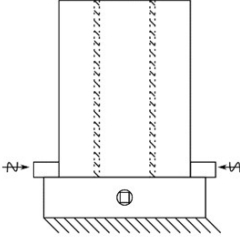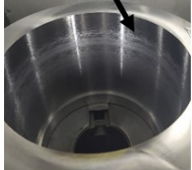*Figure 6.3:* Face milling roughness (1101) finishing (1102) and internal diameter hole milling (1103).
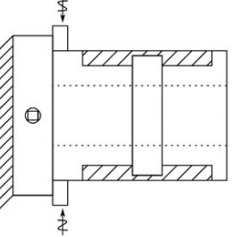
Operation	Tool (Holder and insert)		Cutting conditions		
			Vc [m/min]	**n [rpm]**	**fz [mm/tht]**
			100	221	0.1
	005 54 06 08 08 Micrometer boring head	Turning insert CCMT 060204-PM 4335	**f [mm/min]**	**ap [mm]**	**ae [mm]**
1104 Internal diameter boring			22.1	222	0.5
	Operation scheme and final result				
	Machined Surface				

Operation	Tool (Holder and insert)		Cutting conditions			
			Vc [m/min]	**n [rpm]**	**fz [mm/tht]**	
			145	3077	0.133	
	Torus mil R300- 015-A20L-07L	Round milling insert R300-0724E-PM4340	**f [mm/min]**	**ap [mm]**	**fa[mm/r]**	**e [mm]**
1105 Turn-milling roughing			818	(slot) 0.5 (t-m) 1.25	(slot) 15 (t-m) 3.5	2
	Operation scheme and final result					

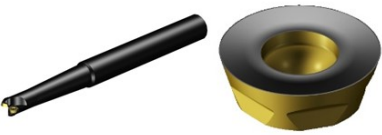***Figure 6.4:*** *Internal diameter boring (1104) and turn–milling roughing (1105).*
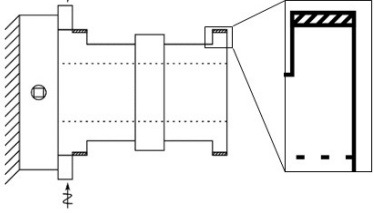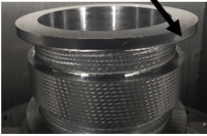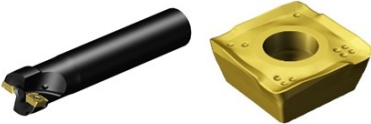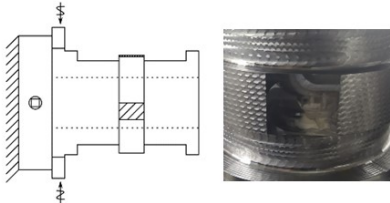
Operation	Tool (Holder and insert)	Cutting conditions		
1106 Turn-milling flange finishing	Flat end mill 490-025A20-08L Square insert 490R-08T304E-ML 2040	Vc [m/min]	n [rpm]	fz [mm/tht]
		253	3221	0.133
		f[mm/min]	ap [mm]	fa[mm/r] e [mm]
		934	1.5	1 0.5
	Operation scheme and final result			

Operation	Tool (Holder and insert)	Cutting conditions		
1107-1108 Boss facing Roughing (2107) Finishing (1108)	Flat end mill 490-025A20-08L Square insert 490R-08T304E-ML 2040	Vc [m/min]	n [rpm]	fz [mm/tht]
		(1107) 238	3030	0.13
		(1108) 243	3094	0.1
		f [mm/min]	ap [mm]	ae [mm]
		(1107) 787	2.5	17.5
		(1108) 618	0.5	
	Operation scheme and final result			
	1107 1108			

Figure 6.5: *Flange turn–milling (1106) and Boss facing roughing (1107) and finishing (1108).*
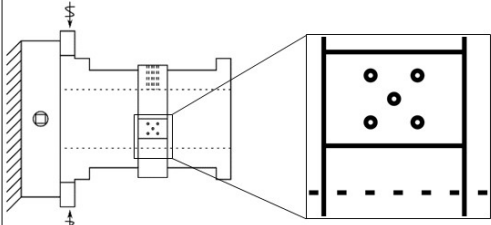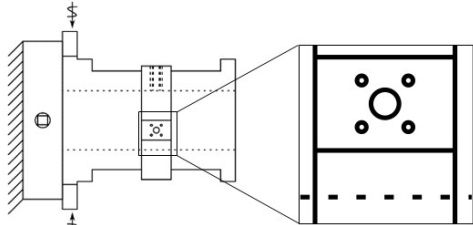
Operation	Tool	Cutting conditions		
		Vc [m/min]	**n [rpm]**	**fz [mm/tht]**
		182	9655	0.1
		f [mm/min]	**ap [mm]**	**ae [mm]**
	Ø6 mm drill bit 860.1-0600-047A1-PM 4234	2124	Thru	—
1109 Boss-drilling	**Operation scheme and final result**			

Operation	Tool	Cutting conditions		
		Vc [m/min]	**n [rpm]**	**fz [mm/tht]**
		(1110) 238 (1111) 243	7576 7735	0.13 0.1
		f [mm/min]	**ap [mm]**	**ae [mm]**
	Flat end mill 1P330-1000-XA 1620	(1110) 2954 (1111) 2320	1.6 15	7.5 0.1
1110-1111 Hole milling Roughing (1110) Finishing (1111)	**Operation scheme and final result**			

Figure 6.6: Boss drilling (1109) and hole milling roughing (1110) and finishing (1111).

Operation	Tool	Cutting conditions		
	Torus mil R300-015-A20L-07L	**Vc [m/min]**	**n [rpm]**	**fz [mm/tht]**
	Round milling insert R300-0724E-PM4340	145	3077	0.133
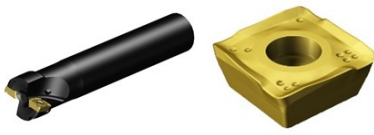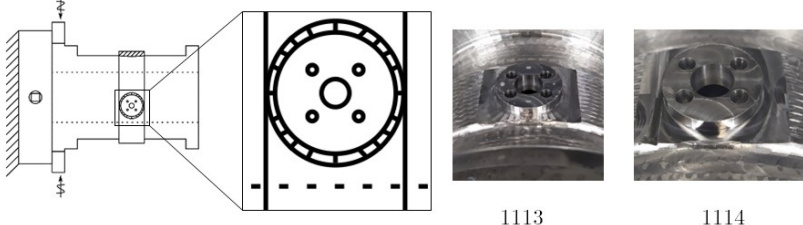
		f[mm/min]	**ap [mm]**	**fa[mm/r]**	**e [mm]**
1112 Supporting ring roughing		818	1.25	3.5	2

Operation scheme and final result

Operation	Tool	Cutting conditions		
	Flat end mill 490-025A20-08L	**Vc [m/min]**	**n [rpm]**	**fz [mm/tht]**
	Square insert 490R-08T304E-ML 2040	(1113) 252	3209	0.142
		(1114) 254	2324	0.1

		f[mm/min]	**ap [mm]**	**fa[mm/r]**	**e [mm]**
1113-1114 Boss wall milling Roughing (1113) Finishing (1114)		(1113) 911	1.25	1.25	7.5
		(1114) 646	2.5	2.5	0.25

Operation scheme and final result

1113   1114

Figure 6.7: Surface between bosses (1112) and interior flange roughing (1113) and finishing (1114).

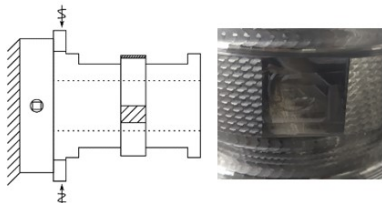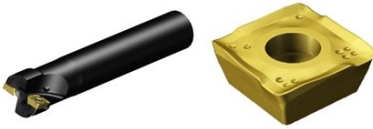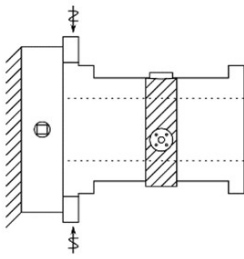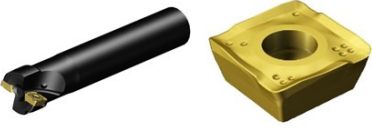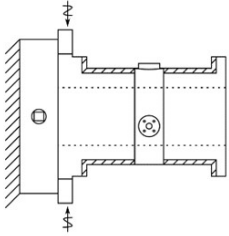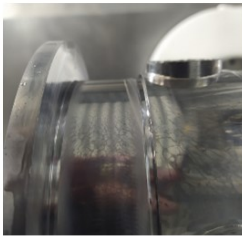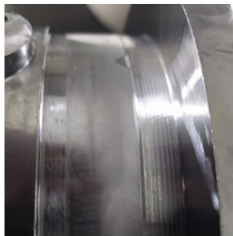| Operation	Tool (Holder and insert)		Cutting conditions		
1115-1116 Support ring floor milling Semi-finishing (1115) Finishing (1116)	Flat end mill 490-025A20-08L	Square insert 490R-08T304E-ML 2040	Vc [m/min]	n [rpm]	fz [mm/tht]
			253	3221	0.133
			f[mm/min]	ap [mm]	fa[mm/r]	e [mm]
			934	(1115) 1.5 (1116) 0.5	1	11

Operation scheme and final result

1115   1116

Operation	Tool (Holder and insert)		Cutting conditions		
1117 Interior flange and floor finishing by turn-milling	Flat end mill 490-025A20-08L	Square insert 490R-08T304E-ML 2040	Vc [m/min]	n [rpm]	fz [mm/tht]
			243	3094	0.133
			f[mm/min]	ap [mm]	fa[mm/r]	e [mm]
			618	(flange) 3 (floor ecc) 1.5 (floor cen) -	0 1 1	0 11 0

Operation scheme and final result

Figure 6.8: Support ring floor milling semi–finishing (1115) finishing (1116) interior flange and floor finishing by turn–milling (1117).
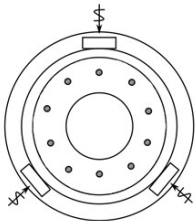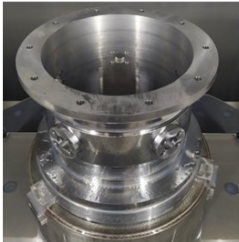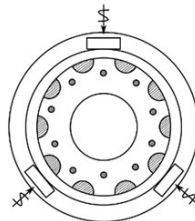
Operation	Tool	Cutting conditions		
1118 Flange drilling	Ø6 mm drill bit 860.1-0600-047A1-PM 4234	Vc [m/min]	n [rpm]	fz [mm/tht]
		182	9655	0.1
		f [mm/min]	ap [mm]	ae [mm]
		2124	15	—
	Operation scheme and final result			

Operation	Tool	Cutting conditions		
1119-1120 Lobe milling Roughing (1119) Finishing (1120)	Flat end mill 1P330-1000-XA 1620	Vc [m/min]	n [rpm]	fz [mm/tht]
		(1119) 184 (1120) 391	5857 12446	0.05 0.15
		f [mm/min]	ap [mm]	ae [mm]
		(1119) 878 (1120) 5600	1 0.5	8
	Operation scheme and final result			

Figure 6.9: *Flange drilling (1118) lobe milling roughing (1119) finishing (1120).*

Operation	Tool	Cutting conditions		
1121 Deburring	326 Slotting, chamfering, tapping mill	**Vc [m/min]**	**n [rpm]**	**fz [mm/tht]**
		182	11586	0.22
		f [mm/min]	**ap [mm]**	**ae [mm]**
		7646	0.5	0.5
	Operation scheme and final result			

Figure 6.10: Edge deburring (1121).

(a) second clamping event, internal diameter clamping.

(b) Result of face milling 1202.
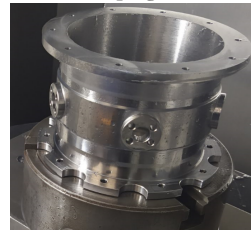
(c) Result of drilling 1203.
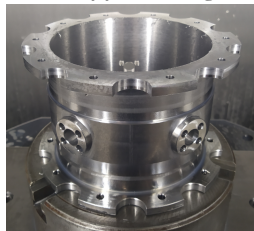
(d) Result of profiling 1205.

(e) Result deburring 1206.

Figure 6.11: Second clamp operations.

The machining operations to manufacture the workpiece in the first clamp have been presented in figure 6.3 to 6.10; at this stage, the workpiece has to be unclamped and rotated to machine the support material, see figure 6.11 (a). To complete the workpiece it is necessary a second clamp where are repeated some machining operations described previously in the first clamp. The operations 1201 and 1202 presented in figure 6.11 (b) are face milling operations that repeats the tool path and uses the cutting conditions of 1101 and 1102, see figure 6.3. The flange drilling 1203 presented in figure 6.11 (c) corresponds to the operation 1118, see figure 6.9. The lobe milling 1204 and 1205 presented in figure 6.11 (d) is described in the operations 1119 and 1120 respectively, see figure 6.9. The last operation is the deburring 1206 presented in figure 6.11 (e) that uses the cutting conditions of operation 1121, see figure 6.10.

6.2   Strategies for improvement

The manufacturing plan presents some improvement opportunities that can be addressed from the developed models of turn-milling in the previous chapters. These opportunities cover different aspects of the process such as geometrical errors, material removal rate, and tool breakage avoidance. However, in this thesis the cutting forces are consider as an indicator of the process limits and the material removal rate is considered the productivity indicator. This means that the magnitude of the cutting forces determine the process limit in determined cutting conditions. Therefore to increase productivity, the cutting conditions suggested by the tool manufacturer are evaluated with the cutting forces models. Those forces are used as input in structural simulations performed in SolidWorks 2017 structural FEA. The variable of study is the nodal displacements result of to the cutting forces. The excessive displacement leads to geometrical errors due to excessive workpiece deformation. Then, regulating the cutting forces, the material removal rate can be increased, and the geometrical errors can be under control. The cutting conditions effect in the tool wear is also considered in this analysis. In this workpiece, the turn-milling operations are the most time consuming activities. Consequently, these operations are going to be engineered to increase the material removal rate because they have great potential to reduce the manufacturing time without impact negatively the workpiece quality.

Turn-milling roughing operations (1105 and 1112)

The roughing operations are performed by the torus mill R300 with circular inserts as shown in figure 6.12 (a and b). The tool path used of these operations are presented in figure 6.12 (c, d, and e). The schemes of the operations are presented in figure 6.12 (f and g). The roughing turn-milling operations looked to remove a large amount of material. In the non-improved version the operation 1105, the helix tool path felt low of charge, but the circular slot tool path was very close to the maximum MRR in the safe operating range. For this reason, the slot conditions remain the same, but the helix conditions were studied and modified. The tool must perform eight complete helix from flange to flange and six interrupted helix tool paths from flange to ring and ring to flange the current

cutting conditions. The complete helix takes nearly 20 minutes per helix, and the incomplete helix operation takes around 9 minutes per helix. Then, augmenting the depth of cut, the number of helices decreased, reducing the overall time of the operation.

(a) Torus mill R300-015-A20L-07L (Sandvik, 2021).
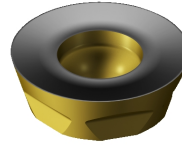
(b) Round milling insert R300-0724E-PM4340 (Sandvik, 2021).
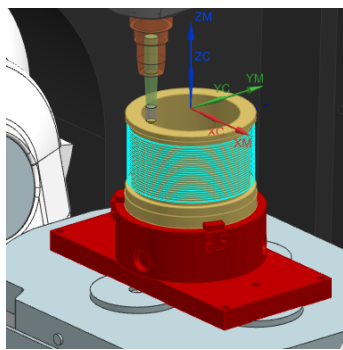
(c) 1105 Tool path complete turn-milling operation flange to flange (20 min per helix).
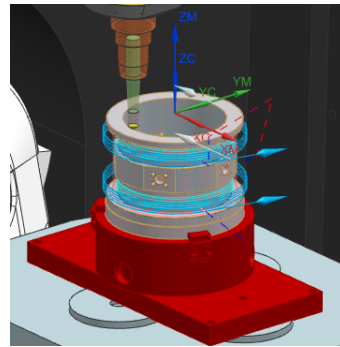
(d) 1105 Tool path incomplete turn-milling operation internal ring stock (8 min per double helix).
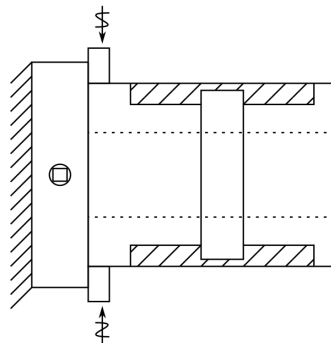
(e) 1105 Scheme turn-milling roughing surfaces between the flanges.
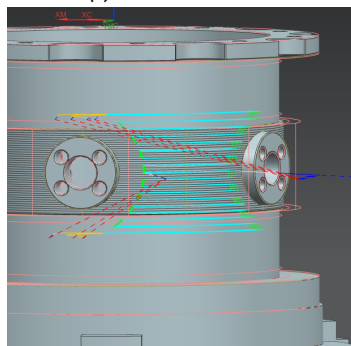
(f) 1112 Tool path support ring roughing between bosses zig-zag.
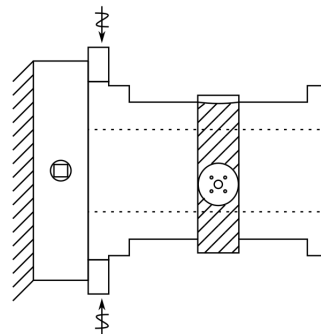
(g) 1112 Scheme support ring roughing.

Figure 6.12: *Cutting tool and tool path used in turn-milling roughing operations.*

The depth of cut (a_p) was increased from 1.25 to 2 mm. This decision evidently results in the increment of the cutting forces, that based on the models developed and the database of the material is presented in table 6.1. The radial, axial and tangential direction refers to the mill coordinate system reliant on the dynamometer that usually coincides with (X, Y, Z) respectively. Then, the increased depth of cut shows augmented cutting forces; however, the number of helical passes was reduced from 8 to 5, saving more than 1 hour (from 4 hours and 02 minutes to 2 hours and 44 minutes). The structural consequences for the cutting force increment were analyzed via Solidworks structural simulations, determining deformation increment in both cases.

Table 6.1: Simulated cutting forces of torus turn–milling operations.

a_p [mm]	F_{radial} [N]	$F_{tangential}$ [N]	F_{axial} [N]
1.25	–120.95	195.66	146.46
2	–172.07	446.68	276.52

(a) 1105 Structural simulation in the minimum stiffness workpiece instant. Node displacement ($a_p = 1.25$ mm).

(b) 1105 Structural simulation in the minimum stiffness workpiece instant. Detail punctual load ($a_p = 1.25$ mm).

(c) 1105 Structural simulation in the minimum stiffness workpiece instant. Node displacement ($a_p = 2$ mm).

(d) 1105 Structural simulation in the minimum stiffness workpiece instant. Detail punctual load ($a_p = 2$ mm).

Figure 6.13: *Displacement simulation due to the cutting forces of turn–milling roughing operation 1105 with torus mill.*

The simulations were a primary way to esteem the displacement of the workpiece due to the cutting forces. This feature is related to the geometrical errors due to an excessive local displacement means that the final dimension would be greater than its nominal value. Figure 6.13 shows the results of the

simulations. In sub-figure (a), the general displacement, and in the (b) sub-figure, a detail of the punctual force is presented. The sub-figures (c and d) show the displacement results with 2 mm of the depth of cut. The resultant force increase is slightly more significant than the double passing from 247.64 N to 552.8 N. The displacement increased proportionally. However, the maximum displacement does not reach $3\mu m$ in the most demanding depth of cut.

(a) *1112 Structural simulation in the minimum stiffness workpiece instant. Node displacement ($a_p = 1.25$ mm).*

(b) *1112 Structural simulation in the minimum stiffness workpiece instant. Detail punctual load ($a_p = 1.25$ mm).*

(c) *1112 Structural simulation in the minimum stiffness workpiece instant. Node displacement ($a_p = 2$ mm).*

(d) *1112 Structural simulation in the minimum stiffness workpiece instant. Detail punctual load ($a_p = 2$ mm).*

Figure 6.14: *Displacement simulation due to the cutting forces of turn-milling roughing operation 1112 with torus mill.*

The simulations were performed in different instants during the manufacturing process. Despite the cutting force are not supposed to change, the cantilever distance and the workpiece stiffness does change. In operation 2105, the workpiece has more material, and the cantilever is maximum. However, in operation 2112, the cantilever distance is reduced, and the stiffness also decreases due to the removed material. Figure 6.14 shows the results comparing the effect of cut depth. Sub-figures (a and b) represent the 1.25 mm, and c and d represent 2 mm of cut depth. The displacement results showed that the effect of the stiffness of the workpiece is more critical than the cantilever distance. Due to the magnitude of the displacement almost doubling the value presented in operation 2105, see figures 6.13 and 6.14. However, 5 μm of geometrical error is far under the tolerance set for the workpiece, see the technical drawing in the Apendix chapter.

The cutting force measurement was done with a Spike tool holder, see

figure 6.15 (a). This instrument is a bending moment and trust force sensor; therefore, the in plane forces are esteemed with the bending moment and tool length. The mechanical feature measurements are performed through strain gauges attached to a conventional tool holder. The instrument is equipped with a wireless transmission data system sending the data to a external receiver. The results of the measured forces are presented in figure 6.15 (b). As expected, the cutting forces presented an increment proportionally with the depth of cut. However, the signal in the Z direction presented unexpected magnitudes. This behavior was consistent in all operations, and it is suspected that the technology of strain gauges has not the sensitivity enough to capture properly the cutting force changes.

(a) *Promicron Spike (R) and the torus mill Sandvik (R300)*
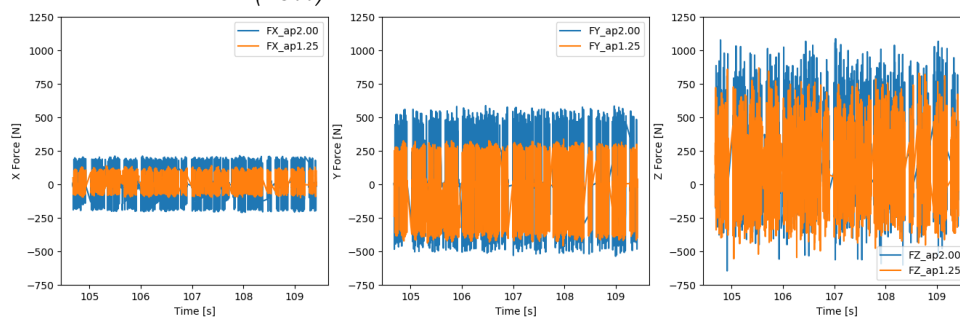
(b) *Resulting force in the time domain obtained by the sensor Spike(R).*

Figure 6.15: *1105 Tool and steady cutting forces measured with Spike(R).*

A comparison of the simulated and the experimental peak forces are presented in table 6.2. This table shows the comparison of the increment of force due to the depth of cut. The simulated and raw experimental data presents some discrepancies mostly due to the measurement system, additionally the dynamic nature of the milling process. Despite of this, in both cases the simulated and experimental the data shows a proportional increment due to the augmented depth of cut.

Besides the time reduction, the augment of the depth of cut showed an

Table 6.2: *Comparison of the impact of increase the depth of cut by experimental and theoretical means.*

a_p [mm]	F_{radial} [N]	$F_{tangential}$ [N]	F_{axial} [N]
1.25 Sim	120	195	146
2.00 Sim	172	446	276
Increment	142%	141%	188%
1.25 Exp	114	277	719
2.00 Exp	237	540	999
Increment	206%	194%	38%

unexpected advantage related to the tool wear. Operation 1105 was divided into two tool paths as shown in figure 6.12. Defining the depth of cut (a_p = 1.25 mm), the complete helix takes 2 hours and 44 minutes, and the incomplete helix takes 1 hour and 28 minutes. Increasing the depth of cut to (a_p = 2 mm) the complete helix tool path takes 1 hour and 45 minutes, and the incomplete helix takes 1 hour. Figure 6.16 shows the measured wear of the same edge after finished the operations mentioned. The 1.25 mm depth of cut accumulated excessive wear of 0.47 mm, considering that it is not recommended to exceed 0.3 mm of wear; however, the wear was reduced to 0.167 mm with the depth of cut 2 mm. It might be explained by the reduction in the friction length, considering that the depth of cut increment reduces the number of helical passes completing the whole part with one set of edges; thus, shortening the overall tool path. Figure 6.16 (e and f) shows the machining results with no remarkable difference between the strategy a_p = 1.25 mm and a_p = 2 mm.
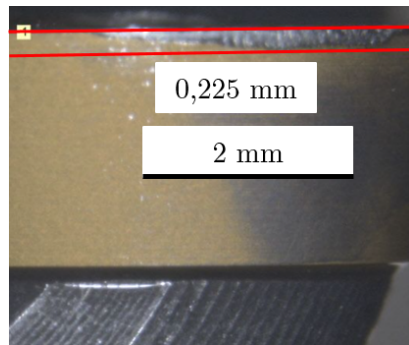
(a) *Wear after complete helical trajectory operation 2105 (2h44m) a_p = 1.25 mm.*
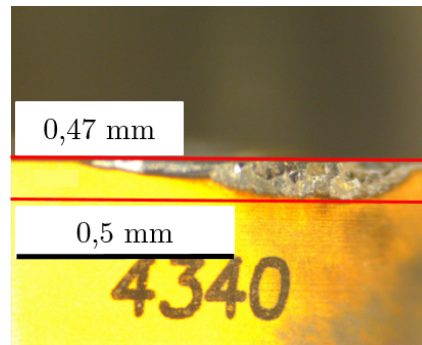
(b) *Wear after incomplete helical trajectory operation 2105 (4h02m) a_p = 1.25 mm.*
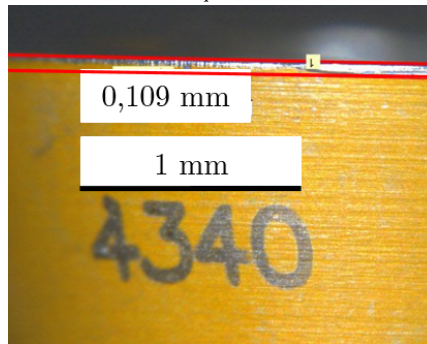
(c) *Wear after complete helical trajectory operation 2105 (1h45m) a_p = 2.00 mm.*
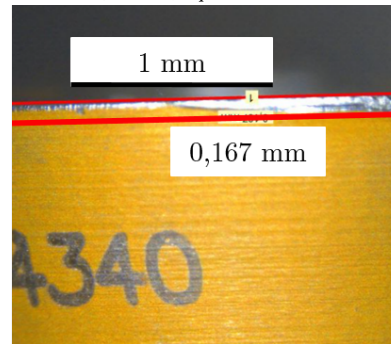
(d) *Wear after incomplete helical trajectory operation 2105 (2h45m) a_p = 2.00 mm.*

(e) *Machining results of operation 2105 with depth of cut (a_p = 1.25 mm).*

(f) *Machining results of operation 2105 with depth of cut (a_p = 2 mm).*

Figure 6.16: *Comparison of the wear after the complete helical trajectory and incomplete helical trajectory in operation 2105.*

Finishing turn–milling operations (1106, 1115, 1116 and 1117)

The turn–milling finishing operations are all performed by a flat end mill Sandvik 490. However, all the operations are semi-finishing and finishing operations, meaning that the opportunity to reduce the number of passes is not available, unlike the roughing operations. Consequently, the strategy for increase the material removal rate was to increase the feed per edge. This decision was made based on the low radial engagement of the cutter due to the wiper geometry. Therefore, the axial nor the radial engagement can be modified; the only parameter to change is the feed per edge. The operations affected by these modifications are presented in figure 6.17; all these operations share the same cutting conditions.
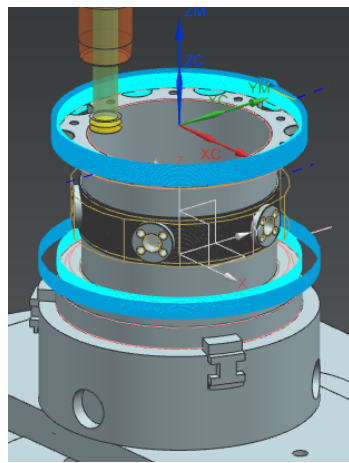
(a) 2106 Flange finishing turn-milling operation.
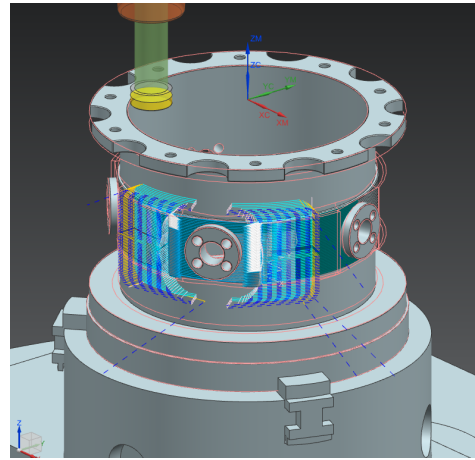
(b) 2115 - 2116 Ring semi-finish and finishing intermittent turn-milling.
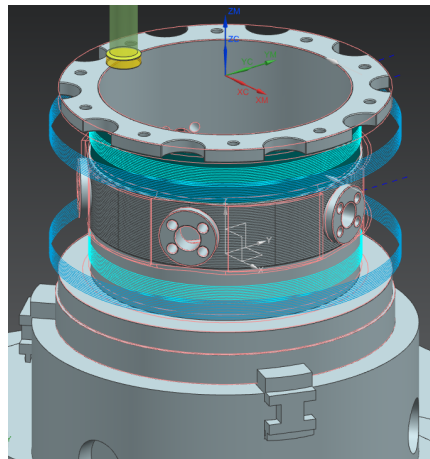
(c) 2117 Floor finishing.

Figure 6.17: Flat end mill turn-milling operations.

The general proposal was to augment the feed per edge from 0.133 mm to 0.2 mm to all turn-milling operations performed with this mill to reduce the time consumed by the finishing operations. The augment in the forces expected present increments in the deformations of the workpiece. However, considering the simulations presented in figures 6.13 and 6.14 showed very low local displacement with maximum values of 5 μm. These simulations had higher

forces than expected for these operations, and the stiffness of the workpiece is the same. Consequently, as the finishing operations presents lower cutting forces is expected even lower displacements.

The resulting cutting forces measured with the Spike(R) are presented in figure 6.18. As expected, the increment of feed per edge increased the cutting forces, and the comparison of the estimation and the experimental measurements are presented in table 6.3. The increment in both cases followed the trend with values relatively consistent. The signal in the Z direction presented magnitudes not expected, and the increment is too large. In detail, this signal is noisy, and it might mean that the load is too low and the sensor is not capturing the value correctly. The obtained surfaces did not presented significant differences qualitatively speaking. Figure 6.19 shows the obtained surfaces from turn-milling operations 1106 (a and b) and 1117 (c and d). The time reduction of each operation is presented in table 6.4. In total, the manufacturing time was reduced from 9 hours and 46 minutes to 7 hours and 39 minutes. Additionally, the workpiece can be manufactured without change the cutting edges in the whole manufacturing process, increasing the manufacturing productivity without compromising the final quality.

(a) Promicron Spike (R) and the flat end mill Sandvik (490)
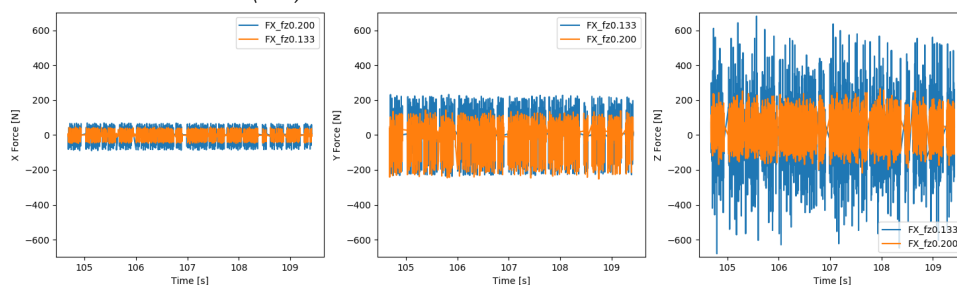
(b) 1106 Steady cutting forces measured with Spike(R).

Figure 6.18: *1106 Tool and steady cutting forces measured with Spike(R).*

(a) 1105 Machining results $f_z = 0.133$ mm.

(b) 1105 Machining results $f_z = 0.2$ mm.

(c) 1117 Machining results $f_z = 0.133$ mm.

(d) 1117 Machining results $f_z = 0.2$ mm.

Figure 6.19: *Comparison of surfaces with $f_z = 0.133$ and $f_z = 0.2$ mm*

Table 6.3: *Comparison of the impact of increase the feed per edge experimental and theoretical means.*

$f_z \frac{mm}{tht}$	F_{radial} [N]	$F_{tangential}$ [N]	F_{axial} [N]
0.133 Sim	18	63	38
0.200 Sim	20	86	47
Increment	11%	37%	24%
0.133 Exp	35	148	228
0.200 Exp	53	175	539
Increment	51%	18%	136%

Table 6.4: *Time reduction due to the f_z increment.*

Operation	Operation time min f_z = 0.133 mm	Operation time min f_z = 0.2 mm
1106	19	14
1115	48	32
1116	49	31
1117	48	39

6.3 Conclusions

Diverse industries are constantly presenting parts that are clear candidates to be manufactured through turn-milling operations, as the aeronautic sector. In this chapter a workpiece that resemble an aeronautic combustion case was manufactured following the tool cutting condition recommendations. Additionally, the turn-milling operations were analyzed with the developed models raising the following conclusions:

1. The specific analysis of turn-milling operations increased the process productivity. The analysis and the new proposal of cutting conditions reduced the manufacturing time around 20%.

2. The increment of the depth of cut a_p for the turn-milling roughing operations resulted in a more efficient use of the cutting edge reducing in more than three times the edge wear accumulated from the whole rough process.

7 | CONCLUSIONS AND FUTURE LINES

The kinematic and mechanical study of orthogonal turn-milling operations elucidates the effect of the cutting parameters on the uncut chip geometry and the cutting forces. However traditional milling models do not consider turn-milling parameters, evidencing the need for specific models for these operations. In the present study analytical and numerical models for orthogonal turn-milling operations have been presented to describe the uncut chip geometry and predict cutting forces. These models consider the increased number of parameters required to define the turn-milling process. These models were validated theoretically and experimentally and the following conclusions can be drawn:

• The analytical approaches accurately represented the uncut chip geometry in the centric case. Additionally, the volume of the collected cut chips corresponded to the prediction, and the qualitative comparison between the modeled uncut and cut chips collected were in good agreement.

• The approaches proposed in this thesis provide a efficient way to understand the effect of the cutting parameters on the uncut chip geometry, and more importantly, on the cutting forces in diverse operating scenarios. The force predictions were in good agreement with the experimental data. Besides of the tool flank zone, the tool end cutting zone is a very important component that must be considered and limits the process increasing considerably the cutting forces.

• The development of these uncut chip geometry predictive models is necessary to develop accurate cutting force models, contributing to appropriate machining strategies and increasing process productivity. In addition, this research promotes to a deeper understanding of the turn-milling process and can propose appropriate conditions for improved quality and higher material removal rates under safe cutting conditions.

• The analytical approach accurately reproduced the effect of the eccentricity in orthogonal turn-milling operations. The represented uncut chip geometry presented an accurate prediction of the geometry, being validated theoretically and experimentally.

• The eccentricity modifies the uncut chip volume presenting a maximum local value that not correspond to a linear function. Once that value is exceeded, the volume decreases considerably below the theoretical value $Vol = a_p a_e f_z$.

• The main effect of the eccentricity over the uncut chip geometry is the end cutting zone reduction and the increment of the instantaneous depth of cut of

the flank zone in flat end mills. It was evidenced in simulations and experimental results in the cutting trials with the reduction of the axial force as the eccentricity increases.

- The developments presented in this research are powerful tools to simulate vast cutting-case scenarios quickly. Additionally, it helps to understand that the eccentricity does modify the chip volume, giving a chance to identify geometrical errors by presenting a threaded excess of material in the workpiece result of the insert geometry.

- The numerical simulations performed provide clear evidence of the importance of the tool profile in the performance of turn-milling operations. This could lead to scenarios where the tool does not remove the material uniformly, resulting in geometrical errors. One such scenarios could occur if the wrong eccentricity were selected. Even when eccentricity is under the considerations presented by (Zhu et al., 2015a), these recommendations are only valid for flat end mills.

- This research did not find theoretical evidence that supports the condition of eccentricity ($e = r_t - l_s$) is "optimum". Indeed, the simulated results showed maximum forces at this condition of eccentricity. This scenario is detrimental to the slender parts, inducing higher dimensional errors.

- The engineered cutting conditions results in a useful way to improve the productivity in industrial scenarios. In the studied workpiece, these improved conditions reduced the overall manufacturing time by around 20%, which is a considerable improvement from the initial manufacturing time. The second workpiece was completely machined without changing the cutting edges, reducing the manufacturing cost and maintaining the workpiece quality.

- The process modeling provided information to make informed decisions that in addition to the workshop experience impacted positively in the process productivity. When proposing recommendations for improvement it is crucial to couple the complementary information of the experimental and theoretical, rather than placing excessive trust in only one method.

Future lines

A number of further research questions arouse in the development of this work, and it is thus recommended that the the following future lines are considered to increase the operation domain:

- The implementation of these models in commercial CAD/CAM software taking in advantage the uncut chip geometry due to the tool path programming. The direct cutting force simulations would work as a machining strategy validation with optimization aims.

- The surface topography in turn-milling seems to be strongly dependent of the cutting conditions and the tool profile. This resulting topography does not seems to be intuitive as presented in figure 6.16 (e and f). With the aim of enhance the industrial applications of this operations, it is recommended to develop models that relate the cutting condition, the tool profile, and the resulting surface in turn-milling.

• Based on the geometrical modeling presented in this thesis, further exploration of temperature modeling is recommended. This would help to complete the thermo-mechanical modeling of the process. Geometrical error and the out of tolerances machining would also be prevented with the develop of the thermo-mechanical models.

• Optimization methodologies should be developed further to determine the optimal operating window of the process.

• It might also be useful to explore approaches based on surfaces instead of points as was the case in this thesis. This recommendation is to develop models compatible with CAD software to integrate the thermo-mechanical models into commercial software.

8 | CONTRIBUTIONS

Articles in peer reviewed journals

● Otalora-Ortega, H., Osoro, P. A., & Arrazola Arriola, P. J. (2019). Analytical modeling of the uncut chip geometry to predict cutting forces in orthogonal centric turn-milling operations. International Journal of Machine Tools and Manufacture, 144. https://doi.org/10.1016/j.ijmachtools.2019.103428 (Q1)

● Otalora-Ortega, H., Aristimuño Osoro, P., & Arrazola Arriola, P. (2021). Uncut chip geometry determination for cutting forces prediction in orthogonal turn-milling operations considering the tool profile and eccentricity. International Journal of Mechanical Sciences, 198, 106351. https://doi.org/https://doi.org/10.1016/j.ijmecsci.2021.106351 (Q1)

International conferences

● Otalora-Ortega Harry, Aristimuñ Patxi, and Arrazola Pedro J. 2019. "odelado de fuerzas de corte en operaciones de torneado-fresdo ortogonal." *1^{e}r Seminario Colombo-Español de procesos de manufactura*, Bogotá-Medellín-Arrasate. Oct. 24 2019. (Oral presentation)

National conferences

● Otalora-Ortega Harry, Aristimuñ Patxi, and Arrazola Pedro J. 2019. "Influencia de los parámetros de corte sobre la geometría de viruta en operaciones de torneado-fresado." *22 Congreso de máquina herramienta*, Donostia-San Sebastian. Oct. 23, 2019-Oct. 25, 2019. (Oral presentation)

BIBLIOGRAPHY

Y Altintas, P Kersting, D Biermann, Erhan Budak, B Denkena, and I Lazoglu. Virtual process systems for part machining operations. *CIRP Annals*, 63(2): 585–605, 2014.

Yusuf Altintas. *Manufacturing automation: metal cutting mechanics, machine tool vibrations, and CNC design*. Cambridge university press, 2012.

Yusuf Altintas and AA Ber. Manufacturing automation: metal cutting mechanics, machine tool vibrations, and cnc design. *Appl. Mech. Rev.*, 54(5):B84–B84, 2001.

Akash Anand. Multi-tasking machine tools market is projected to grow at a cagr of 2.9URL https://www.marketresearchfuture.com/press-release/multi-tasking-machine-tools-market.

Patxi Aristimuño, Xabier Lazcano, Andres Sela, Rosa Basagoiti, and Pedro Jose Arrazola. An optimization methodology for material databases to improve cutting force predictions when milling martensitic stainless steel jethete-m152. *Procedia CIRP*, 77:287–290, 2018.

ArnoWerkzeuge. Arno milling cataloge, 2015. URL https://www.suncoasttools.com/PDFFILES/ARNO/ARNOMILLING.pdf.

PJ Arrazola, D Ugarte, and X Dominguez. A new approach for the friction identification during machining through the use of finite element modeling. *International Journal of Machine Tools and Manufacture*, 48(2):173–183, 2008.

Viktor P Astakhov. *Geometry of single-point turning tools and drills: fundamentals and practical applications*. Springer Science & Business Media, 2010.

Viktor P Astakhov and Xinran Xiao. A methodology for practical cutting force evaluation based on the energy spent in the cutting system. *Machining Science and Technology*, 12(3):325–347, 2008.

F Atabey, I Lazoglu, and Y Altintas. Mechanics of boring processes—part i. *International journal of machine tools and manufacture*, 43(5):463–476, 2003.

JL Boynton, R Tabibzadeh, and ST Hudson. Investigation of rotor blade roughness effects on turbine performance. In *ASME 1992 International Gas Turbine and Aeroengine Congress and Exposition*. American Society of Mechanical Engineers Digital Collection, 1992.

E Budak and Y Altintas. and armarego. eja (1996)."prediction of milling force coefficients from orthogonal cutting data.". *Journal ofEngg. for Industry (VI 18)*, pages 216–224.

E Budak, Y Altintas, and EJA Armarego. Prediction of milling force coefficients from orthogonal cutting data. *Journal of Manufacturing Science and Engineering*, 118(2):216–224, 1996.

Erhan Budak, Alptunc Comak, and Erdem Ozturk. Stability and high performance machining conditions in simultaneous milling. *CIRP Annals*, 62(1): 403–406, 2013.

Yong Lin Cai, Chao Huang, and Jian Yong Li. Experimental study of cutter wear based on turn-milling. In *Applied Mechanics and Materials*, volume 229, pages 538–541. Trans Tech Publ, 2012.

CECIMO. Toolbox - cecimo, 2021. URL https://www.cecimo.eu/economic-data/toolbox/.

Alessandro Checchi, Giuliano Bissacco, and Hans Nørgaard Hansen. A mechanistic model for the prediction of cutting forces in the face-milling of ductile spheroidal cast iron components for wind industry application. *Procedia CIRP*, 77:231–234, 2018.

Ding Chen, Xiaojian Zhang, Yakun Xie, and Han Ding. Precise estimation of cutting force coefficients and cutter runout in milling using differential evolution algorithm. *Procedia CIRP*, 77:283–286, 2018.

SK Choudhury and JB Bajpai. Investigation in orthogonal turn-milling towards better surface finish. *Journal of Materials Processing Technology*, 170(3):487–493, 2005.

SK Choudhury and KS Mangrulkar. Investigation of orthogonal turn-milling for the machining of rotationally symmetrical work pieces. *Journal of Materials Processing Technology*, 99(1-3):120–128, 2000.

A Comak and Y Altintas. Mechanics of turn-milling operations. *International Journal of Machine Tools and Manufacture*, 121:2–9, 2017.

Joel Martins Crichigno Filho. Prediction of cutting forces in mill turning through process simulation using a five-axis machining center. *The International Journal of Advanced Manufacturing Technology*, 58(1-4):71–80, 2012.

Danobat. Danobat danuni grinding machine for landing gear struts | danobat machine tool, 2021. URL https://www.danobatusa.com/danuni-grinding-machine-landing-gear-struts.

Kai Egashira, Takuya Furukawa, Keishi Yamaguchi, and Minoru Ota. Microcutting using a micro turn-milling machine. *Precision Engineering*, 44:81–86, 2016.

Sabahudin Ekinović, Edin Begović, and Amira Silajdžija. Comparison of machined surface quality obtained by high-speed machining and conventional turning. *Machining science and technology*, 11(4):531–551, 2007.

Ferrotall. Specialist in aeronautical machining, 2021. URL `https://www.ferrotall.es/maquinaria-aeronautica/`.

Hao-Jen Fu, RE DeVor, and Shiv Gopal Kapoor. A mechanistic model for the prediction of the force system in face milling operations. 1984.

R Funke and A Schubert. Increase of the coefficient of static friction using turn-milling with an inclined milling spindle. *Procedia CIRP*, 45:83–86, 2016.

Ge Gao, Baohai Wu, Dinghua Zhang, and Ming Luo. Mechanistic identification of cutting force coefficients in bull-nose milling process. *Chinese Journal of Aeronautics*, 26(3):823–830, 2013.

Gf. Mikron mill p 800 u 5 simultaneous axis precision machining, 2021. URL `https://www.gfms.com/country_ES/es/Products/Milling/high-performance-machining-centers/hpm-machine-line/mikron-mill-p-800u.html`.

O Gonzalo, H Jauregi, LG Uriarte, and LN López De Lacalle. Prediction of specific force coefficients from a fem cutting model. *The International Journal of Advanced Manufacturing Technology*, 43(3):348–356, 2009.

Oscar Gonzalo, Jokin Beristain, Haritz Jauregi, and Carmen Sanz. A method for the identification of the specific force coefficients for mechanistic milling simulation. *International Journal of Machine Tools and Manufacture*, 50(9):765–774, 2010. ISSN 0890-6955. doi: https://doi.org/10.1016/j.ijmachtools.2010.05.009. URL `https://www.sciencedirect.com/science/article/pii/S0890695510001070`.

Janez Gradišek, Martin Kalveram, and Klaus Weinert. Mechanistic identification of specific force coefficients for a general end mill. *International Journal of Machine Tools and Manufacture*, 44(4):401–414, 2004.

Niccolò Grossi. Accurate and fast measurement of specific cutting force coefficients changing with spindle speed. *International Journal of Precision Engineering and Manufacturing*, 18(8):1173–1180, 2017.

Chao Huang and Yong Lin Cai. Turn-milling parameters optimization based on cutter wear. In *Advanced Materials Research*, volume 602, pages 1998–2001. Trans Tech Publ, 2013.

Ibarmia. Ibarmia zvh multiprocess: Machining center fixed and mobile table. https://www.ibarmia.com/es/centros-de-mecanizado/centros-de-mecanizado-de-mesa-fija-y-columna-movil/zvh-multiprocess, 2020. URL `https://www.ibarmia.com/es/centros-de-mecanizado/centros-de-mecanizado-de-mesa-fija-y-columna-movil/zvh-multiprocess`.

Yusuf Tansel İç and Mustafa Yurdakul. Development of a decision support system for machining center selection. *Expert systems with Applications*, 36(2):3505–3513, 2009.

Ingersoll. Casing, 2021. URL `https://www.ingersoll-imc.com/industry/aerospace#!casing`.

S Jayaram, SG Kapoor, and RE DeVor. Estimation of the specific cutting pressures for mechanistic cutting force models. *International Journal of Machine Tools and Manufacture*, 41(2):265–281, 2001.

Zenghui Jiang, Xin Liu, and Xiaoye Deng. Modeling and simulation on surface texture of workpiece machined by tangential turn-milling based on matlab. In *2011 2nd International Conference on Artificial Intelligence, Management Science and Electronic Commerce (AIMSEC)*, pages 4072–4075. IEEE, 2011.

Kazuki Kaneko, Isamu Nishida, Ryuta Sato, and Keiichi Shirase. Virtual milling force monitoring method based on in-process milling force prediction model to eliminate predetermination of cutting coefficients. *Procedia CIRP*, 77:22–25, 2018.

Mehmet Emre Kara and Erhan Budak. Optimization of turn-milling processes. *Procedia CIRP*, 33:476–483, 2015.

Umut Karaguzel, Mustafa Bakkal, and Erhan Budak. Process modeling of turn-milling using analytical approach. *Procedia CIRP*, 4:131–139, 2012.

Umut Karaguzel, Emre Uysal, Erhan Budak, and Mustafa Bakkal. Modelling of turn milling processes for increased productivity. In *The 16 th International Conference on Machine Design and Production*, 2014.

Umut Karaguzel, Utku Olgun, Emre Uysal, Erhan Budak, and Mustafa Bakkal. Increasing tool life in machining of difficult-to-cut materials using nonconventional turning processes. *The International Journal of Advanced Manufacturing Technology*, 77(9-12):1993–2004, 2015a.

Umut Karaguzel, Emre Uysal, Erhan Budak, and Mustafa Bakkal. Analytical modeling of turn-milling process geometry, kinematics and mechanics. *International Journal of Machine Tools and Manufacture*, 91:24–33, 2015b.

Umut Karaguzel, Emre Uysal, Erhan Budak, and Mustafa Bakkal. Effects of tool axis offset in turn-milling process. *Journal of Materials Processing Technology*, 231:239–247, 2016.

Umut Karaguzel, Mustafa Bakkal, and Erhan Budak. Mechanical and thermal modeling of orthogonal turn-milling operation. *Procedia CIRP*, 58:287–292, 2017.

B Karpuschewski, C Döbberthin, K Risse, and L Deters. Analysis of the textured surface of tangential turn-milling. *Materials Performance and Characterization*, 6 (2):182–194, 2017.

M Kaymakci, ZM Kilic, and Y Altintas. Unified cutting force model for turning, boring, drilling and milling operations. *International Journal of Machine Tools and Manufacture*, 54:34–45, 2012.

O Kienzle and H Victor. Spezifische schnittkräfte bei der metallbearbeitung. *Werkstattstechnik und Maschinenbau*, 47(5):224–225, 1957.

Hossam A Kishawy, Ali Hosseini, Behnam Moetakef-Imani, and Viktor P Astakhov. An energy based analysis of broaching operation: Cutting forces and resultant surface integrity. *CIRP annals*, 61(1):107–110, 2012.

Janez Kopač and Marjan Pogačnik. Theory and practice of achieving quality surface in turn milling. *International Journal of Machine Tools and Manufacture*, 37(5):709–715, 1997.

J Krystof. Technologische mechanik der zerspanung. *Berichte uber betriebswissenschaftliche Arbeitenz", VDI-Verlag*, 1939.

Laip. Laip s.a. cnc toolholder systems, 2021. URL https://www.laip.es/.

P Lee and Yusuf Altintaş. Prediction of ball-end milling forces from orthogonal cutting data. *International Journal of Machine Tools and Manufacture*, 36(9):1059–1072, 1996.

Yi Zhi Liu, Fang Yu Peng, Sen Lin, Rong Yan, and Sheng Yang. Experimental research of workpiece temperature in orthogonal turn-milling compound machining. In *Advanced Materials Research*, volume 887, pages 1184–1190. Trans Tech Publ, 2014.

ME Martellotti. An analysis of the milling process. *Trans ASME*, 63:677, 1941.

Takashi Matsumura and Eiji Usui. Simulation of cutting process in peripheral milling by predictive cutting force model based on minimum cutting energy. *International Journal of Machine Tools and Manufacture*, 50(5):467–473, 2010a.

Takashi Matsumura and Eiji Usui. Predictive cutting force model in complex-shaped end milling based on minimum cutting energy. *International Journal of Machine Tools and Manufacture*, 50(5):458–466, 2010b.

Matweb. Aluminum 6063-t5, 2021. URL http://www.matweb.com/search/DataSheet.aspx?MatGUID=79875d1b30c94af39029470988004fb6&ckck=1.

M Eugene Merchant. Basic mechanics of the metal-cutting process. *ASME J. of Applied Mechanics*, 11:A168, 1944.

M Eugene Merchant. Mechanics of the metal cutting process. i. orthogonal cutting and a type 2 chip. *Journal of applied physics*, 16(5):267–275, 1945a.

M Eugene Merchant. Mechanics of the metal cutting process. ii. plasticity conditions in orthogonal cutting. *Journal of applied physics*, 16(6):318–324, 1945b.

C Neagu, M Gheorghe, and A Dumitrescu. Fundamentals on face milling processing of straight shafts. *Journal of materials processing technology*, 166(3):337–344, 2005.

D Olvera, LN López De Lacalle, FI Compeán, A Fz-Valdivielso, A Lamikiz, and FJ Campa. Analysis of the tool tip radial stiffness of turn-milling centers. *The International Journal of Advanced Manufacturing Technology*, 60(9-12):883–891, 2012.

Ona. Turbines - ona edm, 2021. URL `https://onaedm.es/sectores/turbinas/`.

Kashfull Orra and Sounak K Choudhury. Mechanistic modelling for predicting cutting forces in machining considering effect of tool nose radius on chip formation and tool wear land. *International Journal of Mechanical Sciences*, 142: 255–268, 2018.

Fangyu Peng, Yizhi Liu, Sen Lin, Rong Yan, Sheng Yang, and Bin Li. An investigation of workpiece temperature in orthogonal turn-milling compound machining. *Journal of Manufacturing Science and Engineering*, 137(1), 2015.

M Pogacnik and J Kopac. Dynamic stabilization of the turn-milling process by parameter optimization. *Proceedings of the Institution of Mechanical Engineers, Part B: Journal of Engineering Manufacture*, 214(2):127–135, 2000.

Matthias Putz, Gerhard Schmidt, Ulrich Semmler, Christian Oppermann, Michael Bräunig, and Umut Karaguzel. Modeling of heat fluxes during machining and their effects on thermal deformation of the cutting tool. *Procedia Cirp*, 46:611–614, 2016.

Wenwang Qiu, Qiang Liu, and Songmei Yuan. Modeling of cutting forces in orthogonal turn-milling with round insert cutters. *The International Journal of Advanced Manufacturing Technology*, 78(5-8):1211–1222, 2015.

Wenwang Qiu, Qiang Liu, Ji Ding, and Songmei Yuan. Cutting force prediction in orthogonal turn-milling by directly using engagement boundaries. *The International Journal of Advanced Manufacturing Technology*, 86(1):963–975, 2016.

Achmad Zaki Rahman, Khairul Jauhari, Helmi Suryaputra, Mulyamin Abubakar, Endarto Tri Wibowo, and Mahfudz Al Huda. The effects of feed rate to dimensional accuracy and roughness on machining process of propeller blade using 5-axis cnc turn-milling machine. *International Journal of Applied Engineering Research*, 12(24):14989–14992, 2017.

Ch Ratnam, K Arun Vikram, BS Ben, and BSN Murthy. Process monitoring and effects of process parameters on responses in turn-milling operations based on sn ratio and anova. *Measurement*, 94:221–232, 2016.

Rk. Rk international signs agreement with integrated production specialist mcm -, 2021. URL `https://www.rk-int.com/rk-international-signs-agreement-with-integrated-production-specialist-mcm/`.

M Salehi, TL Schmitz, R Copenhaver, R Haas, and J Ovtcharova. Probabilistic prediction of cutting and ploughing forces using extended kienzle force model in orthogonal turning process. *Procedia Cirp*, 77:90–93, 2018.

Sandvik. Sandvik coromant - tools and machining solutions, 2021. URL `https://www.sandvik.coromant.com/es-es/pages/default.aspx`.

Vedat Savas and Cetin Ozay. Analysis of the surface roughness of tangential turn-milling for machining with end milling cutter. *Journal of Materials Processing Technology*, 186(1-3):279–283, 2007.

Vedat Savas and Cetin Ozay. The optimization of the surface roughness in the process of tangential turn-milling using genetic algorithm. *The International Journal of Advanced Manufacturing Technology*, 37(3-4):335–340, 2008.

Vedat Savas, Cetin Ozay, and Hasan Ballikaya. Experimental investigation of cutting parameters in machining of 100cr6 with tangential turn-milling method. *Advances in Manufacturing*, 4(1):97–104, 2016.

Herbert Schulz and T Kneisel. Turn-milling of hardened steel-an alternative to turning. *CIRP annals*, 43(1):93–96, 1994.

Herbert Schulz and Guenter Spur. High speed turn-milling—a new precision manufacturing technology for the machining of rotationally symmetrical workpieces. *CIRP annals*, 39(1):107–109, 1990.

Eiji Shamoto and Y Altıntas. Prediction of shear angle in oblique cutting with maximum shear stress and minimum energy principles. 1999.

Sideron. Crankshafts for compressors - sidenor, 2021. URL `https://www.sidenor.com/en/products/crankshafts-for-compressors/`.

Gregor Smyczek, Grigory Rotshteyn, Florian Degen, and Thomas Bergs. Limits to simplified calculation of uncut chip thickness in milling. *Procedia CIRP*, 77: 275–278, 2018.

James Stewart, Daniel K Clegg, and Saleem Watson. *Calculus: early transcendentals*. Cengage Learning, 2020.

Xiao Yang Su, Zhi Jing Zhang, Xin Jin, and Yong Jun Deng. Modeling and prediction research on end mills wear in micro turn-milling process. In *Applied Mechanics and Materials*, volume 423, pages 741–745. Trans Tech Publ, 2013.

E Usui, A Hirota, and M Masuko. Analytical prediction of three dimensional cutting process—part 1: basic cutting model and energy approach. 1978.

Koji Utsumi, Shoki Shichiri, and Hiroyuki Sasahara. Determining the effect of tool posture on cutting force in a turn milling process using an analytical prediction model. *International Journal of Machine Tools and Manufacture*, 150: 103511, 2020.

Emre Uysal, Umut Karaguzel, Erhan Budak, and Mustafa Bakkal. Investigating eccentricity effects in turn-milling operations. *Procedia CIRP*, 14:176–181, 2014.

Jianrong Wang, Ertao Chen, Jianyu Yang, Wanshan Wang, et al. Applications of virtual reality in turn-milling centre. In *2008 IEEE International Conference on Automation and Logistics*, pages 2302–2305. IEEE, 2008.

Wei Wang, Fang Yu Peng, Rong Yan, and Xian Yin Duan. Iso-scallop toolpath generation for orthogonal turn-milling of ruled surfaces. In *Advanced Materials Research*, volume 591, pages 436–440. Trans Tech Publ, 2012.

Szymon Wojciechowski. The estimation of cutting forces and specific force coefficients during finishing ball end milling of inclined surfaces. *International Journal of Machine Tools and Manufacture*, 89:110–123, 2015.

Feng He Wu, Shu Zhi Li, Chong Min Jiang, and Dong Dong Gao. Design of the b-axis of the water chamber special turn-milling center. In *Key Engineering Materials*, volume 621, pages 294–303. Trans Tech Publ, 2014.

HB Wu and SJ Zhang. 3d fem simulation of milling process for titanium alloy ti6al4v. *The International Journal of Advanced Manufacturing Technology*, 71(5-8): 1319–1326, 2014.

Rong Yan, Xiaowei Tang, FY Peng, Yong Wang, and Feng Qiu. The effect of variable cutting depth and thickness on milling stability for orthogonal turn-milling. *The International Journal of Advanced Manufacturing Technology*, 82(1-4):765–777, 2016.

Juhchin A Yang, Venkatraman Jaganathan, and Ruxu Du. A new dynamic model for drilling and reaming processes. *International Journal of Machine Tools and Manufacture*, 42(2):299–311, 2002.

Tianbiao Yu, Xuewei Zhang, Weili Liang, and Wanshan Wang. A web-based virtual system for turn-milling center. *The International Journal of Advanced Manufacturing Technology*, 67(9-12):2395–2409, 2013.

Song Mei Yuan, C Zhang, and YZ Huang. Introduction to turn-milling technology and application. In *Applied Mechanics and Materials*, volume 148, pages 748–752. Trans Tech Publ, 2012.

G Yucesasn and Y Altintas. Prediction of ball end milling forces.

NZ Yussefian, Behnam Moetakef-Imani, and H El-Mounayri. The prediction of cutting force for boring process. *International Journal of Machine Tools and Manufacture*, 48(12-13):1387–1394, 2008.

Norfadzlan Yusup, Azlan Mohd Zain, and Siti Zaiton Mohd Hashim. Evolutionary techniques in optimizing machining parameters: Review and recent applications (2007–2011). *Expert Systems with Applications*, 39(10):9909–9927, 2012.

Peter Zelinski. Applying turn-milling, modern machine shop, 2021. URL `https://www.mmsonline.com/articles/applying-turn-milling`.

G Zheng, QZ Bi, and LM Zhu. Smooth tool path generation for five-axis flank milling using multi-objective programming. *Proceedings of the Institution of Mechanical Engineers, Part B: Journal of Engineering Manufacture*, 226(2):247–254, 2012.

Li Zheng, Yun Shun Chiou, and Steven Y Liang. Three dimensional cutting force analysis in end milling. *International Journal of Mechanical Sciences*, 38(3): 259–269, 1996.

Li Da Zhu, Jia Ying Pei, Tian Biao Yu, and Wan Shan Wang. Kinematics simulation analysis of turn-milling center based on virtual prototype. In *Applied Mechanics and Materials*, volume 43, pages 683–686. Trans Tech Publ, 2011.

Lida Zhu, Liang Tang, Cong Su, Junming Hou, and Wanshan Wang. Co-simulation of rigid-flexible coupling system for turn-milling center. In *2008 7th World Congress on Intelligent Control and Automation*, pages 3683–3686. IEEE, 2008.

Lida Zhu, Haonan Li, and Wansan Wang. Research on rotary surface topography by orthogonal turn-milling. *The International Journal of Advanced Manufacturing Technology*, 69(9):2279–2292, 2013.

Lida Zhu, Zenghui Jiang, Jiashun Shi, and Chengzhe Jin. An overview of turn-milling technology. *The International Journal of Advanced Manufacturing Technology*, 81(1):493–505, 2015a.

Lida Zhu, Haonan Li, Weili Liang, and Wanshan Wang. A web-based virtual cnc turn-milling system. *The International Journal of Advanced Manufacturing Technology*, 78(1-4):99–113, 2015b.

Lida Zhu, Xiaoliang Jin, and Changfu Liu. Experimental investigation on 3d chip morphology properties of rotary surface during orthogonal turn-milling of aluminum alloy. *The International Journal of Advanced Manufacturing Technology*, 84(5-8):1253–1268, 2016a.

Lida Zhu, Haonan Li, and Changfu Liu. Analytical modeling on 3d chip formation of rotary surface in orthogonal turn-milling. *Archives of Civil and Mechanical Engineering*, 16:590–604, 2016b.

Rixin Zhu, Shiv G Kapoor, and Richard E DeVor. Mechanistic modeling of the ball end milling process for multi-axis machining of free-form surfaces. *J. Manuf. Sci. Eng.*, 123(3):369–379, 2001.

GP Zou, I Yellowley, and RJ Seethaler. A new approach to the modeling of oblique cutting processes. *International Journal of Machine Tools and Manufacture*, 49(9):701–707, 2009.

A | Workpiece technical drawing

	Machining Process:	Main Tolerance	A4	Name	Data
	5 Axis Milling	ISO 2768 - mK	Drawer	Harry Otalora-Ortega	12/2019
			Reviewer	Pedro J. Arrazola	12/2019
MONDRAGON UNIBERTSITATEA	Quality4 Bulk material	Quality4 - PhD Thesis Turn-Milling		Initial Dim: D193Xd73XL300	
				Material: E355 (EN-10297-1)	
Scale 1:3					

Note1: All of the edges are chamfered at 0.5 X 45°

Note2: The piece has 5 bosses. Each boss has a center hole D15 and 4 satellite holes D6

Note3: Each flange has 10 lobes and 10 holes and the workpiece have two flanges

Ø170

20 X 36°

20 X 36°

20 X R12.50 ⌵ 8
20 X Ø6 ⌵ 8

DETAIL C
SCALE 2 :3

SECTION B-B
SCALE 1 :3

5 X 72°

0.05

1.6
0.4

0.01

1.6
0.4

1.6
0.4

2

SECTION A-A
SCALE 1 :3

40
5 X Ø34
5 X Ø15 ⌵ 13.5
5 x 20
18.50
7

11.50
Ø144
190

32

104

Ø24

90°

45°

8

8

20 X Ø6 ⌵ 14

// 0.1 D

	Name	Date
Drawer	Harry Otalora-Ortega	12/2019
Reviewer	Pero J. Arrazola	12/2019

A4

Main Tolerance
ISO 2768 - mK

Machining Process:
5 Axis Milling

Weight: 4.053 kg

Material: E355 (AISI 1024)

Quality4 - PhD Tesis
Turn-Milling

Industrial Piece Quality4

Scale
1:3

MONDRAGON
UNIBERTSITATEA
GOI ESKOLA POLITEKNIKOA
ESCUELA POLITECNICA SUPERIOR